

Defect Investigation on Hematite Photoanodes

by

Yutong Liu

A thesis
presented to the University of Waterloo
in fulfillment of the
thesis requirement for the degree of
Doctor of Philosophy
in
Chemistry

Waterloo, Ontario, Canada, 2023

© Yutong Liu 2023

Examining Committee Membership

The following served on the Examining Committee for this thesis. The decision of the Examining Committee is by majority vote.

Supervisor: Rodney D. L. Smith
Assistant Professor
Department of Chemistry, University of Waterloo

Internal Member: Vivek Maheshwari
Associate Professor
Department of Chemistry, University of Waterloo

Internal Member: Pavle Radovanovic
Professor
Department of Chemistry, University of Waterloo

Internal-External Member: Michael Pope
Associate Professor
Department of Chemical Engineering, University of Waterloo

External Member: Sylvie Morin
Professor
Department of Chemistry, York University

Author's Declaration

This thesis consists of material all of which I authored or co-authored: see Statement of Contributions included in the thesis. This is a true copy of the thesis, including any required final revisions, as accepted by my examiners.

I understand that my thesis may be made electronically available to the public.

Statement of Contributions

Prof. Rodney Smith as Yutong Liu's supervisor assisted with the conceptualization of the projects, the creation of the data acquisition, and the analysis of the results. He also took part in writing and editing manuscripts published (**Chapter 3, Chapter 4, Chapter 5, Chapter 6**) and in peer reviewed journals. The first drafts were written by Yutong Liu, and Prof. Smith was involved in the editing process. The details of the contributions of the authors of the publications listed below. I am the sole author of the rest of the thesis.

Part of the work described in **Section 1.4** has been published as:

"Structure–property Correlations for Analysis of Heterogeneous Electrocatalysts"

Elif Pinar Alsaç, Nataraju Bodappa, Alexander W. H. Whittingham, Yutong Liu, Adriana de Lazzari, and Rodney D. L. Smith

Chem. Phys. Rev., **2021**, 2, 031306.

DOI:10.1063/5.0058704.

Copyright 2022 AIP Publishing.

Chapter 3 is reproduced in part with permission the Royal Society of Chemistry from:

"Identifying Protons Trapped in Hematite Photoanodes Through Structure–Property Analysis."

Yutong Liu, Rodney D. L. Smith

Chem. Sci. **2020**, 11, 1085–1096.

DOI: 10.1039/C9SC04853G

Copyright 2020 Royal Society of Chemistry:

- Yutong Liu synthesized all samples and carried out characterization all measurement and primary data analysis.
- Prof. Rodney Smith helped with additional data analysis.

Chapter 4 is reproduced with permission from:

"Differentiating Defects and Their Influence on Hematite Photoanodes Using X-ray Absorption Spectroscopy and Raman Microscopy"

Yutong Liu, Rodney D. L. Smith

ACS Appl. Mater. Interfaces **2022**, 14, 5, 6615–6624.

DOI:10.1021/acsami.1c20951

Copyright 2022 American Chemical Society:

- Yutong Liu synthesized all samples, performed characterization measurement and processed X-ray absorption data.
- Prof. Rodney Smith helped with X-ray absorption data analysis and electrochemical impedance spectroscopy analysis.

Chapter 5 is reproduced in part with permission Wiley & Sons, Inc. publishing from:

"Identification of Three Coexistent Defect Types in Hematite Photoanodes Through Structure–Property Analysis"

Jixi Zhang, Yutong Liu, Rodney D. L. Smith

Energy Technol. **2022**, 10, 2100181

Copyright 2022 Wiley & Sons, Inc.

- Jixi Zhang carried out material preparation and photoelectrochemical measurement experiments.
- Yutong Liu helped with material preparation and Raman spectroscopy.
- Prof. Rodney Smith did data analysis and manuscript writing.

Chapter 6 is reproduced in part with permission from IOP Publishing from:

"Mechanistic Insights into Lepidocrocite Conversion to Hematite from Variable Temperature Raman Microscopy"

Yutong Liu, Jixi Zhang, Nataraju Bodappa, Rodney D. L. Smith

J. Phys. Energy, **2021**, 3, 044002.

Copyright IOP Publishing. Reproduced with permission. All rights reserved.

- Yutong Liu performed majority of experiments.
- Jixi Zhang helped with photoelectrochemical measurement.
- Dr.Nataraju Bodappa helped with Raman data analysis.
- Rodney D.L. Smith helped with data analysis and writing.

Chapter 7 contains research that is not yet published

- Yutong Liu fabricated tin and fluorine doped samples, measured Raman spectrum of those samples and analyzed correlations.
- Justine Bissonnette helped with the XRD measurements and fabricated undoped hematite samples.
- Rodney D.L. Smith helped with data analysis and writing.

Abstract

Efforts to improve the efficiency of photoelectrocatalytic reactions on hematite photoanodes routinely focus on the analysis of photophysics, or on the fabrication of complex material architectures. The discontinuity of experimental results and mechanistic proposals found across the literature, however, reflect a lack of control over detailed structural features. This thesis aims to analyze specific types of structural defects and correlate their presence to photoelectrocatalytic behavior parameters. Following this strategy, we successfully identify coexistent defects in hematite photoanodes. This finding provides a means to rapidly diagnose a specific structural defect with Raman spectroscopy and will aid in the optimization of fabrication protocols for hematite photoanodes.

In this thesis, we use structure-property analysis combined with photoelectrochemical property parameters and structural parameters from X-ray diffraction, Raman and X-ray absorption spectroscopic data on a series of hematite photoanodes with various photoelectrochemical behaviours (**Chapter 3**, **Chapter 4** and **Chapter 5**). The correlations identify oxygen vacancy defects from the oxygen-deficient environment and iron vacancy defects induced by trapped protons from the oxygen-efficient environment as the dominant defects within the hematite lattice. Raman spectra data also proposes the coexistence of three types of structural defects. Each defect type is found to exert a unique influence on photoelectrochemical behaviour and becomes dominant under specific fabrication conditions. Dopants including tin atoms as cation doping and fluorine atoms as anion doping are also introduced in hematite to investigate the influence on hematite structural feature change (**Chapter 7**). Raman spectra show consistent trends with previous point defect types. With the sensitivity of Raman spectroscopy, we employ *insitu* variable temperature Raman spectroscopy and other conventional thermal analysis to study the conversion of lepidocrocite to hematite under varied gaseous environments as a model case (**Chapter 6**). The combined results further prove that protohematite accompanied with iron vacancies can form during the phase transition process and degrade photoelectrocatalytic performance. This research illustrates a powerful method to study solid state phase transitions.

Acknowledgement

First, I would like to express my gratitude to my supervisor Professor Rodney Smith. He trusted and believed in me in our first interview, and gave me this opportunity to work on this project. I have been learning a lot from his knowledge and his attitude toward science. Without his mentorship, I could not achieve this.

I also would like to acknowledge my committee members, Professor Holger Kleinke, Professor Vivek Maheshwari and Professor Pavle Radovanovic for their advice and time over the past four years. I would like to acknowledge Professor Michael Pope and Professor Sylvie Morin for serving on the Examining Committee as well.

I would like to acknowledge Dr. Bruce Ravel from Brookhaven National Laboratory for helping us to carry out X-ray absorption spectrum measurement during the pandemic.

I am thankful for all the former and current members of our group. Alex Whittingham and Elif Pınar Alsac, you are always there and support me over the past five years. I also need to say thanks to all the Smith group members: Dr. Nataraju Bodappa, Adriana de Lazzari, Xinran Liu, Jixi Zhang, Una Hogan, Dr. Viswanathan Mohandoss and Dr. Holly Fruehwald. My gratitude extends to several previous students who helped me with the experiments in this project: Erqian Gao, Mengting Wang, Jixi Zhang, Justine Bissonnette, Pierre Gadras and Hana Hopson.

Last but not least, none of this could have happened without my parents Yidan Tong and Yunsheng Liu. I am really thankful for their sacrifices, love and support for so many years. You always encourage me when I am depressed, especially during the pandemic, which is a hard time for all of us. This accomplishment would not have been possible without you.

Table of Contents

List of Figures	xiii
List of Tables	xx
List of Abbreviations	xxiii
1 Introduction	1
1.1 Motivation	1
1.1.1 Solar Water Splitting	2
1.1.2 Photoanodes in Solar Water Splitting	5
1.1.3 Hematite Photoanode Overview	8
1.2 Iron Oxide and Hydroxide Phases	10
1.2.1 Crystal Structure	10
1.2.2 Phase transition	15
1.3 Defects in Hematite	17
1.3.1 Point Defects	17
1.3.2 Surface State Defects	20
1.4 Structure-Property Analysis	21
1.5 Thesis Objective and Overview	22
2 Characterization Methods and Techniques	24
2.1 Precursor Synthesis	24
2.1.1 Electrodeposition Method for Lepidocrocite Film (γ -FeOOH)	24

2.1.2	Precipitation Method for Lepidocrocite Powder (γ -FeOOH) . . .	25
2.1.3	Hydrolysis Method for Akaganeite Film (β -FeOOH)	26
2.2	Hematite Fabrication	27
2.3	Material Characterization	27
2.3.1	Raman Spectroscopy	28
2.3.2	Infrared Spectroscopy	31
2.3.3	Ultraviolet-visible Spectroscopy (UV-vis)	31
2.3.4	X-ray Absorption Spectroscopy (XAS)	32
2.3.5	Powder X-Ray Diffraction (XRD)	35
2.3.6	X-ray Photoelectron Spectroscopy (XPS)	36
2.3.7	Thermal Analysis	37
2.4	(Photo)Electrochemical Techniques	38
2.4.1	Photoelectrocatalytic Measurement	38
2.4.2	Electrochemical Impedance Spectroscopy	39
3	Revealing Interstitial Protons Through Structure-property Analysis	42
3.1	Introduction	42
3.2	Results	44
3.2.1	Characterization of α -Fe ₂ O ₃ Powders	44
3.2.2	Raman spectroscopy of photoanode films	47
3.2.3	Parametrizing photoelectrocatalysis	51
3.2.4	Band Structure Measurements	53
3.2.5	Correlating structure and behavior	54
3.3	Discussion	57
3.3.1	Control over structural integrity	57
3.3.2	Influence on PEC	58
3.3.3	Nature of the defect	60

3.4	Conclusions	63
3.5	Experimental Details	64
3.5.1	Material fabrication	64
3.5.2	Raman Spectroscopy	65
3.5.3	Infrared Spectroscopy	66
3.5.4	X-ray Diffraction	66
3.5.5	UV-vis Spectroscopy	67
3.5.6	X-ray Photoelectron Spectroscopy	67
3.5.7	PEC analysis	67
4	Differentiate Iron and Oxygen Vacancies	68
4.1	Introduction	68
4.2	Results and Discussion	69
4.2.1	Sample Fabrication	69
4.2.2	X-ray Absorption Spectroscopy	70
4.2.3	Structural Model Development	73
4.2.4	Photoelectrochemical Properties	75
4.2.5	Raman Spectroscopy	76
4.2.6	Correlational Analysis	77
4.2.7	Structure–Property Correlations	78
4.3	Conclusions	84
4.4	Experimental Details	85
4.4.1	Hematite Fabrication	85
4.4.2	Raman Microscopy	85
4.4.3	PEC Measurements	86
4.4.4	X-ray Absorption Fine-Structure Spectroscopy	86
5	Identify Coexistent Defects	88

5.1	Introduction	88
5.2	Results and Discussion	89
5.2.1	Synthesis	89
5.2.2	Behavioral Parameters	91
5.2.3	Structural Information	93
5.2.4	Structure-Property Correlations Detection	95
5.2.5	Correlation Identities	97
5.2.6	Correlation Interpretations	98
5.3	Conclusion	100
5.4	Experimental Details	101
5.4.1	Material fabrication	101
5.4.2	Raman Spectroscopy	102
5.4.3	Photoelectrochemical Analysis	103
6	Mechanistic Insights into Lepidocrocite to Hematite Phase Conversion from Variable Temperature Raman Spectroscopy	104
6.1	Introduction	104
6.2	Results and discussion	107
6.2.1	Variable temperature Raman spectrum	107
6.2.2	Thermal Analysis	112
6.2.3	Photoelectrochemical Performance	120
6.3	Conclusion	123
6.4	Experimental	124
6.4.1	Lepidocrocite Fabrication	124
6.4.2	Photoanode Fabrication	124
6.4.3	Raman Spectroscopy	125
6.4.4	Thermal Analysis	126
6.4.5	Photoelectrocatalysis	126

7	Discovering Correlations between Structure and Properties for Doped Hematite	127
7.1	Introduction	127
7.2	Results and Discussion	128
7.2.1	Raman Spectra Analysis	128
7.2.2	X-ray Diffraction Results	132
7.2.3	Overall Correlations	134
7.3	Conclusion	137
7.4	Experimental	138
7.4.1	Hematite fabrication	138
7.4.2	Raman microscopy measurement	138
7.4.3	X-ray diffraction measurement	139
8	Conclusion and Outlook	140
	References	142
	Appendix A Supplementary Information for: Identifying Interstitial Protons Through Structure-property Analysis	156
	Appendix B Supplementary Information for: Differentiate Iron and Oxygen Vacancies	159

List of Figures

1.1	Schematic illustration of solar water splitting reaction at pH=14. . . .	3
1.2	Spectrum of solar radiation and corresponding band gap values. Red and purple shadows represent the solar radiation absorbed by α -Fe ₂ O ₃ and TiO ₂ respectively. Data is from ASTM G173-03 Reference Spectra derived from SMARTS v. 2.9.2 (AM1.5) ¹³	5
1.3	Band gap values and band positions of common semiconducting materials. ¹⁴	6
1.4	Three different linkages of FeO ₆ octahedra, face-sharing, edge-sharing and corner-sharing octahedra.	11
1.5	Crystal structure of common iron oxide and hydroxide phases.	12
1.6	Schematic representation of major formation and transformation pathways of common iron oxides. ⁴⁸	16
1.7	Concentration of native point defects in hematite at T=1100 K in panel (a) and at T=700 K in panel (b). Reproduced from Ref. 50 with permission from the PCCP Owner Societies. ⁵⁰	19
1.8	Schematic illustration of surface states at the interface between semiconducting photoanode and electrolyte.	21
2.1	Schematic representation of Rayleigh, Stokes and Anti-Stokes scattering.	29
2.2	Raman spectra of common iron oxides and hydroxides	30
2.3	Normalized X-ray absorption spectrum of hematite	33
2.4	Schematic representation of Bragg's law.	36
2.5	The scheme of the photoelectrochemical cell used in the project.	39
2.6	Electrochemical impedance spectroscopy Nyquist plot (A) of the Randles cell and corresponding equivalent circuit (B)	40

3.1	Powder X-ray diffraction patterns obtained from (A) γ -FeOOH and following annealing of (B and C) γ -FeOOH at 600 °C and 800 °C for two hours	45
3.2	Raman spectra acquired on iron oxide powders. (A) γ -FeOOH powder and samples annealed at various temperatures. (B) Spectra as a function of laser power on a powder annealed at 350 °C. (C) Magnified view. (D) K_2SO_4 impurity. (E) Powders annealed for all 12 samples and (F) magnified view.	47
3.3	Infrared spectra for hematite thin film samples annealed at 800 °C for 10 min and 2h.	47
3.4	Raman spectra acquired on α -Fe ₂ O ₃ films. (A) The full spectral range, (B) magnification of key peaks, (C) A Raman spectroscopic map of the 23 × 24 μ m region, (D) Histograms showing intensity ratios of the I_{499} and I_{612} vibrational modes to the I_{660} for Raman spectra. (E) White image of sample, (F) Comparison of the averaged spectrum from two scales.	50
3.5	Photoelectrochemical behavior and characterization of α -Fe ₂ O ₃ films. (A), (B) Voltammetric behavior under illumination (C) Mott–Schottky plots of films prepared at 800 °C for 2h. (D), (E) Rapid cathodic sweep results. (F) UV-visible absorption spectra for the eight films annealed at 800 °C	52
3.6	Method for determining photoelectrocatalytic onset. Samples shown are (A) 800 °C for 2 hours under dry N ₂ and (B) 800 °C for 2 hours under dry O ₂ , and (C) 800 °C for 10 min under dry O ₂	52
3.7	Bulk resistance obtained from fitting EIS data on the α -Fe ₂ O ₃ sample series. (A) Resistance as a function of voltage. Resistance at 1.0 V _{RHE} as a function of Raman intensity ratios (B) I_{499}/I_{660} and (C) I_{612}/I_{660}	54
3.8	Correlations observed between Raman spectra and properties across the sample series. Correlations are shown for the relative intensity of key Raman vibrations and (A) photocurrent density, (B) the onset of photoelectrocatalysis and the flat-band potential, and (C) optical band gap. Correlations between charge carrier concentration, and (D) photocurrent density, (E) flat band potential and onset of photoelectrocatalysis, and (F) Raman intensity ratio.	55
3.9	High resolution X-ray photoelectron spectroscopy results in the (A) O 1s and (B) Fe 2p and (C) valence band regions for selected samples annealed at 800 °C. (D) A magnification of the valence band edge region highlighting differences between samples annealed in O ₂ for 2 h and 10 min.	56

3.10	Possible changes in band structure induced by lattice distortion and the identity of critical vibrations for α -Fe ₂ O ₃ . (A) The influence of an increase in the concentration of donor states and the broadening of donor states. (B) The influence of a cathodic shift in conduction and valence band edges and an anodic shift in intraband states. (C) Unit cell for α -Fe ₂ O ₃ denoting the connectivity and key structural features, and the identity of Raman vibrations that are found to correlate with photoanode properties.	62
3.11	Sample of processing protocol used for Raman spectra showing the sampled annealed at 800 °C for 10 min. under humidified N ₂ environment. (A) The raw spectrum and baseline to be subtracted. (B) Normalized form of the baseline subtracted data.	66
4.1	X-ray absorption fine-structure spectroscopy on hematite photoanode series.(A) Iron <i>K</i> -edge XANES, (B) EXAFS in <i>k</i> -space, and (C) FT-EXAFS spectra. Comparison of (D) XANES and (E) FT-EXAFS results for the 1 h N ₂ sample. (F) Iron <i>K</i> -edge location as a function of annealing time for N ₂ and O ₂ environment.	71
4.2	Comparison of the edge positions for individual XANES spectra to gauge the stability of energy calibration and precision of measurements. The six spectra acquired for four samples are shown for comparison. Each sample is broken into two batches: three collected in a first batch, then three collected approximately 24 hours later	72
4.3	Structure of α -Fe ₂ O ₃ and key features for analysis. (A) Unit cell of hematite with EXAFS distances Fe–Fe ₃ and Fe–Fe ₄ marked. (B) Face-sharing and edge-sharing motifs in hematite with EXAFS distances Fe–O ₁ , Fe–O ₂ , Fe–Fe ₁ , and Fe–Fe ₂ marked. Raman vibrations used in structure–structure analysis at <i>ca.</i> (C) 227, (D) 293, and (E) 411 cm ⁻¹ . Graphics prepared using VESTA. ¹²⁶	74
4.4	Photoelectrochemical behavior and electrochemical impedance spectroscopy results. (A) Voltammetric behavior under illumination for films annealed under different environments. (B) Nyquist plots of the film annealed in N ₂ for 12 min at select voltages to show influence of voltage. (C) Mott–Schottky plots of films prepared by annealing in different conditions.	75
4.5	Raman spectra for hematite sample series. (A) All 75 spectra acquired over three 4 × 4 μm grids on the α -Fe ₂ O ₃ sample annealed under O ₂ for 4 h and (B) histogram showing the distribution of selected peak ratios. The solid line shows a Gaussian distribution fit of each histogram. Vertical shading denoting 85% of all spectra, captured by the ranges noted. (C) Spectra acquired by averaging all 75 individual spectra for each sample. Solid lines represent samples annealed under O ₂ and dashed lines under N ₂	77

4.6	Correlations observed between XANES data and PEC properties across the sample series. (A) Correlation between the Fe <i>K</i> -edge location and $j_{1.23V}$ and (B) between charge carrier density N_d and $j_{1.23V}$ across the entire series. (C) Comparison of change in oxidation states calculated by XANES with the oxidation state calculated from N_d . Error bars represent the standard deviation across six individual spectra for each sample.	79
4.7	Correlations involving XAS-derived parameters for hematite films annealed in N_2 and O_2 . (A) Trends in photocurrent density $j_{1.23V}$ and R_{Fe-Fe1} distances for samples annealed under O_2 , and R_{Fe-O2} distances for those annealed under N_2 . (B) Iron-oxygen bond length increases with Fe <i>K</i> -edge values for samples annealed in N_2 . (C) Location of the E_u vibration as a function of R_{Fe-Fe1} , and (D) Intensity of the FT-EXAFS peak near 2.7 Å against the Raman intensity ratio I_{411}/I_{293} for hematite annealed in O_2 . Correlation between mean standard relative deviation ($2\sigma_{Fe-Fe2}$) with Raman intensity ratios of (E) I_{411}/I_{293} for O_2 samples and (F) I_{411}/I_{227} for hematite annealed in N_2 and O_2 environments.	81
5.1	Akaganeite (β -FeOOH) film Raman spectrum used as precursors for hematite synthesis	90
5.2	Photoelectrochemical properties of α -Fe ₂ O ₃ sample series. (A) Systematically determination of the onset of photoelectrocatalysis E_{PEC} for an electrode sintered at 800°C under humidified O_2 . (B) Comparison of photoelectrochemical behavior for 10 samples prepared using unique conditions. (C) Extraction of the charge carrier density, N_d , and the flat band potential, E_{fb} , using Mott-Schottky plots. (D) The Nyquist impedance representation of data acquired at a subset of the 100 mV voltage steps. (E) Comparison of Mott-Schottky plots for these 10 samples. (F) Mott-Schottky plot for the sample sintered at 800°C under dry O_2	93
5.3	Raman spectra acquired for the α -Fe ₂ O ₃ sample series. (A) Raman spectra acquired by microscopic mapping of 10 samples prepared with unique conditions, with each normalized to the 227 cm ⁻¹ peak. The upper section of the panel contains samples sintered at 600 °C, and the lower section at 800 °C. Non-trivial correlations observed between the intensity ratio I_{499}/I_{660} and (B) $j_{1.23V}$ and (C) E_{fb} . The dashed trend lines highlight the grouping of samples sintered under dry or humid conditions; no such grouping is obvious in panel (C).	95

5.4	Number of structure-property correlation candidates as a function of statistical cutoff value. Linear regression analysis was performed on (A) the entire dataset and after the dataset was broken into segments according to (B) gaseous sintering environment, (C) presence of humidity in the sintering environment, and (D) sintering temperature. An R^2 cutoff of 0.95 is marked for reference.	97
5.5	Prominent correlations between Raman spectroscopic data and photoelectrochemical data for segments of the dataset. Correlations between (A) flat band potential and (B) charge carrier density for samples sintered under N_2 . Correlations between (C) flat band potential and (D) charge carrier density for samples sintered in humidified environments. Comparison of correlations between j_{PEC} and (E) I_{499}/I_{660} for photoanodes prepared under humid and dry conditions, and for (F) I_{293}/I_{660} under dry sintering conditions.	99
6.1	Variable temperature Raman spectra on γ -FeOOH under (A) dry O_2 , (B) dry N_2 , (C) humid O_2 and (D) N_2 conditions.	109
6.2	Sample Raman spectra acquired from a heat ramp under all four conditions.	110
6.3	The integrated peak areas for individual peaks and combined overlapped peaks that are relevant to (A) lepidocrocite, (B) maghemite, and (C) hematite.	110
6.4	Variable temperature Raman and thermal analysis of γ -FeOOH under dry, inert atmospheres. The (A) integrated peak area for major peaks in γ -FeOOH (L_1), γ -Fe $_2$ O $_3$ (M_3) and α -Fe $_2$ O $_3$ (H_2) and (B) the peak locations for L_2 , M_3 and H_2 . Simultaneously performed (C) thermogravimetric analysis and (D) differential scanning calorimetry under an argon environment.	113
6.5	Raman microscopic map of lepidocrocite samples heated to 350 °C in a dry O_2 environment. (A) White light image and (B) a corresponding Raman spectral map where hematite peaks are observed. (C) The spectra averaged across the two $2 \times 2 \mu m$ areas identified in panel A. (D) Comparison of the spectrum for hematite observed at 350°C with spectra acquired for samples heated at 600 °C and 800 °C, with intensities scaled to enable comparison.	116
6.6	Speciation plots showing the normalized area of well-resolved peaks in spectra acquired during variable temperature Raman spectroscopy experiments. Data for γ -FeOOH (L_1 , black), γ -Fe $_2$ O $_3$ (M_3 , red) and α -Fe $_2$ O $_3$ (H_2 , blue) is shown under (A) dry N_2 , (B) humid N_2 , (C) dry O_2 and (D) humid O_2	119

6.7	Position of selected peaks in spectra acquired during variable temperature Raman spectroscopy experiments. Data is shown for strong peaks in (A) γ -FeOOH (L_1 , black), (B) γ -Fe ₂ O ₃ (M_3 , red) and (C) α -Fe ₂ O ₃ (H_2 , blue) under dry N ₂ , humid N ₂ , dry O ₂ and humid O ₂ listed from top to bottom	120
6.8	Pairwise comparison of photoelectrocatalytic oxygen evolution performance of α -Fe ₂ O ₃ films synthesized by a varied three-stage annealing protocol. Comparison of the role of O ₂ versus N ₂ in the intermediate 550 °C annealing step on photocurrents in (A) dry and (B) humid conditions. Comparison of the first derivative of photocurrents to demonstrate the influence of O ₂ versus N ₂ environments in the final 800 °C annealing step on the onset for photoelectrocatalysis under (C) dry and (D) humid conditions.	122
6.9	Variable temperature stage used for Raman spectroscopy.	126
7.1	Raman spectra for a series of (A) fluorine doped hematite samples with dopant concentrations from 0.05 to 10%, (B) tin doped hematite samples with dopant concentrations from 0.01 to 10%, and (C) non doped hematite samples annealed in different environments.	130
7.2	Trends in fluorine dopant concentration and Raman intensity ratios. (A) Positive correlations for two Raman intensity ratios I_{227}/I_{246} and I_{612}/I_{246} . (B) Correlations after conducting logarithm of both Raman intensity ratios of I_{227}/I_{660} and I_{246}/I_{660} and doping concentration.	131
7.3	Trends in tin dopant concentration and Raman intensity ratios. (A-D) Correlations for the logarithm of Raman intensity ratios involving peaks at 246, 299, 411 and 612 cm ⁻¹ with peak at 660 cm ⁻¹ and doping concentration.	132
7.4	(A) X-ray diffraction patterns acquired on fluorine doped hematite powders. The vertical orange lines at the bottom represent α -Fe ₂ O ₃ (COD#9015231). Correlation between (B) lattice parameter a , (C) lattice parameter c and fluorine doping concentration.	133
7.5	X-ray diffraction patterns acquired on tin doped hematite powders. The vertical pink lines at the bottom represent α -Fe ₂ O ₃ (COD#9015231).	134
7.6	Linear correlations colored by dopant types between Raman intensity ratios (A) I_{411}/I_{227} and I_{612}/I_{227} , (B) I_{411}/I_{660} and I_{612}/I_{660} , and (C) peak location of peak 411 cm ⁻¹ and peak 612 cm ⁻¹ . I_{411}/I_{227} distributions with (D) oxygen composition percentage and (E) atomic radius different between dopant and host atoms.	135

7.7	Linear correlations colored by clusters from K-means method classification. between Raman intensity ratios (A) I_{411}/I_{227} and I_{612}/I_{227} , (B) I_{411}/I_{660} and I_{612}/I_{660} , and (C) peak locations of peak 411 cm^{-1} and peak 612 cm^{-1}	136
A.1	Voltammetric behavior of $\alpha\text{-Fe}_2\text{O}_3$ photoanodes in the dark (black lines) and under illumination (red lines), and 1 V s^{-1} cathodic sweeps following equilibration at an oxidizing voltage while under illumination. Data is shown for samples heated at $800\text{ }^\circ\text{C}$ for 10 minutes in (A) humidified N_2 , (B) dry N_2 , (C) humidified O_2 , (D) dry O_2 , and at $800\text{ }^\circ\text{C}$ for 2 hours in (E) humidified N_2 , (F) dry N_2 , (G) humidified O_2 , (H) dry O_2	157
A.2	Correlations between peak width and intensity ratio for observed features in the Raman spectra.	158

List of Tables

1.1	Recent reports on hematite photoanode material design and performance.	10
1.2	Crystallographic information for common iron oxides.	11
3.1	Location, intensity and width of peak components for the 800 °C α -Fe ₂ O ₃ films.	49
3.2	Behavioral parameters for α -Fe ₂ O ₃ films prepared at 800 °C	53
4.1	Photoelectrochemical properties used in correlation analysis.	70
4.2	Raw parameters extracted from X-ray absorption fine structure spectroscopy.	73
4.3	Structural Parameters of Hematite and Protohematite.	83
5.1	Parameters describing the photoelectrochemical behavior of α -Fe ₂ O ₃ sample series.	91
5.2	Top structure-property correlation candidates identified for each dataset segment.	98
6.1	Flat band potential and carrier concentration values for hematite films prepared by three-step annealing.	123
7.1	Absolute values of $\log(I_x/I_{660})$ versus $\log(\text{F or Sn doping}\%)$ slope . .	132
7.2	K-means clustering results for the overall dataset, corresponding Silhouette values and Raman intensity ratios.	137
B.1	Extended X-ray absorption fine-structure spectroscopy simulation parameters used in the first model. ^a	160
B.2	Extended X-ray absorption fine-structure spectroscopy simulation parameters used in the second model. ^a	161

B.3	Normalized intensity of individual peaks in Raman spectrum for the hematite sample series.	162
B.4	Full width at half mass of individual peaks in Raman spectrum for the hematite sample series.	162
B.5	Location of individual peaks in Raman spectrum for the hematite sample series.	163

List of Abbreviations

AC	Alternating current
CB	Conduction band
CFSE	Crystal field stabilization energy
DC	Direct current
DFT	Density function theory
DSC	Differential scanning calorimetry
$E_{F,n}$	Electron quasi-Fermi level
$E_{F,p}$	Hole quasi-Fermi level
E_{fb}	Flat band potential
E_g	Band gap
E_{oc}	Open-circuit voltage
EIS	Electrochemical impedance spectroscopy
EXAFS	Extended X-ray absorption fine structure
FTIR	Fourier-Transform infrared spectroscopy
FTO	Fluorine-doped tin oxide
HER	Hydrogen evolution reaction
OER	Oxygen evolution reaction

PEC Photoelectrochemical

RHE Reversible hydrogen electrode

SCLJ Semiconductor-liquid junction

TAS Transient absorption spectroscopy

TPD Temperature programmed desorption

UV-vis Ultraviolet-visible

V_{ph} Photovoltage

VB Valence band

XANES X-ray absorption near edge spectrum

XPS X-ray photoelectron spectroscopy

XRD X-ray diffraction

Chapter 1

Introduction

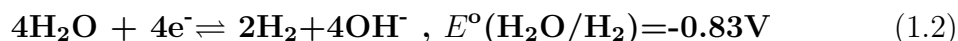
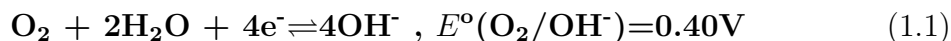
1.1 Motivation

Manufacturing, transportation, industry, and countless other human activities require the usage of energy. Sustainable energy that can satisfy the demand of society while minimally impacting the environment are crucial. As the most abundant and renewable energy resource, solar energy can be a promising solution to this problem. Approximately 100,000 TW of solar energy reaches the planet every year, which is nearly 5000 times as much as the total energy that people all over the world consume every year.¹ The intermittent property, seasonal and regional dependence results in the difficulty of harvesting solar energy.² Therefore, the key issue of solar energy is its storage and utilization. Artificial photosynthesis uses sunlight to drive reactions and convert solar energy into chemicals like carbohydrates and hydrogen.³⁻⁵ Solar water splitting reactions using semiconductors as electrodes can decompose water into hydrogen fuel and oxygen. Since Honda and Fujishima reported using single crystal TiO_2 as the photoanode to achieve electrochemical photolysis in the 1970s,⁶ researchers have been focused on developing new materials for electrodes to apply to photoelectrochemical (PEC) water splitting.

1.1.1 Solar Water Splitting

During conventional PEC water splitting reaction, solar energy reaches the semiconductor photoelectrode in form of sunlight and drives the water oxidation process. Cathodic reduction occurs and produce hydrogen while oxygen evolution reaction takes place at the other side. A common PEC cell contains a (photo)anode for OER and a (photo)cathode for hydrogen evolution reaction (HER). This project focuses on the oxygen evolution reaction (OER). PEC water splitting reaction contains three essential processes.² The first process is the light absorption at *n*-type semiconducting photoanode. Photons with energies larger than the band gap of the semiconductor are absorbed by the photoanode, and excite electrons from the valence band (VB) to the conduction band (CB), leaving holes in the VB. The second process is the charge carrier separation and transportation. Electrons participate in HER or other fuel-forming reduction reactions at the photocathode side. Holes are involved in OER at the interface between the photoanode and the electrolyte. It should be notable that charge carrier recombination can possibly happen during these processes and reduce the efficiency.^{2,7} The third process is the redox reactions themselves at the surface of catalysts.

Water splitting reaction requires 237 kJ mol⁻¹ (per mole of water) under standard temperature and pressure, corresponding to a 1.23 V potential difference between anodic and cathodic reactions.¹ The equations below show the two half reactions in alkaline condition:



The semiconducting photoelectrode is an essential component of PEC water splitting cells. The photoanode absorbs sunlight and generates electrons and holes at the surface. The holes left by electron excitation are involved in OER at the photoanode. Electrons transport to the photocathode side and participate in hydrogen evolution reaction. As shown in **Figure 1.1**, in the ideal case, the band gap energy

(E_g) of the photoanode should be large enough (> 1.23 V vs reversible hydrogen electrode (RHE)) to split water, and the upper valence band and the lower conduction band should locate at proper positions to drive OER and HER respectively.^{2,8} In semiconductors, the valence band is the highest range of electron energies in which electrons are normally present at absolute zero temperature. The conduction band is the band of electron orbitals that electrons can be excited from the valence band where electrons can move freely. As shown in **Figure 1.1**, the redox potential of O_2/OH^- ($E^\circ(O_2/OH^-)$) is 0.40 vs NHE at pH=14, and the redox potential of H_2O/H_2 ($E^\circ(H_2O/H_2)$) equals to -0.83 V vs NHE. The CB potential should be more cathodic than $E^\circ(H_2O/H_2)$ while the VB potential must be more anodic than $E^\circ(O_2/H_2O)$.

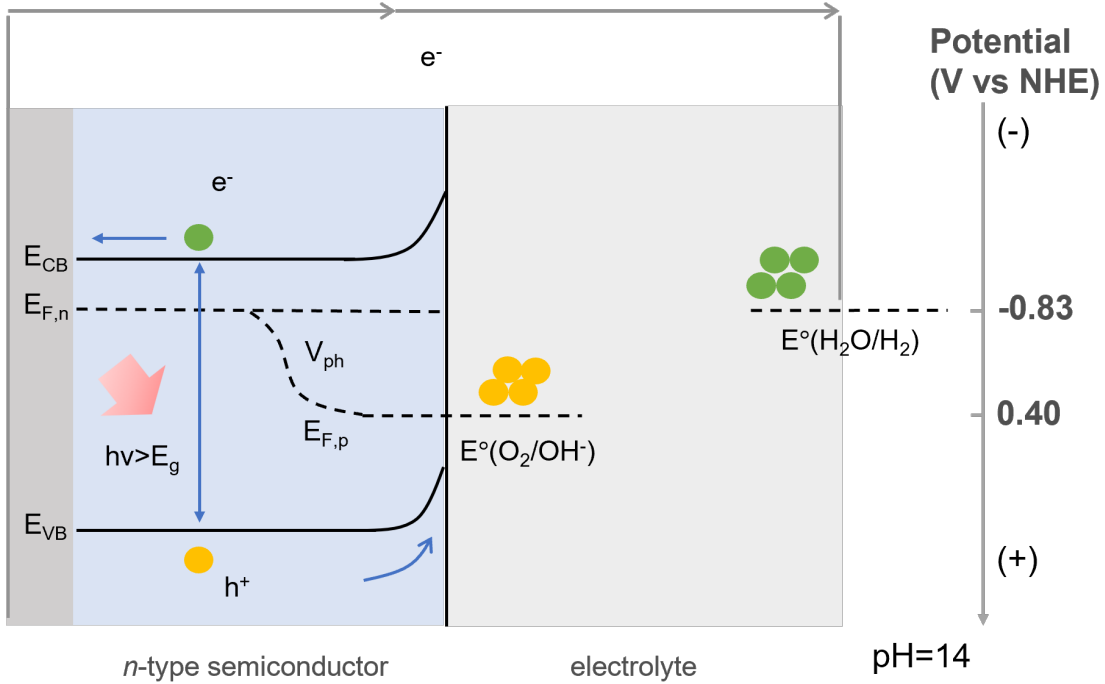


Figure 1.1: Schematic illustration of solar water splitting reaction at pH=14.

When a semiconducting electrode is immersed in an electrolyte, electrons transfer between the semiconductor-liquid junction (SCLJ) to reach an equilibrium.⁹ For an n -type semiconductor, usually the Fermi level should be higher than the Fermi level of electrolyte. When the semiconductor and the electrolyte are in contact, the free electrons will transfer due to different Fermi levels. After equilibrium, the semiconductor will have extra positive charges across a narrow region while the solution

have the extra electrons. The layer in the photoanode is called the space charge region or depletion layer.⁹ The Fermi level is defined as the energy level where there is a 50 % possibility of occupation by electrons. For an n -type semiconductor with electrons as the major charge carrier, the Fermi level is closer to the conduction band and higher than the Fermi level of the electrolyte under disequilibrium condition. Therefore, the Fermi level at the surface is bent closer to the conduction band for an n -type semiconductor with an upward band bending.

It is notable that total equilibrium state is established slowly in the dark.¹⁰ Illumination accelerates the thermalization of charge carriers, making electrons and holes in their quasi-Fermi level respectively. The quasi-Fermi level is the electrochemical potential where the electrons or holes under disequilibrium condition. The difference between hole quasi-Fermi level ($E_{F,p}$) and electron quasi-Fermi level ($E_{F,n}$) as shown in **Figure 1.1** is photovoltage (V_{ph}), known as open-circuit voltage (V_{oc}) in electrochemical measurement.

PEC devices with a variety of configurations have been reported.² The simplest configuration is to use a single n -type semiconductor material as a light absorber to drive the water splitting reaction as shown in **Figure 1.1**. To satisfy this requirement, a semiconductor with a large band gap to absorb enough solar radiation is used as shown in **Figure 1.2**. The specific requirement for the n -type band gap value and position will be introduced in the following section. However, exemplifying TiO_2 in **Figure 1.2**, the band gap of 3.2 eV corresponds to the sunlight under 388 nm wavelength in the solar spectrum, which means that only a very narrow percentage of 5% of the whole solar spectrum can be absorbed.¹¹ In practice, the PEC reaction is often performed with the assistance of an external bias. A dual band gap cell configuration can utilize the solar spectrum better by coupling two or even more semiconductors into heterostructures.¹²

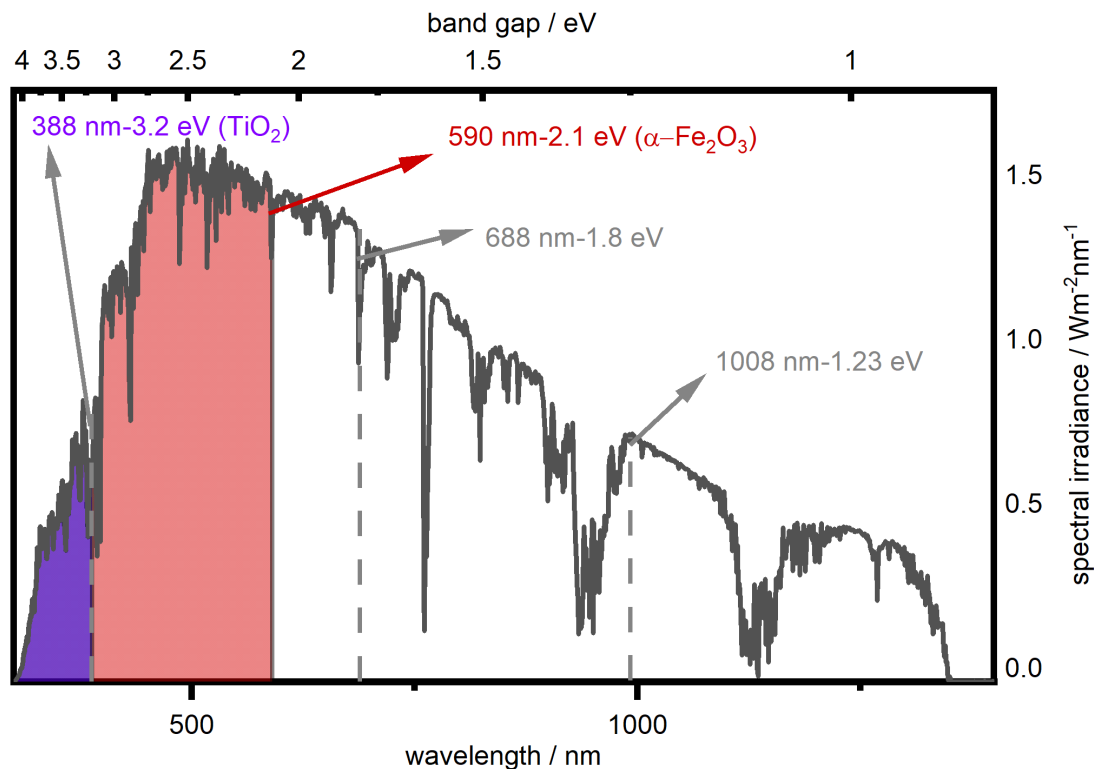


Figure 1.2: Spectrum of solar radiation and corresponding band gap values. Red and purple shadows represent the solar radiation absorbed by $\alpha\text{-Fe}_2\text{O}_3$ and TiO_2 respectively. Data is from ASTM G173-03 Reference Spectra derived from SMARTS v. 2.9.2 (AM1.5)¹³

1.1.2 Photoanodes in Solar Water Splitting

A limited number of semiconducting materials have been found to exhibit the necessary properties to perform photoelectrocatalytic OER. The properties of candidate electrodes have been reported across a significant range. **Figure 1.3** lists some candidates for photoanodes, with black and red bars marking the highest and lowest reported conduction band edges and blue and green bars marking the highest and lowest reported valence band edges. In practice, an overpotential is required to drive OER at appreciable rates. A potential greater than 1.23 V is therefore required. The requirement of overpotential has multiple reasons, including thermodynamic consideration for energy losses during charge carrier transportation (0.3-0.4 eV) and kinetics requirement for surface reactions (0.4-0.6 eV).² Therefore, a band gap value of at least 1.9 eV would be ideal. Besides, to excite electrons from VB to

CB, the band gap must satisfy the following equation:

$$h\nu = \frac{hc}{\lambda} > E_g \quad (1.4)$$

Only solar radiation under certain wavelength ($\lambda < \frac{hc}{E_g}$) can be absorbed by the photoanode. Therefore, semiconductors with band gap in the range of 1.8 to 3.0 eV have been most extensively studied for PEC water splitting.

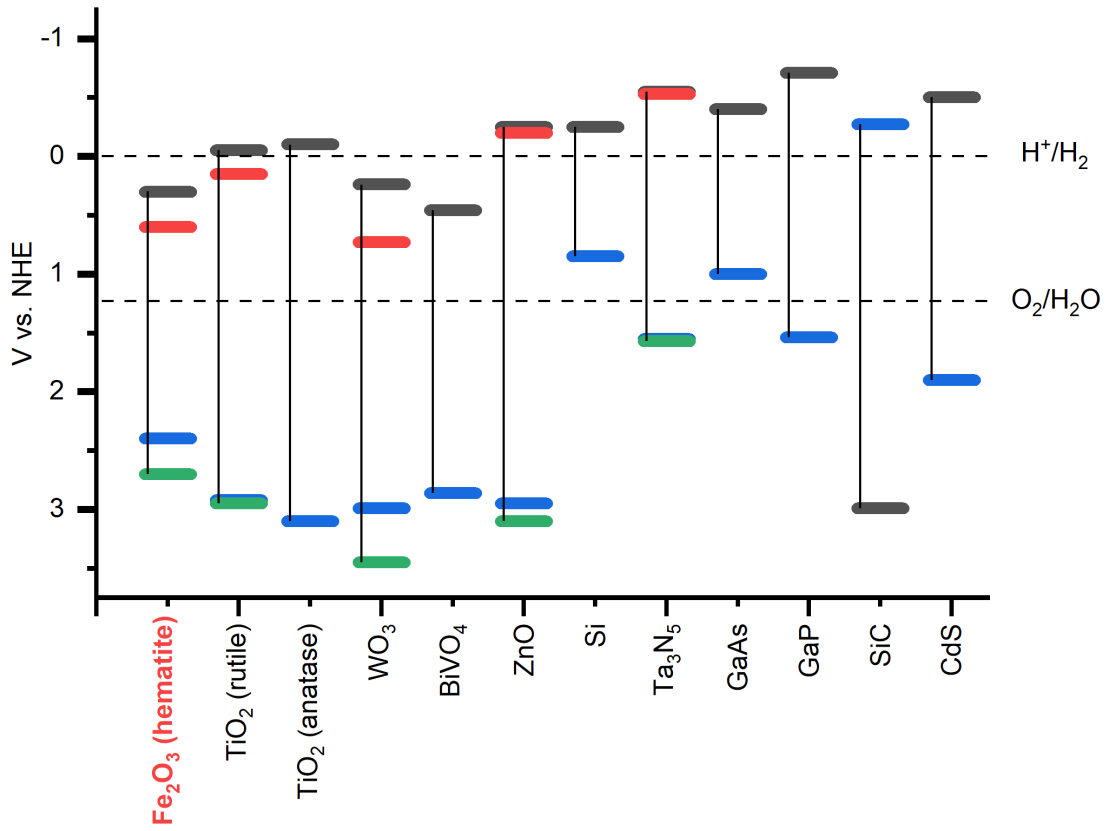


Figure 1.3: Band gap values and band positions of common semiconducting materials.¹⁴

A second consideration is that efficient charge carrier separation and transportation, paired with low charge carrier recombination rates, are essential for the efficiency of both OER and HER.^{2,15} Electrons excited to the conduction band leave holes in the valence band during charge carrier separation. If a photoexcited electron and a hole interact with one another, they will vanish immediately in a harmful process called charge carrier recombination. Charge carrier recombination can reduce the number of charge carriers, decreasing the photocurrent density in the system. This process can happen in the bulk of the semiconductor or in the depletion region. It is facilitated by the presence of intraband states within the band gap. Charge carrier transportation refers to the process when electrons move from the photoanode towards the interface between the photocathode and the electrolyte, and holes participate in OER at the interface between the photoanode and the electrolyte. V_S is defined as the degree of band bending, dependent on the applied bias by $V_S = E - E_{fb}$. Here E and E_{fb} are the applied bias and flat band potential. The flat band potential is defined as the voltage where there is no depletion layer at the semiconductor-liquid junction. The Fermi level of the photoelectrode and electrolyte would differ by energy equal to qE_{fb} , where q is the charge of the carrier involved. The diffusion length of charge carrier (L_D) is defined as the distance of charge carrier migration in the semiconductor before vanishing, and can be calculated as $L_D = \sqrt{D\tau}$ where τ is the lifetime of charge carriers. Those processes depend on intrinsic properties like electron mobility and extrinsic properties like crystallinity of the semiconductor. Thus, facet engineering, interface modification and nanostructure design can be used to improve charge carrier separation and transportation.¹⁵

Lastly, photoanodes must have high stability in the electrolyte, low cost and earth abundance for economic consideration. Considering all the properties mentioned above, transition metal oxides are widely studied as potential photoanodes in the form of pure or doped metal oxides.¹⁶ In the following section, hematite ($\alpha\text{-Fe}_2\text{O}_3$) will be introduced as the focused material of this project.

1.1.3 Hematite Photoanode Overview

Hematite has remained an attractive photoanode candidate of the numerous semiconductors. In this section, the promising properties, early efforts and current issues of hematite as photoanode will be introduced.

As shown in **Figure 1.3**, hematite has a band gap between 1.9 and 2.2 eV, which enables use of a significant part of solar radiation (**Figure 1.2**). The coverage of yellow to ultraviolet light radiation and transmission of orange to infrared gives the crystal an orange to purple range of color.¹⁷ The conduction band position of hematite is located at a more positive potential than the redox potential of H_2/H^+ , requiring an external bias for overall PEC reaction. The relatively low absorption coefficient (α) of hematite, which is on the order of 10^3 cm^{-1} , requiring relatively thick coatings of 400-500 nm layer to absorb solar energy.

Hematite has faced challenges as a photoanode material regarding charge carrier transportation, separation and recombination processes.² First, hematite shows relatively low electrical conductivity. A conductivity lower than $10^{-6} \Omega^{-1}\text{cm}^{-1}$ has been reported for single-crystal hematite,¹⁸ which is on the low end of the typical semiconducting material range of 10^{-6} to $10^4 \Omega^{-1}\text{cm}^{-1}$. The conductivity of a semiconductor depends on the efficient transportation of the majority charge carrier, which is the electron for *n*-type materials like hematite. Introduction of dopants or oxygen vacancies are common strategies for generating free electrons in the hematite system to increase charge carrier density.^{4,19}

Hematite shows a photogenerated carrier lifetime on the order of picoseconds due to charge carrier recombination. Transient absorption spectroscopy using an ultrafast systems have studied charge carrier dynamics. Using hematite nanoparticle as specimen, 70% of the transient absorption vanished after 8 ps and could not be measured after 100 ps.²⁰ The main reason for the short carrier lifetime appears to be the presence of intraband states or called trap states within the band gap of hematite. These trap states accumulate holes and charge carrier recombination. The dominant charge carrier trapping is believed to occur at mid-gap Fe^{3+} *d* states 0.5-0.7 eV below the conduction band.²¹ These states can be observed as an optical transition near 1.5 eV.^{22,23} Fast sweep using cyclic voltammetry has also confirmed

the hole accumulation in these intraband states.²⁴ It has been reported that high temperature (800 °C) annealing can remove the intraband states, thereby improving the photocurrent density in the system.

Different strategies have been applied to improve the photoelectrocatalysis performance and to understand the underlying chemistry of photoanodes. Regarding material design, introducing dopant elements, controlling nanostructure, tuning fabrication protocols and adding co-catalysis or under/overlayers are common methodologies. External doping can increase the charge carrier density and improve the conductivity of hematite photoanodes as previously stated. Designing nanostructures like synthesizing nanorods, nanowires and nanoflakes structures can facilitate hole transportation and overcome the short lifetime of charge carriers.^{25,26} Fabrication protocol modification especially post-heating^{27,28} and alkali/acidic treatment²⁹ is simple in operation and efficient in material modification. Since hematite is often fabricated through thermal treatment from other iron oxide or hydroxide phases, the heating process can be important for the final product (details in **Section 1.2.2**). Oxygen-deficient annealing and Ar plasma treatment establish oxygen vacancy sites (**Section 1.3.1**) and increase the number of charge carriers.^{27,30,31} Adding cocatalyst like cobalt-phosphate (CoPi) has been widely used to enhance the poor (photo)electrocatalysis performance of hematite as well.^{25,28,32} It has been reported that CoPi catalysts can suppress the charge carrier recombination loss through the withdrawal of electrons from hematite to the associated Pi.^{28,33} **Section 1.1.3** lists examples of hematite photoanode structuring methods that have yielded remarkable PEC performance in the recent four years.

Table 1.1: Recent reports on hematite photoanode material design and performance.

Material fabrication	J at 1.23V vs. RHE
chemical vapor deposition followed by plasma etching then annealing ³⁴	1.30 mA cm ⁻²
hydrothermal method with alkali treatment ²⁹	~0.6 mA cm ⁻² ^a
hydrothermal method with facile surfactant assistance +CoPi ²⁵	1.6 mA cm ⁻²
hydrothermal method with protonation+CoPi ²⁸	2.4 mA cm ⁻²
hydrothermal method with short time hybrid microwave annealing ³⁵	~0.74 mA cm ⁻² ^a
thermal oxidation with direct heat Fe/steel, nanowire and nanoflake ²⁶	~0.2 mA cm ⁻² ^a
chemical vapor deposition with grey hematite ³⁶	1.43 mA cm ⁻²
thermal oxidation with Ar plasma+Fe-Pi ³⁷	1.2 mA cm ⁻²
hydrothermal method with Fe foil substrate+fast flame annealing, hematite/Fe ₃ O ₄ heterojunction ³⁸	2 mA cm ⁻²
thermal oxidation with direct annealing into preheated furnace ³⁹	2.35 mA cm ⁻²

^a:Part of approximated photocurrent density values are obtained from published figures directly.

1.2 Iron Oxide and Hydroxide Phases

1.2.1 Crystal Structure

X-ray diffraction and neutron diffraction techniques have been employed to determine the crystal structures of iron (hydro)oxides. **Table 1.2** summarises the crystallographic information for the iron oxides used in this work. Since the O²⁻ and OH⁻ ions are significantly larger than Fe²⁺ and Fe³⁺ ions, the arrangement of those anions can determine the crystal structure. The crystal structure of iron oxide or hydroxides can be represented by either the traditional stacking of close-packed

anions or the linkage between octahedra or/and tetrahedra. The frequent polyhedron types in iron oxides are octahedral FeO_6 or $\text{FeO}_3(\text{OH})_3$ and tetrahedral FeO_4 . The basic units link together to form extended structures, with linkages including corner-sharing, edge-sharing and face-sharing. From X-ray diffraction data or X-ray absorption spectroscopy data, the Fe-Fe distance between polyhedra can be extracted. As shown in **Figure 1.4**, corner-sharing motifs give the longest Fe-Fe distances while face-sharing motifs have the shortest Fe-Fe distances. In this section, the linkage of $\text{FeO}_x(\text{OH})_{3-2x}$ polyhedra will be used to describe the six iron oxide structures: hematite ($\alpha\text{-Fe}_2\text{O}_3$), maghemite ($\gamma\text{-Fe}_2\text{O}_3$), magnetite (Fe_3O_4), goethite ($\alpha\text{-FeOOH}$), lepidocrocite ($\gamma\text{-FeOOH}$) and akaganeite ($\beta\text{-FeOOH}$).

Table 1.2: Crystallographic information for common iron oxides.

Compound	Structural type	Space group	ICSD #
Hematite	Corundum	$R\bar{3}c$	15840
Magnetite	Inverse spinel	$Fd\bar{3}m$	65339
Maghemite	Defective spinel	$P4_32_12$	87121
Goethite	Diaspore	Pbnm	245057
Lepidocrocite	Boehmite	Cmcm	93948
Akaganeite	Hollandite	$I2/m$	69606

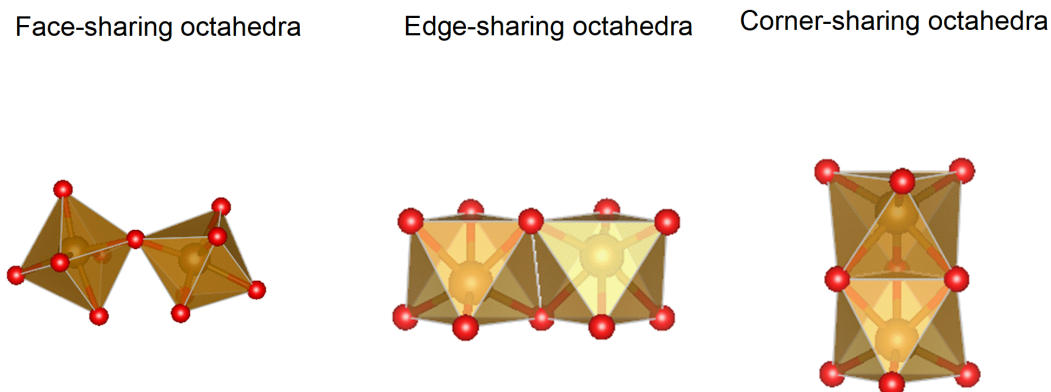


Figure 1.4: Three different linkages of FeO_6 octahedra, face-sharing, edge-sharing and corner-sharing octahedra.

Hematite

Hematite has the corundum crystal structure, where Fe^{3+} ions locate in two-thirds of the octahedral sites with hexagonally close-packed oxide ions. The crystalline c -axis is characterized by columns of alternating dimers of face-sharing Fe^{3+} octahedra and vacant octahedral sites, with and edge-sharing linkages between the columns (**Figure 1.5A**). Inside the FeO_6 octahedron there exist two different Fe-O distances: those facing the vacant octahedral site (1.944 Å) are shorter than these Fe-O distance facing the face-sharing linked octahedron (2.116 Å).⁴⁰ Some O^{2-} ions can be substituted by OH^- with the occurrence of Fe ions to keep charge balance. This so-called *protohematite* structure can result from incomplete dehydroxylation with residual hydrogen in the crystalline structure during FeOOH to hematite phase transition.^{41–43} The details of protohematite and iron vacancy influence on hematite will be introduced in **Section 1.3.1, Chapter 3** and **Chapter 4**.

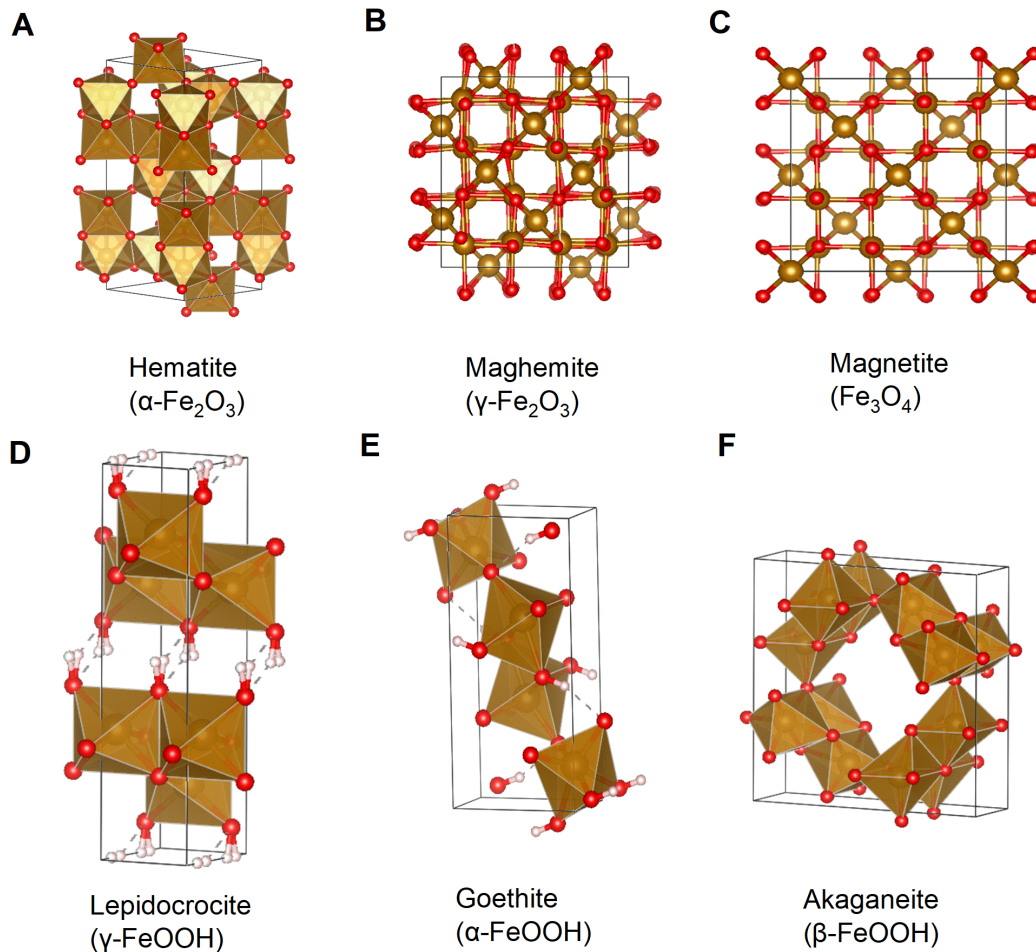


Figure 1.5: Crystal structure of common iron oxide and hydroxide phases.

Magnetite

Magnetite (Fe_3O_4) remains one special phase among the iron oxides because it contains both divalent and trivalent iron in a stable phase. Magnetite has an inverse spinel structure of $\text{Fe}^{3+}(\text{Fe}^{2+}\text{Fe}^{3+})\text{O}_4$. Half of the Fe^{3+} fill 1/8 of tetrahedral sites while the other Fe^{3+} and all Fe^{2+} occupy 1/2 of octahedral sites in the face-centred cubic unit cell with 32 O^{2-} ions. Since Fe^{3+} has d^5 configuration, its crystal field stabilization energy is zero in either octahedral sites or tetrahedral sites. Fe^{2+} in magnetite with d^6 high spin configuration prefers octahedral arrangement. Therefore, the Fe^{2+} ion and one Fe^{3+} occupy octahedral sites whereas the other Fe^{3+} ion occupies the tetrahedral site.

Maghemite

Maghemite ($\gamma\text{-Fe}_2\text{O}_3$) has a similar structure to magnetite structure and is called defective spinel. With all iron ions in trivalent states, cation vacancies are generated to keep charge balance. The cubic cell contains 32 O^{2-} ions still, and eight cations fill tetrahedral sites while the other cations randomly occupy the octahedral sites. Consequently, some octahedral sites are left vacant represented as $\text{Fe}_8(\text{Fe}_{13.3}\square_{2.67})\text{O}_{32}$. However, maghemite especially commercial maghemite, has been reported as a tetragonal unit cell because large crystals can permit complete ordering of the vacancies. It has also been discovered that protons can be trapped in vacant octahedral sites due to the dehydroxylation process from FeOOH precursors. The phase transition will be introduced in the following **Section 1.2.2**.

Goethite

Goethite ($\alpha\text{-FeOOH}$) is isostructural with diaspore ($\alpha\text{-AlOOH}$) with an orthorhombic unit cell as shown in **Figure 1.5E**. Fe^{3+} ions occupy half of the octahedra sites within one layer. $\text{FeO}_3(\text{OH})_3$ octahedra double chains with edge-sharing along the a -axis are followed by double rows of empty octahedra sites. The double chains are linked by corner-sharing to form one-dimensional tunnels within the structure. There are

two types of oxygen atoms in the goethite structure. One is the oxygen atoms shared between octahedra of two different chains. The other is the oxygen within the same chain and linked to protons. Consequently, those two different oxygen environments make the double chains twist slightly, not linearly arranged.

Lepidocrocite

Lepidocrocite (γ -FeOOH) is isostructural with boehmite (γ -AlOOH) and consists of a layered structure unlike the tunnel structure of lepidocrocite and akaganeite. Lepidocrocite has an orthorhombic unit cell with cubic-closed packing of O^{2-} or OH^- ions along [150] direction with iron ions filling in the octahedral sites. Similar to goethite, lepidocrocite also contains double chains of FeO/OH_6 along c -axis. The double chains linked by edge-sharing contain a displacement of one half to form corrugated sheets of octahedra, then the sheets are stacked perpendicular to a -axis with double rows of vacant octahedral sites. Hydrogen bonds exist between the layers and link the oxygen atoms.

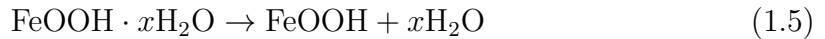
Akaganeite

Akaganeite (β -FeOOH) is isostructural with hollandite (β -AlOOH) with a monoclinic unit cell. Unlike α or γ -FeOOH, β -FeOOH has no hexagonal closed packing or cubic closed packing arrangement of anions, only body-centred cubic instead with Fe^{3+} occupying octahedral sites. As a consequence, akaganeite phase has a less compact structure than the other phases. Similarly, akaganeite has double chains of edge-sharing motifs parallel to b -axis and corner-sharing linked double chains. In this case, a tunnel structure as shown in **Figure 1.5F** along b -axis is established by double rows of octahedra. It should be notable that Cl^- ions are essential in akaganeite to stabilize the tunnels. Chloride anions usually come from $FeCl_3$ precursor with 1.23 Cl^- per unit cell. If the chloride ions are forced to be washed from the crystal, akaganeite can be transformed into goethite or hematite phase.

1.2.2 Phase transition

All the iron oxide and hydroxide phase transition to hematite when exposed to high temperature. One common transformation is the dehydroxylation from FeOOH phases to hematite under high temperature. During this process, hydroxo-bonds are replaced by oxo-bonds and face-sharing motifs form into a more compact structure. Here we focus on the phase conversion in a dry state not in solution because thermal treatment is the widely used approach to fabricating hematite from other phases.

Figure 1.6 illuminates some representative phase transformation. Both akaganeite and goethite go through dehydroxylation and are converted into hematite. Goethite to hematite phase transformation has been reported to happen across a wide temperature range of 250 to 500 °C.⁴⁴ Lepidocrocite is a unique case because it will decompose into maghemite first as an intermediate phase at approximately 300 °C and then be converted into hematite at a higher temperature (600 °C).⁴⁵ During the conversion from lepidocrocite to maghemite, the [150] direction in the orthorhombic cell of lepidocrocite will develop into the [111] direction of the distorted cubic cell in the defective spinel phase. The decomposition of the akaganeite phase can start at 150 °C and finish at 500 °C. Due to the existence of chloride in tunnels, Cl₂ (under oxygen environment) or HCl (under nitrogen environment) will be released.^{46,47} Consequently, this reaction is quite sensitive to the gas environment. The dehydroxylation is usually considered as a two-step reaction:



The first step **Equation** (1.5) is the loss of surface water molecules, which are loosely bonded through intermolecular force. The second step **Equation** (1.6) is the chemical dehydroxylation process where oxygen and hydrogen are removed. It should be notable that the terminology *dehydroxylation* (loss of -OH) differs from *dehydration* (loss of H₂O) process.

The conversion between Fe₃O₄ and α or γ -Fe₂O₃ phases belongs to oxidative and

reductive transformations:

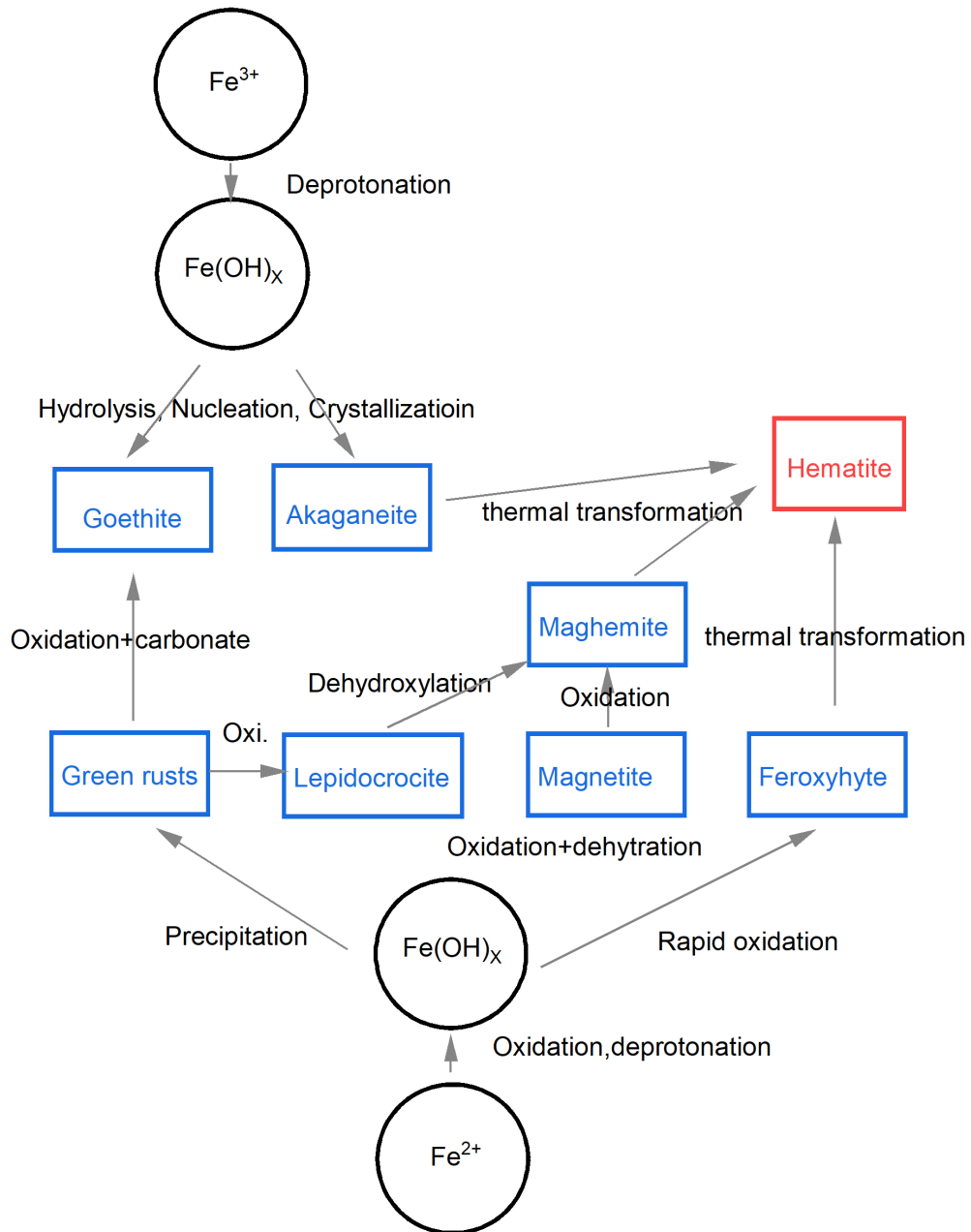


Figure 1.6: Schematic representation of major formation and transformation pathways of common iron oxides.⁴⁸

Magnetite can be oxidized by air at relatively low temperatures, even at room temperature, over a time frame of years. Higher temperature (300 °C) can further convert it into hematite.⁴⁹ As previously stated, maghemite structure can be con-

sidered as a defective spinel structure with cation vacancies, so the oxidation to maghemite reduces the 24 iron atoms in magnetite to $21\frac{1}{3}$ in maghemite. For the reverse reduction reaction, heating under an oxygen-deficient environment can reduce the Fe^{3+} state to Fe^{2+} state and create oxygen vacancies meanwhile by removing oxygen as molecular oxygen gas. Oxygen vacancy defect will be introduced in the following **Section 1.3.1**.

1.3 Defects in Hematite

1.3.1 Point Defects

Point defects are structural defects that occur in zero dimension. Common native point defects include ion vacancy defects, interstitial defects and antisite defects. In hematite crystals, antisites refer to iron ion on oxygen sites, and vice versa. Antisites are not energetically favorable due to high formation energies, as indicated by DFT+ U calculations.⁵⁰ Therefore, it is usually excluded in hematite point defect discussion. Point vacancies and interstitial defects will be introduced here.

Point defects in hematite include oxygen vacancies and iron vacancies. Vacancies are formed when the ions are taken from the original sites. It can be represented as Kroger-Vink notation:



In Kroger-Vink notation, M_S^C represents that M occupies on lattice site S with electronic charge of C relative to S . M can be atom, vacancy (V), interstitial (I), electron or hole. X , \cdot and \prime stand for null, positive charges and negative charges. As stated in **Equation (1.8)**, oxygen vacancies can generate the majority charge carrier in hematite n -type semiconductors, electrons. Consequently, oxygen vacancies are often considered a beneficial defect for hematite. However, it has also been reported that high concentration of oxygen vacancies lead to serious charge carrier recombination by inducing surface states at the SCLJ.³⁷ The role of surface state defect will be introduced in following **Section 1.3.2**. Oxygen vacancies, especially with high concentration, can also induce Fe^{2+} species and even lead to decomposition to

magnetite phase to maintain charge balance.

Oxygen vacancies can be created from post-treatment of hematite. One method is to heat hematite or iron hydroxide phases in an oxygen-deficient environment like nitrogen gas.³¹ Another method is to apply oxygen-plasma treatment on as-synthesized hematite.³⁷ A combination of oxygen-plasma treatment followed by short-annealing was also used to investigate the function of post-treatment on PEC properties and oxygen vacancy formation.^{34,51} X-ray photoelectron spectroscopy is widely used to determine the oxidation state of ions and quantify the concentration of oxygen vacancies. Oxygen vacancies from both methods are generated by removing lattice oxygen and adding -OH at the surface of materials.^{27,34}

Iron vacancies draw less attention compared with oxygen vacancies because of the difficulty in synthetic control, quantitative measurement, and a relatively high formation energy. Formation energy for iron vacancies varies from 55.0 to 55.2 eV, but it is as low as 20.3-23.8 eV for oxygen vacancy formation.^{52,53} It is reported that trapping protons in hematite generates iron vacancies by protonation of oxygen ions on iron vacancy sites.^{41,42} **Chapter 3** and **Chapter 4** further explain the identification of protohematite and iron vacancies. Calculation-based research have provided theoretical proof that iron vacancies are stable in hematite. First-principles methods based on DFT calculation show that oxygen-rich condition can induce charged iron vacancy sites.⁵⁴ DFT+*U* calculation supported that iron vacancies can locate at the surface and be potentially related to the suppression of surface state defects.⁵⁵ Both theoretical and experimental studies agreed that iron vacancies and oxygen vacancies can occur together as shown below:



With the relationship between electron concentration n and hole concentration p :

$$n + 3[V_{\text{Fe}}'''] = p + 2[V_{\text{O}}''] \quad (1.10)$$

The Schottky defect requires a discontinuity in lattice, such as the grain boundary in Leite *et al.* work and dislocation or a free surface.⁵⁶

claim this Raman peak as symmetry breaking induced native defects in hematite.^{60,61}

1.3.2 Surface State Defects

Surface state defects refer to the intraband states at the SCLJ, also known as trapping states where trap electrons and holes as recombination sites as shown in **Figure 1.8**. The nature of surface state defect can be assigned to $\text{Fe}^{2+}\text{-V}_{\text{O}}$.⁷ Simulation results show that oxygen vacancies can work as faster recombination sites than direct VB-CB recombination.⁶² Rapid cathodic sweep voltammetric protocol shows that high temperature annealing can remove the peaks between 0.7 and 1.4 V vs RHE assigned to surface states, enhancing the photocurrent density from around 0.2 mA cm^{-2} to 0.7 mA cm^{-2} and shifting the onset potential by 300 mV.²⁴ High temperature annealing post-treatment can heal surface states by oxidizing Fe^{2+} species, and also improve crystallinity of hematite. This rapid sweep experiment further proves that surface state defects in band structure may arise from oxygen vacancy defects in the crystal structure.

Transient absorption spectroscopy suggests that those states lie hundreds of millivolts below conduction band of hematite photoanodes.^{7,63} With low bias applied, the recombination between trapped electrons and holes from the valence band takes place in ps to ns timescale, which is faster than further trapping in μs timescale. As bias increases anodically, band bending leads to depletion of surface states while electron trapping in ps to ns will dominate rather than hole trapping in μs to ms. Electrochemical impedance spectroscopy (EIS) (**Section 2.4.2**) helps with the electrochemical and photoelectrochemical investigation of OER mechanism by simulating trapping process as part of the equivalent circuits.⁶⁴ Different equivalent models focus on if surface states play as an intermediate where charge transfer and OER take place. Klahr *etal.* believed that both charge transfer and recombination happen at the same surface states due to the evidence of charge transfer resistance change.¹⁰ Zhang *etal.*, however, state that surface states are responsible for recombination and charge transfer.¹⁹ We exclude the possibility that those surface states are reaction intermediates because of the location of onset peaks (**Chapter 3**).

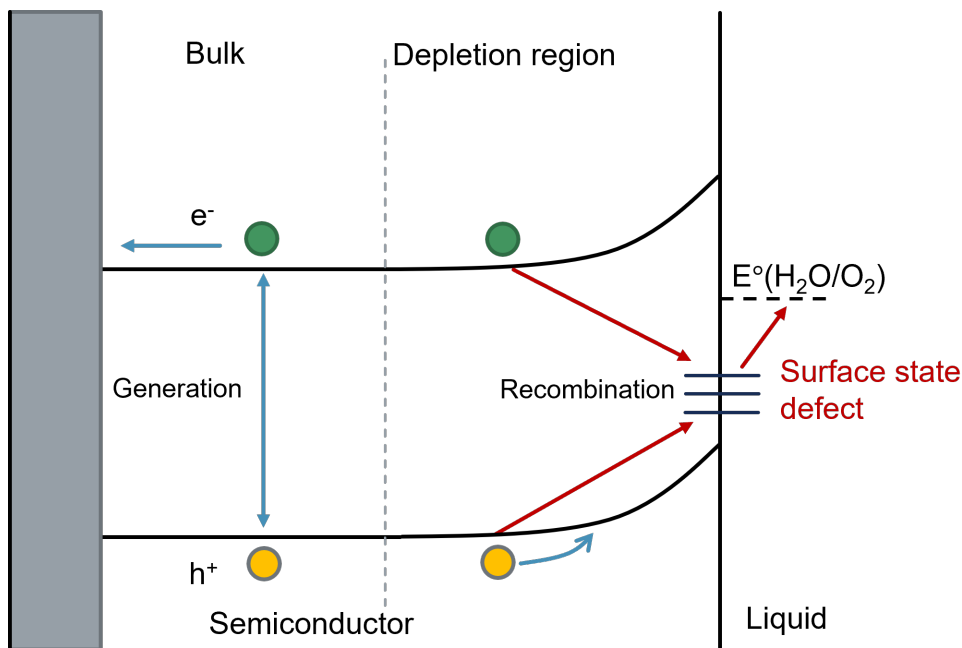


Figure 1.8: Schematic illustration of surface states at the interface between semiconducting photoanode and electrolyte.

1.4 Structure-Property Analysis

Structure-property analysis utilizes the correlation between structural parameters and property descriptors to analyse property-determining structure features. Electrochemistry and photoelectrochemistry have been using structure-property analysis to investigate reaction mechanism.⁶⁵ The correlation is usually described as linear relationship due to the easy extraction from data. However, volcano shape plots have been observed in hydrogen evolution reactions and other electrocatalysis reactions as well.⁶⁶

Correlational analysis can involve more than structure-property analysis and also comparisons between structural descriptors or between properties. While simple in theory, some important factors impede an effective and convincing application of correlation analysis. The first is the ability to synthesize series of materials with a systematic variation of the desired parameter. For example, it is relatively straightforward to introduce secondary elements in hematite materials, but it is significantly more complex to control the concentration of point defects. A second issue is that no single property can be adjusted in a truly independent fashion. Taking the com-

positional tuning of metal oxides as an example, the substitution of transition metal ions leads to changes in electronic structures, lattice distortions, oxidation states, and more. Correlations identified between individual parameters must be weighed in relative importance against other correlations, which may or may not be visible. A third complicated factor is the difficulty in determining type of the relationship between factors. It is possible that a linear correlation is one part of a volcano shape relationship or an exponential correlation.

In this work, we established enough data points to avoid the issues stated above. Besides, software is used to calculate and judge all possible comparisons and then filter the best correlations.

1.5 Thesis Objective and Overview

Combining fabrication protocols and structure-property analysis, we establish a deeper understanding of multiple intrinsic defects and their influence in both photoelectrocatalysis performance and structure of hematite photoanodes. In this work, we highlighted how Raman spectra analysis can assist in identifying point defects in hematite accompanied with structural information from other characterization technique.

Chapter 2 summarizes fabrication techniques to synthesize hematite with various concentration of multiple types of defects, and the characterization measurements used in this work for structure features and PEC performance.

Chapter 3 performs structure-property analysis on a series of hematite films fabricated by annealing lepidocrocite films with varied temperatures, annealing times and atmospheres and find a gradient in the magnitude of a crystal lattice distortion by tracking the relative intensity of a formally Raman inactive vibrational mode. Analysis of the nature of the key Raman vibrations, X-ray diffraction patterns, and the synthetic conditions leads us to assign the distortion to iron vacancies that are induced by the trapping of protons within the crystal lattice.

Chapter 4 expands how iron and oxygen defects leads to the differences in structural distortion in hematite by X-ray absorption spectroscopy. Correlations between

short-range structural parameters and long-range structural parameters, structure-PEC property parameters have been observed.

Chapter 5 explores the usage of Raman spectroscopy in identifying coexistent defect types. A straightforward approach to detecting defects in photoelectrodes and identifying their influence on photoelectrode properties and behavior is provided.

Chapter 6 describes the mechanism during lepidocrocite to hematite phase conversion under different gaseous environments. Variable temperature Raman spectroscopy tracks *in situ* spectrum change in phase transition process accompanied with thermal analysis including DSC and TGA.

Chapter 2

Characterization Methods and Techniques

2.1 Precursor Synthesis

Hematite often can be fabricated by phase conversion from other iron (hydro)oxide phases.⁴⁸ **Figure 1.6** summarizes possible phase conversion routes to synthesize hematite. Atomic layer deposition,^{67,68} hydrothermal method,^{29,31,69} chemical vapour deposition,^{35,36} thermal oxidation,^{26,39,70} and other techniques have been actively applied in hematite photoanode synthesis. Here, lepidocrocite (γ -FeOOH) and akaganeite (β -FeOOH) are selected as precursor phases to study the influence of different post-annealing environments on the distortion in hematite products.

2.1.1 Electrodeposition Method for Lepidocrocite Film (γ -FeOOH)

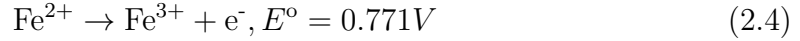
Electrodeposition method can provide homogeneous iron (hydro)oxide phases by tuning the electrodeposition potential.⁷¹ Both anodic and cathodic electrodeposition methods have been used to fabricate FeOOH then followed by annealing to prepare hematite.⁷²

Cathodic deposition of FeOOH uses Fe³⁺ ions as electrolyte for electrodeposition. The common reaction also contains F⁻ to generate FeF²⁺ and H₂O₂ to provide OH⁻ ions:



During this process, the concentration of FeF⁻ decreases with increased OH⁻ concentration and then induces the deposition of FeOOH. In Schreiber et al. work, the as-synthesized FeOOH was annealed at 500 °C for 20 min in air to convert into hematite photoanode

Anodic deposition applies a solution with Fe²⁺ as precursor. The reaction requests acidic condition because Fe²⁺ is soluble in acidic solution but Fe³⁺ is not, which allows FeOOH to precipitate on the substrate (FTO glass):



It has been reported that the as-deposited FeOOH turns out to be γ -FeOOH phase.⁷³ This project adopts anodic electrodeposition because a specific iron hydroxide phase will be ideal for the following phase transformation investigation. The fabrication method is used in **Chapter 3**, **Chapter 4** and **Chapter 6**, and the details of experiment will be described in those chapters.

2.1.2 Precipitation Method for Lepidocrocite Powder (γ -FeOOH)

Fabrication of lepidocrocite powder form is accomplished by oxidation of Fe²⁺ as shown in **Figure 1.6**.⁷⁴ Precipitation method uses condition-dependent solubility of a specific compound/phase to deposit the required material. The solubility of a compound usually relies on the ionic strength of the solution, pH and temperature.

The reaction can be written as:



It should be notable that pH environment, temperature and rate of oxidation all influence on the final product. Consequently, those conditions should be carefully controlled during fabrication, including weakly acidic condition and slow oxidation rate. A pH of 6.5 is maintained by adding KOH solution with the purging of nitrogen gas.

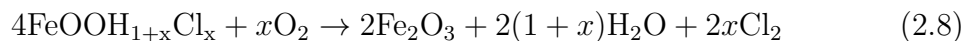
2.1.3 Hydrolysis Method for Akaganeite Film (β -FeOOH)

Hydrolysis or hydrothermal method can be the most frequently used synthesis method for hematite photoanode films because of its simple operation and controllable product orientation. Hydrolysis method only requires keeping Fe^{3+} in a certain solution under heated environment in an autoclave or even in a beaker. It has been reported that hematite nanoparticles can be fabricated directly by hydrothermal method using FeCl_3 solution and ammonium hydroxide at room temperature. The particle size and growth rate can be adjusted by iron concentration, hydroxide concentration and reaction temperature.^{75,76} The other common approach is to synthesize akaganeite phase first then fabricate hematite by heating.³¹ Doped hematite can also be fabricated by adding a secondary element solution into the iron precursor.^{69,77} Since akaganeite has a tunnel structure with Cl located inside, the decomposition reaction of β -FeOOH can be accompanied by a potential release of hydrogen chloride and oxygen. The reaction can differ between oxygen condition and nitrogen condition due to oxygen as a product.

Nitrogen environment:



Oxygen environment:



Therefore, both the oxygen concentration in annealing environment and chloride can influence the generation and concentration of oxygen vacancies.³¹

2.2 Hematite Fabrication

Hematite can be fabricated from other iron hydroxides or oxides by annealing process as described in **Section 1.2.2** and **Figure 1.6**. To investigate how the fabrication environment affects the final hematite photoanode, FeOOH samples are annealed under various conditions, including dry or humid, oxygen or inert, and different temperatures. By adjusting the fabrication condition, hematite with different types and concentrations of distortion can be prepared. It should be notable that we do not control the final defect concentration but rather establish various defects in hematite.

2.3 Material Characterization

Multiple spectroscopic techniques are widely applied in inorganic material characterization field. The core of spectroscopy is that under certain conditions, materials will absorb or emit energy usually in the form of light. Light can be described in terms of both particles and waves while light waves consist of perpendicular, oscillating electric and magnetic fields.

The relationship between energy, frequency and wavelength can be shown as:

$$E = hv = \frac{hc}{\lambda} \quad (2.9)$$

where h is Planck's constant (6.6×10^{-34} J s), c is the velocity of light (2.998×10^{10} cm s⁻¹), f is frequency and λ is wavelength.

It should be notable that waves from different wavelength ranges contain different energy which can interact differently with the molecules. For instance, infrared waves with relatively higher wavelength (700 nm - 1mm) and lower energy (1.7 eV -

1.24 meV) simulated vibrations. Visible (400 nm - 700nm) and ultraviolet (10 nm - 400 nm) radiation can promote electrons to higher energy orbitals. Higher frequency radiation like X-rays can break chemical bonds and ionize molecules.

In this chapter, two vibration spectroscopy techniques, Raman (**Section 2.3.1**) and Infrared spectroscopy (**Section 2.3.2**) will be introduced, among which Raman spectrum is not merely used to identify material but also to analyze defects. Variable temperature Raman spectroscopic technique is specifically introduced to study the mechanisms of thermally-induced phase transition. Ultraviolet-visible spectroscopy (**Section 2.3.3**) would be used to measure the band gap values and determine the band structure. X-ray absorption spectroscopy (**Section 2.3.4**) and X-ray diffraction technique (**Section 2.3.5**) are used to measure structural parameters like bond length, bond angles and determine local geometry. Differential scanning calorimetry (DSC) and thermogravimetric analysis (TGA) (**Section 2.3.7**) are two thermal analysis techniques used to track phase transition regarding temperature change.

2.3.1 Raman Spectroscopy

The fundamental of Raman spectroscopy is based on Raman scattering. Scattering happens when an incident beam hits the target in a certain direction, then the direction and even energy change. The change of energy during light scattering can be classified into three types: Rayleigh scattering ($0-10^{-5} \text{ cm}^{-1}$), Brillouin scattering ($10^{-5}-1 \text{ cm}^{-1}$) and Raman scattering ($>1 \text{ cm}^{-1}$).[ref] In Raman scattering, the frequency of Raman scattered beam (ω) can be larger or smaller than the incident light (ω_0), which are called the Anti-Stokes (ω_{AS}) and the Stokes frequency (ω_S) respectively. If we set ω_0 as 0 on the axis of frequency, we should see that the absolute values of those two frequencies are equal to each other: frequency and wavelength

$$|\omega_S| = |\omega_{AS}| \quad (2.10)$$

However, as shown in **Figure 2.1**, the Stokes scattering is generated from the ground state while the Anti-Stokes scattering happens only when atoms or molecules are in the excited state, and both form virtual energy states. The Anti-Stokes scattering is

much weaker than the Stokes scattering because there are fewer atoms or molecules in the excited state than the ground state. The possibility of the Anti-Stokes scattering occurrence is much less. However, it should be notable that Raman scattering is still very weak compared with Rayleigh scattering. The intensity of Raman scattering is only 10^{-6-12} of the incident light.

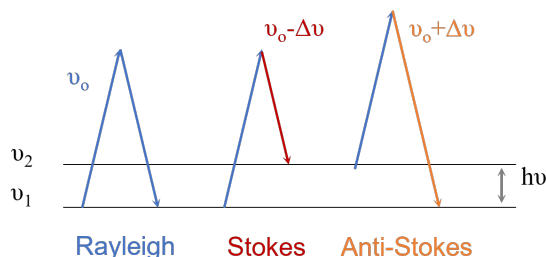


Figure 2.1: Schematic representation of Rayleigh, Stokes and Anti-Stokes scattering.

When we talk about spectroscopy, we refer to the interaction between the system (or sample) and electromagnetic radiation. Electromagnetic radiation can be considered as two perpendicular fields: electric field and magnetic field. Both are perpendicular to the direction of the radiation propagation. In this case, the spectroscopic observations can be the interaction with the either or both fields, which are called electric dipole allowed (T_x, T_y, T_z) or magnetic dipole allowed (R_x, R_y, R_z). Here we only consider x, y and z axes as three independent directions where charge separation occurs. Raman scattering arises from the change in polarizability in molecules, where the wavelength of incident light and the wavelength of the emitted light are different ($x^2, y^2, z^2, xy, yz, zx$).

The most common and important usage of Raman spectroscopy is to identify known compounds with reported Raman spectrum results according to the observed peak locations and relative intensities. One approach is considering the contribution of individual functional groups separately and the whole spectrum as the sum of all different regions, which is called the fragmentation approach. The other approach, the whole molecule approach, uses the whole system movement within a symmetric entity. Compared with the fragmentation approach, the whole molecule approach is more comprehensive and complete, especially for crystalline solids. By factor group

analysis, we can obtain the vibration modes from the crystallographic point group. It should be notable that the point group considers the symmetry inside one unit cell on the scale of 10 Å while the electromagnetic radiation in vibration spectroscopy interacts with the crystal at 100 nm up to 1 μm scale.

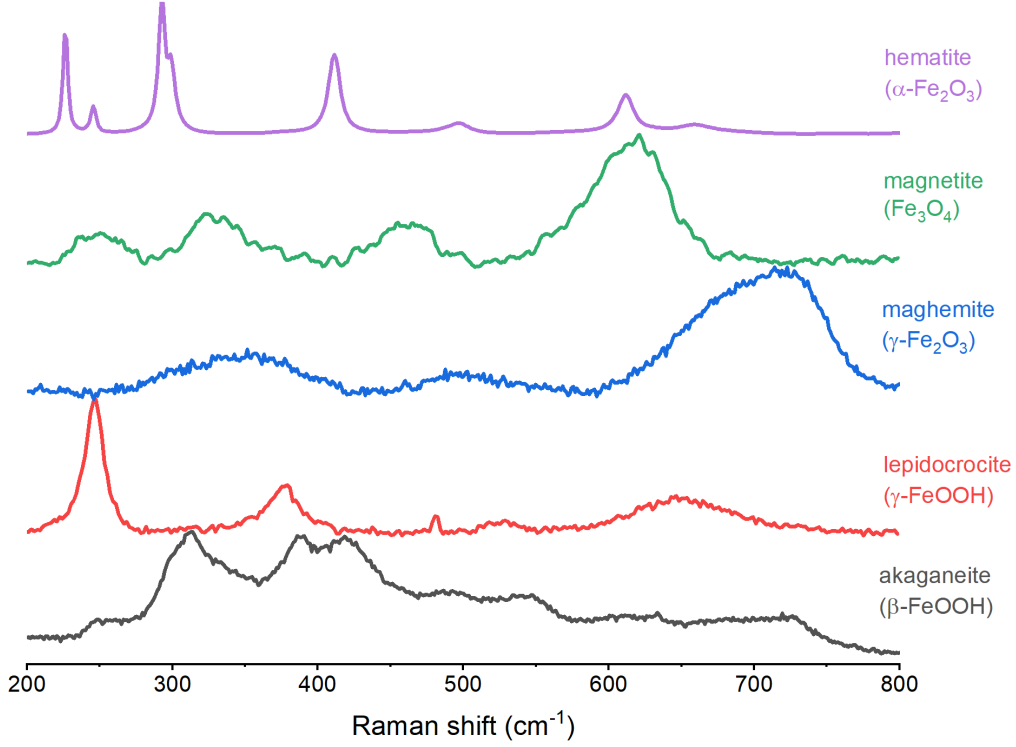


Figure 2.2: Raman spectra of common iron oxides and hydroxides

Raman spectroscopy can not merely be used as a fingerprint in material identification but also be applied in material defect analysis by quantitative study. Raman spectrum has been used in perovskite-type material BaTiO_3 .⁷⁸ Two Raman vibration modes I_{525} and I_{713} are sensitive to both the cation ratio (Ba/Ti) and the oxygen nonstoichiometry. The ratio of I_{525}/I_{713} has been proved to measure the intrinsic oxygen vacancy content and cation ratio. Raman spectroscopy has also been applied in quantifying defects in single layer MoS_2 .⁷⁹ The intensity ratio of the longitudinal acoustic (LA) and A_{1g} mode can be considered as an indicator of the degree of crystallinity $\frac{I(LA)}{I(A_{1g})} = \frac{\gamma}{L_D^2}$, where γ is the correlation constant and L_D is the inter-defect distance. Quantitative Raman spectroscopic analysis often uses the ratios of Raman intensities and widths, or the peak locations of certain peaks. High-

quality spectra are required to obtain accurate values in the Raman spectroscopic analysis.

2.3.2 Infrared Spectroscopy

Fourier-transform infrared spectroscopy (FTIR) is another type of vibrational spectroscopy widely used in material science study. The fundamental theory of IR spectroscopy is when the frequency of incident infrared radiation is the same as the vibrational frequency of the chemical bonds, the bonds or functional groups will be promoted to a higher vibrational level by absorption of energy. Unlike Raman active vibrational modes, vibrational modes with changes in the dipole moment are IR active.

2.3.3 Ultraviolet-visible Spectroscopy (UV-vis)

UV-vis spectroscopy refers to absorption spectroscopy or reflectance spectroscopy in the ultraviolet and visible range of light. The absorbed photon can excite the electron in the ground state to higher energy orbitals called the excited state. For electronic transitions in a solid, usually four types of transitions would be considered:⁸⁰

1. The excitation of an electron to a higher energy orbital **on the same atom**
2. The excitation of an electron from a localized orbital on an atom to a higher energy orbital **on an adjacent atom**
3. The excitation of an electron from a localized orbital on an atom to a delocalized band, which is called the **conduction band**
4. The excitation of an electron from **valence band** to **conduction band**

UV-vis spectroscopy has a large variety of applications. For transition metal compounds, UV-vis spectra in the $d - d$ transition can be used to determine the local

environment of the ions.ref In analytical chemistry, UV-vis is usually carried out to measure the concentration of specific molecules, ions or functional groups. The Beer-Lambert Law states that the absorbance, A , should be proportional to the concentration of measured sample: $A = \epsilon cl = \log(I_0/I)$, where l is the path length of the sample, I_0 is the intensity of the incident light and I is the intensity of the transmitted light.

For semiconducting materials, UV-vis spectrum is used to determine the band gap values like transition type 4. The band gap energy (E_g) is the energy required by a semiconductor to excite an electron from the valence band to the conduction band. The Tauc method is developed to extract E_g from absorption UV-vis spectrum:⁸¹

$$(\alpha \cdot h\nu)^{1/\gamma} = B(h\nu - E_g) \quad (2.11)$$

where α is the absorption coefficient, h is the Plank constant, ν is the photon's frequency, and B is a constant. The value of γ depends on whether it is a direct ($\gamma=1/2$) or indirect ($\gamma=2$) transition band gap. By plotting $(\alpha \cdot h\nu)^{1/\gamma}$ versus $h\nu$, we should get a linear relationship, and the intercept at the x-axis will be the band gap value.

2.3.4 X-ray Absorption Spectroscopy (XAS)

As the name suggests, X-ray absorption spectroscopy has the nature of absorption spectroscopy. X-rays are absorbed by all matters through the photoelectric effect.⁸² As shown in **Figure 2.3A**, X-rays are absorbed by the atom when the energy of the x-rays is transferred to the electron on K , L or M shell ejected from the atom. The atom is left in an excited state with an empty electronic level, and excess energy from the X-ray will be given to the ejected photoelectron. The excited core hole will relax back to the ground state of the atom. Meanwhile, a higher level core electron will drop back into the core hole, during which X-ray fluorescence occurs. X-ray photon has the feature of absorption edge, a sharp rise above 7100 eV in **Figure 2.3B**. Only X-ray photons above the edge have enough energy to excite the electron from a certain orbital. XAS measures the fluorescence (or transmission) of X-rays as a

function of the energy close to the absorption edge. In our example, it takes around 7125 eV to excite an electron from the 1s orbital of iron, which is known as the iron *K*-edge. In XAS experiments, the X-ray absorption coefficient $\mu(E)$ can be measured in both transmission and fluorescence methods. For transmission setup, the absorption is directly measured by the transmission after the sample:

$$I = I_0 e^{-\mu(E)t} \quad (2.12)$$

$$\mu(E)t = -\ln(I/I_0) = \ln(I_0/I) \quad (2.13)$$

where I_0 is the incident X-ray intensity, I is the transmission intensity through the sample, and t is the sample thickness. In X-ray fluorescence mode, it should be represented as $\mu(E) \propto I_f/I_0$, where I_f is the intensity of fluorescence. It should be notable that XAS requires a broad energy range and high-intensity energy. Therefore, XAS experiments usually demand the access to a synchrotron facility. In **Chapter 4**, XAS experiments were carried out in collaboration with Brookhaven National Laboratory in NY, USA.

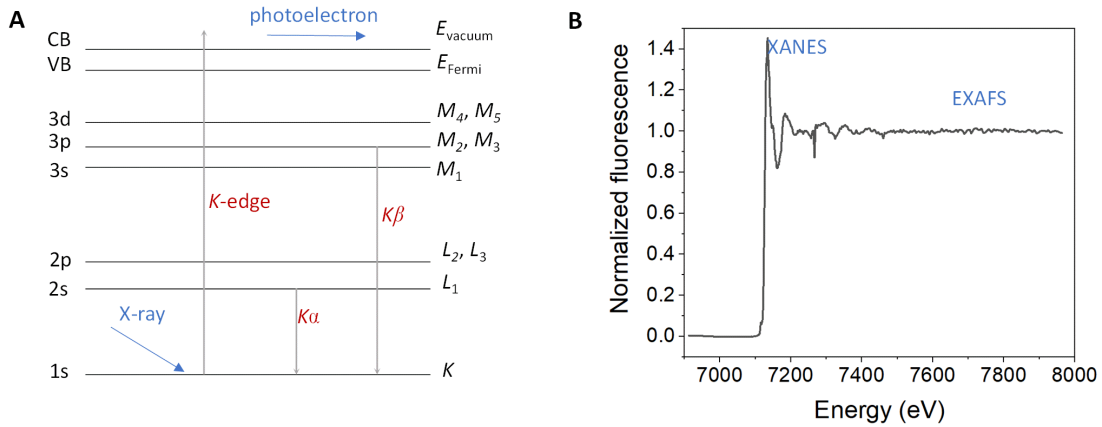


Figure 2.3: Normalized X-ray absorption spectrum of hematite

X-ray absorption near edge spectrum

As shown in **Figure 2.3B**, X-ray absorption fine structure (XAFS) is separated into two regions: the X-ray near edge spectrum (XANES) and the extended X-ray fine structure (EXAFS). As introduced before, the *K*-edge transition refers to the

photo-excitation of a 1s electron. The excitation of electrons involves the symmetry selection rule for spectroscopy, which is the electron transition is more likely to occur when the angular quantum number changes by ± 1 . In this case, the K -edge transition of electrons from 1s to p orbital will be allowed. The most important and most common usage of XANES is to use the shift of the K -edge position to determine the oxidation state of elements. In this thesis, the K -edge location of iron has been known to show a linear relationship with a shift of 4.6 eV per change in the oxidation state.^{83,84}

Extended X-ray absorption fine structure

EXAFS focuses on the oscillations caused by photoelectrons ejected from the central atom by incident X-rays. For those ejected photoelectrons, there is a possibility that they are elastically scattered from the neighbouring atoms. There is also a possibility that they are redirected back to the central atom. The oscillation is the net sum generated by the constructive and destructive interference which is dependent on the incident wavelength. For EXAFS experiments, the energy range is 40-1000 eV above the absorption edge while the mean free path of a photoelectron is 5-10 Å. Therefore, the distance scale of 5-10 Å around the central atom should be the interference patterns generated from EXAFS experiment.

The core of EXAFS can be represented as the EXAFS equation in k -space

$$\chi(k) = S_0^2 \sum_i N_i \frac{f_i(k)}{k D_i^2} e^{-2D_i/\lambda(k)} e^{-2k^2\sigma_i^2} \sin[2kD_i + \delta_i(k)] \quad (2.14)$$

where $\chi(k)$ is the oscillation intensity, $f_i(k)$ is scattering amplitude, S_0^2 is the amplitude reduction factor, $\delta_i(k)$ is the phase shift, $\lambda(k)$ is the mean free path, N_i is the **coordination number**, D_i is the **distance** to the neighbouring atom, σ_i^2 is the mean square relative displacement or called **Debye-Waller factor**. N_i , D_i and σ_i^2 are commonly used parameters in subshell modelling in EXAFS data analysis. S_0^2 is typically taken as a constant between 0.7 and 1.0. $f_i(k)$ and $\delta_i(k)$ are highly depend on atomic number of the neighbouring atom.

To create structural models for EXAFS data, the key is to identify critical coordination shells and use them to fit EXAFS data. $f_i(k)$, $\delta_i(k)$ and $\lambda(k)$ can be calculated using the program FEFF. To generate FEFF files, we require crystallographic data

converted into a list of atomic coordinates and a selected central atom (the studied element). Each FEFF file contains $f_i(k)$, $\delta_i(k)$ and $\lambda(k)$ for a particular shell or scattering path from the cluster of atoms. N_i , D_i and σ_i^2 will be determined to fit the EXAFS curve, especially the peaks within 2-10 Å. According to the position of the peaks, shells from the absorber (the central atom) can be selected. The specific shell should be considered to make the bond length and coordination number reasonable values. Also, restrictions may be applied between the shells. For example, with doping example, the coordination number of dopant and host atoms should keep the same.⁸⁵

2.3.5 Powder X-Ray Diffraction (XRD)

Powder X-ray diffraction is a rapid and common analytical technique used for not merely phase identification of crystalline materials and also structure information on unit cell dimensions by Rietveld refinement. When the incident beam of monochromatic X-rays interacts with the target crystal, the scattered X-rays The laboratory X-rays are produced by a cathode ray tube by heating a filament to generate and accelerate the electrons toward the target material. One of the most common target material can be copper with CuK_α radiation ($\lambda=1.5418$ Å). The wavelength of X-rays should be comparable in scale with the spacing (d) between atoms in the crystal lattice to achieve X-ray diffraction. Bragg's law describes the relationship between the incident X-ray beams with a wavelength of λ to the diffraction angle θ and the lattice spacing of the crystal d :

$$n \cdot \lambda = 2d \cdot \sin\theta \quad (2.15)$$

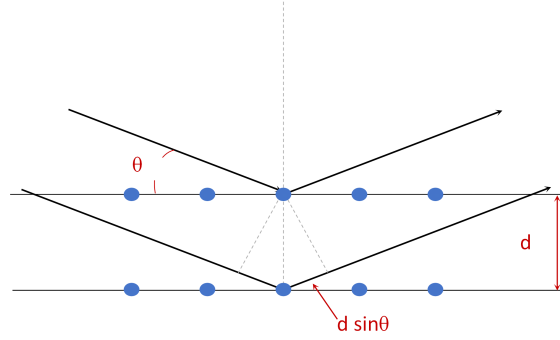


Figure 2.4: Schematic representation of Bragg's law.

As shown in **Figure 2.4**, the distance difference $d \cdot \sin\theta$ must equal an integer number of wavelengths to make the X-ray beams in phase. If the relationship does not fit Bragg's law, the reflected beams are out-of-phase and destructive interference, cancelling occurrence. When Bragg's law is satisfied, the reflected beams are in phase and constructive interference. Then we can obtain peaks at the angle θ . 2θ is used as the x-axis in XRD pattern because of the rotation of the X-ray detector. The intensities of XRD peaks rely on the elements if both X-ray wavelength and angle of incidence are kept the same, since X-rays are scattered by the electrons around the atom nucleus. The intensity (I) can be presented as a function of the structure factor ($F(hkl)$):

$$I \propto F(hkl)^2 \quad (2.16)$$

$$F(hkl) = \sum f_i e^{2\pi i(hx_i + ky_i + lz_i)} \quad (2.17)$$

where (hkl) are the Miller indices of the plane, (x, y, z) are the coordinates of the atom, f is the atomic scattering factor. From the XRD pattern, d-spacing from the crystal can be extracted.

2.3.6 X-ray Photoelectron Spectroscopy (XPS)

X-ray photoelectron spectroscopy, also called electron spectroscopy for chemical analysis, is a surface-sensitive spectroscopic technique that can identify and quantify the elements and their chemical state and electronic structure. Each element has

a unique elemental spectrum, and the XPS peaks from a chemical compound can be considered as the sum of elemental peaks from each individual. Typical analysis depth of XPS is only 3 to 10 nm because of the small mean path of the electrons. Quantitative analysis can be obtained from the peak intensity and areas while the chemical state of the elements can be extracted from the peak position. The principle of XPS technique is based on the photoelectric effect:[ref:handbook of xps]

$$E_k = h\nu - (E_b + \Phi_{\text{spec}}) \quad (2.18)$$

where $h\nu$ is the energy of the photon, E_k and E_b are the kinetic energy and binding energy of ejected electrons respectively, Φ_{spec} is the work function of the spectrometer. The kinetic energies (E_k) of emitted electrons are measured by the detector. The binding energy of each element can be calculated based on equation **Equation** (2.18) and plotted in X-ray photoelectron spectrum. Spin-orbital splitting occurs in the XPS peaks according to the electron configuration. Chemical shift leads to a change in the binding energy of electrons due to the surrounding neighbours of elements.

2.3.7 Thermal Analysis

Thermal analysis is the technique which tracks the enthalpy, mass or heat capacity change of a solid sample with temperature. Thermal analysis contains two parts, thermogravimetric analysis (TGA) and differential scanning calorimetry (DSC) or differential thermal analysis (DTA). Thermal analysis usually performs in an inert gaseous environment like argon gas. With temperature increasing or decreasing at a certain ramp rate, the property change of material can reflect the occurrence temperature of decomposition, melting, or crystal reconstruction.

Thermogravimetric analysis measures the mass of a sample as a function of temperature or time. When decomposition takes place, the mass will drop significantly and then plateau, marking the completion of the reaction. In this case, TGA can only observe reaction or physical change with a change in mass like decomposition or boiling point measurement.

Both the atmosphere and the sample's nature will influence the temperature range. DTA and DSC are similar in functions and experimental setup. Both techniques heat the sample and a reference at the same time. DTA records the temperature difference between those two while DSC measures the heat flow directly. Therefore, we can get a plot of ΔT versus temperature or time from DTA but a plot of heat (ΔQ) versus temperature from DSC. Compared with TGA, DTA and DSC can also record the heat change like recrystallization or phase change without weight loss in addition.

2.4 (Photo)Electrochemical Techniques

2.4.1 Photoelectrocatalytic Measurement

A homemade polyethylene three-electrode cell is used in the photoelectrochemical measurement as shown in **Figure 2.5**. Sample-coated fluorine-doped tin oxide glass (FTO) working electrodes (WE) are mounted as windows in the cell with the area of the electrode exposed to electrolyte solution masked to 1.54 cm^2 by a silicone O-ring with back-side illumination. The blue film as FTO glass piece and red film as deposited hematite are shown in **Figure 2.5**. Copper papers are used to connect the films to the potentiostat as shown in grey sticks in **Figure 2.5**. A Gaskatel HydroFlex Reversible Hydrogen Electrode serves as the reference electrode and a piece of clean FTO as the counter electrode (CE). RHE works as a standard reference electrode with H_2 gas slowly bubbled over a Pt mesh. 1 M KOH is usually used as the electrolyte. The photocurrent density at 1.23V vs.RHE ($j_{1.23\text{V}}$) is defined as the measure of the photocurrent density of OER. The same cell is used in electrochemical impedance spectroscopy measurement.

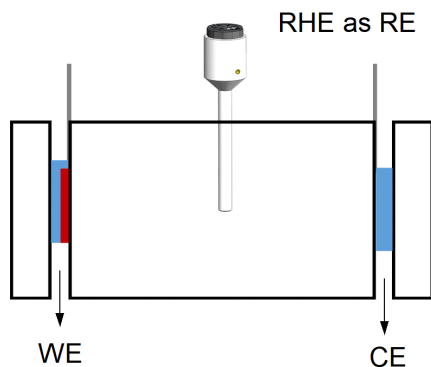


Figure 2.5: The scheme of the photoelectrochemical cell used in the project.

2.4.2 Electrochemical Impedance Spectroscopy

Electrochemical impedance spectroscopy (EIS) is an electrochemical technique to measure the impedance of the system under AC potential. EIS is based on the perturbation of either an equilibrium state or at least a steady state situation, while the standard techniques are dynamic or are based on the change from an initial equilibrium state to a different and final state. Impedance is used instead of resistance because circuit elements in the real world exhibit much more complex behaviour. A resistor (R) follows Ohm's Law, $R = \frac{E}{I}$, and the resistance value should be independent of frequency. Similar to resistance, impedance is a measure of the ability of a circuit to resist the flow of electrical current. The AC voltage and responding current can be expressed as functions of time, and the impedance can be presented as the quotient of AC voltage and current which is similar to Ohm's Law:

$$E_t = E_0 \sin(\omega t) \quad (2.19)$$

$$I_t = I_0 \sin(\omega t + \phi) \quad (2.20)$$

$$Z = \frac{E_t}{I_t} = \frac{E_0 \sin(\omega t)}{I_0 \sin(\omega t + \phi)} = Z_0 \frac{\sin(\omega t)}{\sin(\omega t + \phi)} \quad (2.21)$$

where E_t and I_t are the potential at time t and the corresponding current, E_0 and I_0 are the amplitude of the voltage and current, ω is the radial frequency, ϕ is the phase shift. As shown in **Figure 2.6A**, a pure resistor has no phase shift, then

the impedance Z only has the real part as expected as resistance values. For a pure capacitor, the phase shift is 90° between the AC voltage and AC.

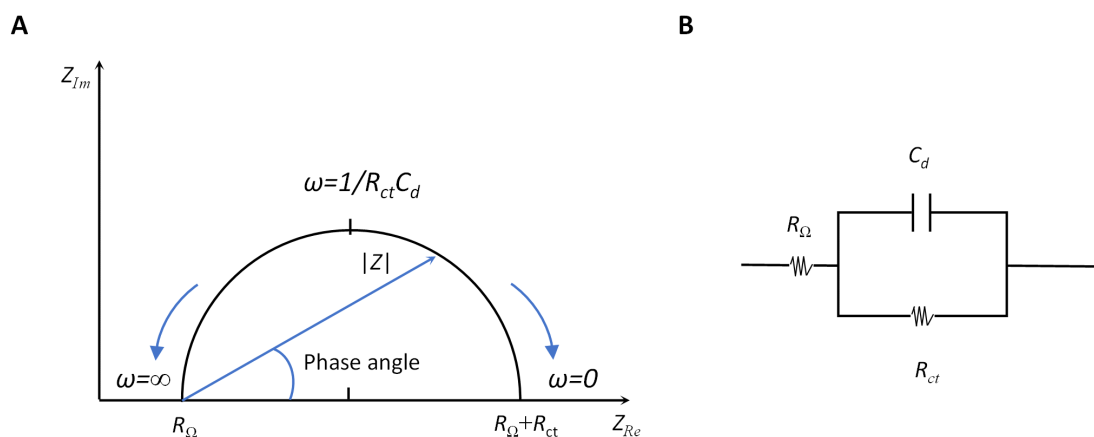


Figure 2.6: Electrochemical impedance spectroscopy Nyquist plot (A) of the Randles cell and corresponding equivalent circuit (B)

Nyquist plot (**Figure 2.6A**) represents the real and imaginary part of vector z as the x and y-axis respectively. The angle between the vector and x-axis is phase angle ϕ . From the Nyquist plot, the length of z can be seen directly, but we can not tell the frequency for data points. From the left side to the right side of the semicircle, the frequency rises from zero to infinity.

Figure 2.6A shows the Nyquist plot of the simplest and most common circuit: the Randles cell with a corresponding equivalent circuit in **Figure 2.6B**. The Randles cell consists of a solution resistance (R_Ω), a double layer capacitor (C_d) and a charge transfer resistance (R_{ct}). The double layer capacitor and charge transfer resistance are in parallel connection and then in series connection with the solution resistance. In the Nyquist plot, the first intercept at the x-axis is equal to the solution resistance value. The second intercept of the semicircle is the sum of solution resistance and charge transfer resistance because at this point phase angle is zero. Consequently, the diameter of the semicircle equals the charge transfer resistance of the system. The Randles cell is used as the equivalent circuit in this project supported by previously reported PEC investigation of OER with hematite electrodes.⁶⁴

Mott-Schottky plot can be plotted using the capacitor data C_d from EIS versus the potential difference between bulk semiconductor and electrolyte. In experiment

setup, EIS is performed under a specific range of potential to obtain the potential-dependent capacitor value. The flat band potential (E_{fb}) and charge carrier density (N_d) can be calculated from Mott-Schottky analysis. Here is the equation:

$$C^{-2} = \frac{2}{qA^2\epsilon_r\epsilon_0N_d}(V + E_{fb}) \quad (2.22)$$

where ϵ_r is the relative permittivity of the semiconductor material, ϵ_0 is the vacuum permittivity, A is the surface area, and q is the elementary charge. The plot of C^{-2} and potential V should be linear. A positive slope refers to an n -type semiconductor while a negative slope value refers to a p -type semiconductor. Charge carrier density can be calculated as:

$$N_d = \frac{2}{qA^2\epsilon_r\epsilon_0}. \quad (2.23)$$

Chapter 3

Revealing Interstitial Protons Through Structure-property Analysis

3.1 Introduction

As one of the most attractive photoanode materials, hematite has a maximum theoretical photocurrent of 12.6 mA cm^{-2} .¹⁷ However, the PEC performance records for hematite photoanodes remain far below the theoretical values. An understanding of the chemical nature of structural defects in hematite and their specific impacts on material structures and properties is the key to improving PEC performance. The performance metrics and fundamental physical properties reported for nominally $\alpha\text{-Fe}_2\text{O}_3$ films are persistently variable across the literature. Examples of variability include properties such as the optical band gap, commonly reported between 1.9 to 2.2 eV,^{7,14,86-88} the location of the conduction band, which ranges from 0.3 to 0.6 V vs. RHE,^{7,88,89} and performance parameters such as the current density at 1.23 V, which varies between *ca.* 1 A cm^{-2} to 3 mA cm^{-2} . The conclusion must thus be drawn that synthetic $\alpha\text{-Fe}_2\text{O}_3$ films are rarely identical. Techniques developed to identify and locate intraband trap states⁹⁰ and to probe associated photophysical processes⁹¹ provide powerful tools to guide development, but without a semblance of

consistency across the literature it is difficult to judge exactly how meaningful any single dataset is. Confident identification of specific structural anomalies or defects responsible for variation in properties and an understanding of how they influence these properties is an important component in advancing the field.

Oxygen vacancies have been identified as a structural defect of interest in hematite and gained experimental control over the concentration.^{19,27,30,31} X-ray photoelectron spectroscopy and X-ray absorption spectroscopy have been successfully employed to confirm and quantify these vacancies,^{34,51} and to show that complete removal of oxygen vacancies from the photoanode surface can result in suppression of PEC performance.^{34,51} The details of oxygen vacancy impacts on hematite has been discussed in **Section 1.3.1**. It must be noted, however, that performance metrics for α -Fe₂O₃ photoanodes annealed under air or pure oxygen atmospheres have been reported that meet or exceed the performance generally acquired through oxygen vacancy engineering.^{24,92} The picture is thus not complete and there is continued need to establish correlations between fabrication conditions, structural properties and performance parameters.

In this chapter, we employ structure-property analysis to obtain insight into the specific chemical nature of one such structural defect. We obtain hematite photoanodes capable of driving OER between $1 \mu\text{A cm}^{-2}$ and 0.48 mA cm^{-2} at $1.23 \text{ V}_{\text{RHE}}$ by annealing electrodeposited lepidocrocite films with varied protocols. The films exhibit negligible differences in X-ray diffraction patterns but all samples exhibit a formally Raman-inactive absorbance band that signifies a crystal lattice defect. The intensity of the peak for this vibrational mode varies with fabrication protocols and is found to correlate with the band structure descriptors and overall PEC performance. Analysis of the results leads us to propose that the trapping of protons induces iron deficiency in the lattice that is responsible for the observed behavior.

3.2 Results

3.2.1 Characterization of α -Fe₂O₃ Powders

The ability to fabricate α -Fe₂O₃ with varied structural integrity by annealing γ -FeOOH under varied atmospheres was explored in the powder form due to ease of fabrication and structural characterization. Powder X-ray diffraction experiments confirm that γ -FeOOH is the predominant iron phase obtained through controlled oxidation of aqueous Fe²⁺ solutions (**Figure 3.1A**).⁷⁴ The transition of γ -FeOOH to α -Fe₂O₃ is a dehydroxylation reaction that proceeds through γ -Fe₂O₃ as an intermediate phase, where both hydrogen and oxygen are removed from the structure.⁴⁵ The initial transition occurs above 300 °C;⁴⁵ the powders here yield the characteristic reflections for γ -Fe₂O₃ and complete loss of reflections attributable to γ -FeOOH when annealed at 350 °C. Annealing at 600 °C yields the diffraction pattern of α -Fe₂O₃ for all four annealing atmospheres, albeit with substantially broadened peaks that indicate significant structural disorder and a peak at *ca.* 27° suggesting residual γ -FeOOH (**Figure 3.1**). Fully region and selectively enlarged regions are shown in **Figure 3.1B** and **C** for comparison. The vertical purple and orange lines at the bottom of each panel depict α -Fe₂O₃ (COD#9000139) and γ -FeOOH (COD#9015231), respectively. Increasing the temperature to 800 °C decreases the XRD peak widths but no differences in the location or width of peaks are detectable between samples annealed at 800 °C under any of the four different atmospheres. Small peaks at 29.7 and 30.7° that persist in the powder samples are due to K₂SO₄ trapped during the fabrication process. Raman spectroscopy supports this assignment and confirms its absence in thin film samples (**Figure 3.2D** and **E**). The XRD results suggest that, irrespective of the reaction atmosphere, γ -FeOOH undergoes complete conversion to γ -Fe₂O₃ at 350 °C, to a disordered form of α -Fe₂O₃ at 600 °C, and finally to a more crystalline form of α -Fe₂O₃ at 800 °C.

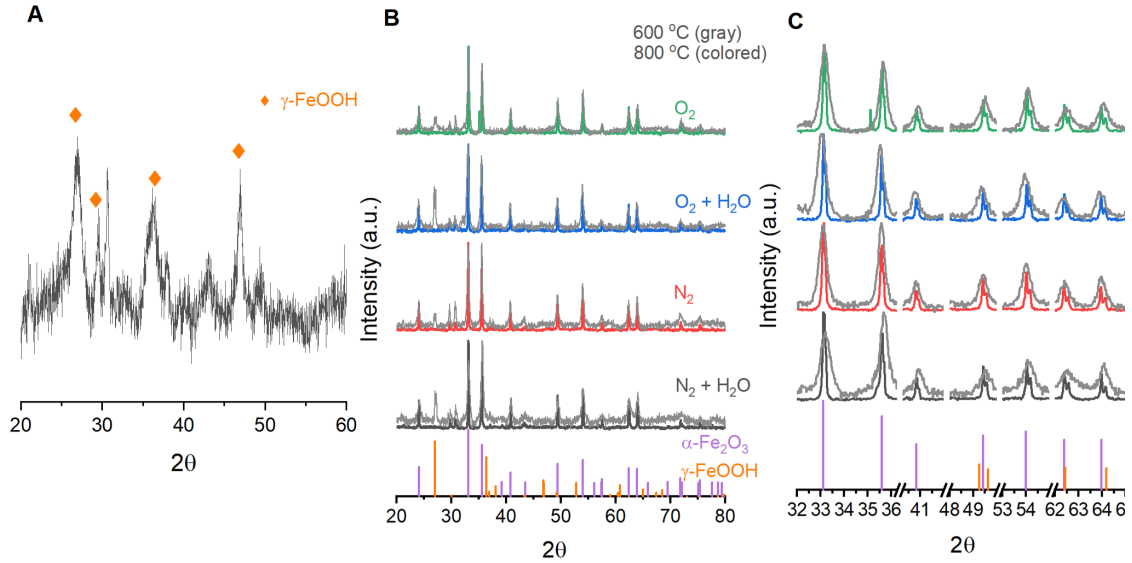


Figure 3.1: Powder X-ray diffraction patterns obtained from (A) γ -FeOOH and following annealing of (B and C) γ -FeOOH at 600 °C and 800 °C for two hours

Raman spectroscopy on powder samples provides evidence that the integrity of the α -Fe₂O₃ crystal lattice is in fact affected by atmospheric conditions during annealing. **Figure 3.2** shows Raman spectra acquired on γ -FeOOH powder and samples annealed at various temperatures for 2h under a dry O₂ atmosphere. Raman spectra on as-prepared γ -FeOOH powders contain the expected vibrations at 247, 379, 525 and 645 cm⁻¹ (**Figure 3.2A**).⁹³ These features are replaced by the characteristic peaks for γ -Fe₂O₃ at *ca.* 348, 498 and 707 cm⁻¹ after annealing at 350 °C for 2 hours, confirming XRD indications of complete structural conversion at these temperatures.⁹³ Annealing at 600 or 800 °C results in the emergence of seven intense peaks in the Raman spectrum (**Figure 3.2A**). These well-documented peaks are assigned to the two A_{1g} (226 and 499 cm⁻¹) and five E_g (246, 293, 412, 497 and 612 cm⁻¹) Raman active vibrational modes for α -Fe₂O₃.⁹³⁻⁹⁷ It is notable that these α -Fe₂O₃ peaks are orders of magnitude more intense than those for γ -FeOOH and γ -Fe₂O₃, which means that if γ -FeOOH or γ -Fe₂O₃ would be very hard to observe in Raman spectra if there are residuals in the samples. This care must be taken in selecting laser intensity as these phases readily transition into defective α -Fe₂O₃ under laser irradiation (**Figure 3.2B**). The intensity of the lower three spectra are increased 10-fold to compensate for the weak scattering cross section of γ -Fe₂O₃. In addition to the seven expected α -Fe₂O₃ vibrational modes, spectra on powders an-

nealed at 600 and 800 °C contain weak peaks at 660 and 710 cm^{-1} . The relative intensity of each of these two features is sensitive to annealing protocols (**Figure 3.2C**). Comparisons across the 12 different spectra show that both peaks diminish in size when annealed at higher temperatures or for longer times (**Figure 3.2E and F**). Two extra small peaks are assigned as K_2SO_4 impurity from precursor (**Figure 3.2D**). Accordingly, samples annealed at 800 °C for 2 hours show the smallest 660 cm^{-1} peak in each series and no discernible peak at 710 cm^{-1} . All iron oxide crystal structures exhibit vibrations in the 600–700 cm^{-1} region,⁹³ making it plausible that the two unexpected features signify phase impurities. The identity of the 660 cm^{-1} peak has been discussed in the literature, with consensus being that this feature is an infrared active (i.e. Raman inactive) E_u vibrational mode that becomes observable in Raman spectra due to distortions in the crystal lattice.^{59–61,94} An infrared-active vibration is observed in the thin film samples here using FTIR reflection-absorption spectroscopy (**Figure 3.3**), leading us to follow literature precedent and assign the 660 cm^{-1} to the formally Raman inactive E_u vibrational mode and attribute the 710 cm^{-1} feature to $\gamma\text{-Fe}_2\text{O}_3$. Raman spectroscopy thus provides a means to track structural distortions in $\alpha\text{-Fe}_2\text{O}_3$ and confirm that structural integrity is systematically dependent on annealing conditions.

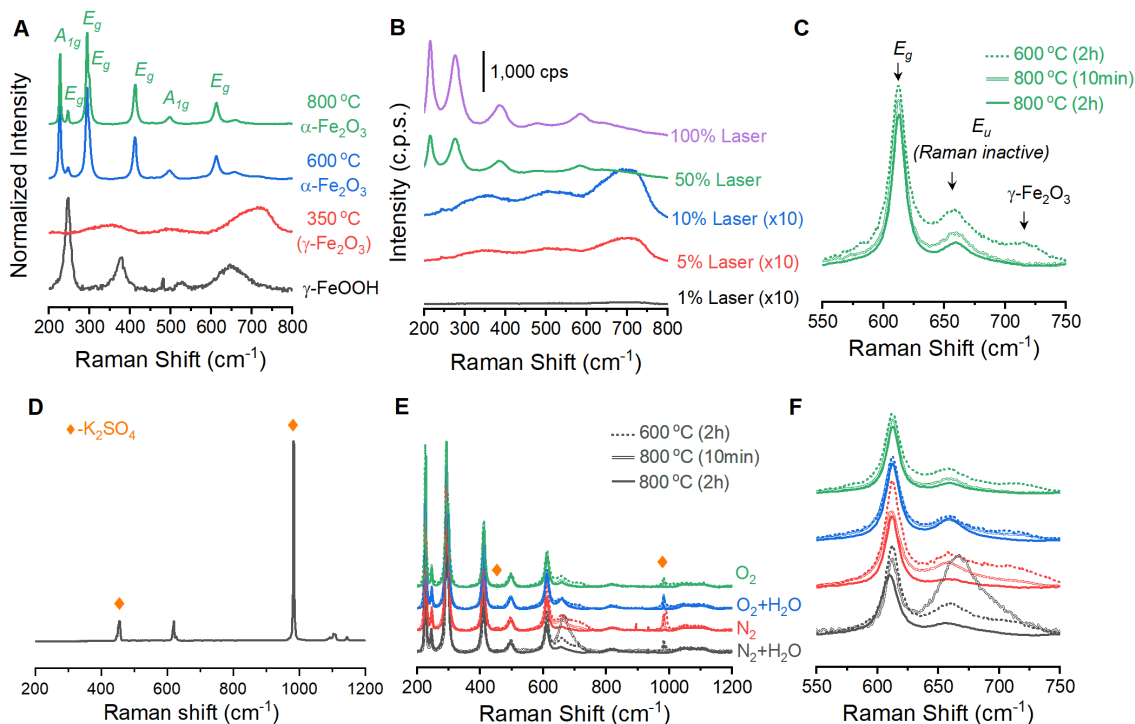


Figure 3.2: Raman spectra acquired on iron oxide powders. (A) γ -FeOOH powder and samples annealed at various temperatures. (B) Spectra as a function of laser power on a powder annealed at 350 °C. (C) Magnified view. (D) K_2SO_4 impurity. (E) Powders annealed for all 12 samples and (F) magnified view.

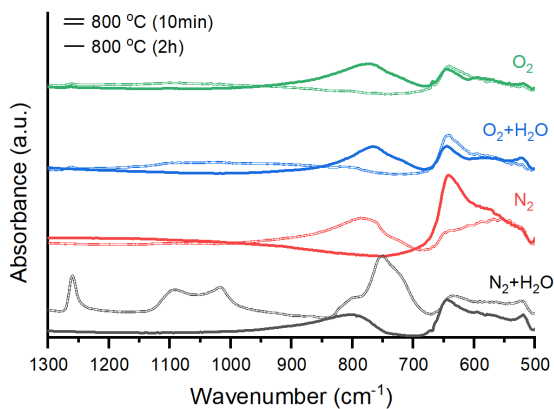


Figure 3.3: Infrared spectra for hematite thin film samples annealed at 800 °C for 10 min and 2h.

3.2.2 Raman spectroscopy of photoanode films

Films prepared by annealing electrodeposited γ -FeOOH under varied environments show behavior analogous to the powder samples. A series of 12 films prepared

with annealing conditions identical to the powder samples were analyzed by spectroscopic mapping to ensure that Raman spectra are representative of the entire surface. Spectra were acquired in 1-micron steps across three distinct 2×2 micron grids for each of the 12 films; each set of 27 spectra was averaged and normalized (**Figure 3.4A**). These 12 spectra are dominated by the characteristic peaks for α - Fe_2O_3 , with secondary peaks once again present at *ca.* 660 and 710 cm^{-1} (**Figure 3.4B**). The presence of a 710 cm^{-1} peak in all four films annealed at 600 °C reveals that an incomplete reaction yields γ - Fe_2O_3 contamination. The 660 cm^{-1} is again observed to decrease as temperature or annealing time are increased. Only the eight 800 °C samples were selected for detailed analysis as phase contamination in the 600 °C samples would impede clean comparisons between the spectroscopic and electrochemical behavior. The spectra were fitted with 8 component curves (7 Raman active and 1 inactive) to obtain component peak locations, intensities and widths for comparison with electrochemical behavior (**Table 3.1**).

Spectroscopic maps acquired over large areas on select samples provide confidence that samples prepared at 800 °C are homogeneous and yield consistent spectra. All eight samples show the same qualitative behavior; the sample annealed at 800 °C for 2 hours under humidified O_2 provided the highest photoelectrocatalytic activity (see below) and will be discussed. Visual inspection under magnification shows a polycrystalline orange surface with a small number of green streaks that were identified as bare FTO (**Figure 3.4E**). A region containing an exposed FTO streak was selected for analysis and a series of Raman spectra were collected in 1-micron steps across a 23×24 micron grid (**Figure 3.4C**). The reproducibility of spectra acquired by the mapping protocol is confirmed by the superimposition of the average of these 600 spectra with that from the smaller 2×2 micron grid (**Figure 3.4F**).

Table 3.1: Location, intensity and width of peak components for the 800 °C α -Fe₂O₃ films.

Sample		A_{1g}	E_g	E_g	E_g	E_g	A_{1g}	E_g	E_u
N ₂ +H ₂ O 10min	Centre	228.02	247.04	294.19	301.02	412.40	497.64	612.93	661.95
	Width	4.65	5.25	6.98	7.34	10.54	19.28	16.94	39.52
	Height	0.80	0.14	0.93	0.34	0.50	0.08	0.26	0.15
N ₂ 10min	Centre	227.38	246.65	293.60	300.33	412.26	497.24	612.98	660.36
	Width	4.42	4.90	6.34	7.14	10.35	21.72	16.04	36.55
	Height	0.81	0.17	0.91	0.40	0.57	0.08	0.29	0.10
O ₂ +H ₂ O 10min	Centre	228.43	247.60	294.56	301.28	413.25	498.10	613.69	662.70
	Width	4.00	4.43	5.49	6.34	9.48	18.57	12.91	38.66
	Height	0.85	0.16	0.93	0.39	0.47	0.07	0.23	0.04
O ₂ 10min	Centre	228.06	247.23	294.27	301.07	413.09	497.79	613.71	661.69
	Width	4.04	4.54	5.59	6.45	9.48	18.44	13.12	34.31
	Height	0.83	0.16	0.95	0.40	0.48	0.07	0.24	0.06
N ₂ +H ₂ O 2h	Centre	227.96	247.06	294.04	300.86	412.65	498.11	613.05	661.73
	Width	4.23	4.64	5.82	6.51	9.90	17.97	13.55	32.29
	Height	0.88	0.14	0.96	0.38	0.44	0.08	0.23	0.05
N ₂ 2h	Centre	227.51	246.75	293.67	300.35	412.28	496.59	612.62	663.06
	Width	4.04	4.51	5.57	6.34	9.59	18.98	13.07	48.11
	Height	0.81	0.17	0.92	0.40	0.51	0.06	0.25	0.03
O ₂ +H ₂ O 2h	Centre	228.26	247.39	294.32	301.09	412.93	498.15	613.29	660.97
	Width	4.06	4.48	5.68	6.54	10.03	18.40	13.34	32.48
	Height	0.85	0.16	0.95	0.38	0.44	0.07	0.23	0.03
O ₂ 2h	Centre	228.44	247.60	294.54	301.31	413.18	498.22	613.52	662.74
	Width	3.99	4.40	5.51	6.26	9.64	18.53	13.11	38.80
	Height	0.85	0.15	0.94	0.39	0.46	0.07	0.23	0.03

Spectroscopic maps showing the location, intensity and width of each individual peak failed to reveal any irregularities in the α -Fe₂O₃ spectra. The ratio of intensities of the 499 and 612 cm⁻¹ components to that of the Raman inactive peak at 660 cm⁻¹ (I_{499}/I_{660} and I_{621}/I_{660} , respectively) were identified to be of importance and are discussed below. Histograms for each of these terms show a Gaussian distribution with *ca.* 80% of the total spectral variation residing within 15% of the distribution maxima (**Figure 3.4D**). Black curves are a fitted Gaussian distribution and gray shaded areas denote 15% variation from the peak in either direction across a larger 23 × 24 μ m region (**Figure 3.4C**) of a film annealed at 800 °C for 2 hours under humidified O₂ atmosphere. Faded histogram at low ratios represents the distributions observed for a sample heated at 600 °C for 2 hours under dry O₂ atmosphere. We therefore adopt $\pm 15\%$ of the maximum as an error estimate for the structure–property correlations below. Pixels on a surface image that fall outside of

this 15% range are randomly scattered on spectroscopic maps (**Figure 3.4C**). This visual confirmation provides further confidence in the uniformity of the surfaces and the viability of using the acquired spectra to represent the overall structure in structure–property analyses.

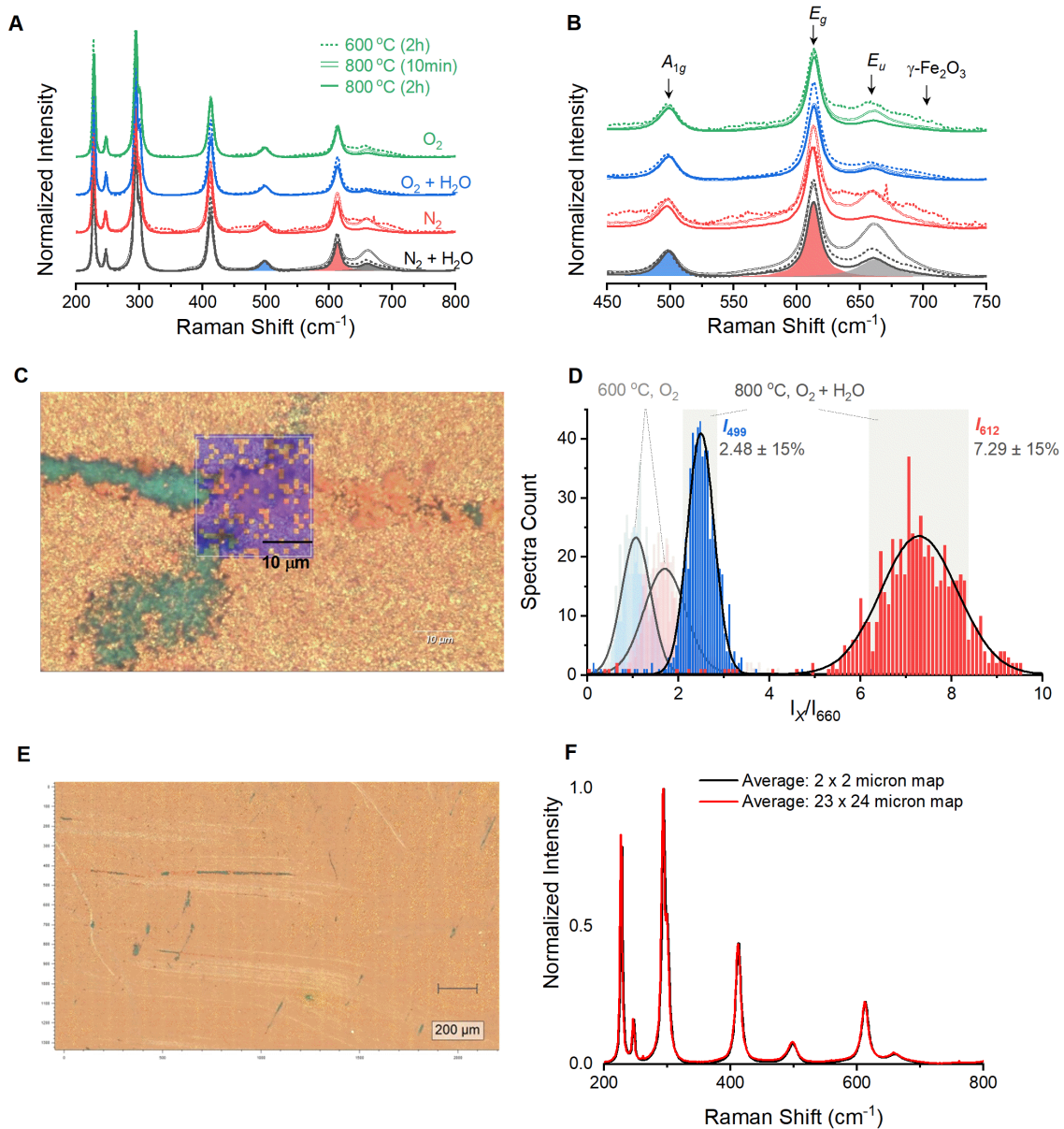


Figure 3.4: Raman spectra acquired on α -Fe₂O₃ films. (A) The full spectral range, (B) magnification of key peaks, (C) A Raman spectroscopic map of the $23 \times 24 \mu\text{m}$ region, (D) Histograms showing intensity ratios of the I_{499} and I_{612} vibrational modes to the I_{660} for Raman spectra. (E) White image of sample, (F) Comparison of the averaged spectrum from two scales.

3.2.3 Parametrizing photoelectrocatalysis

The eight different samples prepared at 800 °C yield markedly different photoelectrochemical behavior. Voltammetric sweeps while under illumination with artificial sunlight in 1M KOH as electrolyte reveal pronounced changes in the onset of photoelectrocatalysis, maximum current densities attained, and even curve shape for each of these α -Fe₂O₃ films (**Figure 3.5A** and B). Rapid cathodic sweeps performed in the dark after equilibration at 2 V_{RHE} under illumination for films. Hematite photoanodes annealed at 350–600 °C are typically found to exhibit low crystallinity and/or incomplete phase transitions.⁹⁸ The samples annealed at 600 °C here suffer from this issue, resulting in unmeasurable PEC performance. The current density at 1.23 V ($j_{1.23V}$), or zero overpotential for OER, is a performance metric widely reported in the literature; values for the samples annealed at 800 °C are provided in **Table 3.2**.^{99,100} The onset of PEC (E_{PEC}) was selected as a second performance metric. The voltage at which derivative dj/dE plots reaches 0.2 mA cm⁻² V⁻¹ has been reported as a means of systematically extracting a numeric value for E_{PEC} .¹⁰¹ This approach works well for samples exhibiting good PEC performance, but fails to capture the onset for poorly performing samples. The first positive peak in second derivative d^2j/dE^2 plots was therefore chosen as a means to systematically represent E_{PEC} (**Figure 3.6**). This approach captures the foot of the catalytic wave, thereby generalizing the metric such that it is not coupled to specific performance values.

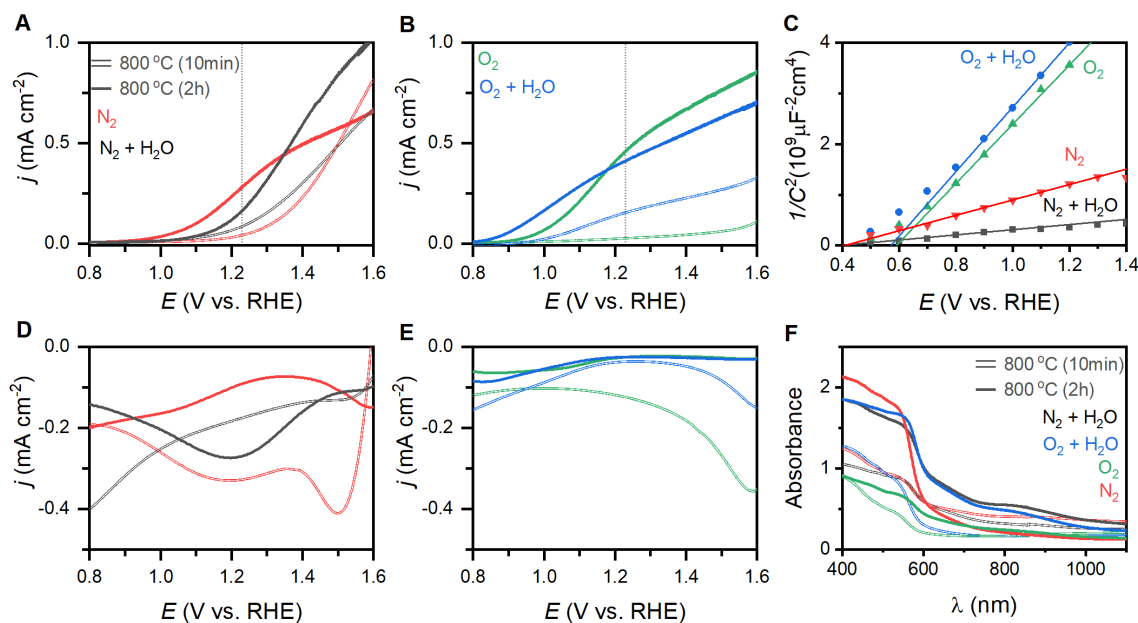


Figure 3.5: Photoelectrochemical behavior and characterization of $\alpha\text{-Fe}_2\text{O}_3$ films. (A), (B) Voltammetric behavior under illumination (C) Mott–Schottky plots of films prepared at 800 °C for 2h. (D), (E) Rapid cathodic sweep results. (F) UV-visible absorption spectra for the eight films annealed at 800 °C

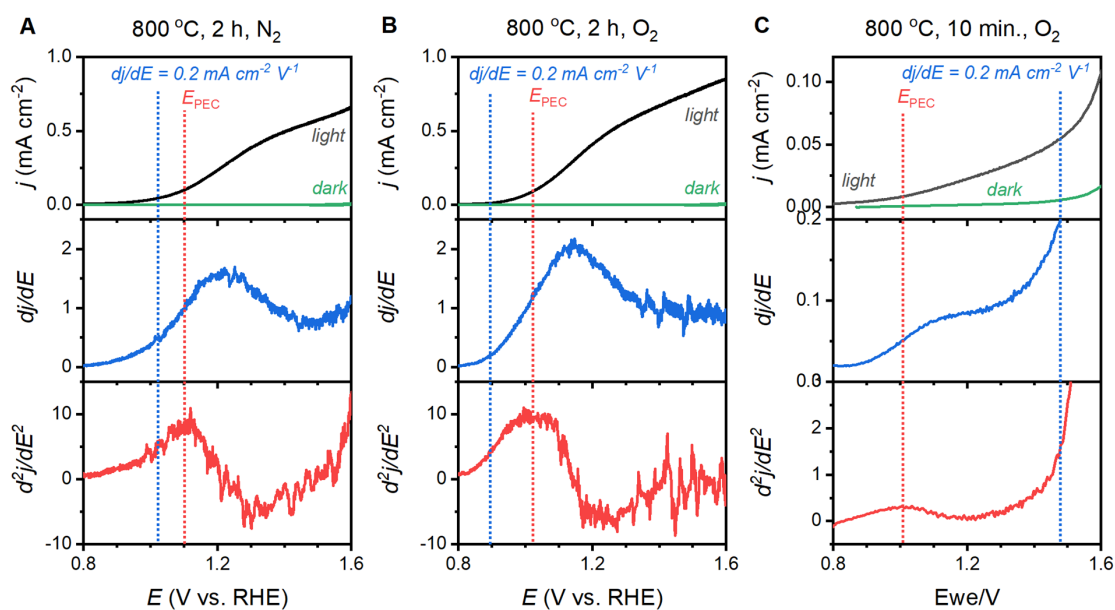


Figure 3.6: Method for determining photoelectrocatalytic onset. Samples shown are (A) 800 °C for 2 hours under dry N_2 and (B) 800 °C for 2 hours under dry O_2 , and (C) 800 °C for 10 min under dry O_2

Table 3.2: Behavioral parameters for α -Fe₂O₃ films prepared at 800 °C

Condition	$j_{1.23V}$ (mA·cm ⁻²)	E_{PEC} (V vs.RHE)	E_{fb} (V vs.RHE)	E_g (eV)	log (N_d /cm ⁻³)
N ₂ +H ₂ O, 10 min	0.08	1.293	0.601	2.06	22.30
N ₂ , 10 min	0.04	1.390	0.310	2.07	22.18
O ₂ +H ₂ O, 10 min.	0.18	1.012	0.420	2.06	20.56
O ₂ , 10 min	0.02	1.004	0.390	2.07	20.32
N ₂ +H ₂ O, 2 h	0.16	1.215	0.392	2.05	21.69
N ₂ , 2 h	0.36	1.095	0.410	2.08	21.06
O ₂ +H ₂ O, 2 h	0.41	0.878	0.575	2.06	20.50
O ₂ , 2 h	0.48	1.029	0.591	2.05	20.48

3.2.4 Band Structure Measurements

The composition of the annealing atmosphere systematically affects the electronic band structure. Electrochemical impedance spectroscopy performed between 0.5 to 1.5 V_{RHE} on each hematite film provides both capacitance and resistance values (**Figure 3.7**). Mott–Schottky analysis using the capacitance values (**Figure 3.5C**) indicates that the flat band potentials (E_{fb}) for the α -Fe₂O₃ conduction band vary between 0.31 and 0.60 V_{RHE} (**Table 3.2**). Free charge carrier concentrations (N_d) calculated from the slope of the Mott–Schottky plots (**Table 3.2**). Peaks observed during rapid cathodic sweeps (performed in the dark) after holding photoelectrodes at catalytic potentials while under illumination have been shown to reveal the location of intraband states.^{101,102} Transient absorbance spectroscopy, EIS, and X-ray absorption studies provide support for such an assignment.^{21,64,67,102–104} Rapid sweep experiments on the thin films here yield cathodic peaks at voltages that correspond to photoelectrocatalytic onset (**Figure 3.5D, E** and **Figure A.1**). The weak intensity and width of these features make it difficult to systematically extract meaningful numeric values for comparison. Following the mentioned relationship between these states and the onset of photoelectrocatalysis, we use E_{PEC} as a proxy for the location of these intraband states as it can be clearly defined and systematically extracted. We note that while examining E_{PEC} behavior as a function of other material parameters grants insight into the intraband states, the term should not be viewed as a quantitatively accurate measure for the location of these states. UV-visible spectra

yield optical band gaps between 2.05 and 2.08 eV (**Figure 3.5F** and **Table 3.2**), with an average of 2.06 ± 0.02 eV across all eight samples.

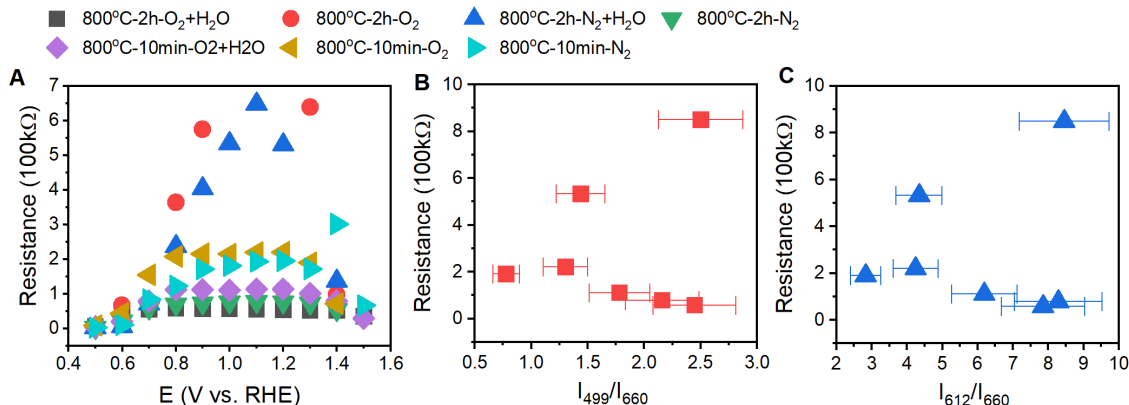


Figure 3.7: Bulk resistance obtained from fitting EIS data on the α -Fe₂O₃ sample series. (A) Resistance as a function of voltage. Resistance at 1.0 V_{RHE} as a function of Raman intensity ratios (B) I_{499}/I_{660} and (C) I_{612}/I_{660}

3.2.5 Correlating structure and behavior

Comparisons of the comprehensive Raman spectroscopy dataset with the extracted metrics show that the I_{499}/I_{660} and I_{612}/I_{660} ratios have special significance. A positive correlation exists between the catalytic metric $j_{1.23V}$ and both I_{499}/I_{660} and I_{612}/I_{660} (**Figure 3.8A**). Similar correlations are not observed for other peak intensities (**Table 3.1**). The lattice distortion that makes the E_u vibrational mode at 660 cm⁻¹ visible in a Raman spectrum must therefore uniquely affect the high energy A_{1g} and E_g vibrations; the magnitude of these distortions, in turn, inhibits photoelectrocatalytic performance. Comparison of I_{499}/I_{660} and I_{612}/I_{660} with other component peak parameters reveals exponential relationships with the full-width at half mass of 5 Raman active vibrations (**Figure A.2**), but no clear correlations with peak positions. The I_{499}/I_{660} ratio correlates positively to measured E_{fb} values for the α -Fe₂O₃ conduction band, with an anodic shift of *ca.* 145 mV per ratio unit, but negatively to the E_{PEC} values that serve as a proxy for the location of intra-band states (**Figure 3.8B**). The optical band-gap is essentially unchanged across the sample series (**Figure 3.8C**). No clear correlation is observed between N_d values and either $j_{1.23V}$, E_{fb} or I_{499}/I_{660} (**Figure 3.8D–F**). The E_{PEC} values, however, shift anodically with increased N_d .

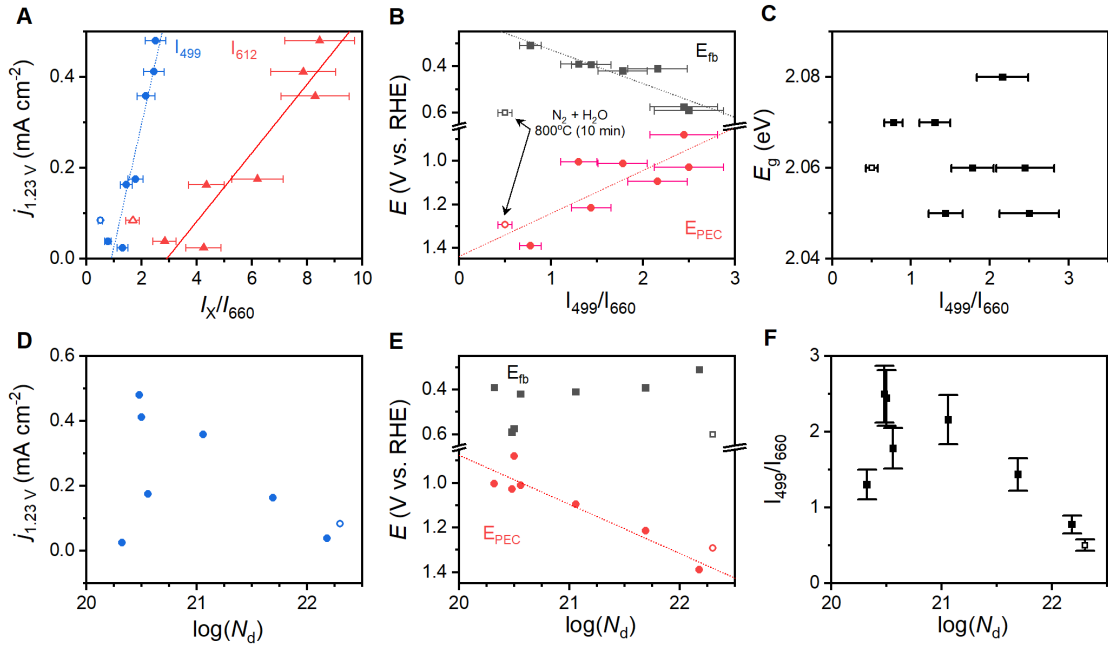


Figure 3.8: Correlations observed between Raman spectra and properties across the sample series. Correlations are shown for the relative intensity of key Raman vibrations and (A) photocurrent density, (B) the onset of photoelectrocatalysis and the flat-band potential, and (C) optical band gap. Correlations between charge carrier concentration, and (D) photocurrent density, (E) flat band potential and onset of photoelectrocatalysis, and (F) Raman intensity ratio.

X-ray photoelectron spectroscopy was performed on a subset of samples, with three selected to span the range of measured $j_{1.23V}$ values and one being the apparent outlier. The O 1s region shows components at *ca.* 531.7 and 530.0 eV that are attributable to OH^- and O^{2-} species, respectively (**Figure 3.9A**). Panels A and B show thick black lines for raw data, component peaks used to fit the data as shaded peaks and the sum of all component peaks as thin red lines. The introduction of oxygen vacancies into $\alpha\text{-Fe}_2\text{O}_3$ has been shown to increase the relative intensity of the high energy component by a factor of 3.⁵¹ The relative intensity of the high energy O 1s component here does not exhibit significant changes for the three samples that lie on structure–property trend lines in **Figure 3.8**; the relative intensity of the feature does decrease for the sample that was annealed for 10 min at 800 °C under humidified N_2 , which is an outlier in structure–property trends. The existence of a low energy shoulder on the Fe $2p_{3/2}$ peak has been previously used to support the presence of oxygen vacancies by observation of associated Fe^{2+} within $\alpha\text{-Fe}_2\text{O}_3$,⁵¹ but detailed XPS studies show that electronic structure of Fe^{3+} based materials

typically yield such features.¹⁰⁵ The energy spacing between the primary Fe 2p_{3/2} peak and the shake-up satellite peak provides a more reliable means to differentiate between Fe³⁺ and Fe²⁺, with spacing for the former being *ca.* 8 eV and the latter *ca.* 5.5 eV for iron oxides.¹⁰⁵ A consistent 7.8 eV spacing is observed here for the three samples that fall on the structure–property trend lines while the outlier exhibits a strong satellite peak located 5.2 eV above the Fe 2p_{3/2} peak (**Figure 3.9B**). High resolution spectra show that the valence band edge location shifts from *ca.* 1.331 eV for the sample heated in O₂ for 10 min to 1.471 eV for that heated in O₂ for 2 hours (**Figure 3.9C and D**; C 1s calibrated to 285.0 eV). Comparison of these values with respective I_{499}/I_{660} ratios suggests that the valence band shifts towards higher potential at a rate of *ca.* 116 meV per ratio unit. These results suggest that the annealing yields negligible changes in the average Fe oxidation state for samples that lie on the trend line, but a measurable amount of Fe²⁺ ions in the sample that is an outlier in all structure–property trends.

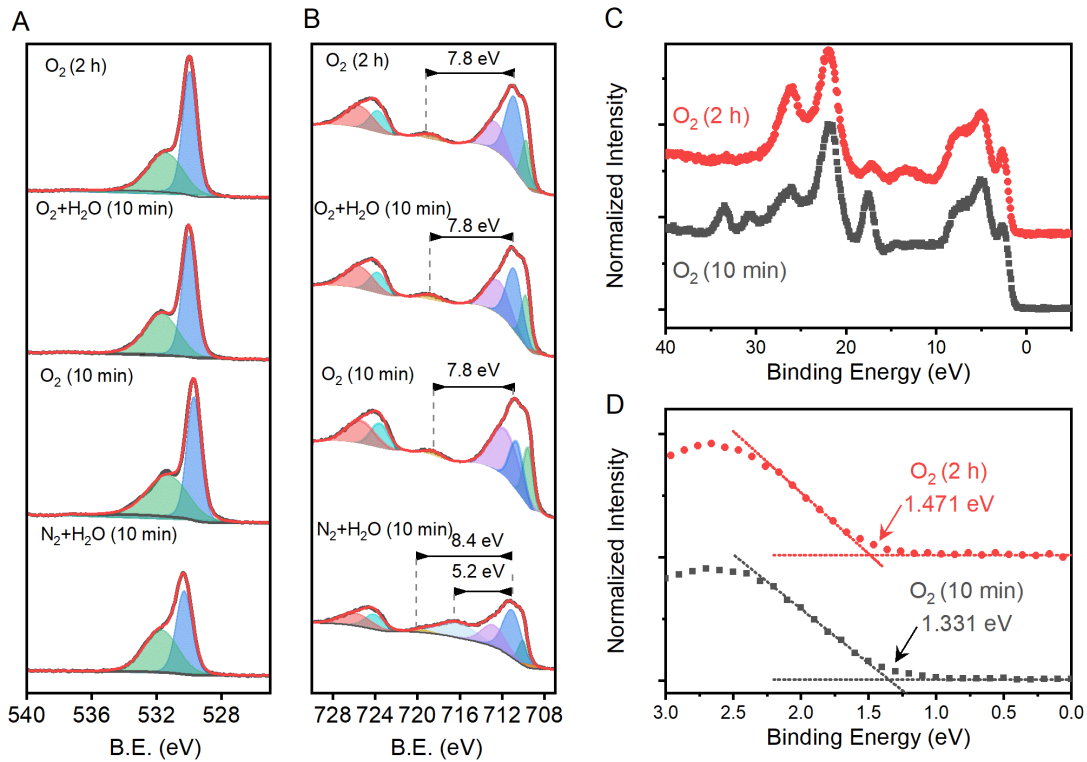


Figure 3.9: High resolution X-ray photoelectron spectroscopy results in the (A) O 1s and (B) Fe 2p and (C) valence band regions for selected samples annealed at 800 °C. (D) A magnification of the valence band edge region highlighting differences between samples annealed in O₂ for 2 h and 10 min.

3.3 Discussion

3.3.1 Control over structural integrity

A series of twelve α -Fe₂O₃ powders prepared by annealing γ -FeOOH under varied conditions confirm that the integrity of the crystal lattice is affected by the temperature, heating time and annealing atmosphere. Powder X-ray diffraction experiments reveal α -Fe₂O₃ in all samples, but samples annealed at 600 °C exhibit broad XRD peaks (**Figure 3.1**). All samples prepared at 800 °C yield well-defined diffraction patterns with no clear variations arising due to changes in annealing time or atmospheric composition. Raman spectra from all 12 samples contain the 7 Raman active vibrational modes expected for α -Fe₂O₃ plus two unexpected peaks: a peak at 710 cm⁻¹ attributed to an incomplete decomposition product (γ -Fe₂O₃) and a peak at 660 cm⁻¹. This latter feature has been previously assigned to an infrared active E_u vibrational mode for α -Fe₂O₃ that becomes observable in Raman spectra when structural distortions break lattice symmetry.^{94,96,106,107} FTIR measurements here support such an assignment (**Figure 3.3**). The exact nature of the distortion, however, remains unclear. Annealing conditions that are expected to improve the quality of the α -Fe₂O₃ lattice. For example, increased temperatures, longer reaction times and the absence of atmospheric H₂O all decrease the intensity of the 660 cm⁻¹ peak (**Figure 3.2**). The intensity of this distortion-induced vibration thus provides a numeric indicator of structural quality by describing the extent of an as-yet unidentified lattice distortion in α -Fe₂O₃. This peak grants the ability to extract insights into the nature of the lattice distortion and its effect on PEC performance through structure–property analyses.

An analogous series of twelve α -Fe₂O₃ films prepared from electrodeposited γ -FeOOH served as the samples for structure–property analysis. Spectra acquired on the film samples mirror those from powder samples, with the exception of the 710 cm⁻¹ peak being unobservable for film samples annealed at 800 °C. The otherwise similar trends and intensities between the powder and film samples suggest that inadvertent doping of α -Fe₂O₃, for example via leeching from the transparent conducting oxide

substrates,⁹² is not occurring here. Further evidence to support this claim comes from previous reports indicating concerted increases in $j_{1.23V}$ and the intensity of the 660 cm^{-1} Raman vibration as the concentration of silicon dopant in $\alpha\text{-Fe}_2\text{O}_3$ films is increased,⁵⁹ which is opposite to the trends observed here. This suggests that cation dopants should not be the reason behind structure-property correlations in this work. The I_{499}/I_{660} and I_{612}/I_{660} peak intensity ratios from spectroscopic maps of the film samples can confidently be taken as numeric indicators of structural quality for the film samples.

3.3.2 Influence on PEC

A linear correlation between Raman intensity ratios and $j_{1.23V}$ signifies that progressive distortion of the hematite lattice directly inhibits photoelectrocatalytic OER in the sample series (**Figure 3.8A**). The remaining correlations in **Figure 3.8** provide insight into the fundamental causes for this relationship. The measured E_{fb} for the conduction band shifts anodically from 0.31 to 0.59 V_{RHE} as I_{499}/I_{660} increases (**Figure 3.8B**), which spans the range of values commonly reported in the literature.^{7,88,89} This shift implies that the observed lattice distortion induces a shift cathodic shift in the Fermi level. As $\alpha\text{-Fe}_2\text{O}_3$ is an intrinsic n -type semiconductor, the direction and systematic nature of this shift could be the result of

- (i) an increased concentration of donor sites (i.e. an increase in film doping),
- (ii) a broadened energy distribution of donor states,
- (iii) a shift in the energy level of the donor sites and/or semiconductor band edges.

A filling or broadening of donor states may be expected to shift E_{fb} cathodically while simultaneously increasing N_d values. Increased N_d values resulting from the introduction of oxygen vacancies have been reported to increase current densities for $\alpha\text{-Fe}_2\text{O}_3$ photoanodes by providing catalytically active sites for OER, but shift E_{PEC} values anodically due to increased recombination rates.²⁷ A correlation is observed here between N_d values and E_{PEC} , but a failure to observe a clear relationships between N_d and $j_{1.23V}$ or E_{fb} (**Figure 3.8E**) suggests that a simple broadening or filling of donor sites is unlikely. A temperature-induced decrease in crystallinity has been demonstrated for zinc ferrite photoanodes, where higher temperatures in-

creased structural disorder that induced a 10-fold increase in bulk resistance and increased the rate of bulk recombination.¹⁰⁸ Electron transfer resistance values obtained from EIS results on the α -Fe₂O₃ films studied here show some variation in resistance across the sample series, and again show no discernible relationship to Raman intensity ratios (**Figure 3.7**) or $j_{1.23V}$ values. A convolution of multiple effects cannot be decisively ruled out, but the linear correlation between I_{499}/I_{660} and $j_{1.23}$ suggests that there is a single factor that dominates PEC behavior across this sample series. The lack of definitive trends between Nd and important material properties suggests that a broadening or filling of donor states is unlikely to be responsible for the behavior observed here.

Shifting of band edge locations and/or the location of intraband states would change the thermodynamics for electron transfer reactions and alter the kinetics of all processes, including photoelectrochemical OER and recombination. A constant optical band gap of *ca.* 2.06 eV across the sample series necessitates that any shift in the conduction band location be mirrored by a shift in the valence band location. Measured E_{fb} values shift at a rate of *ca.* 145 mV per unit of I_{499}/I_{660} (**Figure 3.8B**); XPS results suggest that an increased lattice distortion magnitude causes the valence band to shift anodically at a comparable 116 mV per unit. The rapid voltammetric sweep protocol employed here previously revealed peaks between 0.7 and 1.3 V_{RHE} in α -Fe₂O₃ photoanodes that were assigned to defect states that were either (i) catalytic intermediates for OER or (ii) catalytically inactive defects that pin the Fermi level until depletion by a sufficient voltage.^{24,64,67,103,104} Taking E_{PEC} as a proxy for the location of the intraband states, as has been previously argued,^{24,64,67,103,104} the defect states can be viewed as shifting cathodically from *ca.* 1.38 V_{RHE} in the most distorted and worst performing samples to 0.88 V_{RHE} in the best performing samples (**Figure 3.8B**). The location of these peaks allows us to rule out the possibility that the species observed here are reaction intermediates, or otherwise directly responsible for catalyzing OER, on thermodynamic grounds. We propose instead that the observed E_{PEC} values approximate the location of intraband defects that act as recombination sites. The correlations of I_{499}/I_{660} with both E_{fb} and E_{PEC} thus indicate a concurrent anodic shift in the defect states and cathodic shift in the semiconductor band edges. These opposing shifts would have two effects on catalysis:

1. Relaxation of photoexcited electrons would be facilitated by the movement of recombination sites towards the midpoint in energy of the two bands.
2. The cathodic shift in the valence band location would decrease the thermodynamic driving force to use photoexcited holes in the valence band to drive OER.

3.3.3 Nature of the defect

Oxygen vacancies within the lattice are unlikely to be responsible for the behavior observed here. Annealing under N₂ environments has been widely reported as a means to generate oxygen vacancies in α -Fe₂O₃ photoanodes, which increases the charge carrier density and improves photocatalytic performance.^{27,30,31,34,51} Here, we observe consistently improved performance for samples annealed under oxygen environments and no clear correlations between photocurrents and measured charge carrier densities (**Figure 3.8D**; **Table 3.2**). XPS measurements yield evidence for oxygen vacancies and the associated Fe²⁺ sites only for the sample that does not match all observed structure–property trends (**Figure 3.8**). The inversion of expected behavior here compared to the trends consistently reported in the literature, and XPS results, lead us to rule out oxygen vacancies as the structural defect of interest here.

Analysis of the nature of Raman vibrations leads us to propose that the performance altering distortion observed here is induced by the trapping of protons in the α -Fe₂O₃ lattice. Hematite adopts the corundum crystal structure, where Fe³⁺ ions reside in two-thirds of the octahedral sites in a lattice of hexagonally close-packed oxide ions. The crystalline *c*-axis is characterized by columns of alternating dimers of face-sharing Fe³⁺ octahedra and vacant octahedral sites, with edge-sharing motifs linking columns together (**Figure 3.10B**). The thermal transformation of goethite to α -Fe₂O₃ is known to progress through an intermediate phase termed “protohematite”,^{41,42} where incomplete dehydroxylation results in residual hydrogen content within the solid-state structure. Synchrotron-based XRD on protohematite revealed it to be an Fe-deficient form of α -Fe₂O₃ where Fe³⁺ vacancies are charge-

balanced by protonation of oxygen ions (i.e. substitution of oxide with hydroxide; $\alpha\text{-Fe}_{2-x/3}(\text{OH})_x\text{O}_{3-x}$).^{41,42} Protons within the lattice alter the two unique Fe–O distances in the structure, with those involved the face sharing motifs expanding from 2.11 to 2.15 Å as the concentration of protons increases, and those adjacent to octahedral vacancies contracting from 1.95 to 1.91 Å.⁴¹ In terms of Fe–Fe distances, protonation (1) contracts face-sharing motifs by 0.067 Å or 2.7%, (2) contracts edge-sharing motifs by 0.025 Å or 0.8%, and (3) expands the distance across octahedral vacancies by 0.037 Å or 0.6%. The A_{1g} , E_g and E_u vibrational modes whose intensities correlate to the physical properties and PEC performance measured here involve the simultaneous movement of Fe^{3+} ions linked by the face-sharing motifs (**Figure 3.10C**), while the remaining 5 Raman vibrations that do not correlate with the measured properties involve the simultaneous movements of Fe^{3+} linked through edge-sharing motifs, or the movement of oxide ions (**Figure A.2**). The observed distortion must therefore involve pronounced changes in the face-sharing motifs, but be largely insensitive to edge sharing motifs. This is consistent with the structural changes between $\alpha\text{-Fe}_2\text{O}_3$ and $\alpha\text{-Fe}_{2-x/3}(\text{OH})_x\text{O}_{3-x}$. The exponential relationship between our metric for structural distortion, I_{499}/I_{660} , and all vibrations involving movement of oxygen ions can be attributed to protonation of oxide ions, reinforcing this comparison. Confidence in the assignment is further bolstered by the need to decrease the O:Fe ratio on transitioning from $\gamma\text{-FeOOH}$ to $\gamma\text{-Fe}_2\text{O}_3$, the observation that humidified atmospheres produce higher I_{499}/I_{660} ratios, and previous reports of a Raman vibration at 665 cm^{-1} in protohematite.¹⁰⁹ We therefore conclude that the distortion of interest in the present sample series involves the trapping of protons within the crystal lattice, which induces iron deficiency and displaces face-sharing Fe^{3+} ions away from each other.

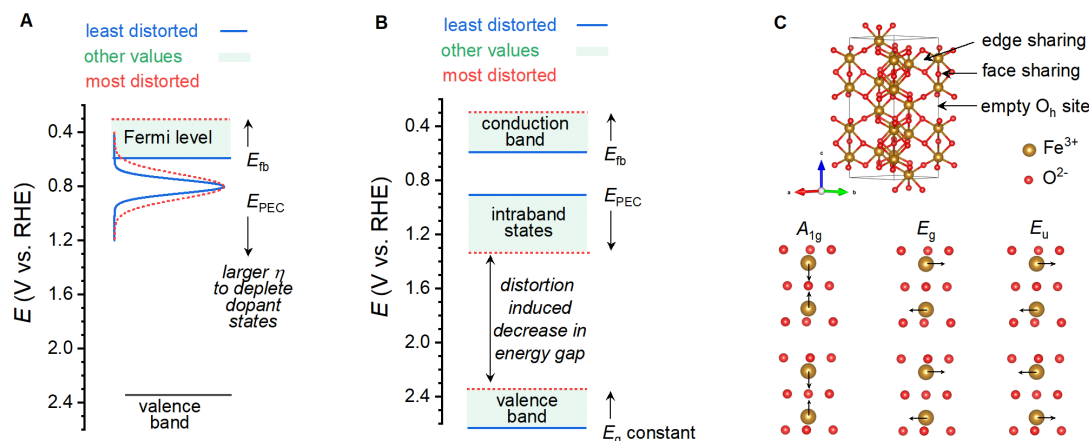


Figure 3.10: Possible changes in band structure induced by lattice distortion and the identity of critical vibrations for $\alpha\text{-Fe}_2\text{O}_3$. (A) The influence of an increase in the concentration of donor states and the broadening of donor states. (B) The influence of a cathodic shift in conduction and valence band edges and an anodic shift in intraband states. (C) Unit cell for $\alpha\text{-Fe}_2\text{O}_3$ denoting the connectivity and key structural features, and the identity of Raman vibrations that are found to correlate with photoanode properties.

The highly variable performance of $\alpha\text{-Fe}_2\text{O}_3$ photoanodes for PEC water oxidation is mirrored by significant dispersion in experimentally measured properties.^{110,111} Structural defects are often cited to explain the experimental variability as they are known to exert significant influence over band structure and photophysics. A lack of information regarding the specific chemical nature of these defects inhibits attempts to remove or avoid them. Here, we establish the trapping of protons within the crystal lattice as a structural defect of interest. This defect is challenging to detect by laboratory XRD but is known to induce iron vacancies within the lattice and to distort the bonding framework of $\alpha\text{-Fe}_2\text{O}_3$.^{41,109} We find that the presence of H_2O or the exclusion of O_2 from the atmosphere during $\alpha\text{-Fe}_2\text{O}_3$ film preparation has a significant impact on the extent of protonation in $\alpha\text{-Fe}_2\text{O}_3$. The measured flat band potentials, PEC onset potentials, and optical band gaps for the sample series analyzed here span the range commonly found in the literature; this distortion may therefore be a factor that contributes to the reported variability. We note that the trend reported here is opposite to that observed by Grätzel and co-workers for Si-doped $\alpha\text{-Fe}_2\text{O}_3$ photoanodes fabricated by atmospheric pressure chemical vapor deposition, where increased intensity of a 660 cm^{-1} Raman vibration correlated to increased silicon dopant concentrations and increased photocurrent densities.⁵⁹

The inversion of trends suggests that multiple defects may induce appearance of the E_u vibration in Raman spectra, necessitating further efforts to deconvolute the effects of relevant structural defects. Our finding that the I_{499}/I_{660} ratio tracks changes in properties for $\alpha\text{-Fe}_2\text{O}_3$ nonetheless identifies Raman spectroscopy as a convenient means to both diagnose a specific structural defect and parametrize it for structure–property analyses. We anticipate that this will greatly facilitate efforts to optimize fabrication protocols for defect-free $\alpha\text{-Fe}_2\text{O}_3$ photoanodes.

3.4 Conclusions

We fabricated a series of $\alpha\text{-Fe}_2\text{O}_3$ films by annealing $\gamma\text{-FeOOH}$ with varied protocols and analyzed the series through structure–property analysis. Raman spectroscopy was found to be particularly useful in acquiring information regarding bonding within the crystals and a spectroscopic mapping technique was established to obtain quality, reproducible spectra for each sample. A Raman inactive E_u vibrational mode observed at 660 cm^{-1} in all samples confirmed a varying degree of crystal lattice distortion across the sample series. The ratios of the A_{1g} (499 cm^{-1}) and E_g (612 cm^{-1}) vibrational modes to the E_u vibration were found to correlate to a number of important properties across the sample series, including the photocurrent density at $1.23\text{ V}_{\text{RHE}}$, the location of intraband trap states, band gap and flat band potential. Analysis of the nature of these three vibrational modes and the annealing conditions that lead to the smallest distortion and best PEC performance leads us to propose that the PEC-inhibiting distortion is the generation of Fe^{3+} vacancies induced by the trapping of protons within the crystal lattice. These defects inhibit PEC reactions by facilitating charge recombination. Our finding of these correlations and trends provides a rapid, simple way in which the community can employ Raman spectroscopy to rationally guide catalyst development or pre-screen the structural integrity of $\alpha\text{-Fe}_2\text{O}_3$ photoelectrocatalysts.

3.5 Experimental Details

3.5.1 Material fabrication

Lepidocrocite Film Deposition

Thin films of lepidocrocite (γ -FeOOH) were electrodeposited on fluorine-doped tin oxide coated glass (FTO) substrates using a literature procedure under neutral conditions.⁹⁸ Samples annealed at 600 °C and below, and those heated at 800 °C for 10 minutes, were deposited on TEC-7 grade FTO (Hartford Glass) while FTO using aluminum borosilicate glass (Solaronix S.A.) was used for samples annealed at 800 °C for 2 hours. All FTO substrates were cleaned by sequential ultrasonication in a detergent solution, milli-Q H₂O (18.2 M Ω), and then isopropanol. The substrates were dried under a stream of N₂ and placed in UV-irradiation chamber (GHO18T5VH lamp, Atlantic Ultraviolet) for 15 minutes. An electrodeposition solution containing 0.02 M ferrous ammonium sulfate hexahydrate (ACS reagent grade, Fisher Chemicals) and 3 M ammonium chloride (ACS reagent grade, EMD Chemicals Inc.) was deaerated with N₂ for 30 min and then adjusted to pH 7.5 by addition of 0.1 M KOH solution (>85%, Sigma-Aldrich). Application of a constant 0.0 V vs. Ag/AgCl (saturated) to FTO substrates submerged in this solution for 7 min at room temperature yielded γ -FeOOH films.

Lepidocrocite Powder Fabrication

Fabrication of γ -FeOOH in powder form was accomplished by oxidation of Fe(NH₄)₂(SO₄)₂·6H₂O in air.⁷⁴ A 200 mL aliquot of milli-Q H₂O in a round bottom flask was acidified by addition of a few drops of 1 M H₂SO₄(aq) (pH 2.4). The solution was purged with N₂ in an ice bath and a 10.0 g portion of Fe(NH₄)₂(SO₄)₂·6H₂O was then dissolved in the flask. Air was bubbled into the solution while continually adding 1 M KOH to maintain a solution pH of 6.5. After 90 minutes the pH of the yellow suspension stabilized at 6.94. The temperature was then increased to 45 °C and bubbled with

air. The orange precipitate was collected by vacuum filtration and thoroughly rinsed with milli-Q H₂O then dried in an oven at 105 °C.

Hematite Fabrication

series of α -Fe₂O₃ powders and films were prepared by heating the γ -FeOOH samples in a tube furnace. Two temperatures chosen, 600 and 800 °C, match those commonly utilized in the field.^{24,112–114} Four different gaseous atmospheres (N₂, O₂, N₂+H₂O, O₂+H₂O) were employed to probe the role of oxidizing atmosphere and H₂O on phase transitions. Humidification of gas streams was accomplished by bubbling the selected purge gas through H₂O at room temperature immediately before entering the tube furnace. Each of the 8 combinations of temperature and atmosphere was executed with a 2-hour heating period and an additional set of 4 samples was created by heating at 800 °C for 10 minutes. In total, 12 powder and 12 film samples of α -Fe₂O₃ were prepared. An additional set of samples prepared by heating γ -FeOOH at 350 °C for 2 hours to obtain Raman spectra for comparison and confirm α -Fe₂O₃ as an intermediate in the transition from γ -FeOOH to α -Fe₂O₃.

3.5.2 Raman Spectroscopy

Measurements were carried out on a Renishaw inVia Reflex system in which a microscope is equipped with an encoded sample stage. Measurements were performed using 532 (Renishaw DPSSL laser, 50 mW) and 633 nm (Renishaw HeNe laser, 17 mW) excitation. Data shown in the manuscript was acquired using 633 nm filtered to 5% of maximum intensity in conjunction with an 1800 lines/mm grating, unless otherwise stated. Raman spectra were analyzed using the Renishaw WiRE 5.2 software package. Data processing included baseline subtraction (sample shown in **Figure 3.11** below) and spectrum normalization.

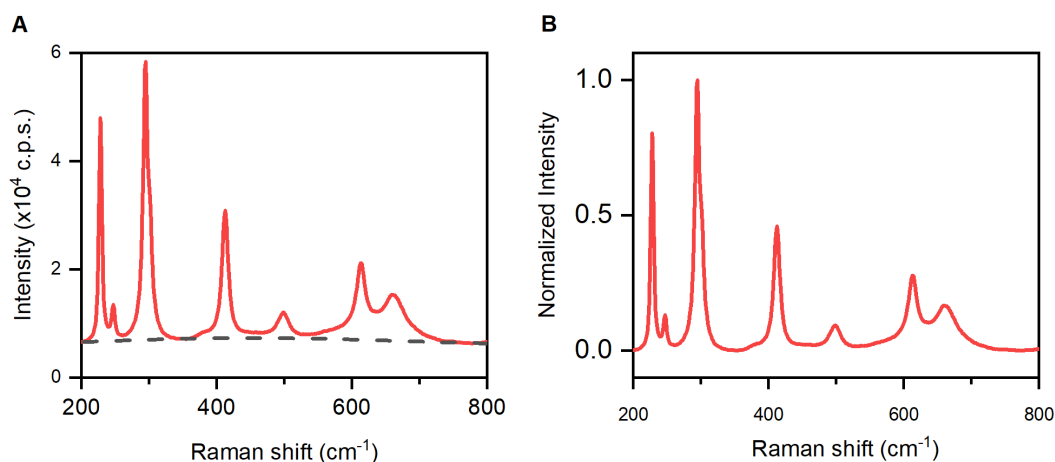


Figure 3.11: Sample of processing protocol used for Raman spectra showing the sampled annealed at 800 °C for 10 min. under humidified N₂ environment. (A) The raw spectrum and baseline to be subtracted. (B) Normalized form of the baseline subtracted data.

3.5.3 Infrared Spectroscopy

Fourier-transform infrared (FTIR) spectroscopic measurements were performed on a Nicolet 6700 FTIR equipped with a Pike Technologies VeeMAX III variable-angle reflection accessory and a DTGS detector with an infrared light source. Spectra were collected with an incident angle of 50°. Cleaned FTO and FTO/ABS were used as the baseline for films deposited on two different types of FTO glass substrates respectively. All spectra are shown in **Figure 3.3**

3.5.4 X-ray Diffraction

Powder X-ray diffraction experiments were carried out using Cu K α radiation on a PANalytical Empyrean diffractometer. Experiments scanned 2θ from 10° to 90° at a rate of 5° min⁻¹.

3.5.5 UV-vis Spectroscopy

Ultraviolet–visible absorption of the samples was recorded on a Perkin-Elmer Lambda 1050 UV-Vis Spectrophotometer equipped with an integrating sphere. Data was collected in a wavelength range of 200 nm to 1100 nm.

3.5.6 X-ray Photoelectron Spectroscopy

X-ray photoelectron spectroscopy measurements were performed on a Thermo-VG Scientific ESCALab 250 microprobe using an aluminum X-ray source. Survey scans were performed using a pass energy of 50 eV and high-resolution scans with 30 eV. The X-ray beam was performed at the current of 7.5 mA and the accelerating potential of 15 kV. All measurements were performed on films deposited on FTO glass with a small strip of conductive carbon tape to make electrical contact. Films were thoroughly rinsed with isopropanol and dried with N₂ gas before loading into the sample chamber. Quantitative analysis of high-resolution scans of Fe 2p_{3/2} and O 1s region was operated by CasaXPS 2.3.19. Spectra were calibrated by shifting the C 1s signal of adventitious hydrocarbons to 285.0 eV binding energy.

3.5.7 PEC analysis

Experiments were carried out using a Bio-logic SP 300 potentiostat and a Sciencetech A1 Lightline solar simulator equipped with an AM1.5G filter. Hematite-coated FTO working electrodes were mounted as windows in a polyethylene cell with the area of the electrode exposed to electrolyte solution masked to 1.54 cm² by a silicone O-ring. A Gaskatel HydroFlex Reversible Hydrogen Electrode (RHE) served as the reference electrode, a piece of clean FTO as the counter electrode, and 1 M KOH as the electrolyte. Photoelectrocatalytic tests utilized back-side illumination and current densities represent the geometric surface area.

Chapter 4

Differentiate Iron and Oxygen Vacancies

4.1 Introduction

Hematite natively accommodates several types of defects,¹⁹ including vacancies in iron^{55,115} or oxygen sites,^{34,54} interstitial iron ions,⁵² and even interstitial protons.^{96,116} Such defects are challenging to diagnose, and even more challenging to quantify. Techniques that facilitate the diagnosis and quantification of all possible defects would enable major advances in the field. Although evidence suggests that oxygen vacancies can be accompanied by iron vacancies,⁵⁶ iron vacancies have received less attention than oxygen vacancies due to the challenges of experimental characterization.

In **Chapter 3** we have utilized key vibration modes in Raman spectra and other characterization techniques to reveal potential structural defects in hematite photoanodes. We assigned the distortion to iron vacancies that are induced by the trapping of protons within the crystal lattice. However, the structural information from Raman spectroscopy is indirect and requires more direct structural information. X-ray absorption spectroscopy (**Section 2.3.4**) is uniquely capable of simultaneously providing information pertaining to both electronic and bonding structures, making it an ideal candidate for comparison with Raman spectra.

Herein, we combine X-ray absorption spectroscopy, Raman spectroscopy and photoelectrochemical measurements to demonstrate that fabrication conditions yield a transition in dominance between two unique defects in hematite electrodes. Structure-property analysis across a series of hematite photoanodes prepared by annealing lepidocrocite shows that N₂ annealing environments favor oxygen vacancies, while O₂ annealing environments favor iron vacancies. The absolute and relative gains in current density at 1.23 V are greater for samples annealed under O₂ than those under N₂, suggesting that removal of iron vacancies is critical to enhancing PEC performance. We propose that peaks observed in Raman spectra can serve to identify defects in hematite.

4.2 Results and Discussion

4.2.1 Sample Fabrication

A series of 12 photoanodes with varied structural integrities were synthesized by systematic tuning of the conditions under which lepidocrocite precursor films were converted to hematite. Precursor films were anodically electrodeposited on FTO-coated glass substrates using a previously published approach.¹¹⁷ These precursor films were heated at 800 °C using combinations of six different annealing times (0.2, 0.5, 1, 2, 4, and 8 h) and two different gaseous environments (O₂ and N₂). Annealing of these films at temperatures above 550 °C is known to induce a phase transition to hematite,^{118,119} but previous results indicate that the consistent synthesis of hematite that is free of phase contaminations requires higher temperatures.^{24,43,117} The synthesis of this photoanode series was strategically targeted to prepare the same nominal crystal structure with varied concentrations and possibly identities of structural defects. Each of these 12 photoanodes was comprehensively analyzed by XAS and Raman microscopy to obtain parameters describing their structure and by PEC experiments to obtain parameters describing their properties and behavior. The application of all techniques to each individual sample provides a robust sample-specific data set that enables structure–property correlations to circumvent

the sample-to-sample variability that is expected following wet-chemical syntheses such as that employed here. High temperatures are known to affect the crystallinity and conductivity of FTO.^{120,121} Uncompensated resistance values measured by EIS were between 10 and 30 Ω for most electrodes, but three increased to *ca.* 300 Ω and the sample annealed under N₂ for 8 h uniquely yielded a cloudy glass substrate and measured uncompensated resistance values of 76 k Ω (**Table 4.1**). The sample prepared under N₂ for 8 h was therefore not used in correlational analysis.

Table 4.1: Photoelectrochemical properties used in correlation analysis.

Condition	$j_{1.23V}$ (mA cm ⁻²)	$j_{1.5V}$ (mA cm ⁻²)	E_{PEC} (V vs RHE)	E_{fb} (V vs RHE)	N_d (10 ¹⁹ cm ⁻³)	R_u Ω
N ₂ -0.2h	0.06	0.15	1.11	0.30	52.7	367.87
N ₂ -0.5h	0.06	0.29	1.09	0.24	20.8	10.56
N ₂ -1h	0.20	0.68	1.15	0.37	92.9	13.83
N ₂ -2h	0.12	0.27	1.03	0.53	48.3	13.23
N ₂ -4h	0.17	0.62	1.18	0.30	24.1	19.19
N ₂ -8h	/	/	/	/	/	76000
O ₂ -0.2h	0.20	0.38	0.89	0.53	6.70	16.36
O ₂ -0.5h	0.16	0.26	0.85	0.44	7.01	22.46
O ₂ -1h	0.40	0.70	0.96	0.67	20.8	32.26
O ₂ -2h	0.19	0.39	0.87	0.65	10.2	22.29
O ₂ -4h	0.26	0.49	0.94	0.70	27.3	241.94
O ₂ -8h	0.10	0.19	0.83	0.54	7.87	295.36

4.2.2 X-ray Absorption Spectroscopy

X-ray absorption spectra confirm similarity in the overall structure for all but one of the hematite photoanodes, with subtle variations between the samples prepared under N₂ and O₂. The consistency of the structure across 11 members of the sample series is visible in comparisons of their XAFS spectra (**Figure 4.1A–C**). The consistency in these spectra enables an average to be calculated from them, with the sample heated under N₂ for 1 h left out. The XANES region for these averaged data exhibits the characteristic structure for hematite,^{122,123} with a minor pre-edge peak giving way to a strong white line with a distinct shoulder on the low energy side (**Figure 4.1D**). The associated EXAFS data contain strong oscillations that yield peaks rising above the noise level until *ca.* 8 Å in the Fourier transformed (FT) data (**Figure 4.1E**). The most prominent features in the FT data are three

peaks, which lie near 1.6, 2.7, and 3.3 Å. The identities of these peaks are discussed in detail below. The XANES region for the sample heated under N₂ for 1 h reveals a shift in the *K*-edge location to lower energy and a loss of the shoulder on the white line (**Figure 4.1D**). The EXAFS oscillations for this sample are clearly shifted relative to the other samples (**Figure 4.1E**); the FT data indicate substantial changes in bonding in the sample, with the shortest coordination shell shifting *ca.* 0.15 Å higher and the third shell shifting *ca.* 0.3 Å shorter. The sample annealed under N₂ for 1 h is clearly contaminated with a second iron oxide phase. It is included in all subsequent analysis but is distinctively marked to indicate this contamination.

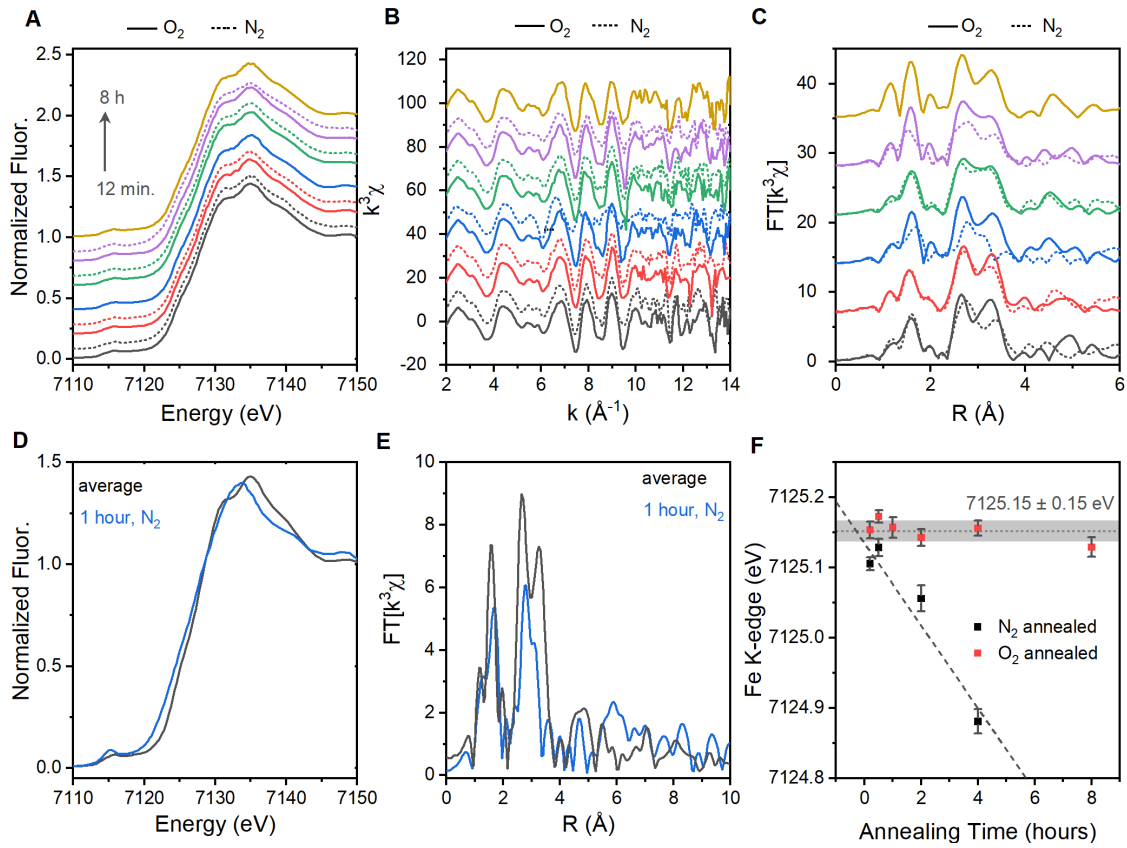


Figure 4.1: X-ray absorption fine-structure spectroscopy on hematite photoanode series. (A) Iron *K*-edge XANES, (B) EXAFS in *k*-space, and (C) FT-EXAFS spectra. Comparison of (D) XANES and (E) FT-EXAFS results for the 1 h N₂ sample. (F) Iron *K*-edge location as a function of annealing time for N₂ and O₂ environment.

The Fe *K*-edge locations for samples prepared under N₂ are at lower energies than the overall average, while those synthesized under O₂ lie above the average.

The K -edge locations (**Figure 4.1F**; **Table 4.2**) were determined by applying the half-height method to the fully processed, averaged spectrum for each sample.^{124,125} The precision of each measurement is represented by the standard deviation across six individual scans that were acquired per sample. These values lie below 0.04 eV for all samples (**Table 4.2**). The six individual spectra for each sample were acquired in two batches of three, with measurements of each batch separated by approximately 24 h. The low variability between these batches (**Figure 4.2**), and the low overall standard deviation values, attest to the temporal stability of the energy calibration of the incident X-ray beam. The K -edge location is known to be linearly correlated to the oxidation state of the ions, with a shift of 4.6 eV per change in the oxidation state expected for iron.^{83,84} The K -edge values for samples annealed under O₂ lie between 7125.13 and 7125.17 eV, making them indistinguishable within the uncertainty of individual measurements (**Figure 4.1F**). Samples annealed under N₂ differ, showing a K -edge shift from 7125.13 to 7124.88 eV between 12 min and 4 h annealing times (with the 1 h N₂ sample left out). This range corresponds to a 0.06 unit change in the average oxidation state of iron ions in the films, or one in *ca.* 15 ions changing oxidation state. The 1 h N₂ sample exhibits an edge position of 7124.39 eV, which would suggest a 0.17 unit change if 1 h N₂ considered.

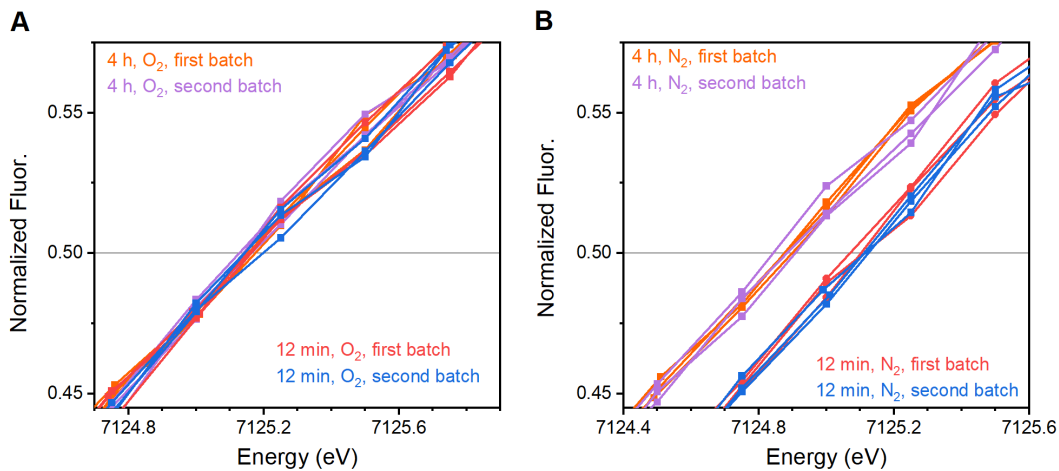


Figure 4.2: Comparison of the edge positions for individual XANES spectra to gauge the stability of energy calibration and precision of measurements. The six spectra acquired for four samples are shown for comparison. Each sample is broken into two batches: three collected in a first batch, then three collected approximately 24 hours later

Table 4.2: Raw parameters extracted from X-ray absorption fine structure spectroscopy.

Condition	Fe <i>K</i> -edge location	Fe <i>K</i> -edge error bar	Peak Height 1.6 Å	Peak Height 2.7 Å	Peak Height 3.3 Å
N ₂ -0.2h	7125.11	0.0091	6.86	8.81	6.03
N ₂ -0.5h	7125.13	0.0126	6.26	8.89	6.68
N ₂ -1h	7124.39	0.0203	5.36	6.06	4.22
N ₂ -2h	7125.06	0.0186	6.02	7.54	6.71
N ₂ -4h	7124.88	0.0176	5.34	6.49	4.74
O ₂ -0.2h	7125.15	0.0121	6.27	9.68	8.95
O ₂ -0.5h	7125.17	0.0089	6.21	9.65	8.54
O ₂ -1h	7125.16	0.0147	7.61	9.69	7.33
O ₂ -2h	7125.14	0.0121	6.47	8.19	7.11
O ₂ -4h	7125.16	0.0109	8.53	9.47	7.31
O ₂ -8h	7125.13	0.0136	8.15	9.12	6.92

4.2.3 Structural Model Development

A total of six coordination shells were selected for the development of structural models from EXAFS data, which exhibit major features between 1.5 and 3.8 Å (**Figure 4.1C**). The hematite crystal structure contains FeO₆ polyhedra arranged in a filled-filled-empty pattern along the crystal c-axis (**Figure 4.3**). Polyhedra are connected along this axis through face-sharing linkages, with each column linked to neighboring columns through edge-sharing and corner-sharing polyhedral motifs. This arrangement yields a single unique iron site with six coordination shells within 3.8 Å. Two unique Fe–O shells with coordination numbers of three exist, with 1.944 Å distances (labeled Fe–O₁) facing the empty interstitial sites and 2.116 Å distances (Fe–O₂) for the oxygen ions involved in face-sharing polyhedral motifs (**Figure 4.3**). The coordination shell for face-sharing polyhedral Fe³⁺ ions has a coordination number of one and a distance of 2.898 Å (Fe–Fe₁), and edge-sharing motifs have a coordination number of three and a distance of 2.969 Å (Fe–Fe₂). Two unique distances to corner-sharing iron ions in neighboring shells fall in this range, with a coordination number of three at 3.362 Å (Fe–Fe₃) and of six at 3.703 Å (Fe–Fe₄). All distances indicated above are from neutron diffraction data (ICSD 161283).⁴⁰

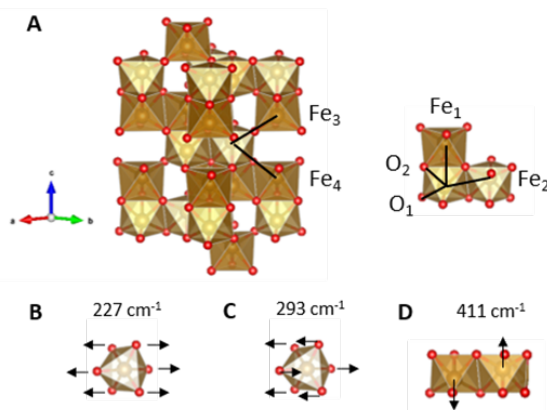


Figure 4.3: Structure of $\alpha\text{-Fe}_2\text{O}_3$ and key features for analysis. (A) Unit cell of hematite with EXAFS distances Fe–Fe₃ and Fe–Fe₄ marked. (B) Face-sharing and edge-sharing motifs in hematite with EXAFS distances Fe–O₁, Fe–O₂, Fe–Fe₁, and Fe–Fe₂ marked. Raman vibrations used in structure–structure analysis at *ca.*(C) 227, (D) 293, and (E) 411 cm⁻¹. Graphics prepared using VESTA.¹²⁶

Two different approaches were employed to develop models for quantitative analysis of the iron coordination environments using the six shells indicated above. To enable consideration of structural information that is not dependent on model development, the total intensity of each of the three observed peaks in the FT data was recorded for all samples (**Table 4.2**). The first simulation approach conservatively focused on fitting only $2\sigma_i^2$, the mean standard deviation values. This approach fixed all N_i at theoretical values and used fixed R_i values. Different R_i values were necessary for samples prepared under N₂ and O₂, with each set of values obtained by fitting an EXAFS spectrum of the average of all six samples in each respective data set. The $2\sigma_i^2$ values were then fitted to provide an effective measure of relative disorder in each of the six coordination shells (**Table B.1**). A second approach allowed both R_i and $2\sigma_i^2$ values to be fitted while maintaining theoretical N_i values. It was necessary to fix $2\sigma_{\text{Fe-Fe1}}^2$ during this approach due to overlap of features and a substantial defect-induced change in $R_{\text{Fe-Fe1}}$ noted in previous reports.⁴⁰ This second fitting process provides an insight into structural expansion or contraction, along with relative disorder in each of the shells (**Table B.2**).

4.2.4 Photoelectrochemical Properties

A series of three parameters describing PEC behavior were extracted to capture variations observed in the onset of photoelectrocatalytic oxygen evolution, the shape of the PEC curves, and the maximum current densities attained. The photocurrent density at 1.23 V vs RHE ($j_{1.23V}$) is a commonly reported performance parameter for OER on photoanodes that broadly captures photophysical and electrocatalytic properties (**Figure 4.4A**). The photocurrent density at 1.5 V vs RHE ($j_{1.5V}$) was selected to capture the plateau in photocurrent density for each sample. The onset potential of photoelectrocatalytic OER (E_{PEC}) is a third term that showed clear trends with structural variation in a previous analysis. This value was calculated using a second derivative approach that was previously discussed.⁴³ Values for each of these three parameters are compiled in **Table 4.1**.

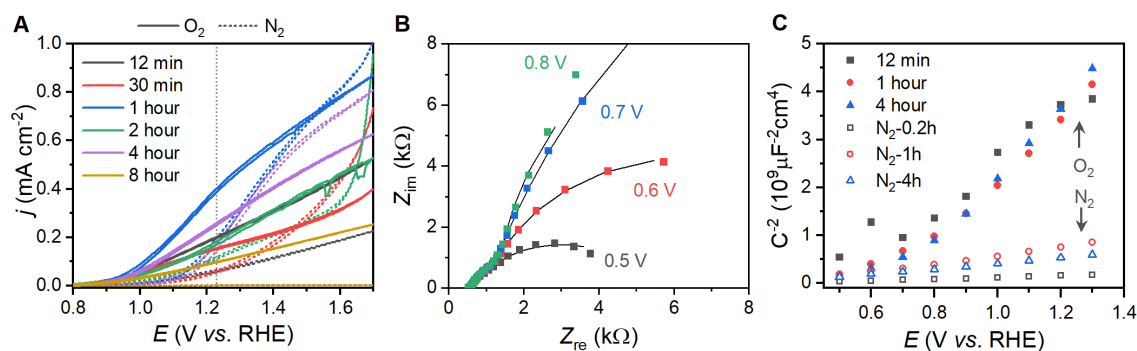


Figure 4.4: Photoelectrochemical behavior and electrochemical impedance spectroscopy results. (A) Voltammetric behavior under illumination for films annealed under different environments. (B) Nyquist plots of the film annealed in N₂ for 12 min at select voltages to show influence of voltage. (C) Mott–Schottky plots of films prepared by annealing in different conditions.

Band structure properties were measured using Mott–Schottky analysis. Potential-dependent EIS spectra acquired on samples in the dark contain a semicircle in Nyquist representations that changes its radius with applied potential (Figure 3B). Simulations of the data using solution resistance (R_s) in series with parallel charge transfer resistance (R_{ct}) and space-charge capacitance (C_{sc}) circuit components enable measurement of these metrics for all samples. Flat band potentials (E_{fb}) and charge carrier concentrations (N_d) for all samples were determined through Mott–Schottky analysis on the C_{cs} values (**Figure 4.4C**; **Table 4.1**).

4.2.5 Raman Spectroscopy

High quality Raman spectra were acquired for each of the photoanodes through a microscopic mapping protocol. The final spectra were acquired by averaging a total of 75 spectra per sample, with three sets of 25 spectra acquired in evenly spaced grids at three different $4 \times 4 \mu\text{m}$ areas on the electrode surface. All 75 spectra are plotted for the sample annealed under O_2 for 4 h to show the consistency of the spectra (**Figure 4.5A**). This approach was shown to yield consistent results that are representative of the overall film, where individual spectra showed a Gaussian distribution of peak intensity ratios with $> 85\%$ of the spectra lying within 15% of the Gaussian maximum.⁴³ The data acquired here were at least as precise: the I_{293}/I_{411} ratio similarly captured $>85\%$ of spectra within 15% of the maxima, but the I_{411}/I_{612} yielded much sharper distribution with $>85\%$ of spectra within 3% of the maximum (**Figure 4.5B**). The averaged spectra all contain the seven characteristic Raman vibrations of hematite (**Figure 4.5C**), with four oxygen-based vibrations at 227, 246, 293, and 300 cm^{-1} and three iron-based vibrations at 411, 496, and 612 cm^{-1} . In addition, a symmetry-forbidden E_u vibration appears at 660 cm^{-1} . The distortion-driven lowering of symmetry responsible for this feature has been discussed in the literature,⁹⁴⁻⁹⁶ and the intensity of the Raman peak was critical in previous identification of defects in hematite.⁴³ This previous analysis showed that annealing lepidocrocite films at $800 \text{ }^\circ\text{C}$ led to a decrease in intensity of the E_u vibration. Leaching of Sn(IV) from the FTO substrate was ruled out by this decrease in intensity, based on previous reports of extrinsic quadrivalent dopants increasing this E_u vibration by an order of magnitude.⁵⁹ In agreement with the XAS analysis, the sample annealed under N_2 for 1 h shows unique differences that suggest phase impurity. The peaks at 246, 300, 411, and 612 cm^{-1} are substantially decreased in intensity or are completely missing. This sample provides a useful demonstration of the effect of phase impurities, but is excluded from correlational analysis. The location, width, and intensity of peaks are influenced by the structural integrity of the hematite photoanodes. Curve fitting of the spectra was performed to determine these three parameters (**Table B.3**, **Table B.5**, **Table B.4**).

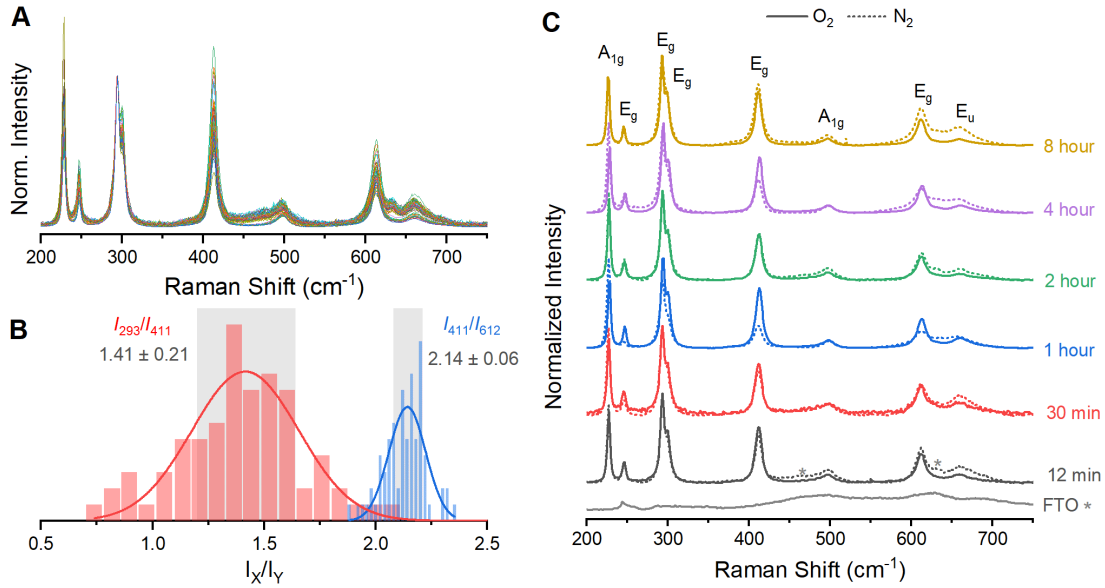


Figure 4.5: Raman spectra for hematite sample series. (A) All 75 spectra acquired over three $4 \times 4 \mu\text{m}$ grids on the $\alpha\text{-Fe}_2\text{O}_3$ sample annealed under O_2 for 4 h and (B) histogram showing the distribution of selected peak ratios. The solid line shows a Gaussian distribution fit of each histogram. Vertical shading denoting 85% of all spectra, captured by the ranges noted. (C) Spectra acquired by averaging all 75 individual spectra for each sample. Solid lines represent samples annealed under O_2 and dashed lines under N_2 .

4.2.6 Correlational Analysis

Systematic comparisons of the structural and the behavioral parameters identify relationships in the photoanode series. Samples were clustered into groups of photoanodes that were synthesized under O_2 and N_2 . Each parameter in the data set was then iteratively compared to all others in the data set. The PEC behavior parameters (N_d , E_{fb} , $j_{1.23V}$, $j_{1.5V}$, and E_{PEC}), the XAFS parameters (Fe K -edge location FT peak intensities, $2\sigma_1^2$, and R_i), and the widths and locations of Raman peaks were used as is. The intensities of Raman vibrations are dependent on experimental parameters such that absolute intensities can be misleading; these values were therefore taken as the peak intensity ratio for all possible combinations of two peaks. Linear regression analysis was performed for each comparison, and the resultant R^2 values were tabulated. Analysis of the results revealed correlations between structure and behavior (structure–property correlations) and between various structural parameters (structure–structure correlations). The relationship across the two

data clusters, discussed below, leads us to conclude that oxygen vacancies are the dominant form of defect when the synthesis is performed under N₂, while iron vacancies become dominant under O₂.

4.2.7 Structure–Property Correlations

Distinct relationships are observed between the iron *K*-edge location and $j_{1.23V}$ for sample clusters prepared under N₂ and O₂. The $j_{1.23V}$ value for the O₂ cluster increases from 0.09 to 0.40 mA cm⁻², while the *K*-edge location remains within the ca. 0.04 eV standard deviation values for individual edge measurements (**Figure 4.6A**). The N₂ cluster is markedly different, with *K*-edge values decreasing by 0.29 eV, while $j_{1.23V}$ increases from 0.06 to 0.17 mA cm⁻² (**Figure 4.6A**). The $j_{1.23V}$ values show signs of reaching a limiting plateau, a feature that is likely related to a tendency for hematite to transition to magnetite as Fe²⁺ accumulates.^{27,67,127} The *K*-edge location of transition metal oxides is known to exhibit a linear correlation with the element’s average oxidation state for small changes, with calibration curves from crystalline iron oxide standards estimating a shift of 4.6 eV per oxidation state for iron.^{83,84} The 0.31 mA cm⁻² increase observed in performance across the O₂ cluster thus occurs without a measurable change in the iron oxidation state, while the average oxidation state of iron decreases by ca. 0.06 units for the 0.11 mA cm⁻² increase in $j_{1.23V}$ for the N₂ cluster.

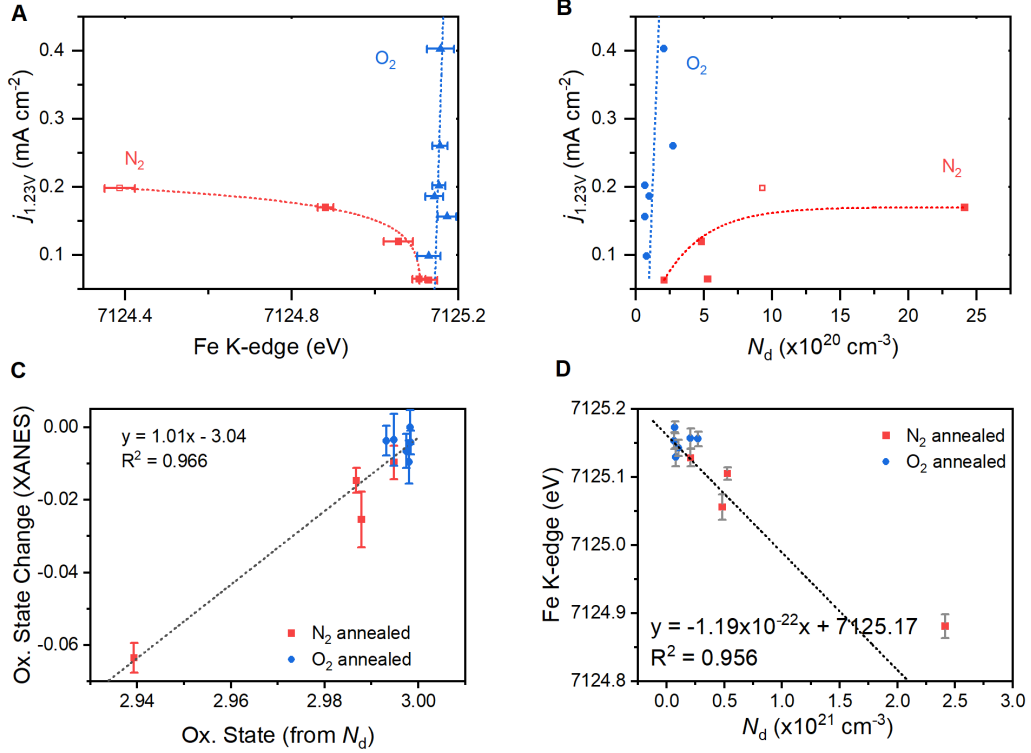


Figure 4.6: Correlations observed between XANES data and PEC properties across the sample series. (A) Correlation between the Fe *K*-edge location and $j_{1.23V}$ and (B) between charge carrier density N_d and $j_{1.23V}$ across the entire series. (C) Comparison of change in oxidation states calculated by XANES with the oxidation state calculated from N_d . Error bars represent the standard deviation across six individual spectra for each sample.

The measured charge carrier densities exhibit a linear correlation to iron *K*-edge locations (**Figure 4.6**), providing a secondary measure that supports the trends seen in the XANES data. Electrons are the majority charge carrier in hematite, generated by native defects reducing the average iron oxidation state.³⁰ The O₂ cluster of samples exhibits a negligible change in N_d as $j_{1.23V}$ increases (**Figure 4.7B**). The N₂ cluster instead shows a 12-fold increase in N_d from 2.08×10^{20} to 2.41×10^{21} cm⁻³ as $j_{1.23V}$ increases. The paired observations of increasing charge carrier density and a negative shift in the XANES *K*-edge location confirm that Fe²⁺ is associated with performance metrics across the N₂-annealed series, consistent with the formation of oxygen vacancies.^{27,128} The absence of such changes in the O₂-annealed series provides evidence that a defect that is not associated with Fe²⁺ within the lattice controls photoelectrocatalytic performance. Crystallographic analysis of hematite shows a unit cell volume of 302 \AA^3 ,^{95,122} yielding an iron ion concentration of 3.97

$\times 1022 \text{ cm}^{-3}$. Assuming that charge carriers represent one electron per iron center (i.e., one Fe^{3+} converts to one Fe^{2+}), the ratio of Nd to total iron ion concentration yields the proportion of Fe^{2+} in each sample. Subtracting this ratio from 3 thus yields an estimate of the average oxidation state for iron ions. The relative oxidation state change across the series can be obtained from the XANES data by dividing the edge shift relative to a reference point, selected here to be the highest energy K -edge measured, by the expected shift of 4.6 eV per oxidation state.^{83,84} The average oxidation state calculated through these two techniques show excellent linear correlation (**Figure 4.6C**), with a slope of unity and an intercept on the XANES-derived axis of 3.04, both of which are exactly what is predicted. The sample annealed under O_2 thus yield a stable average oxidation state for iron ions near 3, while the samples annealed under N_2 experience a decrease in the oxidation state by up to 0.06 units.

Trends involving EXAFS structural parameters show that the unique changes in $j_{1.23\text{V}}$ for the two sample clusters are associated with distinct distortions of the average structure. The O_2 cluster of samples is primarily characterized by an increase in $j_{1.23\text{V}}$ as the distance across face-sharing iron ions ($R_{\text{Fe-Fe1}}$) increases from 2.854 to 2.900 Å (**Figure 4.7A**); the Fe–O shells remain essentially constant (**Table B.2**). The N_2 cluster of samples instead show a *ca.* 0.060 Å contraction in $R_{\text{Fe-O}_2}$ with increasing $j_{1.23\text{V}}$ (**Figure 4.7A**). An overall increase in structural disorder of the N_2 cluster of samples is captured by a decrease in intensity of FT peaks with increasing $j_{1.23\text{V}}$ (**Table 4.1** and **Table 4.2**). The increase in disorder is captured in structural models as an increase in $2\sigma^2$ for all shells as $j_{1.23\text{V}}$ increases (**Table B.1**). The structural distortion within the O_2 cluster of samples is therefore limited to iron–iron linkages, while the N_2 cluster experiences an overall contraction of Fe–O distances that disrupts all Fe–Fe distances in a seemingly nonsystematic fashion.

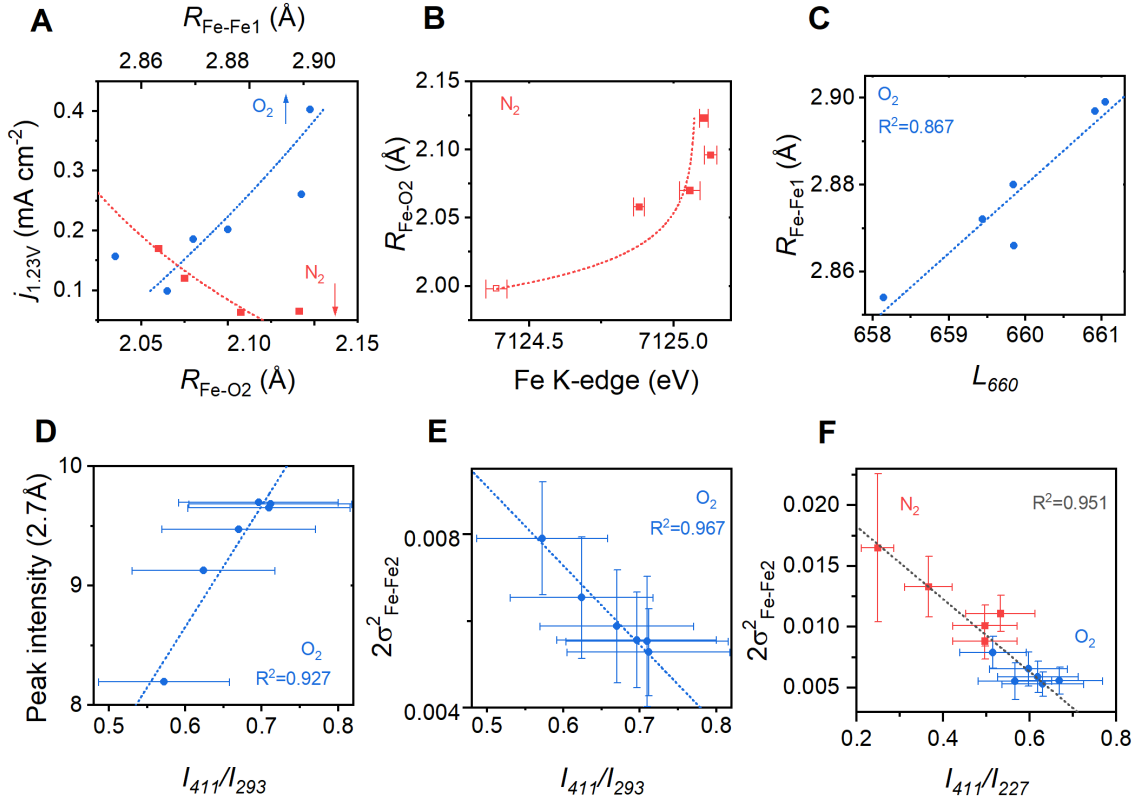


Figure 4.7: Correlations involving XAS-derived parameters for hematite films annealed in N_2 and O_2 . (A) Trends in photocurrent density $j_{1.23V}$ and R_{Fe-Fe1} distances for samples annealed under O_2 , and R_{Fe-O2} distances for those annealed under N_2 . (B) Iron-oxygen bond length increases with Fe K -edge values for samples annealed in N_2 . (C) Location of the E_u vibration as a function of R_{Fe-Fe1} , and (D) Intensity of the FT-EXAFS peak near 2.7 Å against the Raman intensity ratio I_{411}/I_{293} for hematite annealed in O_2 . Correlation between mean standard relative deviation ($2\sigma_{Fe-Fe2}^2$) with Raman intensity ratios of (E) I_{411}/I_{293} for O_2 samples and (F) I_{411}/I_{227} for hematite annealed in N_2 and O_2 environments.

The structural and behavioral parameters obtained for photoanodes prepared by annealing lepidocrocite films under N_2 provide clear evidence for oxygen vacancies being the dominant structural defect. Oxide vacancies are native defects in hematite that are accompanied by reduction of Fe^{3+} to Fe^{2+} within the lattice.⁶⁷ Thermal treatment of hematite under oxygen deficient environments has been reported to improve photoelectrocatalytic performance by increasing N_d by altering the equilibria involving oxygen vacancy formation.³¹ The observed correlations here are well aligned with these reports: the photoelectrocatalytic parameter $j_{1.23V}$ in-

increases as the average oxidation state of iron decreases (**Figure 4.6A**) and as N_d increases (**Figure 4.6B**). Structure–property correlations suggest that $R_{\text{Fe-O}2}$ decreases as $j_{1.23V}$ increases, implying that oxide vacancies decrease Fe-O bond lengths (**Figure 4.7A**). Direct comparisons of oxide vacancy concentration and Fe-O bond lengths for hematite could not be found in the literature. The oxide vacancy-induced decrease in the radius of iron ions observed is nonetheless consistent with established trends in ionic radii, where ionic radius decreases as coordination numbers decrease.¹²⁹ Further, a correlation between the location of the iron K -edge and the Fe–O bond distances measured by EXAFS (**Figure 4.7B**) provides direct experimental support. Oxide vacancies are therefore the dominant defect present in hematite films prepared by thermal conversion of lepidocrocite under N_2 environments. These vacancies boost photoelectrocatalytic performance by increasing N_d , as previously reported.

The observed structural features and their correlations for photoanodes prepared by annealing lepidocrocite under O_2 are consistent with protohematite, $\alpha\text{-Fe}_{2-x/3}\text{O}_{3-x}(\text{OH})_x$,^{41,42} being the dominant structural defect. This structure involves the trapping of positively charged protons within the crystal lattice, which is charge balanced by the formation of Fe^{3+} vacancies. This defect explains the stability of both measured N_d values and XANES K -edge locations across the O_2 -annealed series. Previous variable-temperature synchrotron XRD analysis showed that the trapping of protons and associated iron vacancies in protohematite induces overall compression relative to the hematite unit cell, distorting bonding (**Table 4.3**).^{41,42} The largest magnitude change in bonding in that XRD analysis was a compression of face-sharing motifs ($R_{\text{Fe-Fe}1}$), with smaller expansion of corner-sharing motifs ($R_{\text{Fe-Fe}3}$). The Fe-O shells, in contrast, showed very little change. Structure–property analysis here shows that $j_{1.23V}$ values decrease with compression of $R_{\text{Fe-Fe}1}$ (**Figure 4.7A**), while $R_{\text{Fe-O}1}$ and $R_{\text{Fe-O}2}$ remain static (**Table B.2**). The 660 cm^{-1} Raman peak is known to be an E_u lattice vibration that is formally symmetry forbidden but emerges following lattice distortions;^{96,124} it has been proposed that protohematite induces such distortions.⁴³ The relationship between the E_u vibration, which is a shearing motion of Fe ions across face-sharing motifs, is further strengthened here by observation of a 3 cm^{-1} red shift as $R_{\text{Fe-Fe}1}$ is compressed (**Figure 4.7C**). The results here are therefore consis-

tent with the presence of varied concentrations of interstitial protons and associated iron vacancies being the dominant structural defect for the O₂ cluster. These defects induce structural distortions, readily seen in **Table 4.3** and **Figure 4.7**, that will alter bonding interactions within the material to affect semiconductor properties. Improvements to photoelectrocatalytic OER across the O₂ series are attributed to the removal of these lattice distortions, which yield performance gains that surpass those obtained for annealing under a N₂ environment.

Table 4.3: Structural Parameters of Hematite and Protohematite.

	proto ₃₁₃ ^a	proto ₅₁₇ ^a	proto ₇₇₉ ^a	hematite ^b
$R_{\text{Fe-O1}}$	1.925	1.908	1.929	1.944
$R_{\text{Fe-O2}}$	2.122	2.158	2.137	2.116
$R_{\text{Fe-Fe1}}$	2.823	2.843	2.882	2.898
$R_{\text{Fe-Fe2}}$	2.945	2.955	2.971	2.969
$R_{\text{Fe-Fe3}}$	3.378	3.376	3.367	3.362
$R_{\text{Fe-Fe4}}$	3.686	3.688	3.702	3.703

^a: Values from ref.⁴¹

^b: Values from neutron diffraction experiments in ref.⁴⁰

Additional correlations observed between features in the Raman spectra and structural parameters derived from EXAFS models may provide value in guiding synthetic efforts. Underlying the decrease in magnitude of Fe–Fe peaks in the EXAFS results (**Figure 4.7D**) is an increase in disorder in the Fe crystallographic sites. This disorder is captured by the mean standard relative displacement factor ($2\sigma^2$) in EXAFS models. The Fe–Fe₂ coordination shell yields the strongest peak in the FT-EXAFS data (**Figure 4.1**), making it the most reliable to analyze. The above-mentioned discussion on the defect-induced compression of the crystalline *c*-axis suggests that the 411 cm⁻¹ should be important because it is the only Raman active vibration that involves movement of cations along the crystalline *c*-axis.^{130,131} The $2\sigma_{\text{Fe-Fe2}}^2$ values do indeed yield strong negative correlations to the intensity of the 411 cm⁻¹ peak relative to those at 293 (**Figure 4.7E**) and 227 cm⁻¹ (**Figure 4.7F**), which involve synchronous movement of oxygen ions in the O₁ and O₂ sites. The observation of different structure–structure and structure–property correlations for

the two clusters of samples provides evidence that each defect type has a unique influence on individual Raman vibrations, indicating that successful observation of correlations was reliant upon the ability to synthesize two series of samples where changes in the concentration of a single defect dominated the observed changes in behavior. Variable-temperature Raman spectroscopic analysis of phase transitions that occur when synthesizing hematite by annealing lepidocrocite suggests that protohematite forms between ca. 200 and 400 °C.¹³² The performance gains attained by removal of protohematite marks an understanding of their formation in, and elimination from, photoanodes as an important target for the community. This approach may enable deconvolution, and potentially the quantification, of all defects within a photoelectrode sample using only Raman spectroscopy. A substantial amount of work is clearly necessary to realize this capability, but systematic correlation of Raman spectra to structural information will yield a powerful tool for optimization of fabrication protocols and quality control.

4.3 Conclusions

Parameters describing the structure and PEC properties of a series of hematite photoanodes were compared to each other to identify the prevalence of individual defects as a function of synthetic conditions. A series of 12 samples were synthesized by annealing lepidocrocite for varied times under either N₂ or O₂ environments. The interatomic distances and extent of disorder for short-range coordination shells was measured for each using X-ray absorption fine-structure spectroscopy, and the integrity of longer-range order was measured through Raman microscopy. Correlations between these structural descriptors with performance descriptors for photoelectrocatalytic OER leads us to conclude that the behavior of samples synthesized under N₂ is dictated by oxygen vacancies, while that for samples synthesized under O₂ is dictated by iron vacancies. Performance gains were achieved by either the removal of iron vacancies (O₂) or the introduction of oxygen vacancies (N₂). Comparison of the X-ray absorption results with Raman spectra reveals correlations that suggest it may be possible to calibrate the width, energy, and intensity of peaks in Raman

spectra to enable direct analysis of defects in hematite photoanodes.

4.4 Experimental Details

4.4.1 Hematite Fabrication

Lepidocrocite (γ -FeOOH) thin films were electrodeposited on fluorine-doped tin oxide-coated aluminum borosilicate glass (FTO/ABS; Solaronix S.A.). FTO/ABS glass substrate pieces were cleaned by sequential ultrasonication in a detergent solution, milli-Q H₂O, and then isopropanol. The surface was dried under a stream of N₂ and placed in a custom UV-irradiation chamber (GHO18T5VH lamp, Atlantic Ultraviolet) for 15 min. A solution containing 0.02 M ferrous chloride tetrahydrate (ACS reagent grade, Alfa Aesar) and 1 M ammonium chloride (ACS reagent grade, EMD Chemicals Inc.) was purged with N₂ for 30 min before electrodeposition. A 0.1 M KOH (>85%, Sigma-Aldrich) solution was added to adjust solution pH to 7.0. Freshly cleaned FTO/ABS electrodes were held at 0.0 V vs Ag/AgCl (sat'd KCl) for 7 min at room temperature with continuous N₂ purging. A series of 12 such electrodeposited γ -FeOOH films were converted to hematite by heating at 800 °C under varied conditions. These 12 conditions consisted of combinations of either N₂ or O₂ atmosphere with selected reaction times (0.2, 0.5, 1, 2, 4, and 8 h). Each photoanode was then cut into two pieces and rinsed with isopropanol. Each of the two halves was analyzed by Raman microscopy to ensure consistency (see below). One half of each sample was then used for PEC measurement. The second half was used for analysis by XAS.

4.4.2 Raman Microscopy

Raman microscopic measurements were performed using a Renishaw inVia Reflex system. Raman microscopic mapping of each hematite film was performed using 1 μ m steps across three different 4 \times 4 μ m grids. This approach was previously shown to offer consistent, representative spectra of each photoanode.⁴³ Spectra were

acquired using a 100 \times objective, 633 nm excitation (Renishaw HeNe laser, 17 mW) filtered to 5% of maximum intensity, and an 1800 lines/mm diffraction grating. The Renishaw WiRE 5.3 software package was used for spectrum processing, which included baseline subtraction, normalization, and curve fitting.

4.4.3 PEC Measurements

Photoanode properties and performance were measured using a Biologic SP-300 potentiostat and a Sciencetech A1 Lightline solar simulator equipped with an AM 1.5G filter. Hematite-coated FTO working electrodes were mounted as windows in a custom-made polyethylene cell. The cell contains a 1.54 cm² circular hole surrounded by a silicone O-ring. The hematite-coated FTO electrodes were clamped against the O-ring such that the cell could be operated using back-side illumination. Aqueous 1 M KOH electrolyte solutions were prepared using milli-Q H₂O and KOH (>85%, Sigma-Aldrich). A Gaskatel HydroFlex reversible hydrogen electrode (Gaskatel GmbH, Kassel, Germany) served as the reference electrode and a freshly cleaned piece of FTO as the counter electrode. The PEC properties were measured by cyclic voltammetric sweeps, both in the dark and under illumination, from 0.4 to 1.7 V vs RHE at 20 mV s⁻¹. Electrochemical impedance spectroscopy was performed in the dark at 100 mV intervals between 0.5 and 1.3 V vs RHE using a 10 mV amplitude.

4.4.4 X-ray Absorption Fine-Structure Spectroscopy

XAS was performed at beamline 6-BM (BMM) at the National Synchrotron Light Source II (Brookhaven National Laboratory, NY, USA) using a Si(111) monochromator. The incident energy calibration was performed by beamline staff prior to the experiments. This was accomplished by determining the monochromator's angular position for the *K*-edge location of 10 transition metal elements. These values were then fitted to the Bragg equation using standardized values to obtain an angular offset and lattice constant for the monochromator. The Fe *K*-edge spectra were

recorded between 6910 and 7960 eV in fluorescence mode for all 12 hematite samples. Data were acquired at intervals of 10 eV from 6910 to 7080 eV, 2 to 7100 eV, and then 0.25 to 7135 eV. After this point, the data were acquired with a regular spacing of 0.05 \AA^{-1} in k -space. The detector was positioned 90 degrees relative to the incident beam. The samples were mounted on a motorized polycarbonate sample wheel. The wheel was positioned 45 degrees relative to the incident beam and rotated to change samples. Six spectra were acquired per sample using a four-element Si-drift detector. Real-time energy calibration was not possible due to the X-ray absorption of FTO glass substrates. The experimental protocol was therefore designed to enable estimation of the temporal stability of the energy calibration and enable comparison of relative changes in X-ray absorption near edge structure data. The six spectra for each sample were split into two batches of three spectra, with measurements of each batch separated by approximately 24 h. Comparison of the two batches of measurements show standard deviations of less than 0.04 eV in K -edge locations over the beamtime. X-ray adsorption spectra were prepared for analysis by averaging all relevant spectra, subtraction of a linear baseline determined from the pre-edge region, and subsequent normalization of the post-edge region. The K -edge locations were defined as the point where the normalized data reached 0.5 units, using linear interpolation where necessary. The scattering amplitude, phase correction, and mean free path for photoelectrons were calculated by ab initio calculations on a model crystalline hematite cluster using FEFF 8.4.¹³³ Structure models were then developed using the extended X-ray absorption fine-structure (EXAFS) equation with coordination number (N_i), bond length (R_i), and the mean standard deviation ($2\sigma_i^2$) for each relevant iron coordination shell. Errors in fitted parameters were estimated as previously described, using a useful R -space range of 1.5–4 \AA .¹³⁴

Chapter 5

Identify Coexistent Defects

5.1 Introduction

Structure-property analysis provides a means to use correlations between specific structural features and behavioral parameters to study individual components of a system as stated (**Section 1.4**). Relationships between chemical structure and properties can be explored through multi-variate analyses; analysis of individual peaks in Raman spectra has proven useful in analyzing the density and crystallinity of polymer systems,¹³⁵ the crystallization of organic molecules,¹³⁶ and in measuring non-stoichiometry¹³⁷ and defects⁷⁹ in solid state materials. This approach is applied in both predictive and interpretive ways in modern heterogeneous electrocatalysis, where linear scaling relations between the adsorption strength of reactants on a surface and overall electrocatalytic performance are exploited.^{65,138,139} From a structural analysis perspective, structure-property relationships have assisted in identifying previously unobserved coordination environments in layered transition metal hydroxides and relating them to secondary mechanisms for electrocatalytic OER.^{83,85}

We have used Raman spectroscopy based structure-property analysis of a series of α -Fe₂O₃ samples prepared by thermal treatment of lepidocrocite revealed that the intensity of select peaks in the Raman spectra were highly correlated to band structure and overall PEC performance in **Chapter 3**, and further combined with X-ray

absorption spectroscopy to directly show the role of point defects in structures and PEC performance in **Chapter 4**. Such a capability of Raman spectroscopy would significantly improve our ability to understand the lack of consistency across the literature and open paths for rational improvement of photoanodes. Much more information is required, however, before Raman spectroscopy can be used in such a broad sense.

Both **Chapter 3** and **Chapter 4** use lepidocrocite as precursors and analyze the defects through phase conversion from lepidocrocite to maghemite and then to hematite. **Section 1.2.2** introduces that hematite can be prepared through different iron (hydro)oxide precursors, and the different routes can fabricate hematite with different defects. Herein, we expanded synthetic approach to expand defect analysis in this chapter. We parametrize the structure and photoelectrochemical properties of a series of α -Fe₂O₃ films prepared by sintering akaganeite (β -FeOOH) films under varied conditions. The structure and property datasets are compared to identify correlations, which are then interpreted to identify likely structural defects. Raman spectroscopy serves as the source of structural information, with the location, width and intensity of peaks considered. The properties dataset includes the flat band potential and the charge carrier density of the photoanodes, measured by electrochemical impedance spectroscopy, along with the onset of photoelectrocatalytic OER and the current densities at 1.23 V vs RHE, each measured by linear sweep voltammetry under illumination. Observed structure-property correlations indicate coexistence of three distinct defects are present in the sample series, with fabrication conditions dictating which has most influence over PEC behavior.

5.2 Results and Discussion

5.2.1 Synthesis

Films of α -Fe₂O₃ with varying degrees of structural integrity were fabricated by systematic variation of experimental protocols. The sintering of β -FeOOH was selected as the synthetic route, with β -FeOOH being deposited as thin films on an FTO sur-

face by hydrolysis of FeCl_3 following a published protocol.³¹ The identity of the thin iron oxide films was confirmed by observation of the expected $\beta\text{-FeOOH}$ phonons at 118, 141, 250, 312, 387, 420, 500, 543, 610 and 714 cm^{-1} in Raman microscopy measurements (**Figure 5.1**).^{48,140,141} These precursor films were then sintered under varied gaseous environments, namely ambient air, O_2 or N_2 , in an effort to influence the oxygen stoichiometry in the final material.

The O_2 and N_2 environments were used in either their dry state, or humidified by bubbling the selected purge gas through H_2O to influence the residual proton/ H_2O content within the films. Two different sintering temperatures, 600 and 800 $^\circ\text{C}$, were paired with these five different atmospheres to yield ten samples to yield 10 distinct $\alpha\text{-Fe}_2\text{O}_3$ samples. Five sets of conditions were repeated to obtain a total of 15 samples as listed in **Table 5.1**

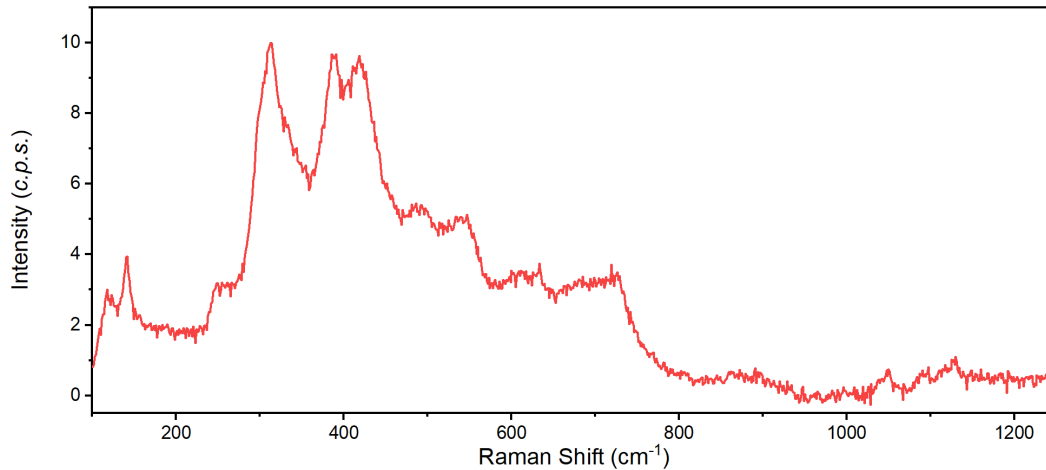


Figure 5.1: Akaganeite ($\beta\text{-FeOOH}$) film Raman spectrum used as precursors for hematite synthesis

Table 5.1: Parameters describing the photoelectrochemical behavior of α -Fe₂O₃ sample series.

Sample	Conditions	E_{PEC} V vs. RHE	j_{PEC} mA cm ⁻²	$\log(N_{\text{d}})$ cm ⁻³	E_{fb} V vs. RHE
1	dry air, 800°C	0.891	0.150	19.59	0.492
2	dry air, 800°C	0.996	0.144	19.97	0.333
3	dry O ₂ , 800°C	0.856	0.088	19.87	0.273
4	dry O ₂ , 800°C	0.98	0.189	19.90	0.464
5	humid O ₂ , 800°C	0.995	0.123	19.77	0.342
6	dry N ₂ , 800°C	0.788	0.056	20.25	0.195
7	humid N ₂ , 800°C	0.972	0.029	20.10	0.224
8	dry air, 600°C	0.983	0.001	20.12	0.157
9	dry air, 600°C	1.63	0.003	20.12	0.117
10	dry O ₂ , 600°C	0.933	0.001	20.21	0.325
11	dry O ₂ , 600°C	1.61	0.005	20.19	0.267
12	humid O ₂ , 600°C	1.150	0.003	19.48	0.506
13	dry N ₂ , 600°C	0.747	0.009	19.46	0.473
14	dry N ₂ , 600°C	1.62	0.002	20.09	0.299
15	humid N ₂ , 600°C	0.764	0.064	20.09	0.201

5.2.2 Behavioral Parameters

Each of the fifteen films was analyzed by linear sweep voltammetry and electrochemical impedance spectroscopy to extract parameters for structure-property analysis. Linear sweep experiments identify the photoelectrochemical response, with OER clearly visible (**Figure 5.2A**, **Table 5.1**). The onset of photoelectrocatalysis, the maximum current densities, and even the shape of the current-potential response are variable across the sample series (**Figure 5.2B**), as anticipated. Samples in upper portion of **Figure 5.2B** and E were sintered at 600 °C, while those in the lower portion were sintered at 800 °C. The photoelectrocatalytic performance was parametrized using the two values depicted in **Figure 5.2A**: the photocurrent density at zero overpotential for OER, labelled $j_{1.23\text{V}}$, and the onset of photoelectrocatalysis, labelled E_{PEC} . The former is readily extract from the data by reading the current density at 1.23 V vs. RHE. The onset of photoelectrocatalysis is more challenging to define. It has previously been defined in a number of ways, including the potential where a given current density is attained, the potential where first derivative plots, dj/dE , reach $0.2 \text{ mA cm}^{-2} \text{ V}^{-1}$,¹⁰¹ and the potential where the first positive

peak occurs in second derivative plots, d^2j/dE^2 .⁴³ The two former approaches fail to capture any value for poorly performing samples; the need to analyze samples across the performance spectrum in this work therefore leads to adoption of the second derivative definition (**Figure 5.2A**). This enables a systematic mathematical definition to be applied across all samples, even when significant resistive effects distort the j - E response, or samples have very poor performance. We note that the performance parameters can be affected by variations in both the bulk and interfacial structures. Two semiconductor properties, the flat band potential (E_{fb}) and charge carrier density (N_{d}), were measured as additional parameters using Mott-Schottky analysis (**Figure 5.2C**). The capacitance of the space-charge layer (C_{SC}) was determined through EIS experiments (**Figure 5.2D and F**). The numeric values measured for E_{fb} and N_{d} vary with fabrication conditions (**Figure 5.2E, Table 5.1**) but fall within the ranges found in literature. The fabrication protocol thus exerts a clear influence on the properties and photoelectrochemical behavior across the α - Fe_2O_3 film series (**Table 5.1**), but no clear trends emerge in this dataset alone.

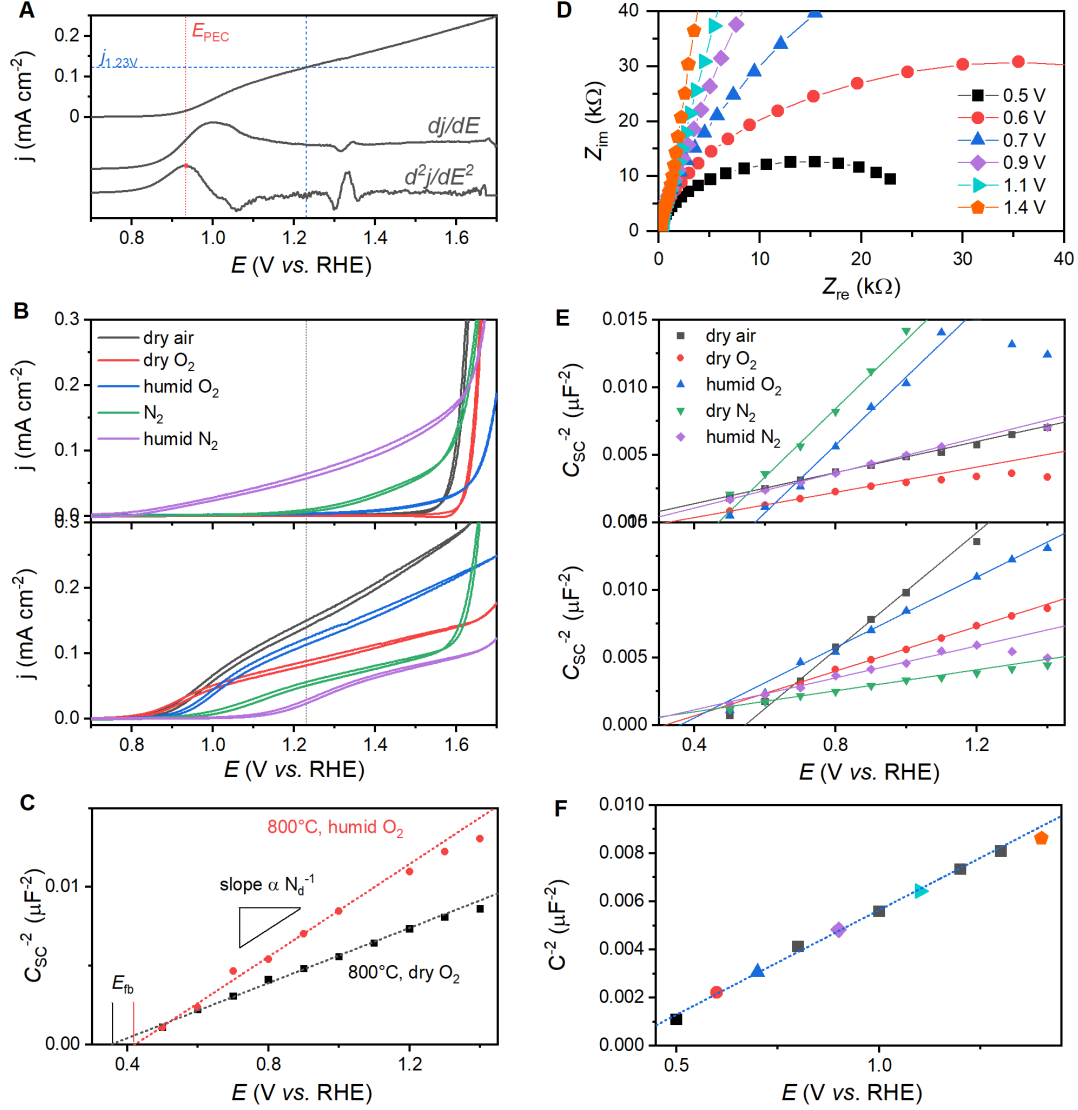


Figure 5.2: Photoelectrochemical properties of α -Fe₂O₃ sample series. (A) Systematically determination of the onset of photoelectrocatalysis E_{PEC} for an electrode sintered at 800°C under humidified O₂. (B) Comparison of photoelectrochemical behavior for 10 samples prepared using unique conditions. (C) Extraction of the charge carrier density, N_d , and the flat band potential, E_{fb} , using Mott-Schottky plots. (D) The Nyquist impedance representation of data acquired at a subset of the 100 mV voltage steps. (E) Comparison of Mott-Schottky plots for these 10 samples. (F) Mott-Schottky plot for the sample sintered at 800°C under dry O₂.

5.2.3 Structural Information

The normal vibrational modes probed by Raman spectroscopy involve the motion of specific atoms within the crystal lattice. The size, shape and location of each

peak observed in a spectrum is therefore uniquely affected by each type of defect, providing valuable but convoluted structural information. Each $\alpha\text{-Fe}_2\text{O}_3$ sample was analyzed using a Raman microscopic mapping protocol with 16 individual spectra acquired over a $3 \times 3 \mu\text{m}^2$ grid. Parameters describing individual peaks, such as full-width at half mass and maximum intensity, were previously shown to reside within a Gaussian distribution over large-scale maps.⁴³ A window spanning 15% above and below the average peak parameter value captures >85% of all individual spectra.⁴³ The average of all 16 spectra acquired for 10 samples prepared using unique fabrication conditions show the two A_{1g} peaks (*ca.* 226 and 499 cm^{-1}) and 5 E_g peaks (*ca.* 246, 293, 299, 412 and 613 cm^{-1}) expected for $\alpha\text{-Fe}_2\text{O}_3$ (**Figure 5.3A**). An additional peak observed near 660 cm^{-1} is a formally Raman inactive E_u vibration that is visible due to symmetry lowering distortions in the crystal lattice.^{59,61,94} Curve fitting was performed to measure the peak location (L_x), maximum intensity (I_x), full-width at half maximum (W_x), and peak area (A_x) for each of the 8 observed peaks.

Preliminary structure-property trends indicate that the photoelectrochemical behavior across the $\alpha\text{-Fe}_2\text{O}_3$ sample series is dependent on multiple factors. Growth in the intensity of this E_u mode was previously correlated with improved performance in heteroatom-doped $\alpha\text{-Fe}_2\text{O}_3$,⁵⁹ but degraded performance in pure $\alpha\text{-Fe}_2\text{O}_3$.⁴³ A positive linear correlation of I_{499}/I_{660} with both $j_{1.23\text{V}}$ and E_{fb} in undoped $\alpha\text{-Fe}_2\text{O}_3$ films prepared by sintering lepidocrocite ($\gamma\text{-FeOOH}$) previously demonstrated the utility of the Raman forbidden E_u vibration at 660 cm^{-1} for diagnosis of trapped protons and associated iron vacancies. Similar handling of the data acquired here reveals separation of the samples into two clear branches for $j_{1.23\text{V}}$, with humidified sintering environments yielding one branch and dry environments a second (**Figure 5.3B**). Correlation plots for E_{fb} show similar separation into two apparent branches, but seemingly scattered distribution of fabrication parameters across both branches indicates that the underlying reasons are non-trivial (**Figure 5.3C**). These correlations confirm that information can be extracted through structure-property correlations, but that at least two dominant types of defect contribute to observed trends.

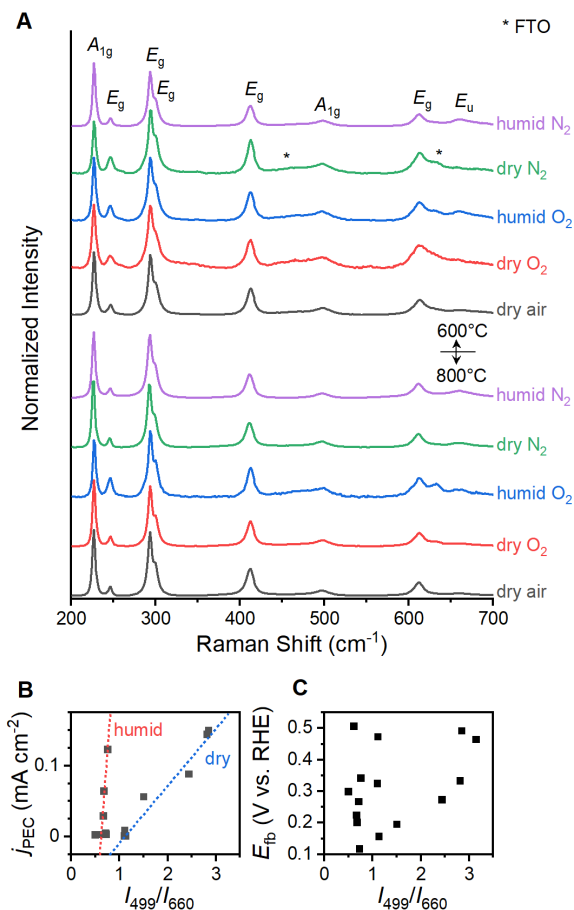


Figure 5.3: Raman spectra acquired for the $\alpha\text{-Fe}_2\text{O}_3$ sample series. (A) Raman spectra acquired by microscopic mapping of 10 samples prepared with unique conditions, with each normalized to the 227 cm⁻¹ peak. The upper section of the panel contains samples sintered at 600 °C, and the lower section at 800 °C. Non-trivial correlations observed between the intensity ratio I_{499}/I_{660} and (B) $j_{1.23\text{V}}$ and (C) E_{fb} . The dashed trend lines highlight the grouping of samples sintered under dry or humid conditions; no such grouping is obvious in panel (C).

5.2.4 Structure-Property Correlations Detection

A systematic approach was designed to facilitate the search for viable structure-property correlations across the entire dataset. The widths, intensities, and locations of all 8 Raman peaks were considered; the ratios of maximum intensities of the 8 normal vibrational modes, I_x/I_y , showed the strongest correlations and were selected as the structural parameters of interest. The four behavior parameters, namely E_{PEC} , j_{PEC} , $\log(N_{\text{d}})$ and E_{fb} , then serve as numeric properties of interest. All possible I_x/I_y combinations were calculated and plotted against each of the four

behavior parameters. The coefficient of determination, R^2 , was then obtained for a linear regression analysis on each structure-property pair. This enables the number of viable structure-property candidates to be visualized as a function minimum R^2 cutoff values. The highest quality candidate found when the entire dataset is used as the basis for calculations is one between I_{293}/I_{660} and j_{PEC} , which appears at a very low cutoff of $R^2 > 0.71$ (**Figure 5.4A**). It is thus clear that no straight forward structure-property correlations span the entire dataset, which is to be expected given the results in **Figure 5.3B** and C. Systematic segmentation of the dataset enables an iterative analysis to deconvolute the dominant linkages between structural features and photoelectrochemical behavior. Viable structure-property correlations appear when the data is split into sets containing those sintered under N_2 (**Figure 5.4B**; selection in **Table 5.2**). An R^2 cutoff of > 0.95 identifies 4 correlations for these samples, and 17 correlations for a cutoff > 0.80 . In contrast, samples sintered under O_2 environments produce 2 candidates for correlation with at a cutoff of > 0.95 , and only 4 candidates larger than 0.8. The addition of data from samples sintered under air to either the N_2 or the O_2 segments of the data dramatically decreases the number of viable candidates in both cases (**Figure 5.4B**). Segmentation of the data into samples sintered under dry and humidified environments reveals 9 and 0 viable correlations for the segments, respectively, for a cutoff of > 0.95 (**Figure 5.4C**). Segmentation by sintering temperature yields no correlations with a cutoff of $R^2 > 0.95$ (**Figure 5.4D**). A total of two candidates arise for the 600 °C samples when the cutoff is lowered to 0.90. These numbers make it clear that the use of N_2 sintering environments and the humidification of the atmosphere yield the strongest direct impact on photoelectrochemical behavior.

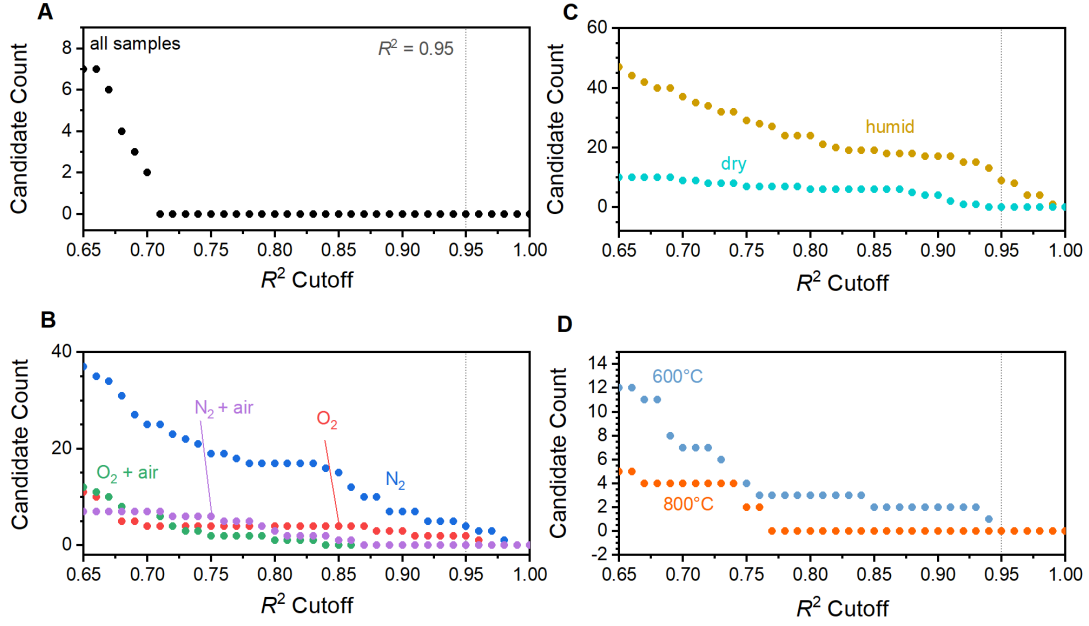


Figure 5.4: Number of structure-property correlation candidates as a function of statistical cutoff value. Linear regression analysis was performed on (A) the entire dataset and after the dataset was broken into segments according to (B) gaseous sintering environment, (C) presence of humidity in the sintering environment, and (D) sintering temperature. An R^2 cutoff of 0.95 is marked for reference.

5.2.5 Correlation Identities

The top 40 correlation candidates for samples sintered in an N_2 environment involve the four lowest energy vibrational modes. Further, the modes at 226, 246, 293, 299 and 412 cm^{-1} are fully responsible for 8 of the top 11 correlation candidates (**Table 5.2**). The viable correlations almost exclusively involve the band structure parameters $\log(N_d)$ and E_{fb} : an R^2 cutoff of > 0.85 yields 17 possible correlations, with only 2 involving $j_{1,23V}$ and none involving E_{PEC} . A lack of meaningful correlations for samples sintered in O_2 stand in stark contrast to the N_2 results. These results together indicate that the absence of O_2 exerts a very strong influence on band structure, but that the presence of O_2 itself in the sintering atmosphere affects little change in the lattice.

Table 5.2: Top structure-property correlation candidates identified for each dataset segment.

Segment	Correlation	R ²	Segment	Correlation	R ²
N ₂	I_{246}/I_{299} vs. E_{fb}	0.998	humid	I_{226}/I_{660} vs. E_{fb}	0.992
	I_{246}/I_{299} vs. $\log(N_d)$	0.911		I_{226}/I_{660} vs. $\log(N_d)$	0.961
	I_{246}/I_{412} vs. E_{fb}	0.975		I_{613}/I_{293} vs. E_{fb}	0.968
	I_{246}/I_{412} vs. $\log(N_d)$	0.950		I_{613}/I_{293} vs. $\log(N_d)$	0.986
	I_{246}/I_{293} vs. $\log(N_d)$	0.886		I_{412}/I_{293} vs. $\log(N_d)$	0.984
O ₂	I_{293}/I_{299} vs. $\log(N_d)$	0.957		I_{412}/I_{293} vs. E_{fb}	0.940
	I_{246}/I_{660} vs. $j_{1.23}$	0.905		I_{499}/I_{660} vs. $j_{1.23}$	0.949
dry	I_{499}/I_{660} vs. $j_{1.23}$	0.938		I_{660}/I_{299} vs. $j_{1.23}$	0.945
	I_{293}/I_{660} vs. $j_{1.23}$	0.918	800 °C	I_{246}/I_{660} vs. $j_{1.23}$	0.748
	I_{226}/I_{660} vs. $j_{1.23}$	0.907		I_{293}/I_{412} vs. $\log(N_d)$	0.762
	I_{299}/I_{660} vs. $j_{1.23}$	0.903	600 °C	I_{246}/I_{412} vs. E_{fb}	0.942

The higher energy normal vibrational modes become important when the data is segmented based on humidity. Samples sintered in humidified environments exhibit correlations largely based on combinations of the oxygen-based normal modes at 226 and 293 with those at 499, 613 and 660 cm⁻¹, which are based on the movement iron ions in adjacent face sharing polyhedral motifs (**Table 5.2**). The top correlations in the humid segment of the data are again those that describe the α -Fe₂O₃ band structure, but $j_{1.23}$ does begin to factor in much earlier than seen in the N₂ data segment. Correlations with $j_{1.23}$ are the strongest observed in the dry segment of the data, where all candidates with an R² cutoff > 0.75 involve $j_{1.23}$. The dry and humid segments of the data are related in that the formally Raman inactive Eu vibration at 660 cm⁻¹ becomes prominent in correlations.

5.2.6 Correlation Interpretations

The identity of Raman peaks and the photoelectrochemical properties involved in each structure-property correlation provides insight into the underlying chemical relationship. The number and quality of correlations show that N₂ and humidity are the two environmental parameters that exert the most significant influence over the final structure and photoelectrochemical behavior of α -Fe₂O₃ photoanodes fabricated by sintering β -FeOOH. The four low energy vibrational modes, which are

strongly correlated with the band structure for samples sintered under N_2 environments (**Figure 5.5A** and B), involve vibrations of oxide ions within the lattice.³¹ This relationship disappears for samples prepared under O_2 , and when samples sintered in air are combined with N_2 samples. Annealing $\alpha\text{-Fe}_2\text{O}_3$ in O_2 deficient atmospheres is known to generate oxygen vacancies within the lattice,^{27,31} which increases N_d by necessitating reduction of Fe^{3+} to Fe^{2+} within the structure. The relationships observed across the N_2 segment of data here can therefore be confidently attributed to the presence of varied concentrations of oxygen vacancies in the $\alpha\text{-Fe}_2\text{O}_3$ samples. The number and quality of structure-property correlations indicate that Raman spectroscopy provides a means to approximate the concentration of oxygen vacancies in $\alpha\text{-Fe}_2\text{O}_3$, at least within a contiguous series of materials, by measuring their structural impact.

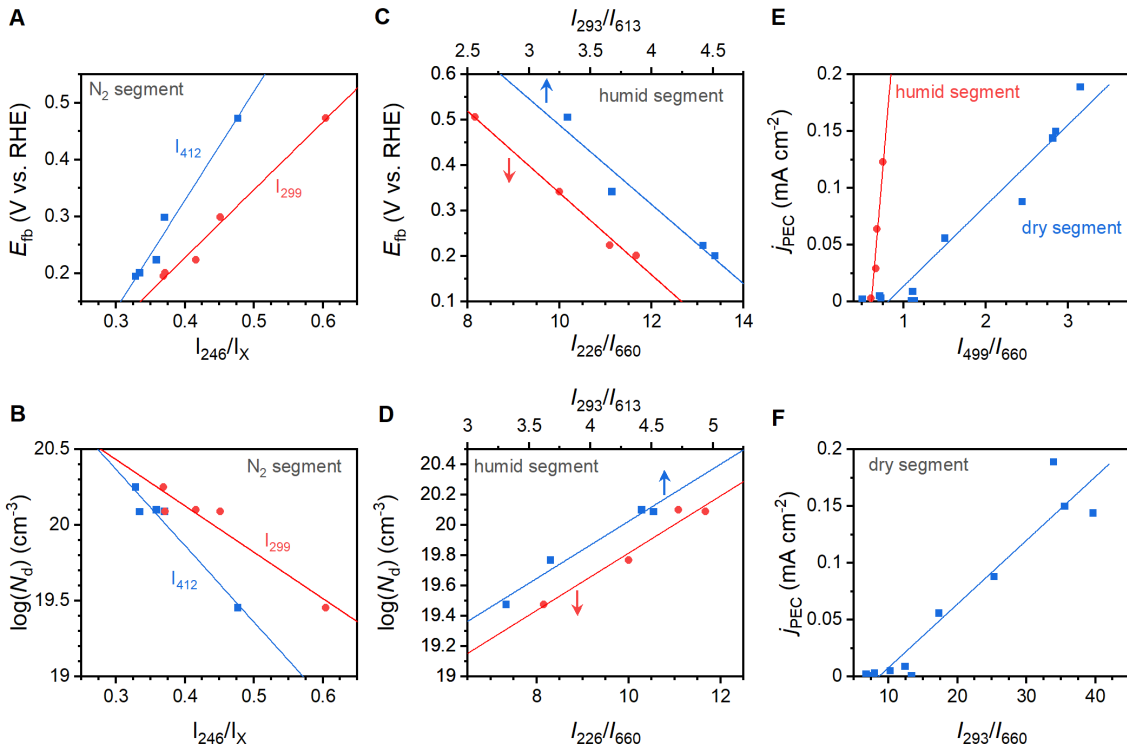


Figure 5.5: Prominent correlations between Raman spectroscopic data and photoelectrochemical data for segments of the dataset. Correlations between (A) flat band potential and (B) charge carrier density for samples sintered under N_2 . Correlations between (C) flat band potential and (D) charge carrier density for samples sintered in humidified environments. Comparison of correlations between j_{PEC} and (E) I_{499}/I_{660} for photoanodes prepared under humid and dry conditions, and for (F) I_{293}/I_{660} under dry sintering conditions.

The role of humidity is less obvious because its presence during synthesis yields correlations involving band structure (**Figure 5.5C** and D) and photoelectrocatalytic performance, while the absence of humidity yields correlations only for photoelectrocatalytic performance (**Figure 5.5E** and F). A previous study showed that environmental humidity increased iron vacancies by trapping residual proton content in α -Fe₂O₃ films.⁴³ These vacancies induce growth of the Raman inactive 660 cm⁻¹ peak, a vibrational mode that involves a shearing movement of iron ions that share polyhedral faces, by lowering local symmetry. The behavior is observed here as a linear increase in $j_{1.23V}$ with respect to I_{499}/I_{660} for samples prepared under dry conditions (**Figure 5.5E**). This correlation identifies a second defect, namely protohematite domains and their associated iron vacancies, in α -Fe₂O₃ prepared by sintering β -FeOOH under dry conditions. A similar correlation appears to exist between $j_{1.23V}$ and I_{499}/I_{660} for humid conditions (**Figure 5.5E**), but these samples exhibit little variation in I_{660} . In fact, $j_{1.23V}$ attains levels comparable to the best “dry” sample while maintaining a very large I_{660} . Further evidence of differences between the dry and humid segments is in the vibrational modes involved in correlations: the dry segment of the data relies entirely upon combinations involving I_{660} , while the humid segment of the data rely upon combinations of vibrational modes at 412, 499, 613 and 660 cm⁻¹. Each of these vibrational modes that are relevant to humid conditions involves the movement of iron ions in the lattice,^{43,93,96} revealing a third defect that is critically dependent on iron sites in the lattice. We tentatively assign this third defect as iron ions residing in interstitial sites, based on this being the second major iron-based defect known to exist natively in α -Fe₂O₃.^{115,142}

5.3 Conclusion

A series of films fabricated by sintering β -FeOOH films with varied gaseous environment, humidity and temperature were analyzed by Raman microscopy, linear sweep voltammetry and electrochemical impedance spectroscopy. The intensity, width, and location of the eight peaks present in the Raman spectra were systematically compared to the flat band potential, charge carrier density, onset of photoelectrocatalytic

alytic oxygen evolution and overall photoelectrocatalytic performance. Not a single structure-property correlation was found to span the entire dataset, but numerous correlations appeared in specific segments of the data. Oxide vacancies were revealed by strong correlations of all vibrations involving the oxygen ions with charge carrier density and flat band potential for samples synthesized in an N_2 environment. Interstitial protons, with associated iron vacancies, were revealed by correlation of a formally Raman forbidden E_u vibrational mode with photoelectrocatalytic performance under dry environments. A third defect, tentatively assigned as interstitial iron ions, was revealed by correlations between all iron-based vibrational modes with charge carrier density and flat band potential in samples prepared under humid environments. The coexistence of three different defects reveals a situation that is much more complex than that reported for α - Fe_2O_3 prepared by sintering of lepidocrocite, where evidence only exists for interstitial protons with paired iron vacancies. These results highlight the challenge in directly comparing the performance of photoanodes fabricated by different approaches and demonstrate Raman spectroscopy to be a powerful tool to address these challenges by using structure-property analysis to analyze structural defects.

5.4 Experimental Details

5.4.1 Material fabrication

Akaganeite Fabrication

Fluorine-doped tin oxide coated glass (FTO; TCO10-10, Solaronix SA) was cleaned immediately prior to use by sequential ultrasonication in a detergent solution, milli-Q H_2O , then isopropanol. The surface was dried under a stream of N_2 and placed in a custom UV-irradiation chamber (GHO18T5VH lamp, Atlantic Ultraviolet) for 15 minutes. Aqueous 0.15 M $FeCl_3$ solutions were prepared using milli-Q H_2O (18.2 M Ω) and $FeCl_3 \cdot 6H_2O$ (99+%, Acros). Aqueous 1 M KNO_3 solutions were prepared using milli-Q H_2O and KNO_3 (>99.0%, EMD Chemicals). Aqueous 1 M KOH

solutions were prepared using milli-Q H₂O and KOH (85%, Sigma-Aldrich). Thin films of β -FeOOH were deposited onto a series of FTO substrates by hydrolysis of aqueous FeCl₃ at elevated temperatures. In a typical synthesis, a 100 mL beaker was filled with 20 mL of aqueous solution with a pH below 1.5 that contained 0.15 M of FeCl₃ and 1 M KNO₃. This beaker was covered with a watch glass and preheated to 95°C in a furnace. Freshly cleaned FTO was then placed into the solution and held at 95°C for 4 hours, then allowed to naturally cool to ambient temperature. The β -FeOOH modified FTO glass was washed with milli-Q water and dried under a stream of air.

Hematite Fabrication

A series of fifteen α -Fe₂O₃ films were prepared by sintering β -FeOOH samples in a tube furnace with systematically varied protocols. The annealing temperature (600 °C, 800 °C) and gaseous atmosphere (air, dry N₂, dry O₂, humidified N₂, humidified O₂) were selected as variables for the sintering process. Dry gases were used directly from high purity compressed gas cylinders. Humidification of the gaseous environment was achieved by passing the relevant purge gas through a porous glass frit submerged in room temperature deionized H₂O immediately prior to entry into the tube furnace. A separate piece of β -FeOOH modified FTO was held for 2-hours under each selected temperature-atmosphere combinations to yield the series of α -Fe₂O₃ films used for analysis.

5.4.2 Raman Spectroscopy

A Renishaw inVia Reflex was used for Raman microscopic analysis of each sample. A 633 nm (Renishaw HeNe laser, 17 mW) laser was paired with an 1800 lines mm⁻¹ grating. Spectra were recorded by mapping a 3 × 3 μ m area in 1 μ m steps to yield 16 spectra. Each individual spectrum was acquired with a 75 second acquisition time, then all spectra were averaged to yield a final spectrum with 1200 second acquisition time. The spectra were then analyzed using the Renishaw WiRE 5.3 software package, where typical processing included a baseline subtract using a 5th

order polynomial and curve fitting.

5.4.3 Photoelectrochemical Analysis

A Bio-logic SP300 potentiostat and a Sciencetech A1 Lightline solar simulator equipped with an AM 1.5G filter were used for photoelectrochemical analysis. Hematite-coated FTO working electrodes were mounted as windows in a custom-made polyethylene cell. A silicone O-ring seals the electrode to the cell and masks the portion of electrode exposed to the electrolyte solution to 1.54 cm². A Gaskatel HydroFlex Reversible Hydrogen Electrode (Gaskatel GmbH, Kassel, Germany) was used as the reference electrode and a freshly cleaned piece of FTO served as the counter electrode. Experiments were carried using back-side illumination in a 1 M KOH electrolyte solution. Cyclic voltammetry experiments were limited between 0.4 and 1.7 V vs.RHE with a scan rate of 20 mV s⁻¹. Electrochemical impedance spectroscopy was carried out in 100 mV steps from 0.5 to 1.5 V.

Chapter 6

Mechanistic Insights into Lepidocrocite to Hematite Phase Conversion from Variable Temperature Raman Spectroscopy

6.1 Introduction

Heterogeneous electrocatalysis and photoelectrocatalysis are at the center of modern efforts to increase the sustainability of industrial fields ranging from energy storage,^{3,143} to waste water treatment,^{144,145} to the synthesis of fine chemicals.^{146,147} Much effort is focused on the identification of structural features or reaction sites that are either beneficial or harmful to catalytic performance; this information may lead to the ability to strategically maximize the number of beneficial features, or minimize the number of harmful ones.

This presents a distinct challenge, however, because the rate limiting step in heterogeneous electrocatalytic reactions are generally minor equilibria that are believed to take place at a minority of sites on the solid-state surface.^{148,149} It is well-accepted that the reaction mechanism of OERthe formation and transformation of OH, O, and OOH intermediates at a catalytic active site, with the formation of OOH as the rate

limiting step. Besides, any structural defect risks shutting down photoelectrocatalysis on semiconductor surfaces.^{19,34,98} Techniques that facilitate the identification, quantification, and removal or circumvention of specific structural features or defects are critical in advancing research in the field.

Being earth-abundant, low cost and the most thermodynamically stable phase of iron oxides, hematite ($\alpha\text{-Fe}_2\text{O}_3$) is widely studied for catalysis,^{150,151} electrocatalysis^{152,153} and photoelectrocatalysis.^{2,4,154,155} multitude of techniques have been employed to synthesize hematite, including the thermal treatment of other iron oxide phases such as lepidocrocite,^{156,157} goethite,^{41,96} magnetite^{158,159} and akageneite.^{31,48} The precursor selected, the atmosphere used, and the thermal treatment protocol influence the structural quality and properties of the $\alpha\text{-Fe}_2\text{O}_3$ product,^{31,43,119} including the performance towards photoelectrocatalytic oxygen evolution reaction. It has further been shown that the kinetics for processes on the surface of iron oxides are altered by exposure to alkali cation solutions.¹⁶⁰ Variability in the structure of $\alpha\text{-Fe}_2\text{O}_3$ is sufficiently high to introduce major inconsistencies in reported photoelectrocatalytic OER performance metrics and physical properties for $\alpha\text{-Fe}_2\text{O}_3$.^{4,159,161} These metrics are sensitive to the quality of the bulk structure, electron transport properties, and the surface structure. Research efforts have, for example, demonstrated that oxygen vacancies in $\alpha\text{-Fe}_2\text{O}_3$ can have a beneficial effect on photoelectrocatalytic OER,^{27,30,67} identified phase segregation in doped $\alpha\text{-Fe}_2\text{O}_3$ that improves photoanode performance,^{162–164} revealed the detrimental influence of iron vacancies,⁴³ and elucidated the role of surface states at the hematite–electrolyte interface.^{24,165} Establishing a detailed understanding of the nature of any potential structural defects, whether in the bulk or on the surface, and their effect on photoelectrocatalytic behavior, would provide a means to rationally optimize synthetic protocols. From a different perspective, which we are particularly interested in, the sensitivity of photoelectrochemical performance of $\alpha\text{-Fe}_2\text{O}_3$ to minute structural variations provides a useful measure of structural quality that can be correlated to spectroscopic results to acquire high quality structural information.

We demonstrated in previous **Chapter 3** and **Chapter 4** that the environmental conditions and heating protocol utilized to convert $\gamma\text{-FeOOH}$ to $\alpha\text{-Fe}_2\text{O}_3$ have significant impact on both structure and photoelectrocatalytic behavior. The cor-

relation of features within Raman spectra from α -Fe₂O₃ films with the band edge positions, photoelectrocatalytic onset and overall performance as a photoanode for OER were proposed to be caused by the trapping of protons and associated creation of Fe³⁺ vacancies within the bulk lattice. These defects persisted to 800 °C, the maximum temperature examined. Electrodeposition provides a facile, accessible means to fabricate uniform thin films of γ -FeOOH, making it a common starting point for α -Fe₂O₃ synthesis for photoelectrocatalysis.^{73,166} Lepidocrocite is different from other iron oxides in that it passes through an intermediate phase, maghemite, before being converted to hematite.^{48,157,167,168} Double-chain edge-sharing Fe(O,OH)₆ octahedra running parallel to crystal c-axis are the characteristic structure for γ -FeOOH, with edge-sharing motifs linking the chains to form two-dimensional layers that are hydrogen-bonded to each other.^{168,169} The intermediate γ -Fe₂O₃ phase presents a spinel structure similar to that of Fe₃O₄, but with exclusively Fe³⁺ the material becomes a defective spinel with cation vacancies in the octahedral sites.⁴⁸ Hematite has the corundum type crystal structure in hexagonally close packing, where Fe³⁺ occupies two-thirds of the octahedral sites.⁴⁸ The phase transformation from γ -FeOOH to α -Fe₂O₃ has been investigated by a range of techniques, including x-ray diffraction,¹⁵⁷ electron paramagnetic resonance spectra,¹¹⁸ differential scanning calorimetry and thermal gravimetric analysis,¹⁷⁰ and *in situ* infrared spectroscopy.⁴⁵ The classic mechanism for this reaction is viewed as starting from a hydrated form of γ -FeOOH and proceeding via a two-step process, with a dehydration reaction at *ca.* 140 °C followed by dehydroxylation to γ -Fe₂O₃ at *ca.* 260 °C and conversion to α -Fe₂O₃ at *ca.* 500 °C.^{45,48,158,167,171} The reported temperatures for each phase transition vary depending on the technique employed, the nature of the precursors, and the heating protocol. The particle morphology and size of lepidocrocite, for example, have been shown to influence the transition temperatures from γ -Fe₂O₃ to α -Fe₂O₃,^{45,172} but have little influence on transition of γ -FeOOH to γ -Fe₂O₃.⁴⁵ Recent *in situ* Fourier-transform infrared spectroscopy studies combined FTIR-temperature programmed desorption (TPD) indicate a mechanism that is more intricate than the classical one, with the possibility of multiple reaction paths.¹⁶⁹ Resolution of vibrational bands for bulk OH and surface Fe-OH, Fe- μ -OH and Fe- μ_3 -OH species in γ -FeOOH enabled the authors to show that *ca.* 50% of monodentate hydroxyl ligands at the surface

are preferentially lost between 50 °C and 120 °C, after which all hydroxyl ligands are removed between 254 °C and 266 °C. TPD results confirmed H₂O release *ca.* 20 °C above the temperature where the bulk OH vibrations were removed.¹⁶⁹ The authors proposed the creation of vacant anion sites at the surface was necessary for the phase transition to proceed, that creation of these vacancies could be facilitated by H-bonding, but that hydroxide migration or water adsorption could fill these vacancies and result in persistence of hydroxyl groups in material. They further showed that simultaneous conversion of γ -FeOOH to γ -Fe₂O₃ and α -Fe₂O₃ is possible, rather than the traditional linear series of reactions.¹⁶⁹ It is clear that there remains much to learn regarding the structural evolution of iron oxides upon heating, and on developing more direct paths to the synthesis of high quality α -Fe₂O₃ through simple and accessible processes.

Herein, we perform *in situ* variable temperature Raman spectroscopy under varied atmospheres for the first time to study the mechanisms of thermally induced conversion of γ -FeOOH to α -Fe₂O₃. We track the growth and decay of all phases between room temperature and 800 °C under inert or oxidizing conditions, with or without humidification. Curve fitting of each series of spectra enables analysis of peak location, width and size as a function of temperature and environment. We compare this information to that obtained via the more traditional DSC and thermal gravimetric analysis. The combined results are used to interpret the observed photoelectrocatalytic behavior of a series of α -Fe₂O₃ photoanodes fabricated by a systematically varied three-stage annealing protocol.

6.2 Results and discussion

6.2.1 Variable temperature Raman spectrum

Variable temperature Raman spectroscopy measurements demonstrate the sensitivity of the mechanism for conversion of γ -FeOOH to α -Fe₂O₃ to atmospheric conditions. Variable temperature Raman spectra show three distinct spectra for iron oxide under both dry and humid conditions (**Figure 6.1**). The average spectrum between

28 and 100 °C contains the series of peaks expected for γ -FeOOH (**Figure 6.2**), denoted here from lowest energy to highest as L_1 – L_4 .^{93,173} The average spectrum between 220 °C and 320 °C contains weak peaks at ca. 350 (M_1) and 500 cm^{-1} (M_2) and one strong, broad peak at 670 cm^{-1} (M_3), indicative of γ -Fe₂O₃. A subsequent transition to α -Fe₂O₃ is seen in the average spectrum between 500 °C and 600 °C, with peaks at ca. 220, 280, 390, 490 and 600 cm^{-1} labeled H_1 through H_5 .^{93,172} A total of seven Raman-active vibrations are expected for α -Fe₂O₃. These seven vibrations, and a formally symmetry-forbidden E_u peak observed at ca. 660 cm^{-1} , are resolved upon cooling to room temperature. The symmetry forbidden peak arises due a structural distortion; this vibrational mode has been shown to grow upon Si-doping of hematite, resulting in improved PEC performance,^{59–61,94} or to grow when iron vacancies form, resulting in a decrease in PEC performance.⁴³

The known thermal phase transitions, where γ -FeOOH is reported to convert to γ -Fe₂O₃ near 260 °C and to α -Fe₂O₃ near 500 °C in the air,⁴⁸ are present in the data acquired under all conditions (**Figure 6.1**). Clear differences are observed, however, in the transition temperatures, the temperature-induced shifting of peak locations and the relative peak intensities.

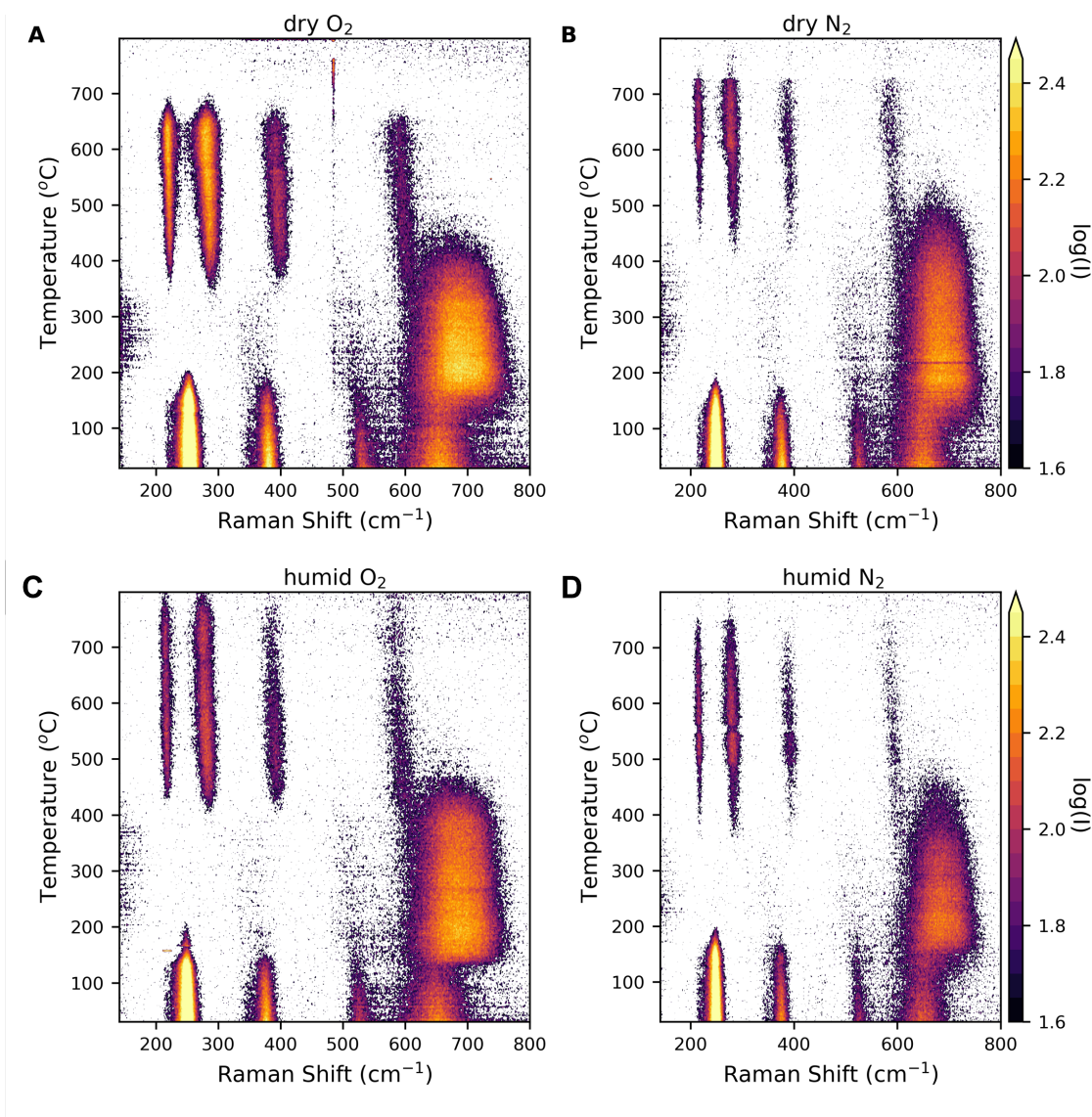


Figure 6.1: Variable temperature Raman spectra on γ -FeOOH under (A) dry O_2 , (B) dry N_2 , (C) humid O_2 and (D) N_2 conditions.

Curve fitting of individual spectra enables the structural transitions observed under different environments to be compared to one another. A subset of peaks was selected for detailed analysis of individual spectra, with each selected to minimize peak overlap with other phases and ensure maximum signal-to-noise ratios by analyzing strong peaks. Selected peaks include L_1 and L_2 for γ -FeOOH, M_3 for γ -Fe $_2$ O $_3$ and H_1 - H_3 for α -Fe $_2$ O $_3$, shown in the sample spectra for the dry N_2 series in **Figure 6.2A** and other conditions in **Figure 6.2B-D**. The changes in area of the remaining peaks for each phase are consistent with those of the selected peaks, but their weaker intensity lead to poor signal-noise (**Figure 6.3**). L-A refers to the

peak at high wavenumber (up to 1300 cm^{-1}) for lepidocrocite.

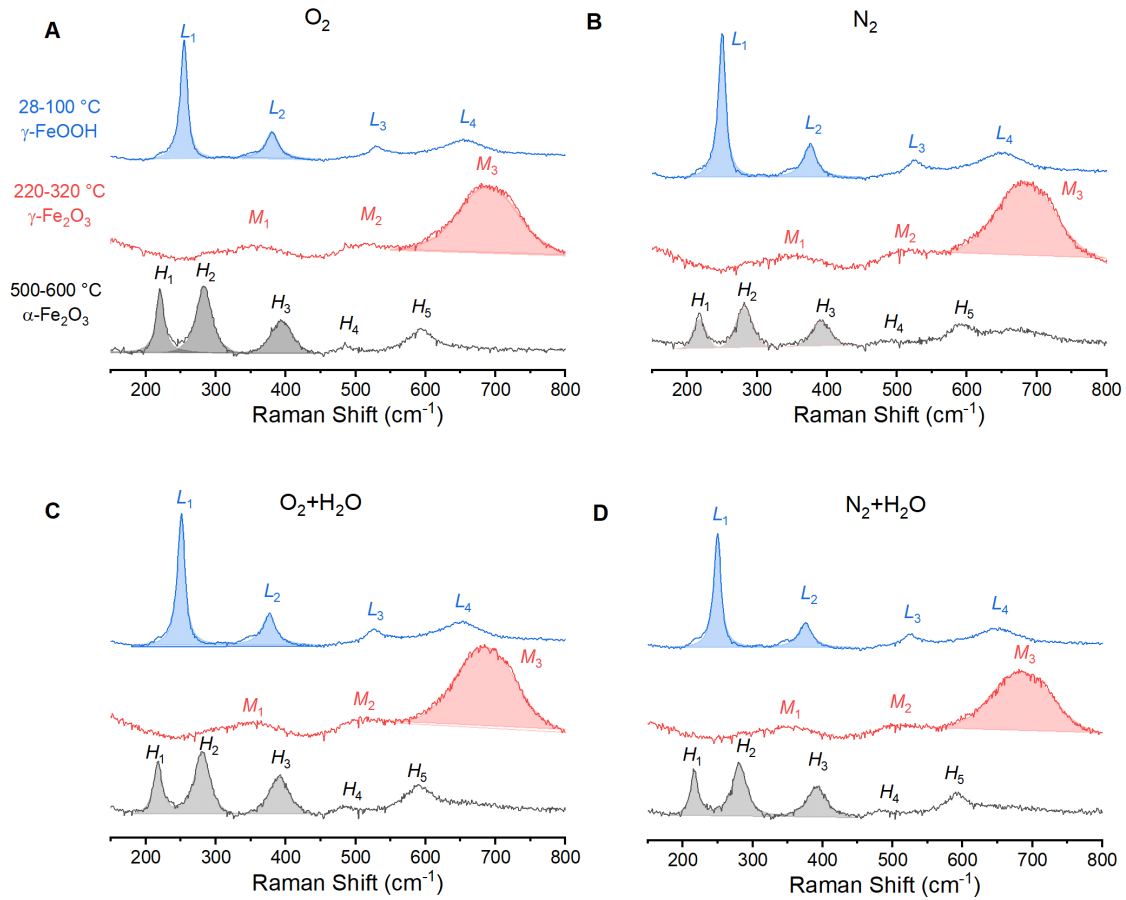


Figure 6.2: Sample Raman spectra acquired from a heat ramp under all four conditions.

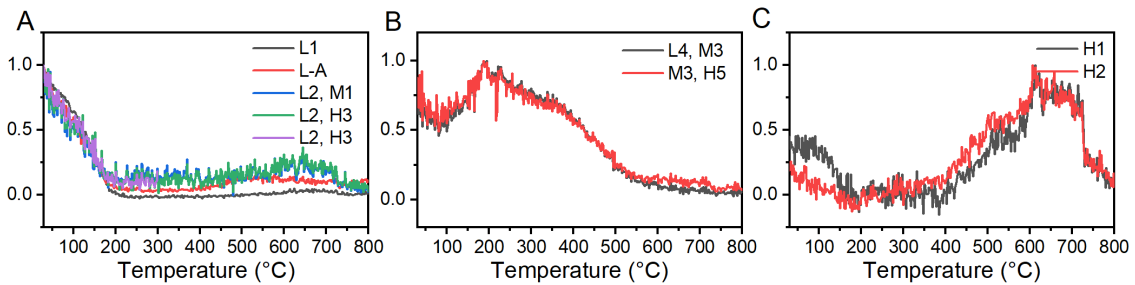


Figure 6.3: The integrated peak areas for individual peaks and combined overlapped peaks that are relevant to (A) lepidocrocite, (B) maghemite, and (C) hematite.

Changes in intensity and energy of the selected Raman vibrational modes indicate a more nuanced phase transition than is implied by the traditional two-step,

lepidocrocite-maghemite-hematite, mechanism. Using the sample heated under dry N_2 as an example, a first stage of γ -FeOOH decay proceeds until ca. 110 °C and involves an approximately linear loss of peak intensities (**Figure 6.4A**) and a red-shift in L_2 (**Figure 6.4B**) with respect to temperature. The rate of intensity loss accelerates in a second stage to yield a clear peak at 160 °C in first derivative plots. This second stage is accompanied by an exponential red shift in L_2 peak location. The loss of intensity for lepidocrocite peaks is mirrored in both direct and derivative plots for M_3 growth, thereby confirming that this second stage involves conversion of lepidocrocite to maghemite. A blue shift in M_3 and an increase in peak intensity are observed until ca. 200 °C–210 °C, which is well-aligned with the complete loss of L_1 . Notably, this lies ca. 50 °C lower than the phase transition temperature often reported by techniques such as TGA, DSC and TPD.^{157,167,168} Maghemite has nonetheless been observed as low as 150 and obtained in phase-pure form as low as 225 °C,¹⁷⁰ both of which also lie below the typically reported phase transition temperature. After reaching a maximum in both intensity and peak location, M_3 decays in a three-stage process. The first stage of maghemite decay is seen as a sudden 8 cm^{-1} red shift in M_3 location and a decay in intensity, which transitions into an approximately linear decrease in intensity and a red shift with respect to temperature. A third stage begins at ca. 370 °C, with a faster linear decay and a more extreme red shift. This third stage of M_3 loss is concomitant with first detected growth in H_2 , with mirrored behavior in M_3 and H_2 peak intensities confirming the conversion of maghemite into hematite. The initial growth of H_2 reaches a plateau at ca. 520 °C that extends until ca. 575 °C, after which a second growth stage yields a first-derivative peak at 588 °C. The intensity of H_2 is then stable until 700 °C, after which it rapidly decays. This apparent decay is induced by decreased signal-to-noise caused by increased baseline signal from blackbody radiation. These *in-situ* spectroscopic results suggest that there are at least two distinct steps within each of the two different structural transitions.

6.2.2 Thermal Analysis

Differential thermal analysis results for γ -FeOOH under a dry argon environment are in agreement with previously reported behavior,^{167,174} but provide a different perspective than the spectroscopic results. TGA traces show gradual mass loss from 80 °C to 200 °C, accelerating thereafter to produce a single peak at 242 °C in dm/dT plots (**Figure 6.4C**). The mass loss tails until *ca.* 400 °C, after which it is stable until 500 °C when slow mass loss once again occurs. The theoretical mass loss of 10.1%, calculated assuming no physisorbed H₂O, is approached at 800 °C. A measured mass loss of 8.4% at 500 °C indicates that the synthetic hematite retains excess hydroxide, which can alternatively be viewed as iron vacancies (*vide infra*). Simultaneously acquired DSC results produce numerous features (**Figure 6.4D**):

1. Exothermic peaks at 77 °C and 107 °C assigned to the loss of singly coordinated hydroxyl or aqua ligands, based on previous variable temperature FTIR and TPD studies.¹⁶⁹ The location of these peaks are aligned with the first stage of L_1 intensity loss. The removal of oxygen from lepidocrocite has been reported to involve proton transfer between adjacent hydroxyl sites to release H₂O and leave a surface vacancy (\square), as in equation **Equation (6.1)**.¹⁶⁹ An associated 0.42% mass loss suggests that $x = 0.02$ is the maximum possible extent of reaction during this stage of decay.



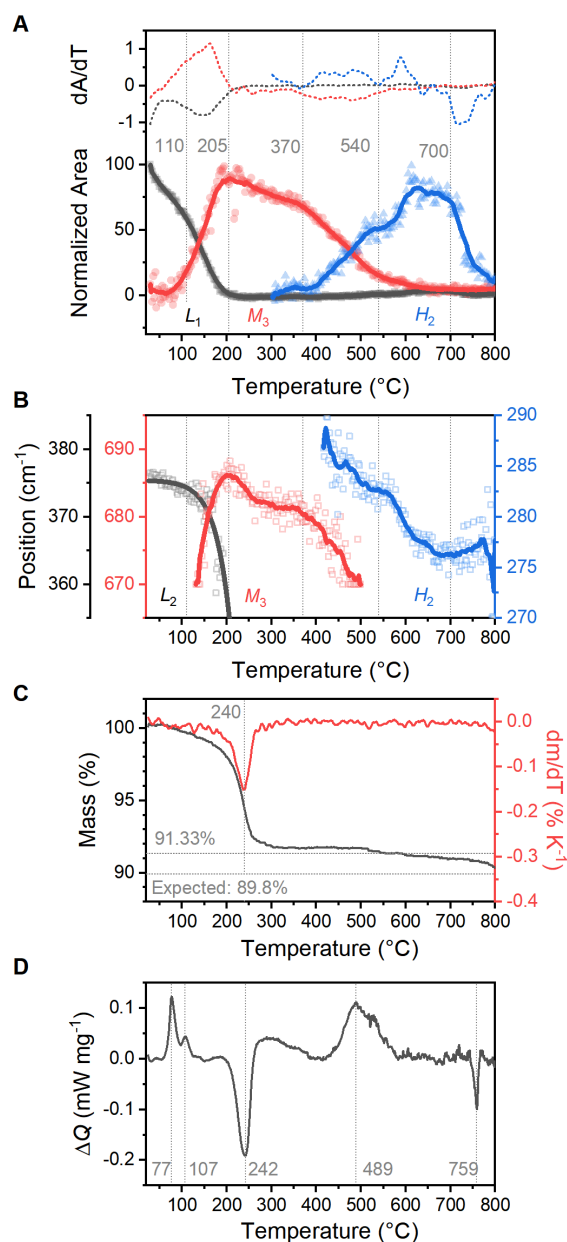
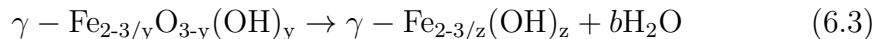


Figure 6.4: Variable temperature Raman and thermal analysis of γ -FeOOH under dry, inert atmospheres. The (A) integrated peak area for major peaks in γ -FeOOH (L_1), γ -Fe $_2$ O $_3$ (M_3) and α -Fe $_2$ O $_3$ (H_2) and (B) the peak locations for L_2 , M_3 and H_2 . Simultaneously performed (C) thermogravimetric analysis and (D) differential scanning calorimetry under an argon environment.

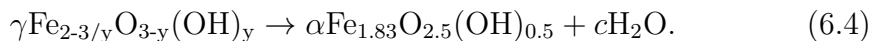
2. An endothermic peak at 242 $^{\circ}\text{C}$ is aligned with the major mass loss event observed by TGA, with the pair of peaks being routinely assigned as direct conversion of lepidocrocite to maghemite.^{167,175} This feature is notably misaligned with L_1 loss, instead beginning at the temperature where L_1 is fully lost and M_2 is at maximum intensity and energy (**Figure 6.4**). The DSC peak is then aligned with a rapid 8 cm^{-1} red shift in M_2 and its sudden drop in inten-

sity. The misalignment of major chemical processes observed via thermal and spectroscopic techniques provides evidence that the transition of lepidocrocite to maghemite occurs in two distinct steps. Magnetic studies have previously suggested that initial dehydroxylation of lepidocrocite between 150 °C and 200 °C yields an ordered but unstable form of maghemite, which decays to a more crystalline form of maghemite at 250 °C.⁴⁵ The temperature regime previously reported for this initial dehydroxylation reaction is perfectly aligned with the major transition observed here via Raman spectroscopy, and with a region of accelerated mass loss via TGA. We therefore assign the major transition observed in Raman spectroscopy to the formation of an initial, highly protonated form of maghemite as in equation **Equation** (6.2). The sudden red shift in M_3 , the endothermic DSC peak and the large mass loss must then be assigned to further dehydroxylation and crystallization of maghemite as in equation **Equation** (6.3). These chemical equations are written from the perspective of the products containing iron vacancies rather than excess oxygen, as is conventional,^{41,96,176} and with variables for H₂O stoichiometry release rather than full fractional amounts. Total mass losses for these two stages are 1.98% and 8.67%, suggesting that $y = 1.26$ and $z = 0.27$ capture the maximum extent of the respective reactions.



3. A broad exotherm stretches from approximately 200 °C to 400 °C in the DSC trace. This feature has been previously assigned as an undefined structural rearrangement in hematite,^{167,170} and is aligned with the second stage of intensity loss and a linear red shift in M_3 . Raman microscopic mapping of samples heated at 350 °C reveal the Raman spectrum for hematite scattered across the surface (**Figure 6.5A-C**), but comparison of these spectra with those acquired on samples synthesized at 800 °C show a 50-fold difference in intensity (**Figure 6.5D**). These observations, and the fact that subsequent hematite formation is also exothermic, lead us to assign the broad exotherm

in the DSC and the associated changes in Raman spectra to the formation of highly defective hematite. A loss of only 0.53% mass occurs between the end of the endothermic DSC peak at 265 °C and 400 °C. This step is therefore believed to yield a phase of hematite with residual hydroxide ions known as protohematite, which is conventionally represented as containing iron vacancies through the formula $\alpha\text{-Fe}_{2-\delta/3}\text{O}_{3\delta}(\text{OH})_{\delta}$.^{41,176,177} This process overlaps with those assigned to reaction **Equation** (6.3) in the DSC and Raman spectra, suggesting that equation **Equation** (6.4) proceeds as a branching reaction path from reaction **Equation** (6.2). Maintaining the approximated value of $y = 1.26$ through reaction **Equation** (6.4) would yield an implausibly high iron vacancy concentration in $\alpha\text{-Fe}_{1.58}\text{O}_{1.74}(\text{OH})_{1.26}$. The lowest crystallographically determined partial occupancy for iron sites in protohematite is 0.88 (i.e. $\alpha\text{-Fe}_{1.76}\text{O}_{2.64}(\text{OH})_{0.72}$),^{41,176} but values of 0.917 ($\alpha\text{-Fe}_{1.83}\text{O}_{2.5}(\text{OH})_{0.5}$) are more common.^{41,42,109} Convolution of mass loss from the overlap of **Equation** (6.2) and **Equation** (6.4) complicates quantitative determination of stoichiometry, so equation **Equation** (6.4) is written to yield the most commonly observed structure.



4. A second exothermic process that produces a peak at 489 °C is assigned as equation **Equation** (6.5), which is the conventionally reported formation of hematite that proceeds from equation **Equation** (6.3).^{158,178} This transition is aligned with the first major growth stage in H_2 and a linear red shift in its location. The DSC trace indicates that the transition is complete at ca. 580 °C, which aligns with the end of the plateau between the first and second stages of H_2 growth. A total mass loss of 8.67% at this temperature suggests that the average structure at this point can be represented as $\alpha\text{-Fe}_{1.91}\text{O}_{2.73}(\text{OH})_{0.27}$, which is equivalent to the composition commonly reported for protohematite.^{41,42,109}



The second stage of H_2 growth begins immediately after completion of this exothermic process, with a rapid increase in intensity paired to a 6 cm^{-1} red shift. The

DSC trace provides no measurable signals during this second process, but the TGA results do exhibit a gradual mass loss to yield a total 8.15% mass loss at 740 °C. This second event is assigned to the dehydration of protohematite as represented in equation **Equation (6.6)**.⁴²

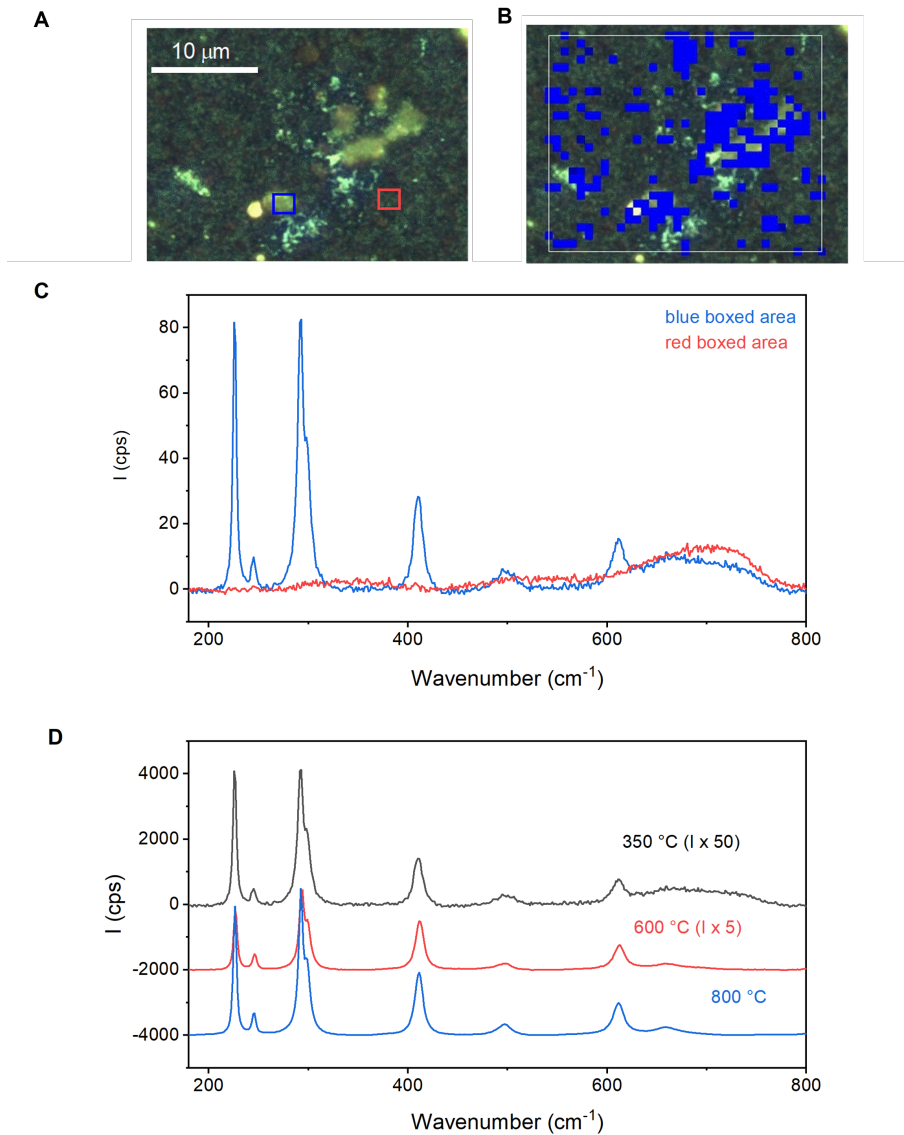
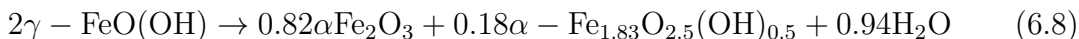
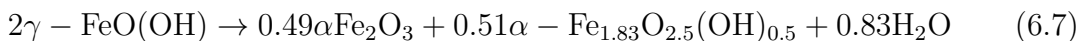


Figure 6.5: Raman microscopic map of lepidocrocite samples heated to 350 °C in a dry O₂ environment. (A) White light image and (B) a corresponding Raman spectral map where hematite peaks are observed. (C) The spectra averaged across the two 2 × 2 μm areas identified in panel A. (D) Comparison of the spectrum for hematite observed at 350 °C with spectra acquired for samples heated at 600 °C and 800 °C, with intensities scaled to enable comparison.



A sharp endothermic peak appears in the DSC trace at 759 °C, which is coincident with a further 0.5% mass loss process in the TGA. The surface of hematite is known to release oxygen gas near 1000 K under oxygen deficient atmospheres to yield magnetite (Fe₃O₄), with the specific transition temperature dependent on O₂ partial pressure.⁵¹ We therefore attribute these thermal features to a reaction on the hematite surface. No clear changes are observed to correspond with this process, but blackbody radiation from the reaction cell at these temperatures dramatically decreases the intensity of observed peaks due to a decrease in signal to noise. If protohematite is represented as a singular composition, which the consistency in past crystallographic reports suggests to be valid,^{42,177} the TGA results indicate that the net reaction at 580 under dry N₂ can be represented by equation **Equation (6.7)**, and that at 800 °C as equation **Equation (6.8)**.



Speciation plots showing the area of Raman peaks versus temperature confirm that the intensity loss and growth phases are observed in each reaction environment, albeit with the environments introducing differences (**Figure 6.6**). The first stage of γ -FeOOH decay contributes 30%–50% of the overall lepidocrocite peak loss, depending on the gaseous environments. Derivative plots show the maximum rate of lepidocrocite loss to be in the second stage near 162 °C for three of the environments; the maximum rate of loss under humid O₂ is 20 °C lower. The rate of red shift for L_2 during this second stage of lepidocrocite loss can be described using an exponential, with the exponential rate constant slightly decreased by humidity (**Figure 6.7A**). This influences the behavior of M_3 , which blue shifts as its intensity grows to a plateau at 685 cm⁻¹ under humid conditions, but a higher 690 cm⁻¹ under dry conditions (**Figure 6.7B**). All four environments produce a maximum peak area for M_3 near 205 °C. The first stage of decay, a rapid 5 cm⁻¹ red shift to 685 cm⁻¹, is only observed in dry conditions. After this, the linear decay with respect to temperature proceeds at a rate of 0.13% K⁻¹ until 400 °C under dry N₂ and humid O₂, but a faster 0.26% K⁻¹ until 330 °C under humid N₂ and dry O₂ (**Figure 6.4**). This

second stage of M_3 decay is aligned with the broad exothermic peak in the DSC results and assigned to the formation of protohematite (**Equation (6.4)**). The M_3 peak then decays at an approximately linear rate of 0.35% K^{-1} in dry and humid N_2 conditions and 0.52% K^{-1} in dry O_2 . A corresponding linear growth in H_2 is observed during the third stage of M_3 decay for each of these conditions. Humid O_2 is unique in this final stage of maghemite decay in that it is the only condition to yield a single, clear peak in first derivative plots for both M_3 and H_2 . Located at 434 °C, this peak is co-located with the intersection of the normalized intensity of the two peaks. Growth of H_2 is sensitive to the gas employed, with humid and dry N_2 , and dry O_2 environments following a two-stage growth process. The dry and humid N_2 environments contain a visible step between the two stages that are centered near 540 °C and 440 °C, respectively, while dry O_2 shows two linear regions (**Figure 6.6**). The first stage of growth is correlated to the final stage of M_3 decay for all three conditions; the second stage of H_2 growth occurs predominantly after M_3 has fully disappeared. Initial formation of hematite must therefore be followed by an evolution of structure. The humid O_2 conditions are again unique, showing single-phase growth that is well-correlated to the decay of L_3 . The intensity of H_2 decays to zero at higher temperatures, with the process starting near 600 °C in humid N_2 and dry O_2 , but 700 °C under dry N_2 and humid O_2 .

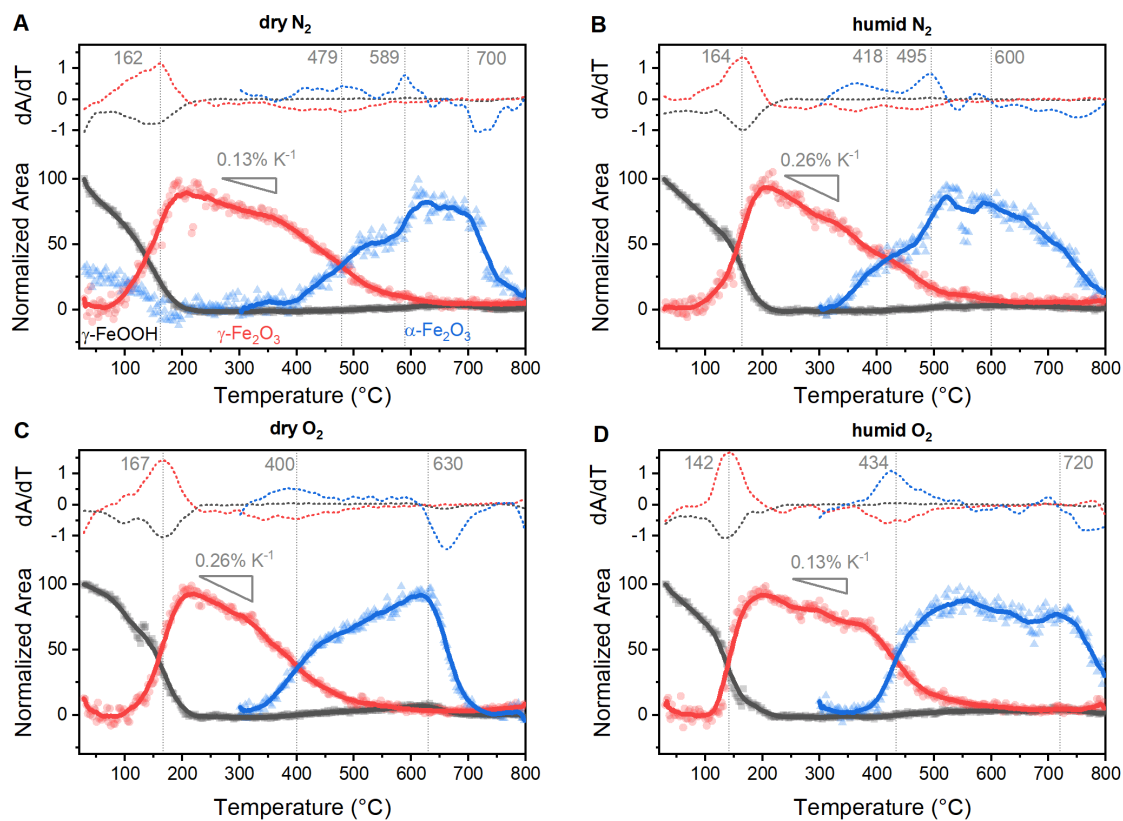


Figure 6.6: Speciation plots showing the normalized area of well-resolved peaks in spectra acquired during variable temperature Raman spectroscopy experiments. Data for γ -FeOOH (L_1 , black), γ -Fe₂O₃ (M_3 , red) and α -Fe₂O₃ (H_2 , blue) is shown under (A) dry N₂, (B) humid N₂, (C) dry O₂ and (D) humid O₂

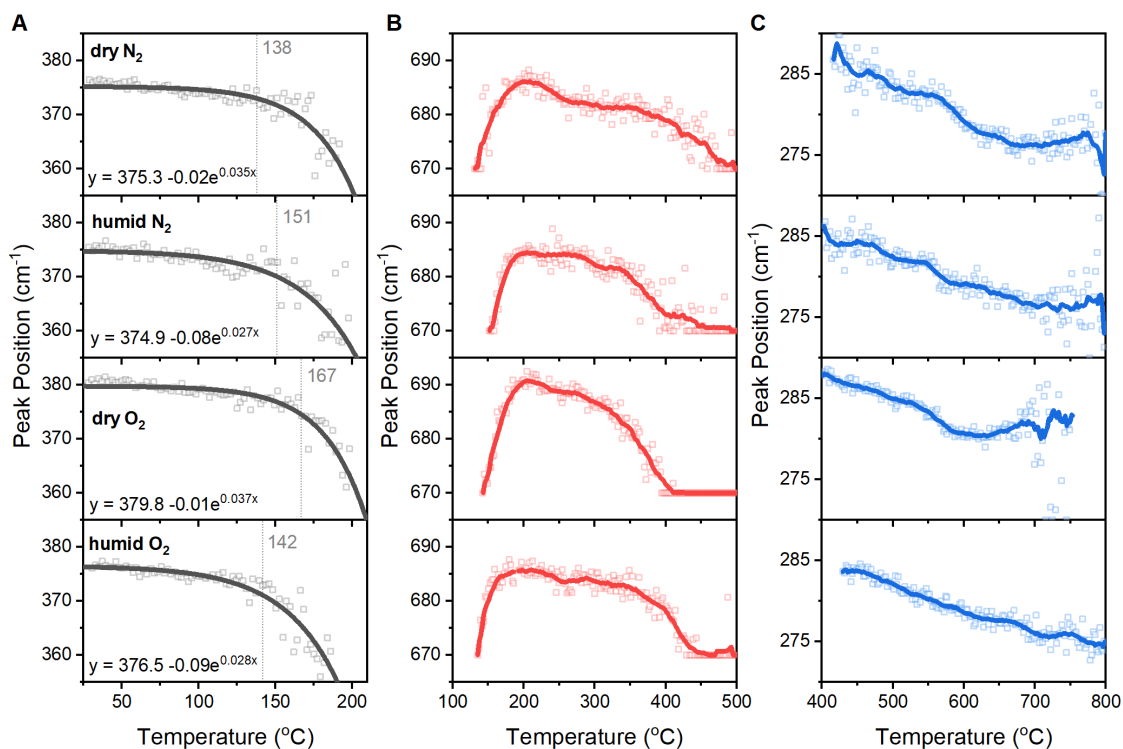


Figure 6.7: Position of selected peaks in spectra acquired during variable temperature Raman spectroscopy experiments. Data is shown for strong peaks in (A) γ -FeOOH (L_1 , black), (B) γ -Fe₂O₃ (M_3 , red) and (C) α -Fe₂O₃ (H_2 , blue) under dry N₂, humid N₂, dry O₂ and humid O₂ listed from top to bottom

6.2.3 Photoelectrochemical Performance

Comparison of PEC performance to the features observed in the thermal profile and variable temperature Raman spectra reveal that the intermediate temperature annealing environment is critically important. The influence of single variations in atmosphere during each annealing stage was examined by pairwise inspection of PEC data from the 16 photoanodes. For example, the samples synthesized using dry N₂ in the second heating stage were compared directly to those using humid N₂ and to dry O₂. No influence can be confidently assigned for atmosphere variation during the first stage of annealing on photoelectrocatalytic OER performance. A pronounced effect appears during the second heating stage, however, where dry O₂ and humid N₂ environments induce poor PEC performance relative to dry N₂ and humid O₂, respectively (**Figure 6.8A** and B). The primary difference in the 210 °C–550 °C temperature range for these two conditions is a more rapid 0.26% K⁻¹

rate of decay in M_3 intensity (**Figure 6.6**). This stage of M_3 decay was noted above to align with the broad exothermic process in the DSC results (**Figure 6.4**), which was assigned as the formation of protohematite through reaction **Equation (6.4)**. The more extreme slope therefore provides a signature of protohematite formation. The third annealing stage yields a trade-off in performance parameters, with N_2 yielding higher photoelectrocatalytic currents (**Figure 6.8A** and **B**) and O_2 inducing a cathodic shift in the onset of photoelectrocatalytic OER (**Figure 6.8C** and **D**). Note that the 16 photoanodes analyzed are distributed across panels **Figure 6.8A** and **B**, and differently across panels **Figure 6.8C** and **D**. Annealing $\alpha\text{-Fe}_2\text{O}_3$ under N_2 is known to introduce oxygen vacancies and reduce Fe^{3+} to Fe^{2+} ,^{37,179} which has been reported to improve PEC performance.^{27,37,67} The root cause of this performance trade-off is revealed by Mott–Schottky analysis, which shows that the N_2 environment yields charge carrier densities between one and two orders of magnitude greater than those annealed under O_2 (**Table 6.1**), but an O_2 environment shifts the flat band potential cathodically. This behavior reflects the balance that is known to exist between electron transfer kinetics at the solution interface and the photovoltage, which are influenced by changes in charge carrier density.^{27,30} Comparison of the PEC curves in **Figure 6.8A** and **B** make it clear that the charge carrier density and flat band potential set by the final annealing environment do not override previous sample handling—samples treated at 550 °C under humid N_2 or dry O_2 in the second heating stage perform poorly regardless of final heating stage. The variable temperature Raman experiments yield another fingerprint for these protohematite-forming conditions, with the decay of $\alpha\text{-Fe}_2\text{O}_3$ Raman vibrations beginning near 600 °C, which is 100 °C lower than the conditions that yield better-performing photoanodes (**Figure 6.4**). The iron vacancies introduced during protohematite formation at intermediate temperatures therefore persist to high temperatures and play a critical role in final PEC performance.

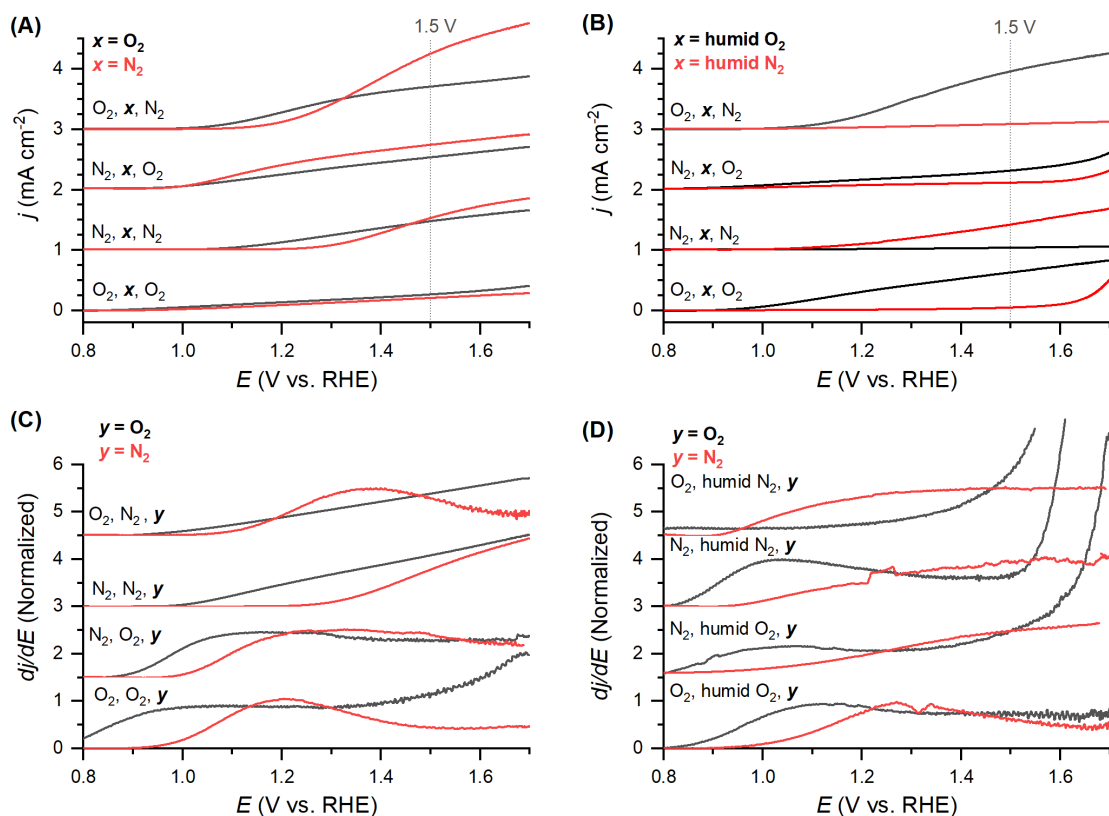


Figure 6.8: Pairwise comparison of photoelectrocatalytic oxygen evolution performance of α - Fe_2O_3 films synthesized by a varied three-stage annealing protocol. Comparison of the role of O_2 versus N_2 in the intermediate 550 °C annealing step on photocurrents in (A) dry and (B) humid conditions. Comparison of the first derivative of photocurrents to demonstrate the influence of O_2 versus N_2 environments in the final 800 °C annealing step on the onset for photoelectrocatalysis under (C) dry and (D) humid conditions.

Table 6.1: Flat band potential and carrier concentration values for hematite films prepared by three-step annealing.

Annealing step 1 at 210 °C for 2h	Annealing step 2	Annealing step 3 at 800 °C for 1h	flat band (V vs RHE)	$\log(\bar{N}_d)$ (cm ⁻³)
dry O ₂	humid O ₂ , 550 °C, 2h	dry O ₂	0.78	20.43
dry O ₂	humid O ₂ , 550 °C, 2h	dry N ₂	0.53	21.69
dry O ₂	dry N ₂ , 530 °C, 1h; 630 °C 1h	dry O ₂	0.72	20.84
dry O ₂	dry N ₂ , 530 °C, 1h; 630 °C 1h	dry N ₂	0.52	22.47
dry N ₂	humid O ₂ , 550 °C, 2h	dry O ₂	0.68	20.43
dry N ₂	humid O ₂ , 550 °C, 2h	dry N ₂	0.59	21.67
dry N ₂	dry N ₂ , 530 °C, 1h; 630 °C 1h	dry O ₂	0.83	20.60
dry N ₂	dry N ₂ , 530 °C, 1h; 630 °C 1h	dry N ₂	0.24	22.09
dry O ₂	dry O ₂ , 550 °C, 2h	dry O ₂	0.61	20.41
dry O ₂	dry O ₂ , 550 °C, 2h	dry N ₂	0.57	21.11
dry O ₂	humid N ₂ , 550 °C, 2h	dry O ₂	0.59	20.12
dry O ₂	humid N ₂ , 550 °C, 2h	dry N ₂		
dry N ₂	dry O ₂ , 550 °C, 2h	dry O ₂	0.74	20.22
dry N ₂	dry O ₂ , 550 °C, 2h	dry N ₂	0.46	21.47
dry N ₂	humid N ₂ , 550 °C, 2h	dry O ₂	0.89	20.32
dry N ₂	humid N ₂ , 550 °C, 2h	dry N ₂		

6.3 Conclusion

The influence of gaseous environments on the multi-step transition of γ -FeOOH to α -Fe₂O₃ was examined using *in situ* variable temperature Raman spectroscopy. The Raman spectra reveal that each of the traditionally reported reaction steps, namely γ -FeOOH to γ -Fe₂O₃ then γ -Fe₂O₃ to α -Fe₂O₃, are convoluted with an additional structural change. Comparison of variable temperature Raman results with TGA, DSC and photoelectrocatalytic OER data leads us to assign this additional process to the conversion of γ -FeOOH to protohematite (α -Fe_{1.83}O_{2.5}(OH)_{0.5}), which occurs between 200 °C and 400 °C. Protohematite is subsequently converted into hematite above 500 °C, but PEC results suggests that it cannot be quantitatively removed. The reaction environment present during initial formation of α -Fe₂O₃ is shown to influence the relative amount of protohematite formed, and fingerprints for the influence of this protohematite on structural evolution are found in the vari-

able temperature Raman spectra. The known ability to increase photocurrents for OER by annealing at high temperatures under N₂ or lower photoelectrocatalytic onset by annealing under O₂ are confirmed. These treatments do not override the effects caused by protohematite formation, however, as a persistent degradation of photoelectrocatalytic performance is superimposed on these effects. Judging from PEC performance, the formation of protohematite is best minimized through use of a dry N₂ environment for the conversion of γ -FeOOH to α -Fe₂O₃.

6.4 Experimental

6.4.1 Lepidocrocite Fabrication

Powder γ -FeOOH for variable temperature Raman microscopy studies were fabricated by oxidation of ferrous chloride tetrahydrate (ACS reagent grade, Alfa Aesar).⁷⁴ The experiment was carried out in an ice bath to maintain a temperature of 5 °C. A total of 10.00 g of FeCl₂·6H₂O was dissolved in 200 ml of milli-Q H₂O (18.2 M Ω) that was acidified with a few drops of 1 M H₂SO₄. The pH of the solution was increased to 6.5 by addition 1 M KOH, then the solution was purged with air while adding 1 M KOH to maintain the pH at 6.5. When solution pH was stabilized at 6.5, the temperature was increased to 45 °C to complete oxidation of Fe²⁺ to Fe³⁺. The suspension was then cooled to room temperature and an orange powder was collected by vacuum filtration and dried in a furnace at 105 °C.

6.4.2 Photoanode Fabrication

Lepidocrocite thin films were electrodeposited on fluorine-doped tin oxide coated aluminum borosilicate (FTO/ABS) glass (Solaronix S.A.) and subsequently annealed to convert them to hematite. Previous reports using this approach indicate film thicknesses to be 500–1000 nm.⁷⁴ FTO/ABS glass substrates were cleaned by ultrasonication using detergent solution, Milli-Q water (18.2 M Ω) and isopropanol.

Then the glasses were dried by compressed air and put in a UV- irradiation chamber (GHO18T5VH lamp, Atlantic Ultraviolet). Thin film γ -FeOOH samples were prepared by purging a solution containing 0.02 M ferrous chloride tetrahydrate (ACS reagent grade, Alfa Aesar) and 1 M ammonium chloride with N_2 for 30 min. A 0.1 M KOH (>85%, Sigma-Aldrich) solution was then added to adjust pH to 7.0. A freshly cleaned FTO/ABS electrode was then held at 0.0 V vs Ag/AgCl (sat'd KCl) for 7 min at room temperature. A series of 16 photoanodes were prepared by systematically varying a three-stage annealing protocol from such γ -FeOOH films as a starting point. The annealing process was initiated by holding each electrode at 210 °C for 2 h under either N_2 or O_2 . The environment was then changed to one of the four used in this study and the temperature increased to 550 °C and held for 2 h. The environment was then changed to either N_2 or O_2 for the final stage of annealing, where electrodes were held at 800 °C for 1 h. The thin film annealed at 350 °C, 600 °C and 800 °C and used in Raman mapping was prepared using a solution containing 0.02 M ferrous ammonium sulfate hexahydrate (ACS reagent grade, Fisher Chemicals) and 3 M ammonium chloride (ACS reagent grade, EMD Chemicals Inc.).

6.4.3 Raman Spectroscopy

Measurements were carried out on a Renishaw inVia Reflex system equipped with a temperature-controlled stage (CCR1000, Linkam Scientific) using 532 nm (Renishaw DPSSL laser, 50 mW) laser excitation. Laser power was decreased to 5% for all measurements. Variable temperature Raman microscopy measurements on γ -FeOOH powders used a linear 4 min^{-1} ramp from room temperature to 800 , with Raman spectra acquired every 2 °C (30 s). Experiments were duplicated to confirm the accuracy of the results. Measurements were repeated under four different gaseous conditions (N_2 , O_2 , $N_2 + H_2O$, $O_2 + H_2O$). The gas flow rate was maintained at 20 $\text{ml} \cdot \text{min}^{-1}$ using a mass flow controller (Masterflex Proportional Flow Controller, Cole-Parmer) and humidification was achieved by bubbling the purge gas through a room temperature H_2O reservoir before entry to the heat stage. Raman spectra were acquired and processed using Renishaw WiRE 5.2 software.

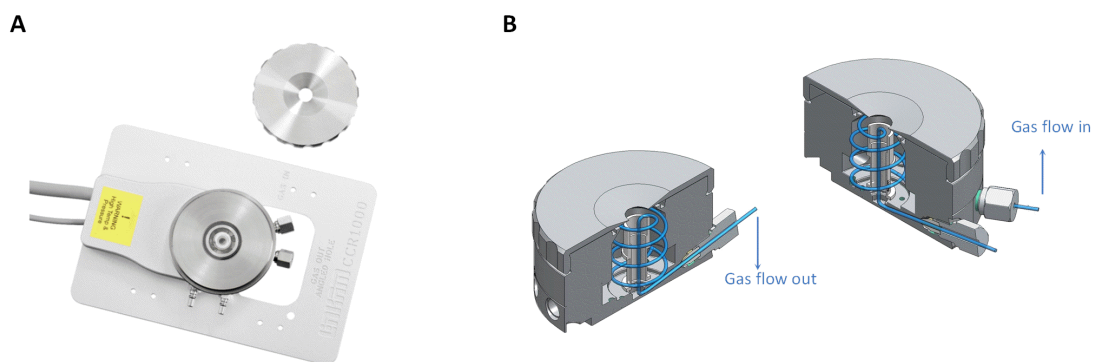


Figure 6.9: Variable temperature stage used for Raman spectroscopy.

6.4.4 Thermal Analysis

DSC and thermal gravity analysis were simultaneously performed using a NETZSCH STA 409PC Luxx. A constant argon purge was maintained during a linear heat ramp of $4\text{ }^{\circ}\text{C}\cdot\text{min}^{-1}$.

6.4.5 Photoelectrocatalysis

Photoelectrochemical measurements were carried out using a Bio-logic SP300 potentiostat and a Sciencetech A1 Lightline solar simulator equipped with an AM1.5G filter. FTO/ABS substrates coated with thin film samples were mounted in a custom-made polyethylene cell. The working electrode window contacted the 1.0 M KOH electrolyte solution and a silicone O-ring masked the active surface area to 1.54 cm^2 . Uncompensated resistance values were measured immediately prior to each electrochemical measurement. Samples prepared at $600\text{ }^{\circ}\text{C}$ and lower typically show $20\ \Omega$ resistance, while those at $800\text{ }^{\circ}\text{C}$ show $30\ \Omega$. Photoelectrocatalytic measurements utilized back-side illumination, a reversible hydrogen electrode (Gaskatel HydroFlex) served as the reference electrode, and clean FTO glass as the counter electrode. Electrochemical impedance spectroscopy was measured at 100 mV step intervals from 0.5 V to 1.5 V vs RHE with an amplitude of 10 mV.

Chapter 7

Discovering Correlations between Structure and Properties for Doped Hematite

7.1 Introduction

In previous chapters, we have studied the intrinsic defects in hematite structure through structural-property analysis and *in situ* characterization techniques. We have proved that Raman spectroscopy can be considered as a sensitive and easily accessible tool to measure and quantify the lattice distortion, especially based on the fact that iron oxides and hydroxides are good materials for Raman vibration study. To further investigate how to employ Raman spectrum in hematite structure analysis, we introduce secondary elements into the hematite crystal structure. Secondary elements can also be intentionally or inadvertently introduced into the lattice, changing the concentration of specific defects and inducing various new types of defects. This strategy has been intentionally pursued using ions such as Si^{4+} , Sn^{4+} , or fluoride to tune semiconductor properties and improve PEC performance.^{180–182} It can be challenging to track structural features in hematite with point defects or low concentration dopants. X-ray absorption spectroscopy is powerful in providing information on bond length which can be in the scale of 1 Å (**Chapter 4**). XRD

measurements would be capable of differentiating the doped hematite but fail to measure the point defects.^{183–185} Therefore, we have the confidence to push this tool and strategy to doped hematite with even larger change in latticed compared with point defect hematite.

The role of dopants in hematite semiconductors has been discussed in **Section 1.3.1**. We started with tin and fluorine dopants because those two elements from commonly used FTO glass can be potentially introduced into the upper hematite layer during high temperature annealing, especially tin diffusion.⁶⁹ Herein, we use Raman spectroscopy and XRD measurements to study the structural influence caused by tin and fluorine dopants in hematite materials. Raman spectra with doping percentages show different trends regarding peak intensity ratios for tin and fluorine respectively since they influence different vibration modes across the spectrum. Connecting with XRD refinement results, we propose that both fluorine and tin dopants will expand the crystal structure of hematite by creating distortion sites. Both will increase the corresponding distortion-related vibration mode. We also find out that a linear regression between I_{411}/I_x and I_{612}/I_x is valid for undoped and doped hematite samples. This correlation reveals that point defects, cation doping and anion doping should all occur consistently across the crystal lattice. This study shall provide a tool to quickly identify the dopant type in hematite-base materials.

7.2 Results and Discussion

7.2.1 Raman Spectra Analysis

Raman spectra of a series of doped hematite samples remain comparable for different dopant elements and different dopant concentrations. Raman spectra of hematite include four oxygen-based vibration modes at a relatively low energy range (227, 246, 293 and 299 cm^{-1}) and three iron-based vibration modes at a higher energy range (411, 499 and 612 cm^{-1}). Besides, a Raman-forbidden E_u vibration at 660 cm^{-1} is always observed in hematite material due to breaking of symmetry.^{96,106,107} Distortion usually decreases the symmetry of crystal lattice and enhances the inten-

sity of the E_u vibration mode (**Chapter 3**). Dopants are well known as one of the resources of symmetry breaking, and various dopant elements have been reported that will induce 660 cm^{-1} peak increasing.^{61,94} Fluorine and tin were used as anion and cation dopants respectively here. Among widely studied dopant elements, Sn^{4+} cations draw attention because SnO_2 is regularly used in the FTO substrate for photoanodes.^{186,187} Investigating the role of tin in iron oxide structure can not merely increase the understanding of dopants but also rule out possible influence of tin from FTO substrate caused by common annealing process. Fluorine, as an anion substituting oxygen in hematite, can also be a potential dopant source from FTO.

For both fluorine and tin doped hematite samples, Raman spectra show increased E_u peak intensity with increased dopant concentration (**Figure 7.1**). The two peaks at 293 and 299 cm^{-1} gradually become closer with higher concentrations of dopants. Comparing **Figure 7.1A** and **B**, tin dopant has a much more significant influence than fluorine. The peak at 411 cm^{-1} becomes one of the most intense peaks while the peak at 246 cm^{-1} intensity drops dramatically in **Figure 7.1B**. Fluorine substitution of oxygen atoms largely influences the vibration modes at low energy range corresponding to M-X vibrations, while tin ions replacing iron can increase the vibration intensities at higher Raman shift, which corresponds to M-M vibrations. This 411 cm^{-1} peak intensity increase can be considered as a fingerprint for tin doped hematite Raman spectra considering the general increasing trend for 660 cm^{-1} vibration for doped hematite. The 411 cm^{-1} peak corresponds to the movement of two iron ions located in two iron octahedra linked by the edge-sharing motif. We can primarily propose that the tin substitution prefers to happen at the edge-sharing sites because it is easier to break the lattice symmetry.

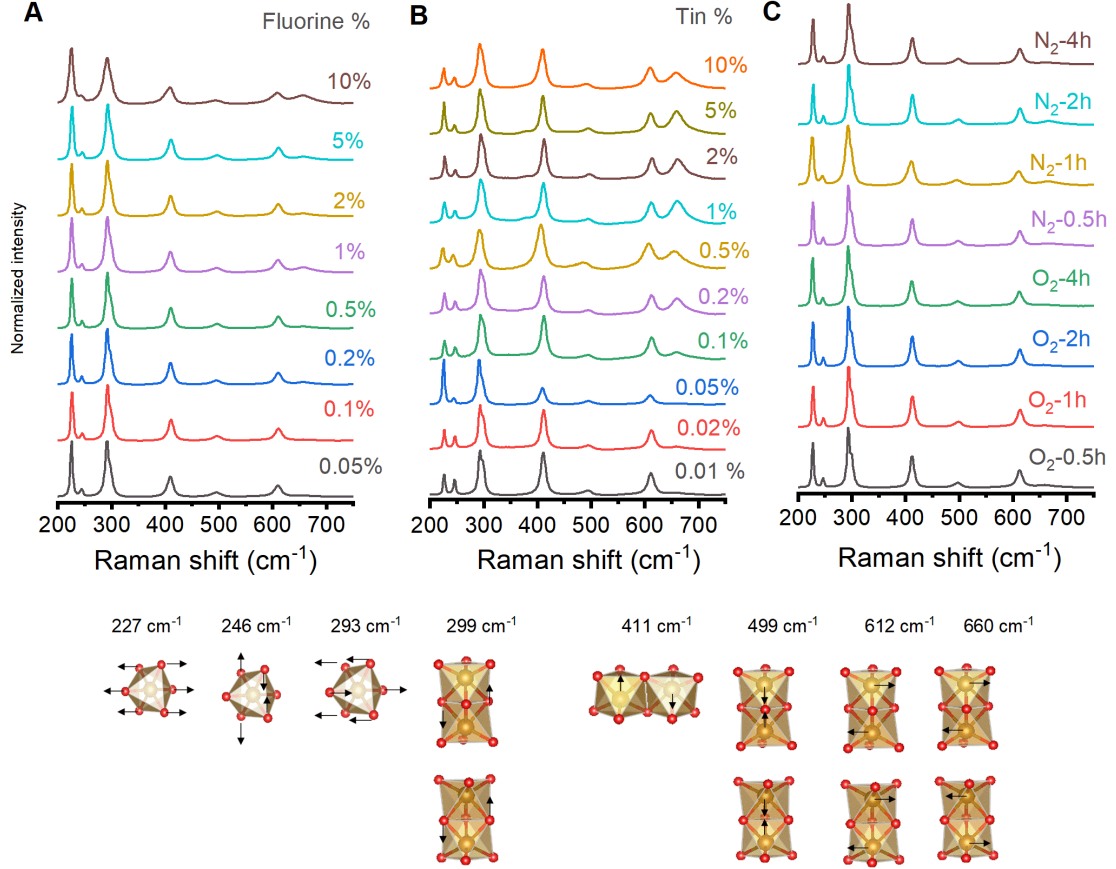


Figure 7.1: Raman spectra for a series of (A) fluorine doped hematite samples with dopant concentrations from 0.05 to 10%, (B) tin doped hematite samples with dopant concentrations from 0.01 to 10%, and (C) non doped hematite samples annealed in different environments.

Specific Raman intensity changes with doping concentration show different trends within fluorine and tin dopants as shown in **Figure 7.2** and **Figure 7.3** respectively. For fluorine doped hematite samples, Raman intensity ratios for peaks at 227 and 612 cm⁻¹ and the peak at 246 cm⁻¹ increase with fluorine doping concentration (**Figure 7.2A**), while Raman intensity ratios for peaks at 227 and 246 cm⁻¹ decrease significantly against the increased percentage of dopants. Here logarithm values of both Raman intensity ratios and doping concentrations are used due to the exponential shape trends of correlations related to 660 cm⁻¹. After conducting power model regression, the logarithm of I_y/I_{660} ($y=227$ and 246) (**Figure 7.2B**) for fluorine doped hematite and I_x/I_{660} ($x=246, 299, 411$ and 612) for tin doped hematite (**Figure 7.3A-D**) and the corresponding concentrations all show quite linear relationships. Those correlations indicate that both fluorine and tin dopants in

hematite can enlarge the Raman intensity at 660 cm^{-1} dramatically as expected.

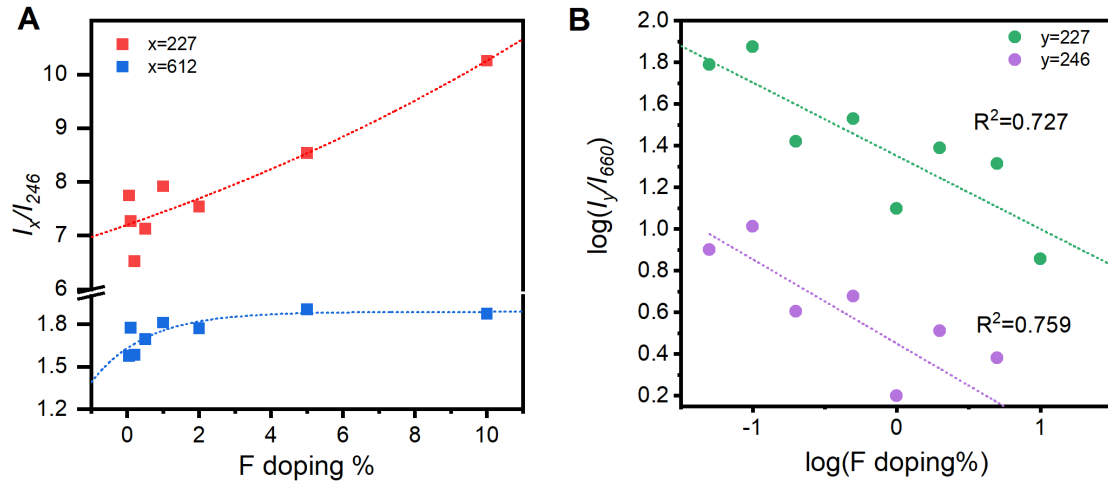


Figure 7.2: Trends in fluorine dopant concentration and Raman intensity ratios. (A) Positive correlations for two Raman intensity ratios I_{227}/I_{246} and I_{612}/I_{246} . (B) Correlations after conducting logarithm of both Raman intensity ratios of I_{227}/I_{660} and I_{246}/I_{660} and doping concentration.

Different vibration modes are involved in the analysis of two types of dopants. For fluorine doped hematite in **Figure 7.2B**, two oxygen relate vibration modes, A_{1g} and at 227 and E_g at 246 cm^{-1} are used. For tin doped hematite in **Figure 7.3**, the trend line for low intensity E_g vibration mode at 246 cm^{-1} with 660 cm^{-1} peak ratio still hold, but other three E_g vibration modes at 299, 411 and 612 cm^{-1} with that E_u peak intensity ratios show clear trends as well. All the six trends $\log(I_x/I_{660})$ versus $\log(\text{F or Sn doping \%})$ discussed here have slope values in a close range of 0.35-0.4 as listed in **Table 7.1**. As previously confirmed in **Figure 7.1**, the increasing trend of 660 cm^{-1} with increasing doping concentration is observed for both dopant types. **Figure 7.2A** indicates that 246 cm^{-1} intensity decreases with increasing fluorine concentration in hematite materials, which may be accompanied by the increase of 227 cm^{-1} and 612 cm^{-1} . The potential growth of 227 cm^{-1} peak explains why $\log(I_{227}/I_{660})$ versus $\log(\text{F doping \%})$ has the smallest absolute value of slope among all the linear correlations (0.351).

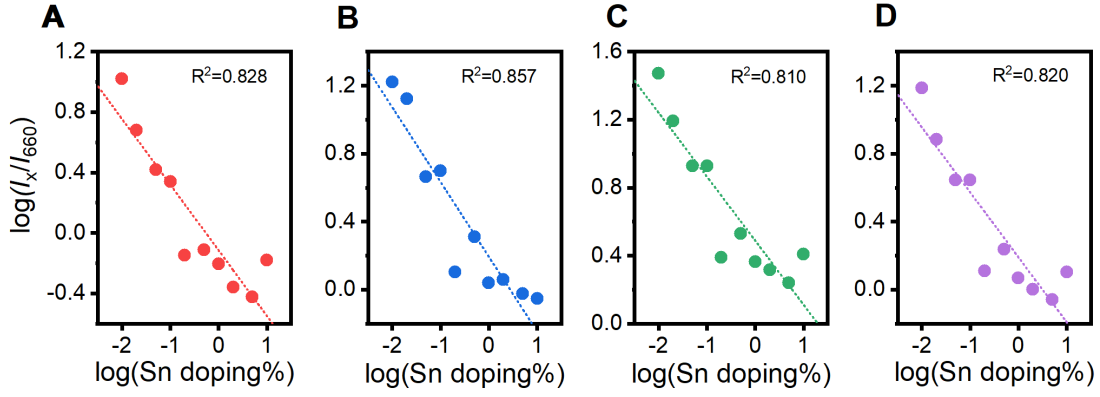


Figure 7.3: Trends in tin dopant concentration and Raman intensity ratios. (A-D) Correlations for the logarithm of Raman intensity ratios involving peaks at 246, 299, 411 and 612 cm^{-1} with peak at 660 cm^{-1} and doping concentration.

Table 7.1: Absolute values of $\log(I_x/I_{660})$ versus $\log(\text{F or Sn doping}\%)$ slope

Doping type	F	F	Sn	Sn	Sn	Sn
I_x/I_{660}	227	246	246	299	411	612
Slope	0.351	0.404	0.435	0.439	0.376	0.382

7.2.2 X-ray Diffraction Results

XRD patterns for fluorine and sin doped hematite sets show quite different features, which distinguish from Raman spectroscopic profiles for those two dopants. All the diffraction patterns of fluorine doped hematite samples match the XRD pattern of hematite without extra peak. Two small peaks at 38 and 45° belong to the XRD measurement sample holder. No obvious change regarding peak position or width within the fluorine sample series is detected. Lattice parameters a and c from XRD Rietveld refinement increase from 5.035 to 5.037 Å and 13.744 to 13.759 Å respectively. An overall expansion occurs in the hematite lattice by increasing fluorine doping with potential Fe charge reduction from Fe(III) to Fe(II). However, for tin doped hematite, XRD pattern show very different features. Extra peaks at 28 and 32° occur, which can be attributed to SnO_2 that fail to be doped in hematite samples. Even with 0.01% tin concentration the extra peaks still exist. Complete substitution of Sn^{4+} (0.83 Å) ions into crystal sites for the smaller size Fe^{3+} (0.785 Å) ions appear challenging.

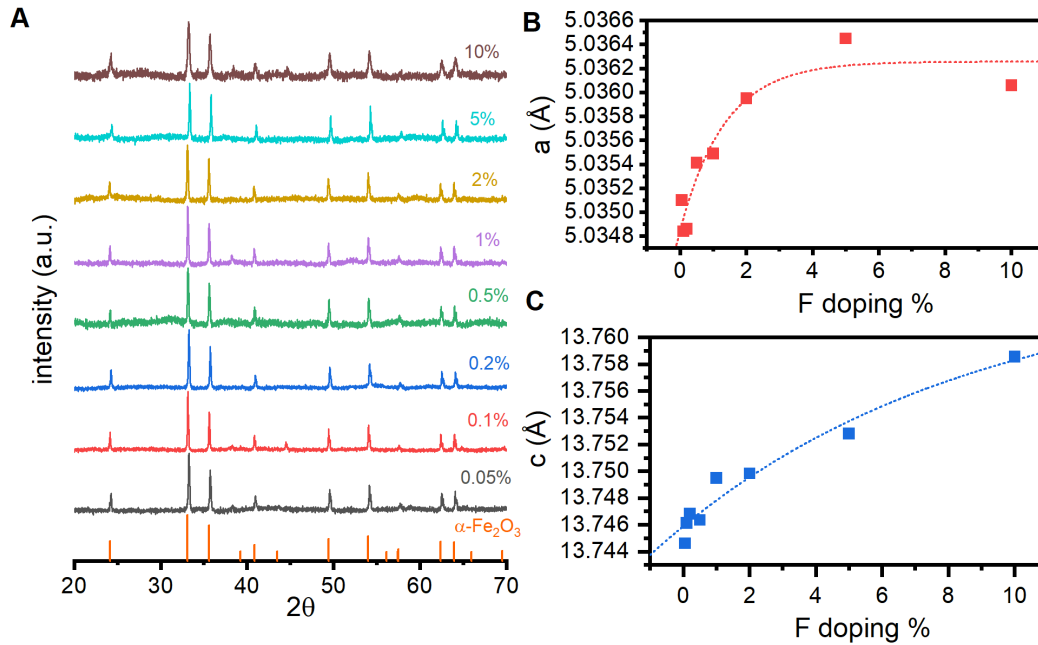


Figure 7.4: (A) X-ray diffraction patterns acquired on fluorine doped hematite powders. The vertical orange lines at the bottom represent $\alpha\text{-Fe}_2\text{O}_3$ (COD#9015231). Correlation between (B) lattice parameter a , (C) lattice parameter c and fluorine doping concentration.

For fluorine doped hematite, XRD patterns prove that fluorine dopants increase the general size of hematite lattice. Hematite shares the same crystal structure with corundum, and the crystalline c -axis is linked by columns of alternating dimers of face-sharing iron-oxygen octahedra and vacant octahedra sites. The synchronous increase in a and c values indicates that the expansion does not simply happen inside the octahedra, though F^- (1.19 Å) has a smaller ion size than O^{2-} (1.26 Å). Combining with the correlations inside Raman data, we already know that the fluorine dopants induce the breaking of lattice symmetry and therefore increase the intensity of E_u vibration at 660 cm^{-1} . Since fluorine replaces the oxygen ions, the substitution will also increase the oxygen movement vibration at 227 cm^{-1} . This interruption causes 0.0016 Å expansion in both a and c lattice parameters.

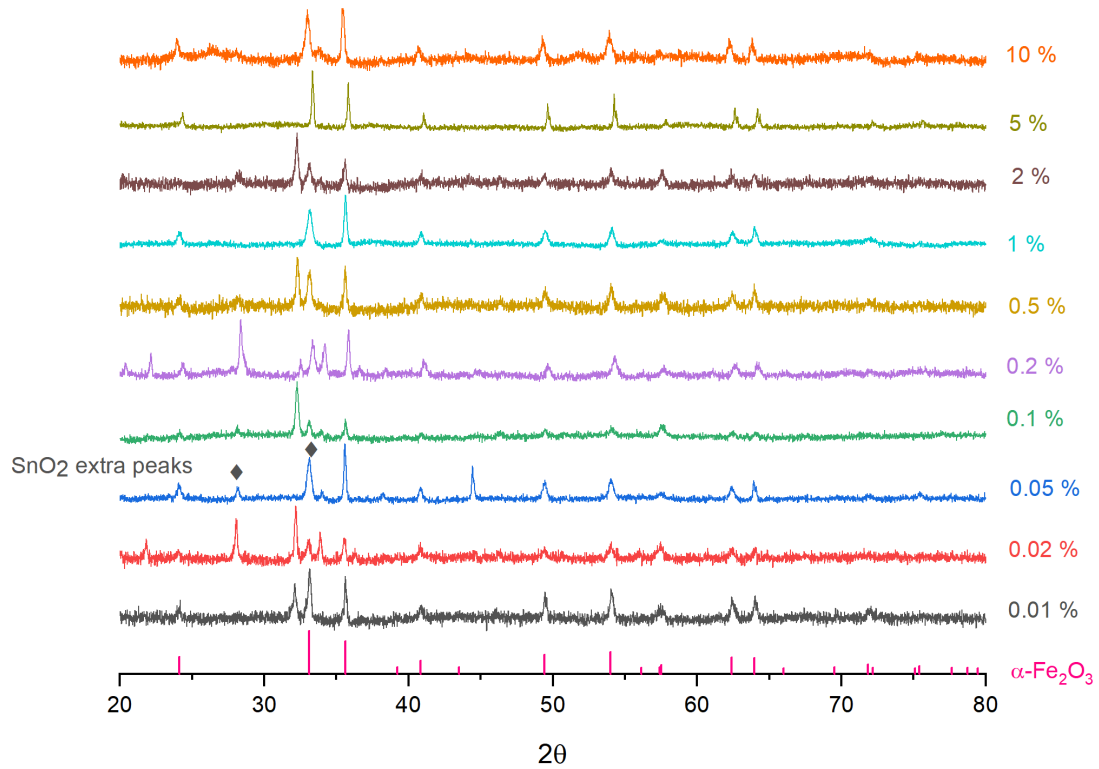


Figure 7.5: X-ray diffraction patterns acquired on tin doped hematite powders. The vertical pink lines at the bottom represent $\alpha\text{-Fe}_2\text{O}_3$ (COD#9015231).

7.2.3 Overall Correlations

The strongest correlations are the linear relationships between vibration mode at 411 cm^{-1} and 612 cm^{-1} (**Figure 7.6A-C**, **Figure 7.7A-C**). I_{411}/I_x and I_{612}/I_x ($x=227$ and 660) are used in the analysis. Strong linear regression with R^2 larger than 0.990 indicates the direct relationship between two iron-related E_g vibration modes. I_{411}/I_x and I_{612}/I_x have proportional relationships. The locations of those two vibrations also shift towards higher energy Raman shift. This correlation should be always valid for hematite-based materials because it maintains the same for various doping concentration and species changes. This regression not merely holds inside fluorine or tin doped hematite, but also is consistent across all the samples. Besides, **Figure 7.6A** and **Figure 7.6B** include two totally different vibration modes, oxygen-related vibration mode A_{1g} at 227 cm^{-1} and defect-induced vibration mode E_u at 660 cm^{-1} , which refer to very different movement in hematite crystal. As

discussed above and in previous chapters (**Chapter 3** and **Chapter 4**), E_u vibration at 660 cm^{-1} grows with iron vacancy defect and doping. This suggests that the regression stands in general hematite based material Raman spectra, not limited in defect related or dopant related hematite.

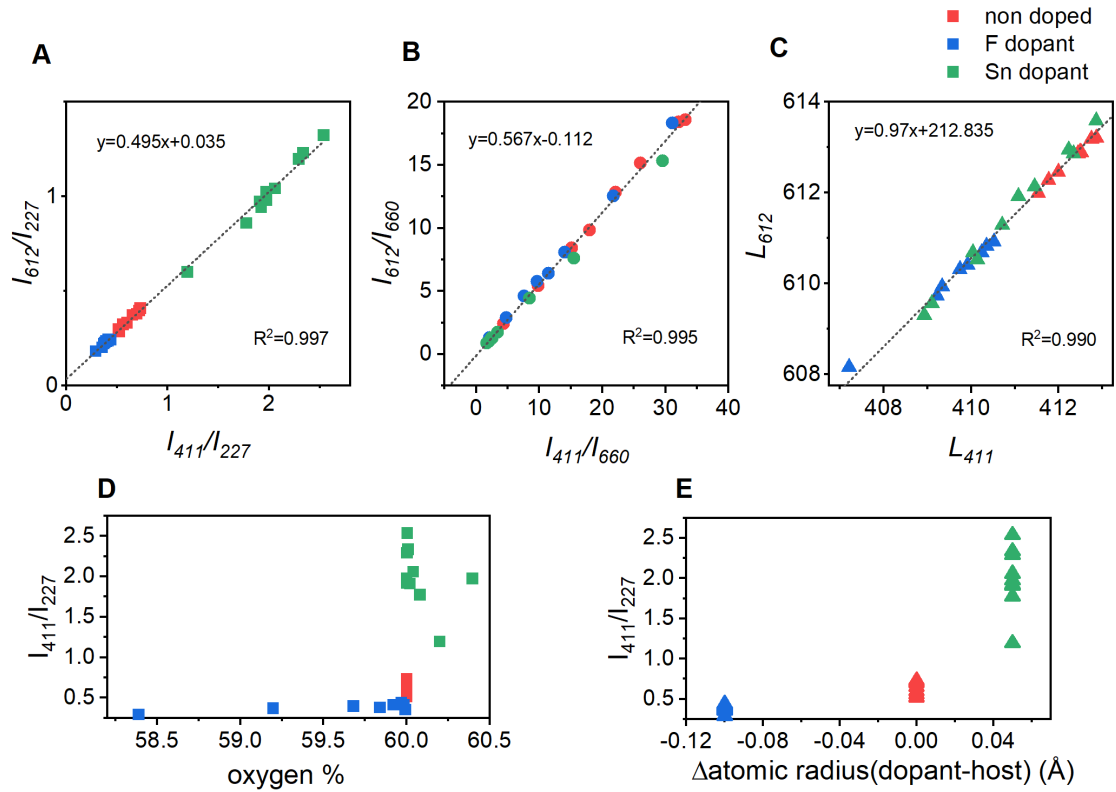


Figure 7.6: Linear correlations colored by dopant types between Raman intensity ratios (A) I_{411}/I_{227} and I_{612}/I_{227} , (B) I_{411}/I_{660} and I_{612}/I_{660} , and (C) peak location of peak 411 cm^{-1} and peak 612 cm^{-1} . I_{411}/I_{227} distributions with (D) oxygen composition percentage and (E) atomic radius different between dopant and host atoms.

K-means clustering results confirm that the difference in Raman spectrum data is able to classify doping types of hematite materials. Different colored spots in **Figure 7.6** and **Figure 7.7** refer to non-doped, fluorine doped and tin doped hematite powders. Raman peak locations, intensities and widths are used as features in K-means clustering. By defining the cluster number as three, the clusters are successfully graded (**Figure 7.7**). Comparing **Figure 7.6A-C** and **Figure 7.7**, only the 0.1% fluorine doped sample mismatches cluster 1 which should belong to cluster 2.

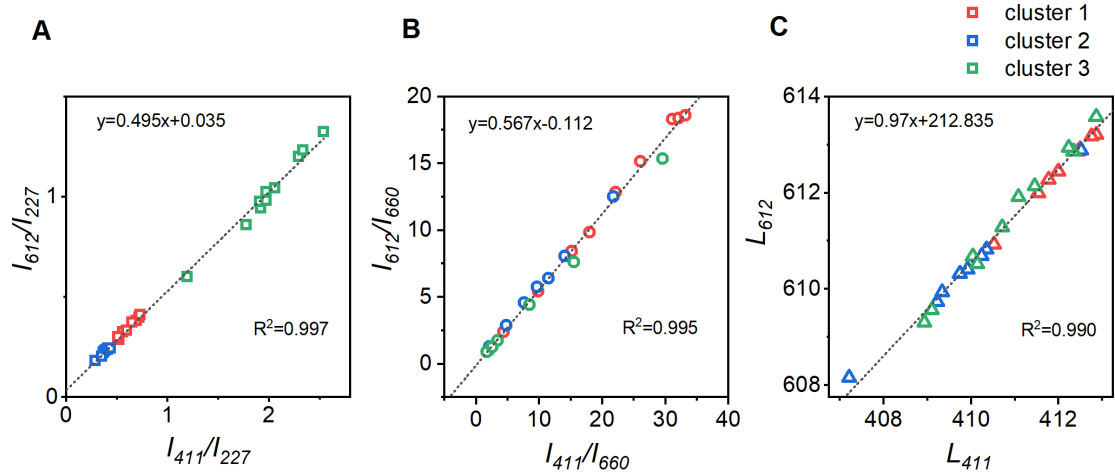


Figure 7.7: Linear correlations colored by clusters from K-means method classification. between Raman intensity ratios (A) I_{411}/I_{227} and I_{612}/I_{227} , (B) I_{411}/I_{660} and I_{612}/I_{660} , and (C) peak locations of peak 411 cm^{-1} and peak 612 cm^{-1} .

Compared with **Figure 7.6B** and **C**, **Figure 7.6A** uniquely shows clear three subgroups by the values of I_x/I_{227} across the dataset of distinguished doping types. It hints that the values of Raman intensity ratio I_x/I_{227} ($x=411$ or 612) can be related to certain chemical properties regarding dopant species, and this relationship has no influence on I_x/I_{660} and L_x values. In other words, we can consider the change of both intensity and location of 660 cm^{-1} vibration as negligible in this regression analysis. A series of intrinsic properties of samples has been studied to discover potential relationships, including electronegativity, the radius of ions, the radius difference of ions and iron/oxygen composition percentage as used in reported literature.¹⁸⁸ Oxygen content percentage (**Figure 7.6D**) shows an increasing trend with I_{411}/I_{227} , especially among fluorine doped and undoped samples. Distributions in **Figure 7.6D** and **E** are valid for I_{612}/I_{227} because of the linear regressions in **Figure 7.6A-C**. Smaller I_x/I_{227} refers to higher intensity at 227 cm^{-1} and correlates with lower oxygen content. Fluorine doping replaces oxygen and reduce oxygen composition from 60.0% to 58.4%. Tin doping substitutes iron and increase oxygen composition from 60.0% to 60.4%. The other parameter included is the atomic radius difference between the dopant atom and host atom. However, atomic radius difference shares the same value for the same doping species, which would be less convincing in the intrinsic chemical property analysis.

Table 7.2: K-means clustering results for the overall dataset, corresponding Silhouette values and Raman intensity ratios.

doping %	Cluster	Silhouette score	I_{411}/I_{227}	I_{612}/I_{227}
O ₂ -0.5	1	0.62302	0.69537	0.38044
O ₂ -1h	1	0.65383	0.73144	0.41005
O ₂ -2h	1	0.65677	0.65374	0.37359
O ₂ -4h	1	0.60383	0.5147	0.29918
N ₂ -0.5	1	0.6354	0.60003	0.33343
N ₂ -1h	1	0.5838	0.52537	0.28717
N ₂ -2h	1	0.62539	0.72106	0.39683
N ₂ -4h	1	0.64289	0.55898	0.32493
F-0.05%	2	0.60319	0.35405	0.20354
F-0.1%	1	0.51121	0.41457	0.2442
F-0.2%	2	0.6209	0.43672	0.24285
F-0.5%	2	0.58969	0.41413	0.23784
F-1%	2	0.64814	0.38015	0.22888
F-2%	2	0.63834	0.39597	0.23513
F-5%	2	0.60878	0.37158	0.22321
F-10%	2	0.59383	0.29189	0.18289
Sn-0.01%	3	0.54039	1.97456	1.02459
Sn-0.02%	3	0.56673	1.92161	0.94266
Sn-0.05%	3	0.60498	2.29211	1.19925
Sn-0.1%	3	0.55371	2.53759	1.32489
Sn-0.2%	3	0.63191	2.33614	1.23088
Sn-0.5%	3	0.56059	1.90992	0.97444
Sn-1%	3	0.61336	2.05886	1.04274
Sn-2%	3	0.56924	1.77502	0.86021
Sn-5%	3	0.58336	1.19438	0.60103
Sn-10%	3	0.57391	1.97582	0.98008

7.3 Conclusion

By fabricating a series of undoped hematite in different environment and various doping concentration of fluorine and tin hematite powders, we create a dataset with three different subgroups. Raman spectroscopic data and XRD data are used to analyze the structural change. The correlations with subgroups prove that the size of hematite unit cell increases with fluorine doping concentration by generating distortion sites. The linear regressions between Raman intensity ratios and locations

across all three subgroups suggest that point defects and dopants should have a consistent influence on hematite crystal.

7.4 Experimental

7.4.1 Hematite fabrication

Undoped hematite powders were prepared using the same method as stated in **Chapter 4**. Tin and fluorine doped hematite powders were prepared using previously reported co-precipitation methods respectively.^{77,189,190} To prepare Sn-doped hematite, milli-Q water with 0.1M iron chloride tetrahydrate (99+%, Acros) and different low concentration of tin chloride (99+%, Acros) (0.01%, 0.02%, 0.05%, 0.1%, 0.2%, 0.5%, 1%, 2%, 5% and 10%) was strongly mixed. 1M KOH (85%, Sigma-Aldrich) was gradually added to the solution to adjust pH to 13.5. The solution was heated at 130 °C for 24h. Fluorine doped hematite samples were synthesized by dissolving 0.05 M iron chloride and ammonium fluoride in the mixture of 1:1 water and ethanol solution with a series of concentrations (0.05%, 0.1%, 0.2%, 0.5%, 1%, 2%, 5% and 10%). 0.1M urea was added as a mineralizer. The solution was heated at 180 °C for 12h. Both tin and fluorine doped hematite collected powders were afterwards washed by water and ethanol and dried. The powders were heated at 800 °C to convert the doped iron hydroxides to the doped hematite phase.

7.4.2 Raman microscopy measurement

Raman spectroscopy measurements were performed on a Renishaw inVia Reflex system microscope. 633 nm (Renishaw HeNe laser, 17 mW) excitation filtered to 5% of maximum intensity in conjunction with an 1800 lines/mm grating was selected for data acquisition in the manuscript. Spectra were acquired on several different spots from the powder samples and then averaged. Renishaw WiRE 5.3 software package was used for Raman spectra analysis, including baseline subtraction, spectrum nor-

malization and spectrum curve fitting.

7.4.3 X-ray diffraction measurement

Powder X-ray diffraction measurements were carried out on a PANalytical Empyrean diffractometer with Cu K α radiation. Experiments scanned 2θ from 10° to 90° at a rate of 5 min⁻¹. Structural parameters were obtained from Rietveld refinement of XRD patterns on GASA-II software package.

Chapter 8

Conclusion and Outlook

This thesis investigates hematite photoanodes in solar water splitting reaction. We used structure-property analysis combined with Raman spectroscopy and other characterization techniques including X-ray diffraction and X-ray absorption spectrum to identify and quantify the defects in photoelectrocatalytic performance. Iron vacancy defects and oxygen vacancy defects are identified as dominant defects and can coexist in hematite structure, dependent on the fabrication environment. *In situ* variable temperature Raman spectrum and other thermal analysis are employed to study the phase transformation.

Raman spectrum shows good sensitivity in hematite characterization and defect analysis. The first part of the thesis reveals a defect related vibration mode in hematite Raman spectrum can be assigned to protohematite defect and limit the photoelectrocatalytic performance by structure-property analysis using a series of lepidocrocite films annealed in various gaseous conditions. We also propose that the onset of photoelectrocatalysis should be related to the location of defects which act as intraband recombination sites. Analysis of the nature of the key Raman vibrations, X-ray diffraction patterns, and the synthetic protocols leads us to assign the distortion to iron vacancies that are induced by the trapping of protons within the crystal lattice.

However, we still need direct structural information to capture the structural parameter changes. In the further study, we combine X-ray absorption spectroscopy

and Raman spectrum to a series of hematite samples with variable performance. Distinct relationships inside oxygen and nitrogen annealed hematite show that the primary defects are assigned as iron vacancies and oxygen vacancies. These distortions are readily observed by Raman spectroscopy, convincing us that it may be possible to calibrate the width, energy, and intensity of peaks in Raman spectra to enable direct analysis of defects in hematite photoanodes.

To further prove the usage of Raman spectrum in hematite defect analysis, we fabricate a series of photoanodes with varying quality of hematite by sintering akaganeite films instead of lepidocrocite. Data acquired through Raman microscopy and photoelectrochemical measurement is used as structural and property parameters. Correlations between the structural information contained within the Raman spectra and PEC parameters enable the identification of three types of structural defects within the material. Each defect type is found to exert unique influence on PEC behavior and each became dominant under specific fabrication conditions. This study enhance the idea of using Raman spectroscopic data in hematite defect identification.

The following study focuses on the mechanism of lepidocrocite to hematite phase transition under various gaseous environments which correspond to the conditions used in previous studies. Variable temperature Raman spectrum combined with conventional thermal analysis technique to study the phase transition reactions. A series of hematite photoanodes by three-step annealing process are prepared as well. The results further prove that protohematite balanced by iron vacancies forms in 200 to 400 °C region.

The last part of the thesis introduces secondary elements as dopants in powder form hematite. Tin and fluorine are used as cation and anion dopants respectively. Raman spectroscopic data and XRD refinement results show that both dopants can increase the size of unit cell and contribute to the defect related vibration in Raman spectrum. The correlations inside Raman spectrum data reveal that point defects and dopants should equally affect the distortion in hematite crystal.

In conclusion, this thesis provides a comprehensive understanding of the influence of defects in hematite photoanodes. We also highlight the importance and potential in applying Raman spectroscopy as a tool to identify those defects. In the extensive

research, the doping study of hematite can be continued to investigate their role in structural parameters and also photoelectrocatalysis. We also need to point out that only a limited number of fabrication protocols have been studied in this thesis. More synthesis methods including other iron hydroxide precursors can be explored.

References

- (1) Walter, M. G.; Warren, E. L.; McKone, J. R.; Boettcher, S. W.; Mi, Q.; Santori, E. A.; Lewis, N. S. *Chemical Reviews* **2010**, *110*, 6446–6473.
- (2) Jiang, C.; Moniz, S. J. A.; Wang, A.; Zhang, T.; Tang, J. *Chemical Society Reviews* **2017**, *46*, 4645–4660.
- (3) Govind Rajan, A.; Martirez, J. M. P.; Carter, E. A. *ACS Catalysis* **2020**, *10*, 11177–11234.
- (4) He, Y.; Hamann, T.; Wang, D. *Chemical Society Reviews* **2019**, *48*, 2182–2215.
- (5) Park, K.; Kim, Y. J.; Yoon, T.; David, S.; Song, Y. M. *RSC Advances* **2019**, *9*, 30112–30124.
- (6) Fujishima, A.; Honda, K. *Nature* **1972**, *238*, 37–38.
- (7) Barroso, M.; Pendlebury, S. R.; Cowan, A. J.; Durrant, J. R. *Chemical Science* **2013**, *4*, 2724–2734.
- (8) Sivula, K.; van de Krol, R. *Nature Reviews Materials* **2016**, *1*, 15010.
- (9) Zhang, Z.; Yates, J. T. *Chemical Reviews* **2012**, *112*, 5520–5551.
- (10) Klahr, B.; Gimenez, S.; Fabregat-Santiago, F.; Hamann, T.; Bisquert, J. *Journal of the American Chemical Society* **2012**, *134*, 4294–4302.
- (11) Xu, H.; Ouyang, S.; Liu, L.; Reunchan, P.; Umezawa, N.; Ye, J. *Journal of Materials Chemistry A* **2014**, *2*, 12642–12661.
- (12) An, X.; Li, T.; Wen, B.; Tang, J.; Hu, Z.; Liu, L.; Qu, J.; Huang, C. P.; Liu, H. *Advanced Energy Materials* **2016**, *6*, 1502268.
- (13) Gueymard, C. A.; Myers, D.; Emery, K. *Solar Energy* **2002**, *73*, 443–467.

- (14) Tamirat, A. G.; Rick, J.; Dubale, A. A.; Su, W. N.; Hwang, B. J. *Nanoscale Horizons* **2016**, *1*, 243–267.
- (15) Xiao, M.; Luo, B.; Wang, Z.; Wang, S.; Wang, L. *Solar RRL* **2020**, *4*, 1900509.
- (16) Thursfield A.; Kruth A.; Irvine J.T.S; Metcalfe I.S. In *Metal Oxides: Chemistry and Applications*; CRC Press: Boca Raton, 2005.
- (17) Sivula, K.; Le Formal, F.; Grätzel, M. *ChemSusChem* **2011**, *4*, 432–449.
- (18) Launay, J.C.; Horowitz, G. *Journal of Crystal Growth* **1982**, *57*, 118–124.
- (19) Zhang, J.; Eslava, S. *Sustainable Energy and Fuels* **2019**, *3*, 1351–1364.
- (20) Cherepy, N. J.; Liston, D. B.; Lovejoy, J. A.; Deng, H.; Zhang, J. Z. *The Journal of Physical Chemistry B* **1998**, *102*, 770–776.
- (21) Sivula, K. *Journal of Physical Chemistry Letters* **2013**, *4*, 1624–1633.
- (22) Pendlebury, S. R.; Wang, X.; Le Formal, F.; Cornuz, M.; Kafizas, A.; Tilley, S. D.; Grätzel, M.; Durrant, J. R. *Journal of the American Chemical Society* **2014**, *136*, 9854–9857.
- (23) Ahmed, S. M.; Leduc, J.; Haller, S. F. *The Journal of Physical Chemistry* **1988**, *92*, 6655–6660.
- (24) Zandi, O.; Hamann, T. W. *Journal of Physical Chemistry Letters* **2014**, *5*, 1522–1526.
- (25) Liu, G.; Li, N.; Zhao, Y.; Wang, M.; Yao, R.; Zhao, F.; Wu, Y.; Li, J. *ACS Sustainable Chemistry & Engineering* **2019**, *7*, 11377–11385.
- (26) Chnani, A.; Strehle, S. *ACS Applied Nano Materials* **2022**, *5*, si, 1016–1022.
- (27) Wang, Z.; Mao, X.; Chen, P.; Xiao, M.; Monny, S. A.; Wang, S.; Konarova, M.; Du, A.; Wang, L. *Angewandte Chemie International Edition* **2019**, *58*, 1030–1034.
- (28) Si, W.; Haydous, F.; Babic, U.; Pergolesi, D.; Lippert, T. *ACS Applied Energy Materials* **2019**, *2*, 5438–5445.
- (29) Zhang, X.; Wang, X.; Yi, X.; Ye, J.; Wang, D. *ACS Sustainable Chemistry & Engineering* **2019**, *7*, 5420–5429.

- (30) Zhao, X.; Feng, J.; Chen, S.; Huang, Y.; Sum, T. C.; Chen, Z. *Physical Chemistry Chemical Physics* **2017**, *19*, 1074–1082.
- (31) Ling, Y.; Wang, G.; Reddy, J.; Wang, C.; Zhang, J. Z.; Li, Y. *Angewandte Chemie* **2012**, *124*, 4150–4155.
- (32) Bedin, K. C.; Muche, D. N. F.; Melo Jr., M. A.; Freitas, A. L. M.; Gonçalves, R. V.; Souza, F. L. *ChemCatChem* **2020**, *12*, 3156–3169.
- (33) Wang, T.; Hung, H.-T.; Cheng, Y.-R.; Huang, M.-C.; Hsieh, Y.-K.; Wang, C.-F. *RSC Advances* **2016**, *6*, Publisher: The Royal Society of Chemistry, 28236–28247.
- (34) Pyeon, M.; Ruoko, T.-P.; Leduc, J.; Gönüllü, Y.; Deo, M.; Tkachenko, N. V.; Mathur, S. *Journal of Materials Research* **2018**, *33*, 455–466.
- (35) Geerthana, M.; Ramachandran, K.; Maadeswaran, P.; Navaneethan, M.; Harish, S.; Ramesh, R. *ECS Journal of Solid State Science and Technology* **2021**, *10*, 061007.
- (36) Liu, P.-F.; Wang, C.; Wang, Y.; Li, Y.; Zhang, B.; Zheng, L.-R.; Jiang, Z.; Zhao, H.; Yang, H.-G. *Science Bulletin* **2021**, *66*, 1013–1021.
- (37) Wang, L.; Zhu, J.; Liu, X. *ACS Applied Materials & Interfaces* **2019**, *11*, 22272–22277.
- (38) Lei, B.; Xu, D.; Wei, B.; Xie, T.; Xiao, C.; Jin, W.; Xu, L. *ACS Applied Materials & Interfaces* **2021**, *13*, 4785–4795.
- (39) Chnani, A.; Kurniawan, M.; Bund, A.; Strehle, S. *ACS Applied Nano Materials* **2022**, *5*, 2897–2905.
- (40) Hill, A. H.; Jiao, F.; Bruce, P. G.; Harrison, A.; Kockelmann, W.; Ritter, C. *Chemistry of Materials* **2008**, *20*, 4891–4899.
- (41) Gualtieri, A. F.; Venturelli, P. *American Mineralogist* **1999**, *84*, 895–904.
- (42) Wolska, E.; Schwertmann, U. *Crystalline Materials* **1989**, *189*, 223–237.
- (43) Liu, Y.; Smith, R. D. L. *Chemical Science* **2020**, *11*, 1085–1096.
- (44) Yariv, S.; Mendelovici, E.; Villalba, R. *Journal of the Chemical Society, Faraday Transactions 1: Physical Chemistry in Condensed Phases* **1980**, *76*, 1442–1454.

- (45) Gendler, T. S.; Shcherbakov, V. P.; Dekkers, M. J.; Gapeev, A. K.; Gribov, S. K.; McClelland, E. *Geophysical Journal International* **2005**, *160*, 815–832.
- (46) Petkov, M. P.; Jones, S. M.; Tsapin, A.; Anderson, M. S. *The Journal of Supercritical Fluids* **2015**, *106*, 100–104.
- (47) Ishikawa, T.; Inouye, K. *Bulletin of the Chemical Society of Japan* **1975**, *48*, 1580–1584.
- (48) Cornell, R.; Schwertmann, U. *The Iron Oxides: Structure, Properties, Reactions, Occurrences and Uses*; Wiley-VCH Verlag: Darmstadt, Germany, 2003.
- (49) Murad, E.; Schwertmann, U. *Hyperfine Interactions* **1988**, *41*, 835–838.
- (50) Shousha, S.; Khalil, S.; Youssef, M. *Physical Chemistry Chemical Physics* **2021**, *23*, 25518–25532.
- (51) Hu, Y.; Boudoire, F.; Hermann-Geppert, I.; Bogdanoff, P.; Tsekouras, G.; Mun, B. S.; Fortunato, G.; Graetzel, M.; Braun, A. *Journal of Physical Chemistry C* **2016**, *120*, 3250–3258.
- (52) Kim, C.-Y. *Nano-Structures & Nano-Objects* **2020**, *23*, 100497.
- (53) Warschkow, O.; Ellis, D. E.; Hwang, J.; Mansourian-Hadavi, N.; Mason, T. O. *Journal of the American Ceramic Society* **2002**, *85*, 213–220.
- (54) Da Silva Alvim, R.; Ribeiro, F. N.; Dalpian, G. M. *Physical Chemistry Chemical Physics* **2020**, *22*, 25380–25389.
- (55) Negreiros, F. R.; Pedroza, L. S.; Souza, F. L.; Dalpian, G. M. *Physical Chemistry Chemical Physics* **2017**, *19*, 31410–31417.
- (56) Soares, M. R. S.; Gonçalves, R. H.; Nogueira, I. C.; Bettini, J.; Chiquito, A. J.; Leite, E. R. *Physical Chemistry Chemical Physics* **2016**, *18*, 21780–21788.
- (57) McBriarty, M. E.; Kerisit, S.; Bylaska, E. J.; Shaw, S.; Morris, K.; Ilton, E. S. *Environmental Science & Technology* **2018**, *52*, 6282–6290.
- (58) Anenburg, M.; Wykes, J. L.; Troitzsch, U.; Losq, C. L.; Chen, J. *Materials Advances* **2021**, *2*, 5195–5202.
- (59) Cesar, I.; Sivula, K.; Kay, A.; Zboril, R.; Grätzel, M. *The Journal of Physical Chemistry C* **2009**, *113*, 772–782.

- (60) Zandi, O.; Hamann, T. W. *Physical Chemistry Chemical Physics* **2015**, *17*, 22485–22503.
- (61) Jang, J.-W.; Du, C.; Ye, Y.; Lin, Y.; Yao, X.; Thorne, J.; Liu, E.; McMahon, G.; Zhu, J.; Javey, A.; Guo, J.; Wang, D. *Nature Communications* **2015**, *6*, 7447.
- (62) Zhou, Z.; Liu, J.; Long, R.; Li, L.; Guo, L.; Prezhdo, O. V. *Journal of the American Chemical Society* **2017**, *139*, 6707–6717.
- (63) Barroso, M.; Mesa, C. A.; Pendlebury, S. R.; Cowan, A. J.; Hisatomi, T.; Sivula, K. *Proceedings of the National Academy of Sciences* **2012**, *109*, 15640–15645.
- (64) Klahr, B.; Gimenez, S.; Fabregat-Santiago, F.; Bisquert, J.; W. Hamann, T. *Energy & Environmental Science* **2012**, *5*, 7626–7636.
- (65) Alsaç, E. P.; Bodappa, N.; Whittingham, A. W. H.; Liu, Y.; de Lazzari, A.; Smith, R. D. L. *Chemical Physics Reviews* **2021**, *2*, 031306.
- (66) Trasatti, S. *Journal of Electroanalytical Chemistry and Interfacial Electrochemistry* **1972**, *39*, 163–184.
- (67) Forster, M.; Potter, R. J.; Ling, Y.; Yang, Y.; Klug, D. R.; Li, Y.; Cowan, A. J. *Chemical Science* **2015**, *6*, 4009–4016.
- (68) Gurudayal; John, R. A.; Boix, P. P.; Yi, C.; Shi, C.; Scott, M. C.; Veldhuis, S. A.; Minor, A. M.; Zakeeruddin, S. M.; Wong, L. H.; Grätzel, M.; Mathews, N. *ChemSusChem* **2017**, *10*, 2449–2456.
- (69) Ling, Y.; Wang, G.; Wheeler, D. A.; Zhang, J. Z.; Li, Y. *Nano Letters* **2011**, *11*, 2119–2125.
- (70) Wang, S.; Liu, G.; Wang, L. *Chemical Reviews* **2019**, *119*, 5192–5247.
- (71) Martinez, L.; Leinen, D.; Martín, F.; Gabas, M.; Ramos-Barrado, J. R.; Quagliata, E.; Dalchiale, E. A. *Journal of The Electrochemical Society* **2007**, *154*, D126.
- (72) Kang, D.; Kim, T. W.; Kubota, S. R.; Cardiel, A. C.; Cha, H. G.; Choi, K. S. *Chemical Reviews* **2015**, *115*, 12839–12887.

- (73) Spray, R. L.; McDonald, K. J.; Choi, K. S. *Journal of Physical Chemistry C* **2011**, *115*, 3497–3506.
- (74) Chopra, G. S.; Real, C.; Alcalá, M. D.; Pérez-Maqueda, L. A.; Subrt, J.; Criado, J. M. *Chemistry of Materials* **1999**, *11*, 1128–1137.
- (75) Khalil, M.; Yu, J.; Liu, N.; Lee, R. L. *Journal of Nanoparticle Research* **2014**, *16*, 2362.
- (76) Tadic, M.; Trpkov, D.; Kopanja, L.; Vojnovic, S.; Panjan, M. *Journal of Alloys and Compounds* **2019**, *792*, 599–609.
- (77) Wang, C.; Zhang, Y.; Li, Y.; Liu, J.; Wu, Q.-H.; Jiang, J.; Li, Y. Y.; Lu, J. *Nanotechnology* **2017**, *28*, 065401.
- (78) Urban, M. W.; Cornilsen, B. C. In *Advances in Materials Characterization II. Materials Science Research*; Springer, Boston, MA; Vol. 19.
- (79) Aryeetey, F.; Ignatova, T.; Aravamudhan, S. *RSC Advances* **2020**, *10*, 22996–23001.
- (80) West, A. R., *Solid State Chemistry and its Applications*; Aptara Inc.: New Delhi, India, 1985.
- (81) Makuła, P.; Pacia, M.; Macyk, W. *The Journal of Physical Chemistry Letters* **2018**, *9*, 6814–6817.
- (82) Newville, M. *Reviews in Mineralogy and Geochemistry* **2014**, *78*, 33–74.
- (83) Smith, R. D. L.; Pasquini, C.; Loos, S.; Chernev, P.; Klingan, K.; Kubella, P.; Mohammadi, M. R.; Gonzalez-Flores, D.; Dau, H. *Nature Communications* **2017**, *8*, 2022.
- (84) Berry, A. J.; O'Neill, H. S.; Jayasuriya, K. D.; Campbell, S. J.; Foran, G. J. *American Mineralogist* **2003**, *88*, 967–977.
- (85) Smith, R. D. L.; Pasquini, C.; Loos, S.; Chernev, P.; Klingan, K.; Kubella, P.; Mohammadi, M. R.; González-Flores, D.; Dau, H. *Energy & Environmental Science* **2018**, *11*, 2476–2485.
- (86) Piccinin, S. *Physical Chemistry Chemical Physics* **2019**, *21*, 2957–2967.
- (87) Dghoughi, L.; Elidrissi, B.; Bernede, C.; Addou, M.; Lamrani, M. A.; Re-gragui, M.; Erguig, H. *Applied Surface Science* **2006**, *253*, 1823–1829.

- (88) Huda, M. N.; Walsh, A.; Yan, Y.; Wei, S. H.; Al-Jassim, M. M. *Journal of Applied Physics* **2010**, *107*, 123712.
- (89) Van de Krol, R.; Liang, Y.; Schoonman, J. *Journal of Materials Chemistry* **2008**, *18*, 2311–2320.
- (90) Le Formal, F.; Sivula, K.; Grätzel, M. *Journal of Physical Chemistry C* **2012**, *116*, 26707–26720.
- (91) Huang, Z.; Lin, Y.; Xiang, X.; Rodríguez-Córdoba, W.; McDonald, K. J.; Hagen, K. S.; Choi, K. S.; Brunschwig, B. S.; Musaev, D. G.; Hill, C. L.; Wang, D.; Lian, T. *Energy and Environmental Science* **2012**, *5*, 8923–8926.
- (92) Sivula, K.; Zboril, R.; Le Formal, F.; Robert, R.; Weidenkaff, A.; Tucek, J.; Frydrych, J.; Grätzel, M. *Journal of the American Chemical Society* **2010**, *132*, 7436–7444.
- (93) De Faria, D. L. A.; Venâncio Silva, S.; de Oliveira, M. T. *Journal of Raman Spectroscopy* **1997**, *28*, 873–878.
- (94) Jubb, A. M.; Allen, H. C. *ACS Applied Materials & Interfaces* **2010**, *2*, 2804–2812.
- (95) Chamritski, I.; Burns, G. *Journal of Physical Chemistry B* **2005**, *109*, 4965–4968.
- (96) Chernyshova, I. V.; Jr, M. F. H.; Madden, A. S. *Physical Chemistry Chemical Physics* **2007**, *9*, 1736–1750.
- (97) Shim, S. H.; Duffy, T. S. *American Mineralogist* **2002**, *87*, 318–326.
- (98) Zandi, O.; Schon, A. R.; Hajibabaei, H.; Hamann, T. W. *Chemistry of Materials* **2016**, *28*, 765–771.
- (99) Kay, A.; Cesar, I.; Grätzel, M. *Journal of the American Chemical Society* **2006**, *128*, 15714–15721.
- (100) Guo, X.; Wang, L.; Tan, Y. *Nano Energy* **2015**, *16*, 320–328.
- (101) Formal, F. L.; Grätzel, M.; Sivula, K. *Advanced Functional Materials* **2010**, *20*, 1099–1107.
- (102) Zandi, O.; Beardslee, J. A.; Hamann, T. *Journal of Physical Chemistry C* **2014**, *118*, 16494–16503.

- (103) Moir, J.; Soheilnia, N.; Liao, K.; O'Brien, P.; Tian, Y.; Burch, K. S.; Ozin, G. A. *ChemSusChem* **2015**, *8*, 1557–1567.
- (104) Braun, A.; Sivula, K.; Bora, D. K.; Zhu, J.; Zhang, L.; Grätzel, M.; Guo, J.; Constable, E. C. *Journal of Physical Chemistry C* **2012**, *116*, 16870–16875.
- (105) Grosvenor, A. P.; Kobe, B. A.; Biesinger, M. C.; McIntyre, N. S. *Surface and Interface Analysis* **2004**, *36*, 1564–1574.
- (106) Bersani, D.; Lottici, P. P.; Montenero, A. *Journal of Raman Spectroscopy* **1999**, *30*, 335–360.
- (107) Xu, Y. Y.; Zhao, D.; Zhang, X. J.; Jin, W. T.; Kashkarov, P.; Zhang, H. *Physica E* **2009**, *41*, 806–811.
- (108) Zhu, X.; Guijarro, N.; Liu, Y.; Schouwink, P.; Wells, R. A.; Le Formal, F.; Sun, S.; Gao, C.; Sivula, K. *Advanced Materials* **2018**, *30*, 1801612.
- (109) Burgina, E. B.; Kustova, G. N.; Isupova, L. A.; Tsybulya, S. V.; Kryukova, G. N.; Sadykov, V. A. *Journal of Molecular Catalysis A: Chemical* **2000**, *158*, 257–261.
- (110) Du, C.; Yang, X.; Mayer, M. T.; Hoyt, H.; Xie, J.; McMahon, G.; Bischofing, G.; Wang, D. *Angewandte Chemie International Edition* **2013**, *52*, 12692–12695.
- (111) Grave, D. A.; Yatom, N.; Ellis, D. S.; Toroker, M. C.; Rothschild, A. *Advanced Materials* **2018**, *30*, 1706577.
- (112) Zandi, O.; Hamann, T. W. *Nature Chemistry* **2016**, *8*, 778–783.
- (113) Kim, J. Y.; Magesh, G.; Youn, D. H.; Jang, J. W.; Kubota, J.; Domen, K.; Lee, J. S. *Scientific Reports* **2013**, *3*, 2681.
- (114) Šutka, A.; Lagzdina, S.; Käämbre, T.; Pärna, R.; Kisand, V.; Kleperis, J.; Maiorov, M.; Kikas, A.; Kuusik, I.; Jakovlevs, D. *Materials Chemistry and Physics* **2015**, *149-150*, 473–479.
- (115) Kraushofer, F.; Jakub, Z.; Bichler, M.; Hulva, J.; Drmota, P.; Weinold, M.; Schmid, M.; Setvin, M.; Diebold, U.; Blaha, P.; Parkinson, G. S. *The Journal of Physical Chemistry C* **2018**, *122*, 1657–1669.

- (116) Liu, Y.; Smith, R. D. L. *ACS Applied Materials & Interfaces* **2022**, *14*, 6615–6624.
- (117) Spray, R. L.; Choi, K. S. *Chemistry of Materials* **2009**, *21*, 3701–3709.
- (118) Gehring, A. U.; Hofmeister, A. M. *Clays and Clay Minerals* **1994**, *42*, 409–415.
- (119) Glotch, T. D.; Kraft, M. D. *Physics and Chemistry of Minerals* **2008**, *35*, 569–581.
- (120) Lin, C.; Chiang, M.; Chen, Y. *Thin Solid Films* **2009**, *518*, 1241–1244.
- (121) Yang, J. K.; Liang, B.; Zhao, M. J.; Gao, Y.; Zhang, F. C.; Zhao, H. L. *Scientific Reports* **2015**, *5*, 15001.
- (122) Darab, J. G.; Amonette, A. B.; Burke, D. S.; Orr, R. D.; Ponder, S. M.; Schrick, B.; Mallouk, T. E.; Lukens, W. W.; Caulder, D. L.; Shuh, D. K. *Chemistry of Materials* **2007**, *19*, 5703–5713.
- (123) Canepa, P.; Schofield, E.; Chadwick, A. V.; Alfredsson, M. *Physical Chemistry Chemical Physics* **2011**, *13*, 12826–12834.
- (124) Calvin, S., *XAFS for Everyone*; CRC Press: Boca Raton, 2013.
- (125) Dau, H.; Liebisch, P.; Haumann, M. *Analytical and Bioanalytical Chemistry* **2003**, *376*, 562–583.
- (126) Momma, K.; Izumi, F. *Journal of Applied Crystallography* **2008**, *41*, 653–658.
- (127) Mohanty, B.; Wei, Y.; Ghorbani-Asl, M.; Krashennnikov, A. V.; Rajput, P.; Jena, B. K. *Journal of Materials Chemistry A* **2020**, *8*, 6709–6716.
- (128) Mohamad Noh, M. F.; Ullah, H.; Arzaee, N. A.; Ab Halim, A.; Abdul Rahim, M. A. F.; Mohamed, N. A.; Safaei, J.; Mohd Nasir, S. N. F.; Wang, G.; Mat Teridi, M. A. *Dalton Transactions* **2020**, *49*, 12037–12048.
- (129) Shannon, R. *Acta Crystallographica Section A* **1993**, *10*, 751–767.
- (130) Iishi, K. *Physics and Chemistry of Minerals* **1978**, *3*, 1–10.
- (131) Pezzotti, G.; Zhu, W. *Physical Chemistry Chemical Physics* **2015**, *17*, 2608–2627.

- (132) Liu, Y.; Zhang, J.; Nataraju, B.; Smith, R. *Journal of Physics: Energy* **2021**, *3*, 044002.
- (133) Ankudinov, A. L.; Ravel, B.; Rehr, J. J.; Conradson, S. D. *Physical Review B* **1998**, *58*, 7565–7576.
- (134) Risch, M.; Klingan, K.; Heidkamp, J.; Ehrenberg, D.; Chernev, P.; Zaharieva, I.; Dau, H. *Chemical Communications* **2011**, *47*, 11912–11914.
- (135) Sato, H.; Shimoyama, M.; Kamiya, T.; Amari, T.; Šašić, S.; Ninomiya, T.; Siesler, H. W.; Ozaki, Y. *Journal of Applied Polymer Science* **2002**, *86*, 443–448.
- (136) Calvo, N. L.; Arias, J. M.; Altabef, A. B.; Maggio, R. M.; Kaufman, T. S. *Journal of Pharmaceutical and Biomedical Analysis* **2016**, *129*, 190–197.
- (137) *Advances in Materials Characterization II*; Snyder, R. L., Condrate, R. A., Johnson, P. F., Eds.; Springer US: Boston, MA, 1985.
- (138) Maldonado, A. G.; Rothenberg, G. *Chemical Society Reviews* **2010**, *39*, 1891.
- (139) Liu, K.; Lei, Y.; Wang, G. *The Journal of Chemical Physics* **2013**, *139*, 204306.
- (140) Rémazeilles, C.; Refait, P. *Corrosion Science* **2007**, *49*, 844–857.
- (141) Réguer, S.; Neff, D.; Bellot-Gurlet, L.; Dillmann, P. *Journal of Raman Spectroscopy* **2007**, *38*, 389–397.
- (142) Lee, J.; Han, S. *Physical Chemistry Chemical Physics* **2013**, *15*, 18906.
- (143) Zhang, S.; Fan, Q.; Xia, R.; Meyer, T. J. *Accounts of Chemical Research* **2020**, *53*, 255–264.
- (144) Heck, K. N.; Garcia-Segura, S.; Westerhoff, P.; Wong, M. S. *Accounts of Chemical Research* **2019**, *52*, 906–915.
- (145) Garedew, M.; Lin, F.; Song, B.; DeWinter, T. M.; Jackson, J. E.; Saffron, C. M.; Lam, C. H.; Anastas, P. T. *ChemSusChem* **2020**, *13*, 4214–4237.
- (146) Manßen, M.; Schafer, L. L. *Chemical Society Reviews* **2020**, *49*, 6947–6994.
- (147) Kondratenko, E. V.; Mul, G.; Baltrusaitis, J.; Larrazábal, G. O.; Pérez-Ramírez, J. *Energy and Environmental Science* **2013**, *6*, 3112–3135.

- (148) Chen, H.; Liang, X.; Liu, Y.; Ai, X.; Asefa, T.; Zou, X. *Advanced Materials* **2020**, *32*, 2002435.
- (149) Wang, Y. et al. *Chemical Reviews* **2020**, *120*, 12217–12314.
- (150) Zhu, Y.; Zhu, R.; Xi, Y.; Zhu, J.; Zhu, G.; He, H. *Applied Catalysis B: Environmental* **2019**, *255*, 117739.
- (151) Ashraf, M.; Khan, I.; Usman, M.; Khan, A.; Shah, S. S.; Khan, A. Z.; Saeed, K.; Yaseen, M.; Ehsan, M. F.; Tahir, M. N.; Ullah, N. *Chemical Research in Toxicology* **2020**, *33*, 1292–1311.
- (152) Xue, Y.; Wang, Y. *Nanoscale* **2020**, *12*, 10912–10932.
- (153) Song, J.; Wei, C.; Huang, Z. F.; Liu, C.; Zeng, L.; Wang, X.; Xu, Z. J. *Chemical Society Reviews* **2020**, *49*, 2196–2214.
- (154) Li, C.; Luo, Z.; Wang, T.; Gong, J. *Advanced Materials* **2018**, *30*, 1707502.
- (155) Shen, S.; Lindley, S. A.; Chen, X.; Zhang, J. Z. *Energy & Environmental Science* **2016**, *9*, 2744–2775.
- (156) Stanjek, H. *Zeitschrift für Pflanzenernährung und Bodenkunde* **1987**, *150*, 314–318.
- (157) Morris, R. V.; Golden, D. C.; Shelfer, T. D.; Lauer, H. V. *Meteoritics and Planetary Science* **1998**, *33*, 743–751.
- (158) Darezereshki, E. *Materials Letters* **2011**, *65*, 642–645.
- (159) Gonçalves, R. H.; Leite, E. R. *Energy and Environmental Science* **2014**, *7*, 2250–2254.
- (160) Singh, N. J.; Wareppam, B.; Ghosh, S.; Sahu, B. P.; Ajikumar, P. K.; Singh, H. P.; Chakraborty, S.; Pati, S. S.; Oliveira, A. C.; Barg, S.; Garg, V. K.; Singh, L. H. *Nanotechnology* **2020**, *31*, 425703.
- (161) Paracchino, A.; Laporte, V.; Sivula, K.; Grätzel, M.; Thimsen, E. *Nature Materials* **2011**, *10*, 456–461.
- (162) Scherrer, B.; Li, T.; Tsyganok, A.; Döbeli, M.; Gupta, B.; Malviya, K. D.; Kasian, O.; Maman, N.; Gault, B.; Grave, D. A.; Mehlman, A.; Visoly-Fisher, I.; Raabe, D.; Rothschild, A. *Chemistry of Materials* **2020**, *32*, 1031–1040.

- (163) Zhang, X.; Li, H.; Wang, S.; Fan, F. R. F.; Bard, A. J. *Journal of Physical Chemistry C* **2014**, *118*, 16842–16850.
- (164) Malviya, K. D.; Klotz, D.; Dotan, H.; Shlenkevich, D.; Tsyganok, A.; Mor, H.; Rothschild, A. *Journal of Physical Chemistry C* **2017**, *121*, 4206–4213.
- (165) Zhu, H.; Zhao, M.; Zhou, J.; Li, W.; Wang, H.; Xu, Z.; Lu, L.; Pei, L.; Shi, Z.; Yan, S.; Li, Z.; Zou, Z. *Applied Catalysis B: Environmental* **2018**, *234*, 100–108.
- (166) Govindaraju, G. V.; Wheeler, G. P.; Lee, D.; Choi, K.-s. *Chemistry of Materials* **2017**, *29*, 355–370.
- (167) De Bakker, P. M.; De Grave, E.; Vandenberghe, R. E.; Bowen, L. H.; Pollard, R. J.; Persoons, R. M. *Physics and Chemistry of Minerals* **1991**, *18*, 131–143.
- (168) Cudennec, Y.; Lecerf, A. *Solid State Sciences* **2005**, *7*, 520–529.
- (169) Song, X.; Boily, J. F. *Journal of Physical Chemistry A* **2016**, *120*, 6249–6257.
- (170) Dinesen, A. R.; Pedersen, C. T.; Bender Koch, C. *Journal of Thermal Analysis and Calorimetry* **2001**, *64*, 1303–1310.
- (171) Chen, Y. H. *Journal of Alloys and Compounds* **2013**, *553*, 194–198.
- (172) El Mendili, Y.; Bardeau, J. F.; Randrianantoandro, N.; Gourbil, A.; Greneche, J. M.; Mercier, A. M.; Grasset, F. *Journal of Raman Spectroscopy* **2011**, *42*, 239–242.
- (173) Sklute, E. C.; Kashyap, S.; Dyar, M. D.; Holden, J. F.; Tague, T.; Wang, P.; Jaret, S. J. *Physics and Chemistry of Minerals* **2018**, *45*, 1–26.
- (174) Fan, J.; Zhao, Z.; Ding, Z.; Liu, J. *RSC Advances* **2018**, *8*, 7269–7279.
- (175) Morris, R. V.; Lauer, H. V. *Journal of Geophysical Research* **1981**, *86*, 10893–10899.
- (176) Kustova, G. N.; Burgina, E. B.; Sadykov, V. A.; Poryvaev, S. G. *Physics and Chemistry of Minerals* **1992**, *18*, 379–382.
- (177) Burgina, E. B.; Kustova, G. N.; Tsybulya, S. V.; Kryukova, G. N.; Litvak, G. S.; Isupova, L. A.; Sadykov, V. A. *Journal of Structural Chemistry* **2000**, *41*, 396–402.

- (178) Eggleton, R. A.; Fitzpatrick, R. W. *Clays and Clay Minerals* **1988**, *36*, 111–124.
- (179) Souza, F. L.; Lopes, K. P.; Nascente, P. A.; Leite, E. R. *Solar Energy Materials and Solar Cells* **2009**, *93*, 362–368.
- (180) Allieta, M.; Marelli, M.; Malara, F.; Bianchi, C. L.; Santangelo, S.; Triolo, C.; Patane, S.; Ferretti, A. M.; Kment, Ponti, A.; Naldoni, A. *Catalysis Today* **2019**, *328*, 43–49.
- (181) Yang, Y.; Niu, S.; Han, D.; Liu, T.; Wang, G.; Li, Y. *Advanced Energy Materials* **2017**, *7*, 1–26.
- (182) Xie, J.; Liu, W.; Xin, J.; Lei, F.; Gao, L.; Qu, H.; Zhang, X.; Xie, Y. *ChemSusChem* **2017**, *10*, 4465–4471.
- (183) Jansi Rani, B.; Ravi, G.; Yuvakkumar, R.; Ravichandran, S.; Ameen, F.; AlNadhary, S. *Renewable Energy* **2019**, *133*, 566–574.
- (184) Lassoued, A. *Journal of Molecular Structure* **2021**, *1239*, 130489.
- (185) Krehula, S.; Ristić, M.; Kubuki, S.; Iida, Y.; Kratofil Krehula, L.; Musić, S. *Journal of Alloys and Compounds* **2016**, *658*, 41–48.
- (186) Li, M.; Yang, Y.; Ling, Y.; Qiu, W.; Wang, F.; Liu, T.; Song, Y.; Liu, X.; Fang, P.; Tong, Y.; Li, Y. *Nano Letters* **2017**, *17*, 2490–2495.
- (187) Quang, N. D.; Van, P. C.; Le, D. D.; Majumder, S.; Chinh, N. D.; Jeong, J.-R.; Kim, C.; Kim, D. *Applied Surface Science* **2021**, *558*, 149898.
- (188) Wang, Z.; Gu, Y.; Zheng, L.; Hou, J.; Zheng, H.; Sun, S.; Wang, L. *Advanced Materials* **2022**, *34*, 2106776.
- (189) Popov, N.; Ristić, M.; Robić, M.; Gilja, V.; Kratofil Krehula, L.; Musić, S.; Krehula, S. *Chemical Papers* **2021**, *75*, 6355–6366.
- (190) Popov, N.; Ristić, M.; Bošković, M.; Perović, M.; Musić, S.; Stanković, D.; Krehula, S. *Journal of Physics and Chemistry of Solids* **2022**, *161*, 110372.

Appendix A

Supplementary Information for: Identifying Interstitial Protons Through Structure-property Analysis

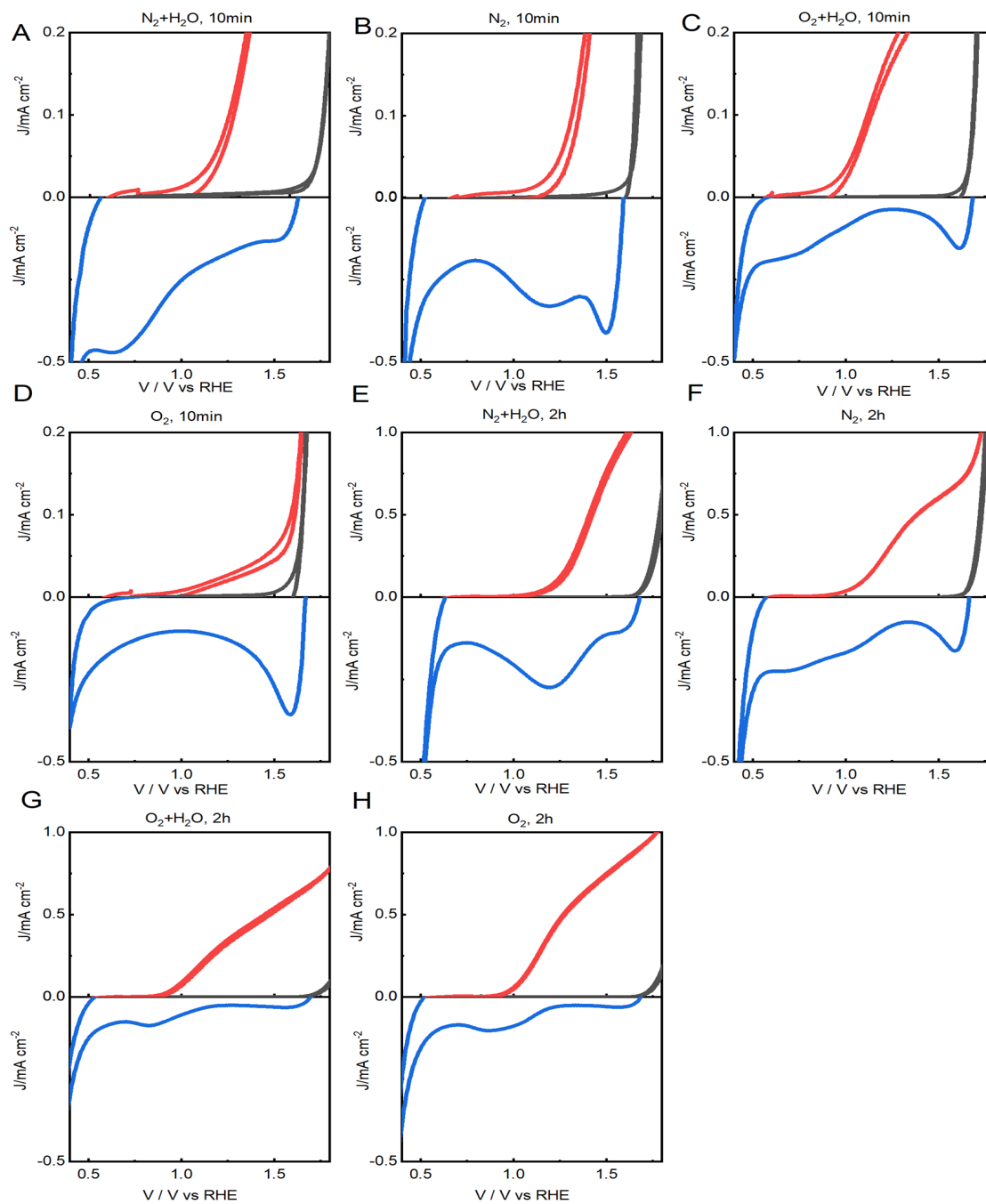


Figure A.1: Voltammetric behavior of $-\text{Fe}_2\text{O}_3$ photoanodes in the dark (black lines) and under illumination (red lines), and 1 V s^{-1} cathodic sweeps following equilibration at an oxidizing voltage while under illumination. Data is shown for samples heated at $800 \text{ }^\circ\text{C}$ for 10 minutes in (A) humidified N_2 , (B) dry N_2 , (C) humidified O_2 , (D) dry O_2 , and at $800 \text{ }^\circ\text{C}$ for 2 hours in (E) humidified N_2 , (F) dry N_2 , (G) humidified O_2 , (H) dry O_2 .

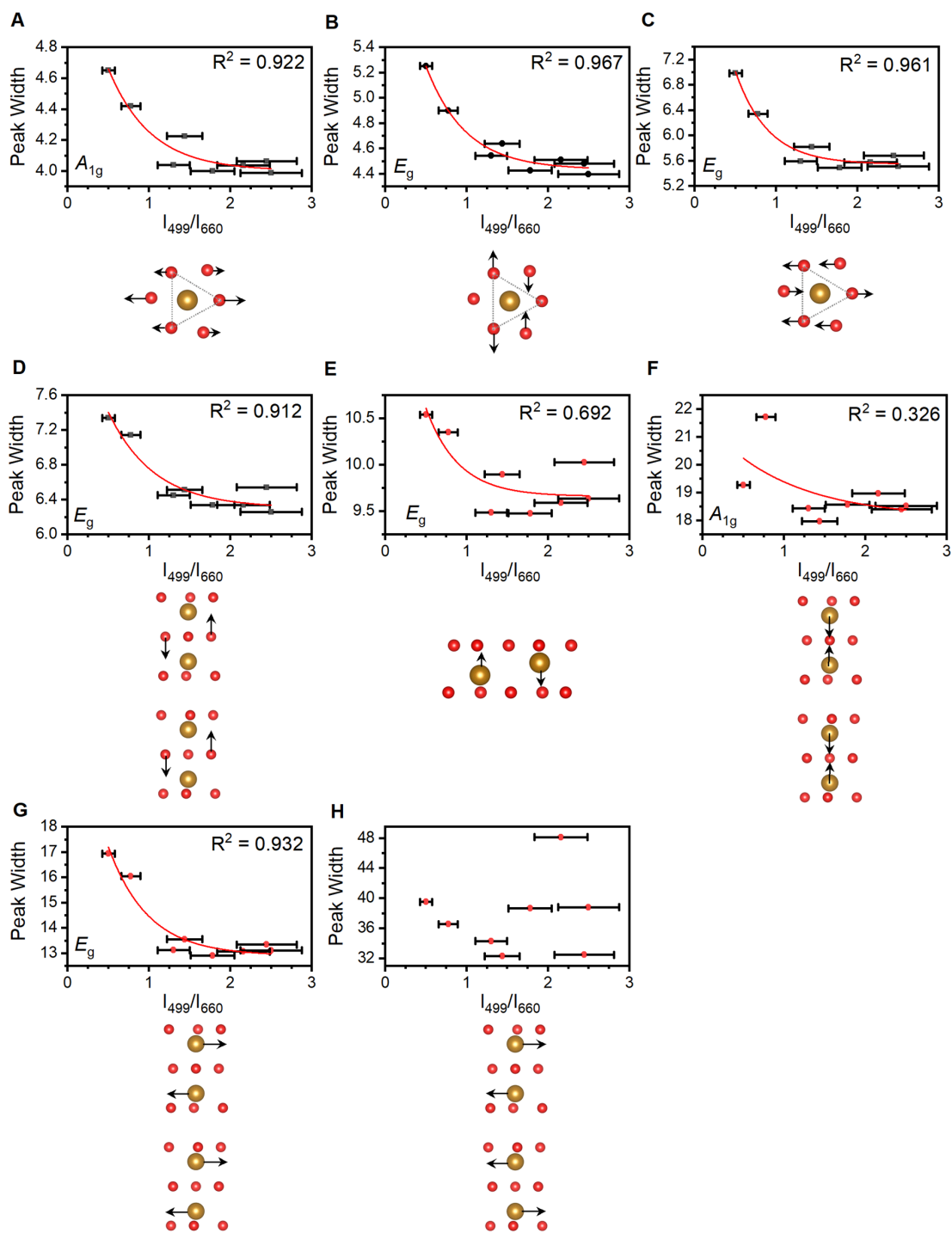


Figure A.2: Correlations between peak width and intensity ratio for observed features in the Raman spectra.

Appendix B

Supplementary Information for: Differentiate Iron and Oxygen Vacancies

Table B.1: Extended X-ray absorption fine-structure spectroscopy simulation parameters used in the first model.^a

Condition	$2\sigma_{\text{Fe-O1}}^2$	$2\sigma_{\text{Fe-O2}}^2$	$2\sigma_{\text{Fe-Fe1}}^2$	$2\sigma_{\text{Fe-Fe2}}^2$	$2\sigma_{\text{Fe-Fe3}}^2$	$2\sigma_{\text{Fe-Fe4}}^2$	E_o	R_f
N ₂ -0.2h ^b	0.0062 (0.0021)	0.0193 (0.0080)	0.0094 (0.0045)	0.0101 (0.0017)	0.0110 (0.0028)	0.0127 (0.0021)	3.86	24.79
N ₂ -0.5h ^b	0.0082 (0.0027)	0.0194 (0.0083)	0.0106 (0.0055)	0.0088 (0.0015)	0.0070 (0.0017)	0.0150 (0.0027)	4.42	17.86
N ₂ -1h ^b	0.0109 (0.0052)	0.0923 (0.1300)	0.0243 (0.0370)	0.0165 (0.0061)	0.0170 (0.0082)		1.74	59.68
N ₂ -2h ^b	0.0089 (0.0020)	0.0301 (0.0100)	0.0092 (0.0035)	0.0111 (0.0015)	0.0051 (0.0010)	0.0170 (0.0025)	4.24	19.91
N ₂ -4h ^b	0.0136 (0.0041)	0.0294 (0.0130)	0.0137 (0.0077)	0.0133 (0.0025)	0.0123 (0.0033)	0.0163 (0.0031)	4.66	29.71
O ₂ -0.2h ^c	0.0072 (0.0020)	0.0232 (0.0088)	0.0021 (0.0018)	0.0053 (0.0010)	0.0037 (0.0009)	0.0120 (0.0015)	3.86	18.32
O ₂ -0.5h ^c	0.0076 (0.0034)	0.0177 (0.0100)	0.0048 (0.0040)	0.0055 (0.0015)	0.0070 (0.0020)	0.0101 (0.0018)	4.38	26.99
O ₂ -1h ^c	0.0041 (0.0014)	0.0231 (0.0093)	0.0017 (0.0018)	0.0056 (0.0011)	0.0071 (0.0015)	0.0113 (0.0015)	3.42	19.66
O ₂ -2h ^c	0.0074 (0.0019)	0.0288 (0.0110)	0.0048 (0.0025)	0.0079 (0.0013)	0.0062 (0.0012)	0.0128 (0.0017)	3.75	19.99
O ₂ -4h ^c	0.0012 (0.0011)	0.0103 (0.0041)	0.0051 (0.0032)	0.0059 (0.0013)	0.0046 (0.0012)	0.0137 (0.0022)	4.30	19.82
O ₂ -8h ^c	0.0021 (0.0013)	0.0119 (0.0049)	0.0042 (0.0028)	0.0065 (0.0014)	0.0076 (0.0018)	0.0139 (0.0023)	4.20	23.13

Table B.2: Extended X-ray absorption fine-structure spectroscopy simulation parameters used in the second model.^a

Condition	$2\sigma_{\text{Fe-O1}}^2$	$2\sigma_{\text{Fe-O2}}^2$	$2\sigma_{\text{Fe-Fe1}}^2$	$2\sigma_{\text{Fe-Fe2}}^2$	$2\sigma_{\text{Fe-Fe3}}^2$	$2\sigma_{\text{Fe-Fe4}}^2$	$R_{\text{Fe-O1}}$	$R_{\text{Fe-O2}}$	$R_{\text{Fe-Fe1}}$	$R_{\text{Fe-Fe2}}$	$R_{\text{Fe-Fe3}}$	$R_{\text{Fe-Fe4}}$	E_o	R_f
N ₂ -0.2h	0.0048 (0.0027)	0.0163 (0.0100)	0.002b	0.0063 (0.0020)	0.0117 (0.0041)	0.0117 (0.0025)	1.9620 (0.0150)	2.1230 (0.0380)	2.8890 (0.0250)	3.0020 (0.0160)	3.3760 (0.0230)	3.7110 (0.0150)	6.52	23.81
N ₂ -0.5h	0.0059 (0.0016)	0.0118 (0.0036)	0.002b	0.0048 (0.0007)	0.0061 (0.0011)	0.0161 (0.0020)	1.9370 (0.0091)	2.0960 (0.0160)	2.8680 (0.0130)	2.9840 (0.0078)	3.3800 (0.0070)	3.6860 (0.0096)	5.09	11.28
N ₂ -1h	0.0090 (0.0024)	0.0740 (0.0360)	0.002b	0.0065 (0.0010)	0.0067 (0.0019)	0.0208 (0.0051)	1.9800 (0.0120)	1.9980 (0.1400)	2.8730 (0.0200)	3.0180 (0.0160)	3.4460 (0.0170)	3.6130 (0.0270)	5.54	20.51
N ₂ -2h	0.0086 (0.0028)	0.0238 (0.0120)	0.002b	0.0059 (0.0010)	0.0045 (0.0011)	0.0174 (0.0029)	1.9320 (0.0140)	2.0700 (0.0350)	2.8570 (0.0170)	2.9760 (0.0120)	3.3740 (0.0079)	3.6760 (0.0130)	3.76	15.48
N ₂ -4h	0.0094 (0.0034)	0.0106 (0.0047)	0.002b	0.0072 (0.0011)	0.0127 (0.0033)	0.0155 (0.0026)	1.9050 (0.0110)	2.0580 (0.0150)	2.8530 (0.0140)	2.9810 (0.0093)	3.3700 (0.0140)	3.6820 (0.0110)	3.50	21.39
O ₂ -0.2h	0.0061 (0.0015)	0.0135 (0.0039)	0.002b	0.0054 (0.0011)	0.0030 (0.0007)	0.0137 (0.0014)	1.9350 (0.0079)	2.0880 (0.0150)	2.8800 (0.0140)	2.9790 (0.0068)	3.3830 (0.0047)	3.6870 (0.0075)	4.96	8.52
O ₂ -0.5h	0.0056 (0.0024)	0.0103 (0.0049)	0.002b	0.0036 (0.0009)	0.0048 (0.0015)	0.0118 (0.0022)	1.9270 (0.0140)	2.0850 (0.0230)	2.8540 (0.0210)	2.9750 (0.0120)	3.3890 (0.0100)	3.6790 (0.0110)	4.67	17.47
O ₂ -1h	0.0036 (0.0017)	0.0175 (0.0084)	0.002b	0.0069 (0.0028)	0.0068 (0.0019)	0.0120 (0.0020)	1.9530 (0.0099)	2.1180 (0.0290)	2.8990 (0.0250)	2.9900 (0.0110)	3.3870 (0.0110)	3.7060 (0.0120)	5.94	16.63
O ₂ -2h	0.0085 (0.0025)	0.0387 (0.0250)	0.002b	0.0062 (0.0013)	0.0061 (0.0015)	0.0133 (0.0020)	1.9600 (0.0150)	2.0570 (0.0710)	2.8730 (0.0200)	2.9870 (0.0130)	3.3730 (0.0110)	3.6940 (0.0130)	4.61	14.96
O ₂ -4h	0.0016 (0.0013)	0.0118 (0.0057)	0.002b	0.0063 (0.0028)	0.0052 (0.0016)	0.0133 (0.0026)	1.9390 (0.0096)	2.1100 (0.0240)	2.8970 (0.0270)	2.9920 (0.0120)	3.3660 (0.0110)	3.6950 (0.0140)	4.88	17.63
O ₂ -8h	0.0019 (0.0009)	0.0102 (0.0033)	0.002b	0.0047 (0.0009)	0.0052 (0.0011)	0.0164 (0.0024)	1.9470 (0.0067)	2.1210 (0.0150)	2.8660 (0.0150)	2.9800 (0.0081)	3.3950 (0.0071)	3.6890 (0.0100)	5.75	12.83

Table B.3: Normalized intensity of individual peaks in Raman spectrum for the hematite sample series.

Condition	I_{227}	I_{246}	I_{293}	I_{300}	I_{411}	I_{491}	I_{612}	I_{660}
N ₂ -0.2h	0.86	0.21	0.88	0.34	0.50	0.11	0.34	0.18
N ₂ -0.5h	0.99	0.15	0.91	0.34	0.50	0.12	0.32	0.19
N ₂ -1h	1.00	0.05	0.43	0.35	0.25	0.08	0.16	0.11
N ₂ -2h	0.98	0.22	0.91	0.38	0.53	0.12	0.26	0.11
N ₂ -4h	1.00	0.14	0.35	0.60	0.37	0.07	0.22	0.13
O ₂ -0.2h	0.80	0.23	0.89	0.42	0.63	0.08	0.31	0.08
O ₂ -0.5h	0.85	0.23	0.80	0.37	0.57	0.08	0.27	0.12
O ₂ -1h	0.80	0.23	0.96	0.44	0.67	0.08	0.32	0.10
O ₂ -2h	0.88	0.19	0.90	0.39	0.52	0.08	0.25	0.06
O ₂ -4h	0.75	0.22	0.92	0.45	0.62	0.08	0.29	0.07
O ₂ -8h	0.81	0.21	0.96	0.44	0.60	0.07	0.29	0.059

Table B.4: Full width at half mass of individual peaks in Raman spectrum for the hematite sample series.

Condition	W_{227}	W_{246}	W_{293}	W_{300}	W_{411}	W_{491}	W_{612}	W_{660}
N ₂ -0.2h	4.2	8.1	6.2	8.5	9.9	43.8	15.5	60.8
N ₂ -0.5h	4.7	6.3	6.6	8.0	11.0	31.8	17.9	51.6
N ₂ -1h	5.0	6.2	5.3	16.7	12.1	18.6	26.3	48.9
N ₂ -2h	4.5	5.7	6.5	7.6	10.4	35.3	15.6	69.9
N ₂ -4h	4.5	11.3	3.9	15.7	10.6	17.1	24.8	56.9
O ₂ -0.2h	4.2	5.6	6.1	7.1	9.9	27.9	14.3	46.6
O ₂ -0.5h	4.5	8.2	6.7	11.2	10.3	19.3	14.7	73.6
O ₂ -1h	4.0	4.6	5.7	6.3	9.6	19.7	13.4	30.6
O ₂ -2h	4.1	5.6	5.9	7.1	10.0	26.6	14.2	51.6
O ₂ -4h	3.9	4.6	5.6	6.4	9.6	19.7	13.6	34.0
O ₂ -8h	4.0	4.4	5.5	6.3	9.6	18.7	13.1	34.75

Table B.5: Location of individual peaks in Raman spectrum for the hematite sample series.

Condition	L_{227}	L_{246}	L_{293}	L_{300}	L_{411}	L_{491}	L_{612}	L_{660}
N ₂ -0.2h	226.97	245.93	293.07	300.01	411.62	490.85	611.90	659.30
N ₂ -0.5h	226.66	245.63	292.92	300.00	411.32	493.27	611.92	660.48
N ₂ -1h	226.92	246.08	293.14	295.74	411.18	498.36	612.02	655.59
N ₂ -2h	227.26	246.31	293.56	300.76	412.06	492.66	612.39	655.73
N ₂ -4h	226.81	246.00	292.81	295.10	411.22	497.70	611.63	654.43
O ₂ -0.2h	226.86	246.03	293.11	299.93	411.67	494.72	611.88	659.84
O ₂ -0.5h	226.77	245.72	292.92	299.61	411.46	490.60	611.56	658.14
O ₂ -1h	227.61	246.81	293.88	300.55	412.43	496.25	612.74	661.05
O ₂ -2h	227.01	246.20	293.24	300.19	411.88	495.23	612.15	659.44
O ₂ -4h	227.84	247.03	294.06	300.73	412.69	496.40	613.02	660.91
O ₂ -8h	226.41	245.68	292.66	299.34	411.33	495.70	611.69	659.85